UNIVERSITY COLLEGE LONDON

Dynamics of Spatially Evolving Dispersed Flows

by
Victor Voulgaropoulos

Submitted to the Department of Chemical Engineering
in partial fulfilment of the requirements for the degree of

Doctor of Philosophy in Chemical Engineering

at University College London

November, 2017

"Science always presupposes the existence of man and we must become conscious of the fact that we are not merely observers but also actors on the stage of life."

Werner Heisenberg

I, Victor Voulgaropoulos, confirm that the work presented in this thesis is my own. Where information has been derived from other sources, I confirm that this has been indicated in the thesis.

November 2017

London, United Kingdom

Abstract

Dynamics of Spatially Evolving Dispersed Flows

by

Victor Voulgaropoulos

Submitted to the Department of Chemical Engineering
on November 10, 2017, in partial fulfilment of the
requirements for the degree of
Doctor of Philosophy in Chemical Engineering

This dissertation provides a unique insight into the flow dynamics of evolving dispersed pipe flows. Kinetically unstable liquid-liquid dispersions are actuated in two horizontal flow loop systems. Novel conductivity and optical laser-based experimental methods are developed and applied at several axial locations capturing the flow characteristics and separation properties of the dispersions downstream the pipe with combined measurements of drop sizes, phase fractions and velocities.

Flow pattern transitions are recorded for low mixture velocities as the dispersions flow. Drops segregate and coalesce forming a second continuous layer. Drop size measurements exhibit growth of the drops along the streamwise direction independent of the flow pattern, with larger drops recorded closer to the direction of buoyancy. A phenomenological model based on batch vessel settlers is modified and is found to predict well the axial evolution of the dispersions. Holdup and velocity measurements acquired from laser diagnostics are compared with CFD predictions obtained using a mixture approach implementing an effective viscosity model. Good comparisons are obtained by considering sedimentation, shear-induced diffusion and lift. The dispersions behave as suspensions of solid rigid spheres for the conditions investigated. Asymmetry in the velocity profiles is found for both experiments and simulations as the dispersions separate, with the maxima of the velocity located in the drop-free layer.

Due to the prominent role of coalescence in the system, its dynamics are studied both during pipe flow and in a Hele-Shaw cell. For the former, high resolution velocity field measurements illustrate the vortices generated from the rupture point of the film inside a coalescing drop and its expanding neck until it fully merges with the bulk, being in agreement with scaling laws for immobile systems. The latter cases are used to investigate the effect of surface active agents and complex fluids. Surfactants are found to deform the interface, increase locally their concentration at the neck and change the propagation direction of the vortices. Xanthan gum addition in the coalescing phase slows down the neck expansion velocity and causes a spatial variation of the viscosity affecting the velocity field inside the drop.

Acknowledgements

I am deeply grateful to my supervisor Prof. Panagiota Angeli for her advice, patient guidance, and for shaping me as a scientist. I am sincerely thankful for all the opportunities she provided to disseminate my work and for going out of her way to support me through these three years. I also want to thank Chevron Corporation for sponsoring this project and especially Dr. Karolina Ioannou, Dr. Carlos Avila and Dr. Lee Rhyne for their insightful comments and suggestions.

This work would not be the same if it were not for Dr. Maxime Chinaud. I appreciate the time spent with me, discussing experimental techniques, exploring the beauty of fluid dynamics, and talking about politics and history. I want to thank Dr. Rashid Jamshidi for all the help with the numerical simulations and for the engaging discussions on the physics of two-phase flows. I would also like to acknowledge the help from Dr. Lusheng Zhai, Dr. Simon Barras and Albert Corredera in the design of the circuit for the conductivity probe, and the mechanical workshop for manufacturing the test section of the flow loops and the Hele-Shaw cell.

I want to thank all the members of the Advanced Multiphase Systems (ThAMeS) group for their collaborative attitude and joyful spirits that I will certainly miss. Last but not least, I would like to thank my parents Tania and Pavlos, and my brother Ilias for their unconditional love, untiring support and unwavering confidence in me for all the things great and small.

Contents

List of Figures

List of Tables

List of Abbreviations

Ar	Archimedes number
BF	bright-field
Bo	Bond number
Bu	Buoyancy number
Ca	Capillary number
CC	cross-correlation
CAD	computer aided design
CAF	core annular flow
CDF	cumulative distribution function
CFD	computational fluid dynamics
CHT	circular Hough transform
CLAHE	contrast-limited adaptive histogram equalisation
DC	dual-continuous flow
DCP	dual conductance probe
De	Deborah number
DFT	discrete Fourier transformation
DOF	depth of field
ERT	electrical resistance tomography
FBRM	focus beam reflectance measurement
Fr	Froude number
ID	inner diameter
ILV	inertially limited viscous
KHI	Kevin-Helmholtz instability
La	Laplace number
LAR	least absolute residuals
LBP	linear back projection
LSCM	laser scanning confocal microscopy
LV	lower vortex
o/w	oil in water dispersion
o/w & w	oil in water dispersion with a drop-free water layer
o/w & w & o	oil in water dispersion with a drop-free water layer and an oil continuous layer
OD	outer diameter
Oh	Ohnesorge number
Pe	Péclet number
PIV	particle image velocimetry

PLIF	planar laser induced fluorescence
PMMA	polymethylmethacrylate
PTFE	polytetrafluoroethylene
PTV	particle tracking velocimetry
PVC	polyvinyl chloride
QCV	quick closing valves
RM	relaxation method
RMS	root-mean-square
Re	Reynolds number
St	Stokes number
ST	stratified flow
TLM	transmission light microscopy
UV	upper vortex
Vi	viscosity number
w/o	water in oil dispersion
We	Weber number

List of Symbols

Roman		
a	drop or particle radius	m
a	parameter in eq. 2.6	$-$
a_i	parameters in eq. 5.7 and eq. 5.8	$-$
A	area	m^2
b	turbulent kinetic energy ratio of carrier to dispersed phase	$-$
b	parameter in eq. 2.6	$-$
B	parameter in eq. 2.8	$-$
c	mass fraction	$-$
c	molar concentration	$\mathrm{mol\,m^{-3}}$
C_1, C_2	coefficients in eq. 2.32	$-$
C_D	drag coefficient	$-$
C_H, C_K	respective coefficients in eqs. 2.42 and 2.44	$-$
C_W	friction coefficient in eq. 2.27	$-$
$\mathcal{C}$	coordinate of the centre of a drop	m
d	drop diameter $\equiv 2a$	m
d_{32}	Sauter mean drop diameter	m
D	pipe diameter	m
$\mathcal{D}$	diffusivity coefficient	$-$
$\mathcal{D}_\Gamma$	surface diffusivity coefficient	$-$
e	rate of energy dissipation per unit mass	$\mathrm{J\,s^{-1}\,kg^{-1}}$
E_p	evolution parameter	$-$
f	friction factor	$-$
f_h	hindrance function of v_t	$-$
F_B	buoyancy force	N
F_L	lift force	N
F_P	pressure force	N
F_V	asymmetrical component of F_P during film drainage	N
F_Z	symmetrical component of F_P during film drainage	N
F_σ	interfacial tension force	N
g	acceleration due to gravity	$\mathrm{m\,s^{-2}}$
h	layer thickness	m
h_{py}	drop packing height above coalescing drop	m
I	image/pixel intensity	$-$
j	slope of DCP sensor signal	$\mathrm{V\,s^{-1}}$

k	wavenumber	$\mathrm{rad\,m^{-1}}$
k_d	proportionality constant in eq. 4.14	–
$\mathcal{k}$	thickness ratio parameter in eq. 2.6	–
$\mathrm{K_{HR}}$	Hadamard-Rybczynski factor in eq. 2.27	–
K_L	equilibrium constant in Langmuir isotherm	$\mathrm{m^3\,mol^{-1}}$
K_ε	proportionality constant in eq. 2.15	–
K_η	proportionality constant in eq. 2.16	–
l	wave mode	rad
ℓ_k	Kolmogorov microscale	m
L	length	m
$\mathcal{L}$	turbulence fluctuation scale	m
m	parameter in eq. of footnote 3	–
$\mathcal{m}$	viscosity ratio parameter in eq. 2.6	–
n	refractive index	–
$\mathcal{n}$	paremeter in eq. 2.7	–
$\hat{n}$	power index in the Carreau model eq. 3.4	–
N	number of sample	–
N_d	drop flux due to collision and viscosity effects	$\mathrm{m^2\,s^{-1}}$
N_ε	drop flux due to collision frequency gradients	$\mathrm{m^2\,s^{-1}}$
N_η	drop flux due to viscosity gradients	$\mathrm{m^2\,s^{-1}}$
p	pixel neighbourhood	–
P	pressure	Pa
Q	volumetric flow rate	$\mathrm{m^3\,s^{-1}}$
r	radius	m
r_a	radius of channel contour in dense-packed arrangement	m
r_F	radius of contact area during film drainage	m
r_V	asymmetry radius during film drainage	m
R	radius of curvature	m
$\mathcal{R}$	cross-correlation function	–
$\mathcal{R}^2$	coefficient of determination	
$\tilde{R}$	universal gas constant($\equiv$ 8.314J $\mathrm{mol^{-1}\,K}$)	$\mathrm{J\,mol^{-1}\,K}$
s	standard deviation of a sample	
$\hat{s}$	standard deviation of a log-normally distributed sample	
S	perimeter	m
t	time	s
t_h, t_l	upper and lower velocity thresholds in eq. 3.15	$\mathrm{m\,s^{-1}}$
T	total time	s
$\mathcal{T}$	temperature	K
u	streamwise velocity	$\mathrm{m\,s^{-1}}$
u'	streamwise velocity fluctuation	$\mathrm{m\,s^{-1}}$
u^*	streamwise friction velocity	$\mathrm{m\,s^{-1}}$
u^+	normalised streamwise velocity	–

u_L	lift velocity	meter/s
u_{light}	velocity of light	meter/s
u_r	streamwise relative velocity	$\mathrm{m\,s^{-1}}$
U	velocity	$\mathrm{m\,s^{-1}}$
v	vertical velocity	$\mathrm{m\,s^{-1}}$
v'	vertical velocity fluctuation	$\mathrm{m\,s^{-1}}$
V	voltage	V
$\mathcal{W}$	interrogation window size	m
x	axial length	m
x^+	normalised axial length	–
$\tilde{x}$	axial length where settling/floatation stops	m
X	length	m
y	vertical length	m
y^+	normalised vertical length	–
z	depth	m
z^+	normalised depth	–

Greek

α	proportionality constant in eq. 6.6	–
β	difference of radii of two circles/drops	pixels/m
$\hat{\beta}$	parameter in eq. 3.12	pixels/m
$\dot{\gamma}$	shear rate	$\mathrm{s^{-1}}$
$\dot{\underset{\sim}{\gamma}}$	shear rate tensor	$\mathrm{s^{-1}}$
Γ_ω	circulation based on an iso-contour of vorticity	$\mathrm{s^{-1}}$
Γ	surface excess of the surfactant	$\mathrm{mol\,m^{-2}}$
δ	distance between the centres of two circles/drops	pixels/m
ε	local in-situ volume fraction	–
$\tilde{\varepsilon}$	local in-situ volume fraction where settling/floatation stops	–
η	viscosity	Pa s
$\hat{\eta}$	effective shear viscosity	Pa s
θ	angle of incident light	rad
ϑ	angle	rad
$\varkappa$	parameter in eq. 2.8	–
κ	electrical conductivity	$\mathrm{S\,m^{-1}}$
$\tilde{\kappa}$	reconstructed electrical conductivity from the LBP	$\mathrm{S\,m^{-1}}$
λ	wavelength	m
$\hat{\lambda}$	relaxation time in the Carreau model eq. 3.4	s
μ	mean of a sample	
$\hat{\mu}$	mean of a log-normally distributed sample	
ν	settling/floatation parameter in eq. 2.27	–
ξ	settling/floatation parameter in eq. 2.27	–
ξ	growth exponent in eq. 6.1	–

π	circumference to diameter ratio of a circle	$-$
ρ	volumetric mass density	$\mathrm{kg\,m^{-3}}$
σ	interfacial tension	$\mathrm{N\,m^{-1}}$
τ	shear stress	N
τ_d	coalescence time of drops	s
τ_{delay}	delay time of cross-correlation	s
$\tau_{\mathcal{D}}$	time-scale of diffusion	s
τ_{iner}	inertial time-scale during coalescence	s
τ_I	coalescence time of drop/interface	s
τ_k	Kolmogorov timescale	s
τ_p	relaxation time of drops/particles	s
τ_{visc}	viscous time-scale during coalescence	s
φ	input volume fraction	$-$
χ	parameter in eq. 2.32(b)	$-$
$\hat{\psi}$	drop growth rate	$\mathrm{s^{-1}}$
ω	vorticity	$\mathrm{s^{-1}}$
ω_l	wave pulsation frequency of mode l	$\mathrm{rad\,s^{-1}}$

Subscripts

$annulus$	annulus
c	continuous or carrier phase
ca	Capillary
$crit$	critical
d	dispersed or drop phase
$equiv$	equivalent
f	floating
i	index
$iner$	inertia
inv	inversion
I	interface
j	index
m	mixture
max	maximum
n	neck
$nozzle$	nozzle
o or oil	organic, oil phase
p	packed-region
p	particle
res	residence
s	settling
t	terminal
$total$	total

$visc$	viscous
w or $water$	aqueous or water phase
$wall$	wall
$wave$	wave
WRS	water-reach stream
x, y, z	spatial coordinates
0	initial or zero
32	Sauter mean
95	95^{th} percentile of the overall distribution
∞	infinite

To my parents,
Tania Marioglou & Pavlos Voulgaropoulos

Chapter 1

Introduction

1.1 Motivation

Liquid-liquid pipe flows are commonly encountered in many engineering applications and predominantly in the oil and gas industry. New development challenges lie in deepwater and in marginal fields with smaller reserves (Lake and Holstein 2007). For heavy oils and mature wells, waterflooding is essential for efficient production. However, increased levels of water in the pipelines impact the flow and spatial configuration of the two phases. Considering the increased cost of these upstream processes with the recent trends in farther offshore drilling, flow assurance is key in successfully accounting for such effects and designing optimal transport and separation operations. In the recent years, as discussed in the review by Wu et al. (2016), subsea separation facilities have been an attractive method towards reducing cost and space for deepwater operations at remote areas.

Especially in deepwater, subsea or arctic fields, pipe separators are frequently used for oil-water mixtures (Grave et al. 2015). The pipes are usually of relatively small diameter to allow shorter sedimentation distances for the drops. Horizontal orientation is preferable for oil-water pipe separators, because gravity enhances sedimentation dynamics, compared to vertical pipes. Spatially evolving dispersed flows at low velocities are commonly encountered in these pipes as shown in Fig. 1.1. The oil drops float due to buoyancy effects and change their size due to coalescence, while generation of a second continuous layer is expected as the dispersion flows along the pipe. The changes in the topology of the two phases play an important role in the effective viscosity of the mixture, which affects pressure drop in the pipeline.

Understanding the local fluid dynamics and the separation properties of oil-water mixtures is a crucial step towards improving flow assurance in such processes. Experimental data are very important towards that direction. Most field measurements are usually conducted with flowmeters, which are limited to information on overall in-situ phase fractions and pressure drops (Oddie and Pearson 2004). Further details on the spatial evolution of the distribution of the phases, drop size distributions and velocity fields are needed, as these parameters control the main separation characteristics. The lack of such data constrains current modelling efforts, which

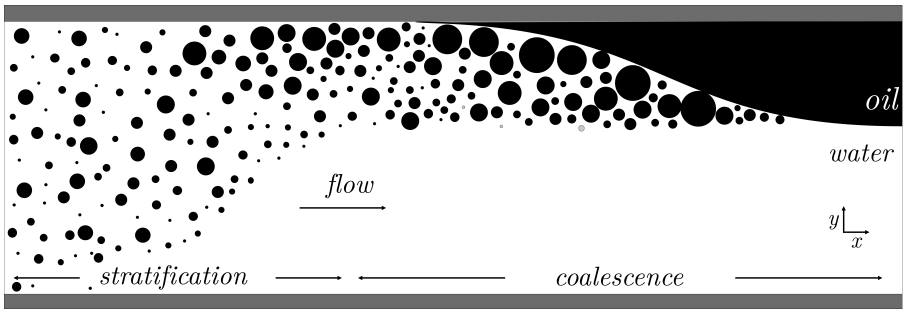

Figure 1.1: Illustration of the problem: Oil in water dispersion gradually separating as it flows.

vary from multiphase simulators such as OLGA and Leda Flow to more elaborate computational fluid dynamics (CFD) models, based on a variety of approaches such as finite element/volume, Reynolds averaged Navier-Stokes and direct numerical simulations (Ekambara et al. 2008; Pouraria et al. 2016; Xie et al. 2017). Drop size evolution dynamics have also troubled the community with very few works directly predicting the change in the distribution of drop size during pipe flows through population balance equation (PBE) models (Bourdillon et al. 2016).

1.2 Objectives

This work builds on previous projects in the same framework of liquid-liquid pipe flows. Recent works have tackled problems concerning flow assurance applications, such as phase inversion (Hu 2006; Ioannou 2006; Ngan 2011) and interfacial wave characteristics (Barral 2014), by conducting detailed experimental measurements in the pilot-scale facilities at the Department of Chemical Engineering, University College London. The nature of the present work is also mainly experimental, and follows up on recent findings in liquid-liquid systems, while aims to extend current understanding on the dynamics of spatially evolving and concentrated liquid-liquid dispersed pipe flows.

To reproduce the conditions typically encountered in in-line separators (Fig. 1.1), kinetically unstable dispersed flows will be generated with different mixers at low velocities. Measurements will be conducted at several axial (streamwise) locations downstream the mixer in two horizontal pipe flow loops to investigate the evolution and separation properties of the mixture along the pipe. Conductivity measurements with dual-conductance probes, developed based on previous efforts (Lovick and Angeli 2004a; Ioannou et al. 2005), are implemented in a $37\ \mathrm{mm}$ ID pipe of approximately $7\ \mathrm{m}$ length, for a water-kerosene flow. An additional electrical resistance tomography (ERT) system will be used, following the work by Ngan et al. (2011), together with quick closing valves (QCV) to test the accuracy of the probe. The goal of these measurements is to acquire information on the drop size distributions along the axial and vertical (normal direction to the pipe wall) directions. To further investigate the drop size distributions and how the packing of the drops affects the

flow characteristics in the pipe, additional experiments will be conducted in a 26 mm ID pipe of approximately 4 m length, containing a water/glycerol mixture and silicone oil. The two phases share the same refractive index and thus accurate optical measurements in dense dispersed flows are possible.

As velocities are kept low and turbulent dispersive forces are weak, sedimentation or floatation due to gravity takes place, which depends on the density difference between the drops and the continuous phase. While the effects of packing have been shown to significantly affect the velocity fields in suspensions (Yan and Koplik 2009) and gas-liquid (Ekambara et al. 2008) horizontal flows at low velocities, the same trends have not been sufficiently explored in liquid-liquid systems. The packing of the drops causes a stratification of the local apparent viscosity and density of the mixture, leading to collective effects that can significantly influence the flow characteristics and pressure drop. The interactions between the drops and the continuous phase together with the effects of the spatial configuration of the phases on the flow will be investigated.

As coalescence is dominant at low Reynolds numbers, it is important to explore its dynamics in liquid-liquid systems. While coalescence between drops understandably causes an increase in the drop size of the population, when it takes place close to the wall and a continuous film of the dispersed phase is generated, the dynamics are more complex. The film gradually expands due to further drop-interface coalescence and in turn a flow pattern transition occurs. Understanding these coalescence mechanisms during pipe flow is crucial for the separation properties of the dispersion. Indirect measurements of the coalescence efficiency will be conducted in this work by tracking the changes in the drop size distributions as the dispersion evolves. Additional time-resolved high-speed measurements will be used to capture this phenomenon as they can provide direct information on the mechanism, while experiments in confined systems will explore how surfactants and complex fluids can affect these dynamics during the coalescence, as these additives are usually naturally present in crude oils.

The objectives of this work can be summarised as follows:

- Characterise the spatial configuration of the two phases and the complex flow patterns that occur during liquid-liquid flows.
- Analyse the drop size distributions along the axial (streamwise) and vertical (crossstream) direction.
- Predict the phase separation dynamics at low velocity dispersed flows.
- Study experimentally and predict numerically the impact of the segregation of the two-phases on the velocity field.
- Investigate the coalescence mechanism during pipe flow and compare with the dynamics in confined systems.

1.3 Outline

The dissertation is structured in seven Chapters. A brief introduction to the topic and current state of art was given in this Chapter and a thorough literature review follows in Chapter 2. The aim is to outline the fundamental theory needed to understand and predict the phenomena observed in the experiments. Starting from pipe flow theory in dispersed conditions, the effects of drops on the flow field are discussed. An examination on the forces acting on the dispersed phase and the motion of the drops is given together with explanations of the physical mechanisms that can affect the drop size distributions. The framework for the models predicting the separation dynamics and the velocity field are also provided. Chapter 3 describes in detail the experimental systems along with the techniques implemented to acquire in-situ information on the phase fractions, drop size distribution and the velocities of both phases.

Chapters 4 and 5 present a discussion of the results that were acquired with the dual conductance probe and through optical measurements respectively. The results are coupled with predictions from a mechanistic model to investigate the connection between batch settlers in vessels and pipe separators similarly to Pereyra et al. (2013). The optical measurements capture the velocity field and are compared to the results from numerical simulations based on a mixture modelling approach. Chapter 6 of this dissertation is a study on coalescence between a drop and a flat interface, motivated by the coalescence observed during pipe flow. The effects of surfactants and complex fluids are discussed. Finally, Chapter 7 summarises all important conclusions and gives recommendations for future work.

Chapter 2

Background and Theoretical Considerations

2.1 Pipe flow

In this Section, the theory and literature describing the characteristics of the spatial configuration of the two-phases in horizontal pipe flows are discussed and the resulting velocity fields under different Re conditions are analysed.

2.1.1 Flow structures

2.1.1.1 Patterns

When two immiscible liquids are introduced into a pipe they can create different structures depending on certain parameters including fluid properties, pipe geometry and operating conditions (Angeli and Hewitt 2000a; Brauner 2003). As discussed in Chapter 1, the flow pattern identification is crucial for the design and operation of oil and gas facilities. Four main flow patterns exist in the literature of horizontal liquid-liquid pipe flows and they are schematically illustrated in Fig. 2.1. A review dealing with the patterns encountered is given by Ibarra et al. (2014). Various experimental methods have been implemented to investigate the flow patterns in lab-scale facilities. The main methods include optical measurements (e.g. direct visualisations (Grassi et al. 2008), planar laser induced fluorescence (PLIF) (Liu et al. 2006), optical probes (Chakrabarti et al. 2007), conductivity probes (Angeli and Hewitt 2000a; Zhai et al. 2012; Voulgaropoulos et al. 2016) together with electrical resistance (Ngan et al. 2011), gamma densitometers (Soleimani et al. 2000) and X-ray (Schümann et al. 2016a) tomography systems.

Stratified (*ST*) flow has been well established in the literature, with works exploring mainly the interface location and curvature analytically (Brauner et al. 1998) and numerically (Ng et al. 2002). The transitions from stratified flow have been explored both theoretically and experimentally (Yiantsios and Higgins 1988; Brauner and Maron 1992; Al-Wahaibi and Angeli 2007), while they still remain an active topic of research (Barral and Angeli 2014; Barmak et al. 2016). The goal of these works is to investigate the initiation and growth of interfacial waves that can cause ligament

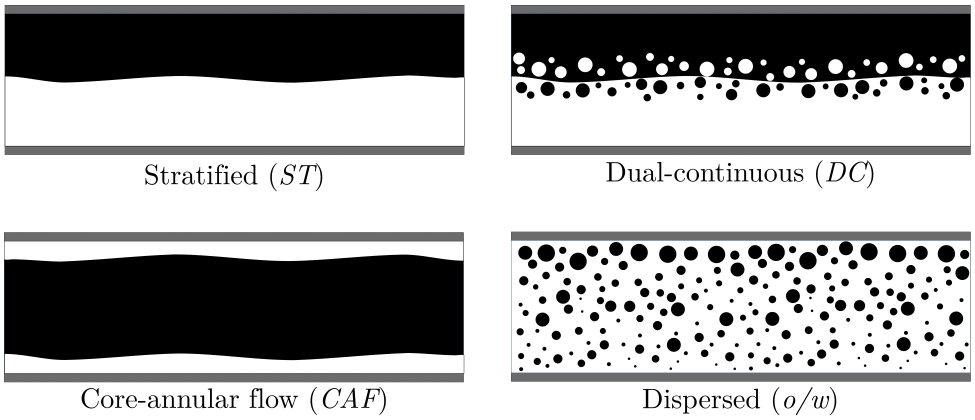

Figure 2.1: Illustrations of the main flow patterns observed during horizontal liquid-liquid pipe flows. Black denotes the oil phase, while white the water phase.

breakup and droplet generation with entrainment. Recently, the ligament breakup mechanism was localised with a cylindrical bluff body immersed below the interface level (Chinaud et al. 2017). Information on the wave frequency and the flow characteristics was given experimentally through particle image velocimetry (PIV) measurements.

Once drops appear at the interface, the flow pattern transitions to a dual-continuous configuration (*DC*), where both phases are continuous, with drops entrained on either or both phases (Fig. 2.1). This pattern has many sub-categories, which depend on the density, location and nature of the drops. Several works have been dedicated on studying this flow configuration, with Trallero et al. (1997), Lovick and Angeli (2004b), and Rodriguez and Oliemans (2006) investigating the pattern onset boundaries, its pressure drop and the shape of the interface. The drop size distributions close to the interface have also been explored (Lovick and Angeli 2004a), with higher drop sizes located closer to the interface level. Recently, the PLIF technique was employed to investigate both the interfacial characteristics and the relevant drop sizes (Morgan et al. 2012; Morgan et al. 2017). When the velocities are sufficiently high, the interfacial waves become very strong, and one of the continuous phases breaks down completely to entrained drops. This pattern is called dispersed flow and will be discussed in more detail in the next Section.

Core-annular flow (*CAF*) appears as the most attractive flow configuration for transporting viscous oils, where usually the low viscosity water phase wets the walls and thus decreases pressure losses (Brauner 2003). Fundamental work was conducted by Oliemans (1986), which illustrated the hydrodynamic stability of *CAF*, while Ooms and Poesio (2003) expanded these findings by theoretically investigating the interfacial wave characteristics of the annulus and their link to the pattern stability. In laboratory scale experiments, stable *CAF* is not commonly encountered. It only occurs for a limited range of velocities, small diameter pipes (Al-Wahaibi and Angeli 2007) and very high viscosity oils (> 0.5 Pa s) (Oliemans 1986), as the viscosity forces need to be strong enough to counteract the effects of buoyancy and shear,

so the flow can be considered quasi-stable in time.

Dispersed pipe flows of two-immiscible liquids are often observed, where one phase is entrained in the form of drops in the other continuous phase. Depending on the entrained phase, the patterns are categorised as water in oil (*w/o*) or oil in water (*o/w*) dispersions (cf. Fig. 2.1). Similarly to *CAF*, *o/w* dispersed flow configuration can be exploited to transfer high viscosity oils with small pressure losses, as long as the dispersed phase fraction is kept low and the velocities relatively high (Pilehvari et al. 1988). Dispersed flows will be characterised in terms of a homogeneous (mixture) approach in this work; the mixture viscosity, the slip velocity between the dispersed and continuous phase, along with the drop size characterisation will be considered, as they controls the interfacial area between the two phases and the separation dynamics causing flow pattern transitions.

2.1.1.2 Dispersed flow evolution

A number of researchers have investigated liquid-liquid horizontal dispersed pipe flows over the years by mainly conducting drop size measurements. A comprehensive list is provided in Table 2.1 – where papers in journals or conference proceedings were available, the corresponding PhD theses were omitted.[1] Due to the challenging nature of drop size measurements, a variety of techniques has been implemented during the years. While conductivity techniques have matched well with direct visualisations with an endoscope (Angeli and Hewitt 2000b), optical measurements have not been met with the same success. Simmons et al. (2000) compared the results between a laser diffraction and a laser backscatter technique for liquid-liquid dispersed flows and found significant deviations. Maaß et al. (2011) compared optical reflectance measurements with a fibre optical sensor and a focus beam reflectance measurement (FBRM) system. While the probes did manage to capture the trends, large deviations were recorded compared to direct visualisations. Maaß et al. (2011) underlined the need to calibrate any data recorded from such probes. A more recent work by Morgan et al. (2013) using planar laser induced fluorescence has provided promising results.

While Table 2.1 paints the picture that a rigorous database of experimental measurements is readily available, this is not the case. Most works involve limited and very low phase fractions and the dispersions are usually actuated from strong turbulent dispersive forces. For this reason, they can be considered quasi-stable in space. Yang (2014) showed that for a mixture (average) velocity $u_m = 2\,\mathrm{m\,s^{-1}}$ the drop size does not considerably change between $\sim 250D$ equivalent pipe diameters. In this work, the interest is shifted in spatially evolving dispersions (unstable) and thus it is crucial that drop size measurements take place at more than one axial location (x)

1. There have also been works on drop size measurements in vertical liquid-liquid systems, conducted with various experimental techniques (Hamad et al. 2000; Nigmatulin et al. 2000; Galinat et al. 2005; Hu and Angeli 2006; Augier et al. 2007; Hamad and Ganesan 2015; Han et al. 2017), but will not be discussed in this dissertation.

Table 2.1: Works on drop size measurements in liquid-liquid horizontal pipe flows

	Pipeline			Fluids		Experimental Runs			Drop Sizes	
	Material	ID mm	Inlet/Mixer	x, y positions D	η_{oil} mPa s	σ mN m^{-1}	Dispersion	φ_d %	Flow	Measurement	Technique
Scott et al. (1958)	aluminium	25.4	orifice	x: 7	∼1.64	48	*w/o*	2-20	13-81 l/min	CDF	imgaging
Sleicher (1962)	iron	38.1	needle	x: 26	0.5-2.1	8.1-45	*o/w*[a]	< 1.7	0.5-3 m/s	d_{95}, d_{max}	imaging
Paul and Sleicher (1965)	iron	12.7	needle	n/a	0.62-28.1	29-46.5	*o/w*[b]	≤35	1.5-2.5 m/s	n/a	imaging
Ward and Knudsen (1967)	copper	21.1	nozzle	x: 123	0.95-261	48-52	*o/w*	1-47	15-115 kg/min	d_{10}, d_{32}, d_{95}	imaging
Collins and Knudsen (1970)	brass	19	nozzle	x: 27-576, y: 0.05- 0.4	1-17	13-40.3	*o/w*	0.6-10	4.2-6.1 m/s	d_{10}, d_{32}, d_{95}, d_{max}	imaging
Middleman (1974)	glass	12.7, 25.4	static mixer	n/a	0.6-26	5-46	*o/w*	0.5-30	∼0.5-3 m/s	d_{32}, CDF	imaging
Kubie and Gardner (1977)	glass	17.2	injectors	x: 218	0.7-4.80	4.86-14.5	*o/w*, *w/o*	<1	0.85-3.4 m/s	d_{max}	imaging
Karabelas (1978)	acrylic	50.4	injector	x: 575, 595	1.77-18.27	31.7-35	*w/o*[c]	0.16-0.26	1.18-3 m/s	d_{32}, d_{95}, d_{max}	encapsulation, imaging
Percy and Sleicher (1983)	glass	38.1	orifices	x: 47.2	0.61	43	*o/w*[d]	few drops	1.25-1.80 m/s	d_{10}, d_{100}, d_{max}	imaging
Hanzevack et al. (1987)	PVC	76.2	T junction	x: 80	1.17	32	*w/o*	0.9-1.18	0.9-2.2 m/s	d_{95}, d_{max}	laser imaging
Hanzevack and Demetriou (1989)	PVC	82	T junction	x: 80, y: 5 positions	1.17	32	*w/o*[e]	0.2-3.81	1-2.4 m/s	d_{99}	laser imaging
El-Hamouz and Stewart (1996)	n/a	38	static mixer	x: 9.3, 18.7, 28.0	0.96	38	*o/w*	2	1 m/s	d_{10}, number distr.	laser backscatter
Angeli and Hewitt (2000b)	steel, acrylic	24.3, 24	T junction	x: 375	1.6	17	*o/w*, *w/o*	3.4-9	1.1-1.7 m/s	d_{32}, d_{95}, d_{max}	imaging, endoscope
Simmons et al. (2000)	glass	63	porous section	y: ± 0.11	164	25	*w/o*	1.2-3.3, >5	1-4 m/s	d_{32}	laser diffraction/back-scatter
Simmons and Azzopardi (2001)	PVC	63	porous section	x: ∼60, y: ± 0.11	1.8	10	*w/o*	1.2-3.3, 6-42	0.8-3.1 m/s	d_{max}	laser diffraction/back-scatter
Lovick and Angeli (2004a)	steel	38	Y junction	x: 184, Δy: 0.05	6	39.6	*o/w*, *w/o*[f]	20-80	1.5-2.5 m/s	d_{32}, d_{50}, d_{99}	impedance probe
Pérez (2005)	PVC	95	static mixer	24, 43	15	33	*o/w*[g]	10-70	0.13-0.18 m/s	η_d, σ_d	borescope
Al-Wahaibi and Angeli (2008)	steel	38	Y junction	x: 184, Δy: 0.05	5.5	39.6	*o/w*, *w/o*	∼20-80	0.2-1.4 m/s	d_{10}, d_{32}	impedance probe
Habchi et al. (2009)	n/a	8	needle	x: ∼ 250	52	19.2	*w/o*	≤10	0.66-2.33 l/min	d_{32}, d_{max}	imaging
Pouplin et al. (2011)	PMMA	50	electrovalves	x: 40	40	31	*o/w*[h]	5-25	0.28-1.2 m/s	volume distr.	laser granulometer
Morgan et al. (2012)	steel	25.4	T junction	x: 244	2.3	25	*o/w*, *w/o*[i]	10-90	0.14-0.29 m/s	d_{10}, number distr.	PLIF
Yusoff (2012)	acrylic	68	orifice	x: 10, 20, 34, Δy: 0.25	5.2	44	*o/w*[j], *w/o*	20-80	0.20-0.35 m/s	d_{32}	FBRM
Morgan et al. (2013)	steel	25.4	T junction	x: 244	2.3	25	*o/w*, *w/o*[k]	10-90	0.22-0.42 m/s	d_{10}, number distr.	PLIF
Yang (2014)	steel	69, 135	choke valves	x: 14, 261	90-202	n/a	*o/w*[l]	40	2 m/s	number distr.	FBRM
Schümann et al. (2016b)	PVC	100	static mixer	x: 2.5, 166, 210, Δy: 0.2	4, 67, 135	14	*o/w*, *w/o*	10-90	0.5, 1.0 m/s	d_{32}, number distr.	FBRM

a. Blue dye was added to the water. Further addition of corn syrup was employed in one run to increase the viscosity of the inorganic phase.
b. Cyclohexene was added to stabilise one of the organic phases used (carbon tetrachloride).
c. Additives introduced: 0.05% w/w piperazine in the aqueous continuous phase and 0.05% w/w terephthalic acid chloride in the dispersed phase.
d. Cyclohexene was added to stabilise the organic phase(mixture of carbon tetrachloride and 2,2,4-trimethyl pentane saturated with water).
e. A very dilute mixture of water latex paint is used as the inorganic phase of the system.
f. Conducted for *DC* conditions.
g. Also conducted for *DC* conditions.
h. A mixture of glycerol/water (43% v/v) was used. The aqueous phase was seeded with hydrophilic microparticles.
i. Conducted for *DC* conditions. A mixture of glycerol/water (80% w/w) was used. A fluorescent dye (Eosyn Y) was added to the aqueous phase.
j. See footnote *f*.
k. See footnote *i*.
l. The continuous phase was salt water.

to study the development of the drop population. To accomplish that, low velocities along with an artificial way to generate the dispersions at the inlet are needed, as turbulent dispersive forces are kept low. In order to study the separation properties, as explained in Chapter 1, the gravity forces need to be dominant, which can in turn lead to packing of drops and more intense coalescence. Only a few works from Table 2.1 fulfil these requirements.

El-Hamouz and Stewart (1996) investigated the effect of pipe length on the drop size distributions, which were measured between ~ 10 and 28 pipe diameters downstream the inlet. The dispersions were generated by using a static mixer at $u_m = 1$ $\mathrm{m\,s^{-1}}$. As the dispersions evolved, the size distributions became flatter with higher probability to find larger drops and a 43% increase in the d_{10} was recorded. Almost a decade later, Pérez (2005) investigated the development of unstable *o/w* at very low mixture velocities and recorded cases where the dispersed phase developed into a continuous film. Drop growth rates varied from negative to positive values with no consistent effect from any flow parameters. Due to the high experimental uncertainties, inconclusive results for the drop size evolution in flow pattern transition regimes were provided. Yusoff (2012) also did not manage to illustrate any direct effects of the mixture velocity and input dispersed volume fraction, φ_d, on the drop growth rates. Schümann et al. (2016b) studied dispersions at low velocities and recorded positive growth rates for a wide range of phase fractions and three different oil viscosities. Larger sizes were recorded in the direction of buoyancy of the dispersed phase, while a consistent decrease close to the wall, where the drops packed, was recorded. Drop size was also increased with increasing input dispersed phase volume fractions and decreasing mixture velocities.

2.1.1.3 Phase inversion

Phase inversion in liquid-liquid dispersed flows can take place for certain drop concentrations and change the flow structure of the dispersion, namely shift from an *o/w* to a *w/o* dispersion and vice versa. This behaviour can critically influence pressure drop and thus is usually avoided in the oil and gas industry. Arirachakaran et al. (1989) arrived at a simple correlation able to predict the drop concentration, i.e. the input dispersed phase volume fraction, where phase inversion occurs by neglecting any interfacial tension effects. Nädler and Mewes (1997) followed a different approach by developing a model based on momentum equations for stratified flow, assuming a negligible interfacial shear and no-slip between the two layers. However, as Brauner (2003) explains, predicting phase inversion should be based on minimising the free energy of the system, which can be considered equal to the interfacial energy, assuming negligible effects of the temperature on liquid properties.

As the interfacial energy is directly related to the drop size and concentration, these parameters need to be known a-priori for more accurate predictions. Brauner and Ullmann (2002) combined a methodology to predict the drop size during pipe

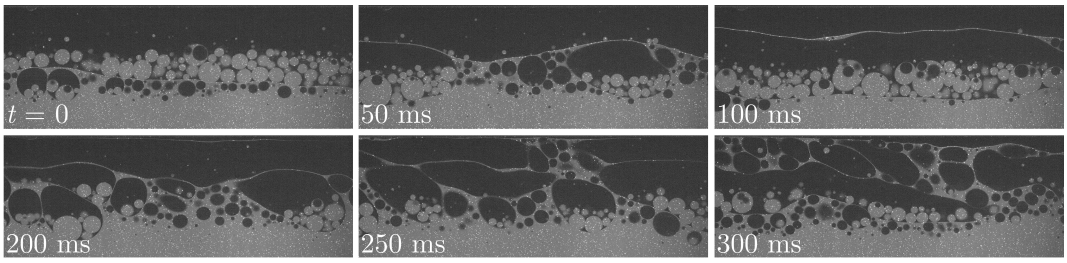

Figure 2.2: Images acquired downstream a static mixer in liquid-liquid flow for phase fractions of both phases equal to 0.5 and during partial phase inversion. Black denotes the oil (organic) phase, while grey the water/glycerol (aqueous) phase.

flow and used it as a closure for a model predicting the phase inversion point. Ngan et al. (2009) suggested that phase inversion should happen when the difference in viscosities between the two possible dispersions, oil continuous and water continuous, is zero, which enables the transition from one continuous phase to the other. Interestingly, for static mixers Tidhar et al. (1986) found that there was a strong influence of the nature of the surfaces of the mixer elements on the inversion phenomenon for low flow rates, while for high flow rates the system inversed at phase fractions equal to 0.5 independent of the viscosity ratio and interfacial tension. Several works have been focused on experimentally capturing the phase inversion dynamics and the drop size during the inversion in liquid-liquid dispersed pipe flows, with Ioannou et al. (2005) and Ngan et al. (2011) using conductivity probes, Schümann et al. (2016b) FBRM probes and Liu et al. (2006) PLIF measurements.

Figure 2.2 illustrates a partial inversion taking place at the top of a horizontal pipe at 15 equivalent diameters downstream a helical static mixer. More information on the liquids and the technique used will be given in the following Chapters. It is clear, that for $t = 0$ ms, *DC* flow conditions exist, where drops of the aqueous heavy phase are located above the interface in the organic light phase and vice versa. As the input oil volume fraction φ_o was set close to the inversion point for this run and the flow rate was kept low, the small disturbances to the flow field advected from the static mixer cause the oil continuous phase to disperse in the aqueous continuous medium, as shown in the last frame of (300 ms). The inversion happens gradually with the aqueous film at the top of the pipe getting trapped between the oil continuous phase at the top and the drops that have coalesced at the interface level. The aqueous film finally reaches the top by pushing all the oil to the bottom and dispersing it. As discussed by Liu et al. (2006), secondary dispersions favour inversion to take place, which is the case close to the interface of Fig. 2.2, where drops of one phase have been trapped in larger drops of the other.

2.1.2 Velocities

Assuming fully developed dispersed flow in pipes, the pressure losses in the axial (streamwise) direction x for horizontal flow can be taken equal to the frictional

pressure losses as

$$-\frac{\mathrm{d}P}{\mathrm{d}x} = 2f_m \frac{\rho_m u_m^2}{D}, \tag{2.1}$$

since the gravitational pressure gradient term ($-\rho_m g sin\vartheta$) is equal to zero for a horizontal orientation (ϑ=0). The mixture density and velocity are respectively ρ_m and u_m, while f_m is the friction factor for smooth pipes and is given by the Hagen-Poiseuille law for laminar and by Blasius' law for turbulent conditions as:

$$f_m = 16/Re_m \quad \text{and} \quad f_m = 0.079 Re_m^{-1/4}, \tag{2.2}$$

where the mixture Reynolds number for the pipe flow can be written as

$$Re_m = \rho_m u_m D/\eta_m. \tag{2.3}$$

The mixture dynamic viscosity is noted as η_m. Both the mixture density and viscosity will be discussed in Sec. 2.2.2. Depending on Re_m different velocity profiles are obtained in the pipe.

2.1.2.1 Laminar flow regime

As illustrated by Reynolds (1883) for single phase flow at relatively low Re, the streamlines of a fluid flowing in a pipe will remain undisturbed and parallel to the main advection direction. It can be thus assumed that the flow can be considered as a series of concentric cylinders with length L and diameter D. In equilibrium the shearing forces, $\tau\pi DL$, are equal to the pressure forces, $\Delta P \pi D^2/4$. For Newtonian fluids the shear stresses in Poiseuille flow are equal to

$$\tau = \eta \mathrm{d}u/\mathrm{d}y. \tag{2.4}$$

Applying this force balance on the vertical normalised direction $y^+ = y/D$, and by integrating over the pipe diameter, it results in the analytical solution for the parabolic velocity profile

$$u^+ = 2 - 8(y^+ - 0.5)^2. \tag{2.5}$$

For laminar conditions in a pipe, the maximum velocity is equal to $u_{max} = 2u_m$ and $u^+ = u/u_m$. As a liquid starts flowing in a pipe it needs an entry length until the shear stresses and the velocity reach fully developed conditions. That length for single-phase flow has been found equal to $x^+ \simeq 0.05Re$ for laminar conditions (Shah and Bhatti 1987), where x^+ is the axial (streamwise) distance normalised with the pipe diameter D.

Pouplin et al. (2011) recorded similar velocity profiles in horizontal liquid-liquid homogeneous flows and reported that Newtonian behaviour is expected for concentrations by volume up to 60%, as long as the Capillary number is kept low ($Ca = \eta_m u_m/\sigma \lesssim 0.1$), so that no deformation of the drops takes place. A maximum Capillary number in a pipe flow can be computed as $Ca_{max} = \eta_m \dot{\gamma}_{max} d/\sigma$,

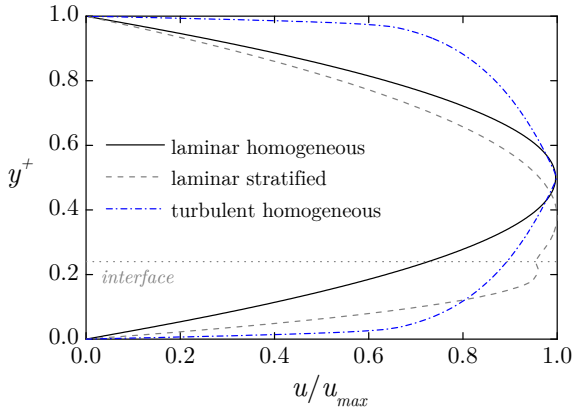

Figure 2.3: Velocity profiles for showing the laminar (eq. 2.5) and turbulent (eq. 2.7) velocity profiles for homogeneous dispersed flow. For stratified flow the velocity profile for laminar conditions (eq. 2.6) is also shown together with the corresponding interface location for $m = 1.83$.

by considering the maximum velocity gradient at the wall $\dot{\gamma}_{max} = 4u_{max}/D$ and the drop size d. For the same liquid-liquid system, Conan et al. (2007) recorded non-Newtonian behaviour for concentrations higher than 0.6 with drop diameters of the order of $d = \mathcal{O}\{10^{-3}\}$ m, while Pouplin et al. (2011) for a concentration of 0.7 and $d = \mathcal{O}\{10^{-5}\}$ m.

When a second continuous layer forms in the pipe (*DC* flow conditions), the velocity profile cannot be calculated from eq. 2.5, as the mixture approach fails to describe the physical properties of the two-phase system. The presence of the drops close to the interface will cause a local increase of the viscosity and is thus more difficult to compute theoretically. Similarly to Yiantsios and Higgins (1988) for plane Poiseuille flow, the analytical solution for stratified flow with no drops (*ST*) consists of two parabolic profiles and can be written as

$$\begin{aligned} u_w^+ &= 4 + 2a_w y^+ + 2b_w (y^+)^2 \\ u_o^+ &= 4 + 2a_o y^+ + 2b_o (y^+)^2 \end{aligned} \tag{2.6}$$

where

$$\begin{aligned} a_o &= 2\left((m - k^2)/(k^2 + k)\right), \quad a_w = a_o/m \\ b_o &= 2\left(-(m + k)/(k^2 + k)\right), \quad b_w = b_o/m \end{aligned}$$

and the parameters m and k are equal to the viscosity and thickness ratios defined in terms of the water over the oil phase. The flow configuration for *ST* computed from eq. 2.6 is compared against the homogeneous one of eq. 2.5 in Fig. 2.3.

2.1.2.2 Turbulent flow regime

At higher Reynolds numbers, the inertial forces in pipe flow become stronger and the viscous forces are not able to suppress any disturbances to the flow. Turbulence

occurs, which is characterised by complex and spatiotemporal fluctuations in the flow field. In a recent stimulating review, Barkley (2016) discusses that the majority of large-scale phenomena observed in turbulent pipe flow can currently be captured qualitatively, but also dictates the need for further experimental and direct numerical simulation studies.

For pipe flow, it has been well-established in the literature that the velocity profiles in the turbulent regime ($Re > 4000$) can be described with a universal power law which reads

$$u/u_{max} = \left(1 - 2|y^+ - 0.5|\right)^{1/n}, \tag{2.7}$$

where n is a parameter dependent on the Reynolds number and is usually taken equal to 7. The entrance length for fully developed turbulent flow is approximately equal to $10D$. For vertical single phase flow at high Reynolds numbers, Hu and Angeli (2006) found a good agreement with eq. 2.7, but the results started deviating for homogeneous liquid-liquid dispersed flows by using the respective Re_m. For horizontal flow and lower Reynolds numbers, Pouplin et al. (2011) illustrated that their results can be fitted with the power law profile for both single phase and dispersed flows by setting n = 6.5. Conan et al. (2007) found asymmetrical velocity profiles for dispersed flows, when packing of the drops was observed. This can be attributed to the high viscosity gradients of the mixture stemming from the drop concentration gradients.

The friction (shear) velocity, $u^* = \sqrt{\tau_c/\rho_c}$, can be estimated from the classical logarithmic law in the inertial and viscous layer regions correspondingly as

$$\frac{u}{u^*} = \frac{1}{\varkappa} \ln y^* + B \qquad \text{for} \qquad y^* \geqslant 30 \tag{2.8a}$$

$$\frac{u}{u^*} = y^* \qquad \text{for} \qquad 0 \leqslant y^* \leqslant 5 \tag{2.8b}$$

where $y^* = yu^*\rho_c/\eta_c$ with τ_c, ρ_c and η_c being respectively the shear stress, the density and the viscosity of the continuous phase. For single phase flow in circular pipes it has been empirically found that $\varkappa$ = 0.41 and B = 5.5 (Wallis 1969). While the continuous phase properties have been used by Conan et al. (2007), Pouplin et al. (2011) illustrated a collapse of data for different velocities and drop concentrations when the mixture properties are used instead. It is possible to deduce the friction velocity from pressure drop measurements as

$$u^* = \sqrt{\frac{D}{4}\frac{1}{\rho_m}\left|\frac{\mathrm{d}P}{\mathrm{d}x}\right|}. \tag{2.9}$$

2.1.2.3 Fluctuating motions

Turbulence plays a key role in the velocity distribution, which can significantly affect the drop size distribution and the separation properties of dispersions. For that

reason, it is crucial to investigate the modification of turbulence in the presence of a secondary phase. The main parameters that control this phenomenon are the density ratio along with the volume fraction φ_d and drop size d of the dispersed phase. As Balachandar and Eaton (2010) describe, the dispersed phase (drops, bubbles or particles) can either dampen or enhance the turbulence levels. Enhanced inertia of the dispersed phase flow, increased dissipation arising from the drop drag and enhanced effective viscosity can lead to a reduction of the turbulence levels. Conversely, enhanced velocity fluctuations can be generated due to wake dynamics and self-induced vortex shedding from droplets, while the rise of buoyancy-induced instabilities can take place due to density fluctuations, arising from local concentration gradients. Even for laminar conditions, the superposition of many laminar-like wakes randomly positioned in space and time contributes to velocity fluctuations (Chen and Faeth 2001).

The slip (or relative) velocity $u_r = u_d - u_c$ together with the phase fraction have been found to control the fluctuations. According to Lance and Bataille (1991) for relatively small drop sizes

$$b = \frac{1}{2}\frac{\varphi_d u_r^2}{u_c'^2}, \tag{2.10}$$

where u_c' are the velocity fluctuations experienced by the continuous phase and b is the ratio of the drop-induced kinetic energy and the kinetic energy of the flow without drops. It follows, that single phase turbulent fluctuations are computed for the case of $b = 0$, while $b = \infty$ represents the case where all the turbulence stems from the presence of drops (i.e. pseudo-turbulence) (Pope 2001). For bubbly flows, recent works (Mercado et al. 2010; Mendez-Diaz et al. 2013; Riboux et al. 2013) have established a spectral density behaviour with a dependence on the wavenumber as k^{-3} (for $\sim b > 1$), which deviates from the Kolmogorov spectrum of $k^{-5/3}$ (for $\sim b < 1$).

These velocity fluctuations can been measured experimentally with various techniques, such as hot-wire/film anemometers (HFA) (Lance and Bataille 1991; Hu 2006; Mercado et al. 2010; Hamad and Ganesan 2015; Prakash et al. 2016), laser Doppler anemometers (LDA) (Lance and Bataille 1991) and particle image/tracking velocimetry (PIV/PTV) (Augier et al. 2007; Conan et al. 2007; Mercado et al. 2010). The velocity measured is expressed as the sum of a time-averaged velocity component $\langle u \rangle$ and a fluctuating component u' as

$$u = \langle u \rangle + u'$$

and it follows that the time-averaged of the fluctuating component $\langle u' \rangle$ should be zero.[2]

2. The local shear stresses in turbulent flow are affected both by the friction between the layers in the flow direction and between the fluctuating drops and fluid body. Consequently, the turbulent velocity profile equation cannot be directly derived from eq. 2.4 as for laminar flow of eq. 2.5.

For in-line separators the velocities are usually kept relatively low (Pérez 2005) and therefore the main interest lies in the pseudo-turbulent regime ($b > 0$). For bubbly flows, Lance and Bataille (1991) wrote $e = \left(\langle u_c'^2 \rangle\right)^{3/2} / \mathcal{L} = F_D u_r$, assuming equilibrium between the pseudo-turbulence dissipation rate and the mean power of the drag, giving

$$\frac{\langle u_c'^2 \rangle}{u_r^2} \propto (\varphi_d C_D)^{2/3} \left(\frac{\mathcal{L}}{d}\right)^{2/3}, \tag{2.11}$$

where $\mathcal{L}$ is the turbulent length-scale, u_c is the continuous phase velocity, u_r is the slip/relative velocity, e the turbulent energy dissipation, F_D the drag force and C_D drag coefficient. Most works in the literature explore vertical bubbly flows. For dilute concentrations ($\varphi_d < 0.04$) the scale of the fluctuations was found weakly dependent on φ_d with $\mathcal{L} \sim 0.8d$ (Lance and Bataille 1991). For dispersed phase volume fractions up to 0.2, Garnier et al. (2002) found a linear scaling as $\langle u_c'^2 \rangle \approx \varphi_d u_r^2$. For higher volume fractions they reported deviating results from this relationship. They attributed these deviations to large scale fluctuations that lead to higher fluctuating energy and therefore concluded that at high concentrations the pseudo-turbulence induced by the bubbles is not solely determined by local flow conditions, but also by spatial heterogeneities of the volume fraction.

Augier et al. (2007) studied vertical dispersed liquid-liquid flows at high dispersed phase fractions to investigate the effects of the volume fraction. Remarkably, they found agreement with eq. 2.11 when $\mathcal{L} \sim 0.8d$, by using a variation of the slip velocity and drag coefficient dependant on the dispersed phase volume fraction (Augier et al. 2003). Augier et al. (2007) used local in-situ values for the dispersed phase volume fraction ε_d and for the liquid properties in the computation of the adjusted slip velocity and drag coefficient. Recently, for turbulent conditions, Dodd and Ferrante (2016) explored numerically the exchange pathways of the turbulent kinetic energy between the carrier flow and the flow inside the drop by also considering interfacial phenomena (deformation, breakup and coalescence) and linking the interfacial tension to the dissipation rates. Maxey (2017) discusses current developments in the field and underlines the need to further investigate how interfacial phenomena can affect the energy spectra and how the dynamics behave in more general engineering contexts.

2.2 Drop motion

In the current Section, an overview of the physical mechanisms that apply to dispersed two-phase flow will be described. The background on predicting the motion of drops in wall bounded shear flows will be portrayed through a CFD mixture approach based on suspension flows, while the separation dynamics will be described through a phenomenological one-dimensional approach based on liquid-liquid batch settlers.

2.2.1 Physical mechanisms

Developing accurate models for dispersed liquid-liquid pipe flows is crucial for the advancement of the oil and gas industry. Due to the complexity of these flows at high dispersed phase fractions, difficulties arise in the computation of the interfacial momentum exchange, which is usually described through a slip velocity u_r. In this Section the main mechanisms contributing to slip between the drops and the carrier phase will be discussed.

2.2.1.1 Gravity, drag and lift forces

In two-phase flows of two immiscible liquids, gravity force causes an acceleration of the spherical drops in the vertical direction, dependent on the density difference between the two liquids (buoyancy force) as $F_B = g\left(\rho_d - \rho_c\right)\left(\pi d^3/6\right)$. Due to this relative motion, the fluid exerts a drag force on the drop. The drag force for steady flow can be computed as $F_D = (1/2)\, C_D \rho_c \left(\pi d^2/4\right) u_r^2$, where C_D is the drag coefficient depending on a Reynolds number based on the drop as $Re_t = d\rho_c u_r/\eta_c$. According to Stokes' law for $Re_t < 0.1$, $C_D = 24/Re_t$, derived from calculating the viscous energy dissipation for potential flow past a sphere (Levich 1962). It follows that the terminal velocity of a single drop settling in an infinite medium can be computed by balancing the drag and gravity force giving

$$v_t = \frac{1}{18}\frac{d^2\left(\rho_c - \rho_d\right)}{\eta_c} g. \tag{2.12}$$

For higher Re_t, in the range of $0.1 < Re_t < 1000$, the drag coefficient is better described by $C_D = (24/Re_t)\left(1 + 0.14 Re_t^{0.70}\right)$ (Perry et al. 1997).

It has been well-established that for concentrated mixtures, drop hydrodynamic interactions become significant and the terminal velocity of the drops can be estimated by equating the product of v_t with a monotonically decreasing function of the in-situ dispersed phase fraction as $f_h(\varepsilon_d)$ (Schaflinger et al. 1990; Zhang and Acrivos 1994).

$$f_h = \frac{\eta_c\left(1 - \varepsilon_d\right)}{\eta_m}. \tag{2.13}$$

Yin and Koch (2007) have reviewed more recent findings on the computation of drag coefficients and hindered functions, f_h, and illustrated that small deviations can be caused at higher Reynolds numbers and dilute systems due to anisotropic microstructures resulting from wake interactions among the dispersed phase.

When a rigid sphere (particle, bubble or drop) is immersed in a spatially varying shear flow (e.g. Poiseuille flow), it will undergo a cross-stream (lateral) motion in the presence of inertia. Inertia is necessary to break the linearity of Stokes equations, under which lateral migration is forbidden (Bretherton 1962). It has been predicted theoretically that a particle's lateral motion away from a solid boundary becomes

stronger close to the walls (Vasseur and Cox 1976; Cox and Hsu 1977) with Schonberg and Hinch (1989) expanding these results for Poiseuille flows. These studies are developed for a single particle at low Reynolds numbers $Re < 100$.

According to Belfort et al. (1994), the inertial lift velocity of spherical particles under laminar flow conditions in dilute suspensions, where particle-particle interactions are negligible, can be written as

$$u_L = \frac{C_L \rho_c d^3 \dot{\gamma}^2}{128 \eta_c}, \tag{2.14}$$

where u_L is the lift velocity and $C_L(y)$ is a coefficient which varies with the distance from the pipe wall. Its maximum value is 1.3 for pipe flow (Ishii and Hashimoto 1980).

Asmolov (1999) and Matas et al. (2004) expanded the theory for higher Reynolds numbers in Poiseuille channel flows with Re reaching 3000. The lift force is much stronger close to the wall, while it is practically zero in the middle of the channel. Matas et al. (2009) developed similar formulations for pipe flow at Reynolds numbers covering the laminar flow regime. Nevertheless, the particle concentration was kept below 1%. It is unclear how the lift force is affected at higher dispersed phase concentrations, where the interactions between the dispersed phase become important.

2.2.1.2 Diffusion

Detailed calculations of the interactions between the drops and the continuous phase can be proven challenging and require significant computational resources. However, it has been shown that excellent results can be obtained by modelling the most important mechanisms through a diffusion equation for suspension flows. Phillips et al. (1992) described the particle migration processes by modelling the main interactions between particles that would cause an irreversible displacement from a particle's streamline, and would thus eventually lead to migration of the dispersed phase. Especially for dense systems, the surface roughness can play a significant role to the reversibility of these two-body interactions and hence on the final particle displacement dynamics (Yilmazer and Kalyon 1989; Kalyon 2005). Based on two-body irreversible interactions and assuming smooth rigid spheres for the dispersed phase Phillips et al. (1992) wrote the particle flux accounting for effects of spatially varying interaction/collision frequencies due to shear gradients and of spatially varying viscosity due to concentration gradients in the cross-section of the pipe.

Local shear gradients can affect particle motion by altering the collision frequency a particle experiences. According to Phillips et al. (1992) the number of collisions can be scaled as $\dot{\gamma}\varepsilon_d$, while they will take place over a distance of the order of the particle radius $\mathcal{O}\{a\}$. The variation of the collision frequency can be thus written as $(a)\,\nabla\,(\dot{\gamma}\varepsilon_d)$, which is assumed to be linearly proportional to the migration velocity

of the particles. This collision effect causes a flux of the dispersed phase as

$$\mathbf{N_{\varepsilon}} = -\mathrm{K}_{\varepsilon} a^2 \varepsilon_d \nabla \left(\varepsilon_d \dot{\gamma}\right), \tag{2.15}$$

where K_{ε} is a proportionality constant of order unity. The gradient of eq. 2.15 describes the behaviour of the particles moving from high shear regions to low and from high concentrations to low.

Local gradients of the viscosity of the mixture $\eta_m\left(\varepsilon_d\right)$ can have an impact on the frequency of irreversible collisions, by changing the resistance to motion of the two colliding bodies. This difference in their resistance can displace the centre of rotation of the particles leading them to areas of lower viscosity. This flux is proportional to the change in viscosity over a distance of $\mathcal{O}\{a\}$ relative to the overall magnitude of the viscosity $\left(a/\eta_m\right)\nabla\eta_m$. For the same scaling of the frequency of collisions $\dot{\gamma}\varepsilon_d$, the flux then scales as $\left(\dot{\gamma}\varepsilon_d a^2/\eta_m\right)\nabla\eta_m$ (Leighton and Acrivos 1987). As the mixture viscosity depends on the concentration, to express the gradient of viscosity in terms of $\nabla\varepsilon_d$ the relation is written instead as

$$\mathbf{N_{\eta}} = -\mathrm{K}_{\eta} a^2 \dot{\gamma} \varepsilon_d^2 \left(\frac{1}{\eta_m}\frac{\mathrm{d}\eta_m}{\mathrm{d}\varepsilon_d}\right)\nabla\varepsilon_d, \tag{2.16}$$

where K_{η} is a rate constant of order unity. This theory can be extended to liquid-liquid systems, assuming small non-deformable drops. This assumption will be further examined next.

2.2.2 Mixture model

2.2.2.1 Physical properties

Due to the presence of two immiscible phases in dispersed flows, the mixture properties and flow characteristics need to be considered as illustrated previously. While the mixture density is well described as

$$\rho_m = \varepsilon_d \rho_d + (1-\varepsilon_d)\rho_c, \tag{2.17}$$

the same linear relationship has limited applicability for the viscosity of the mixture (Li et al. 2015).

Predicting the viscosity in mixtures dates back to the relation developed by Einstein (1906) for dilute suspensions giving $\eta_m = \eta_c\left(1+2.5\varepsilon_d\right)$ for systems of solid particles. For more concentrated systems, particle interactions become important. An extensive list of theoretical models exists based on different approaches, such as the cell models (Yaron and Gal-Or 1972; Choi and Schowalter 1975) and the effective medium models (Taylor 1932; Brinkman 1952; Phan-Thien and Pham 1997). These approaches have been tested against experimental data of liquid-liquid emulsions in the review by Pal (2001).

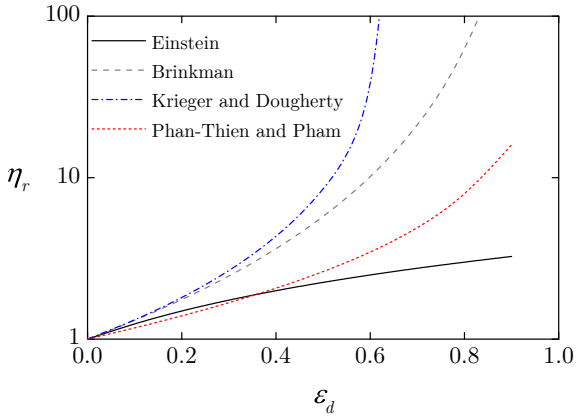

Figure 2.4: The viscosity models by Einstein (1906), Brinkman (1952), Krieger and Dougherty (1959) (with $\varepsilon_{max} = 0.74$) and Phan-Thien and Pham (1997).

For liquid-liquid pipe flows, Ngan (2011) and Mukhaimer et al. (2015) investigated their effect on the phase inversion predictions, while Pouplin et al. (2011) found good agreement between their experimental pressure drop measurements and the model by Krieger and Dougherty (1959)

$$\eta_m = \eta_c \left(1 - \frac{\varepsilon_d}{\varepsilon_{max}}\right)^{-2.5\varepsilon_{max}} . \tag{2.18}$$

The maximum packing volume fraction, ε_{max}, is equal to 0.64 for random packing of equal sized spheres, but can take higher values for polydispersed populations. Figure 2.4 illustrates the differences between some well-established models from the literature that have been used in liquid-liquid systems over the years. It is clear that the model by Krieger and Dougherty (1959) gives the highest values when the maximum packing is considered at ε_{max} = 0.74 as the relative viscosity $\eta_r = \eta_m/\eta_c$ increases to infinity at that limit.

Both the relation of the mixture viscosity (eq. 2.18) and the particle fluxes (eqs. 2.15 and 2.16) have been developed for rigid solid spheres. Extending these formulations for liquid-liquid flows can be considered, as the drops can also be assumed to have non-deformed interfaces, considering that surfactants and contaminants are naturally present in such systems. To be able to accurately compute the local collective effects, the in-situ volume fractions ε_d are used instead of the input φ_d in the aforementioned relations, as the drops are not homogeneously distributed along the pipe cross-section in unstable dispersed flows.

2.2.2.2 Constitutive equations

The mixture model solves the continuity and momentum equations for the mixture and a transport equation for the dispersed drop phase. It also allows for the two phases to move at different velocities assuming a slip velocity between the two. As

an algebraic formulation of slip will be used, the two phases should be strongly coupled. A local equilibrium should be reached over short spatial lengths (Manninen et al. 1996). Therefore, the Stokes number for the dispersed phase should be smaller than unity

$$St = \frac{\tau_p}{D/u_m}, \tag{2.19}$$

where the relaxation time for the drops $\tau_p = \rho_d d^2/18\eta_c$ and the characteristic convective time scales as the pipe diameter over the mixture velocity.

The unsteady momentum transport equation for the mixture can be written as

$$\rho_m \frac{\partial \boldsymbol{U}}{\partial t} + \rho_m \left(\boldsymbol{U} \cdot \nabla\right) \boldsymbol{U} = \\ -\nabla P - \nabla \cdot \left(\rho_m c_d \left(1 - c_d\right) \boldsymbol{U_r} \boldsymbol{U_r}\right) + \nabla \cdot \left[\eta_m \left(\nabla \boldsymbol{U} + \nabla \boldsymbol{U}^{\mathsf{T}}\right)\right] + \rho_m \boldsymbol{g}, \tag{2.20}$$

where the bold symbols denote vectors or tensors and c_d is the dispersed phase mass fraction. The rate of deformation tensor can be written as

$$\underset{\sim}{\dot{\gamma}} = \nabla \boldsymbol{U} + \nabla \boldsymbol{U}^{\mathsf{T}},$$

with a magnitude of shear rate equal to

$$\dot{\gamma} = \sqrt{\frac{1}{2}\left(\underset{\sim}{\dot{\gamma}} : \underset{\sim}{\dot{\gamma}}\right)},$$

which for a two-dimensional problem results in

$$\dot{\gamma} = \sqrt{\frac{1}{2}\left(4\left(\frac{\partial u}{\partial x}\right)^2 + 2\left(\frac{\partial u}{\partial y} + \frac{\partial v}{\partial x}\right)^2 + 4\left(\frac{\partial v}{\partial y}\right)^2\right)} \tag{2.21}$$

The unsteady continuity equation can be written as

$$\left(\rho_c - \rho_d\right)\left[\nabla \cdot \left(1 - c_d\right) \boldsymbol{U_r}\right] + \rho_c \left(\nabla \cdot \boldsymbol{U}\right) = 0,$$

while the unsteady transport equation for the dispersed phase volume fraction is

$$\frac{\partial \varepsilon_d}{\partial t} + \nabla \cdot \left(\varepsilon_d \boldsymbol{U_d}\right) = 0.$$

The velocity of the dispersed phase is equal to $\boldsymbol{U_d} = \boldsymbol{U} + \left(1 - c_d\right) \boldsymbol{U_r}$ and thus the previous relation can now be written as

$$\frac{\partial \varepsilon_d}{\partial t} + \nabla \cdot \left(\varepsilon_d \boldsymbol{U} + \varepsilon_d \left(1 - c_d\right) \boldsymbol{U_r}\right) = 0.$$

Following the formulations by Rao et al. (2002), the continuity and the dispersed phase transport equation can be written by defining a flux of the dispersed phase,

$\mathbf{N_d}$. The continuity equation then transforms to

$$\nabla \cdot \boldsymbol{U} = \frac{\rho_d - \rho_c}{\rho_d \rho_c} \left(\nabla \cdot \mathbf{N_d}\right) \tag{2.22}$$

and the dispersed phase transport equation to

$$\frac{\partial \varepsilon_d}{\partial t} + \nabla \cdot (\varepsilon_d \boldsymbol{U}) = -\frac{\nabla \cdot \mathbf{N_d}}{\rho_d}, \tag{2.23}$$

where $\mathbf{N_d}$ is the flux of the dispersed phase. The two different formulations for the continuity and the dispersed phase transport equation, should result in the same slip velocity, as shown by Subia et al. (1998)

$$\boldsymbol{U_r} = \frac{\mathbf{N_d}}{\varepsilon_d \rho_d \left(1 - c_d\right)}. \tag{2.24}$$

The final drop transport equation can be written by combining eqs. 2.23 with 2.15, 2.16 and 2.12/2.13 as

$$\mathbf{N_d} = -\left[\mathrm{K}_\varepsilon a^2 \varepsilon_d \nabla \left(\varepsilon_d \dot{\gamma}\right) + \mathrm{K}_\eta a^2 \dot{\gamma} \varepsilon_d^2 \left(\frac{1}{\eta_m} \frac{\mathrm{d}\eta_m}{\mathrm{d}\varepsilon_d}\right) \nabla \varepsilon_d\right] \cdot \rho_d + f_h \boldsymbol{v_t} \varepsilon_d \rho_d \tag{2.25}$$

According to Leighton and Acrivos (1987) the diffusion coefficients are proportional to the square of the drop radius with

$$\mathrm{K}_\varepsilon = 0.43 a^2 \quad \text{and} \quad \mathrm{K}_\eta = 0.65 a^2, \tag{2.26}$$

while Phillips et al. (1992) found proportionality constants equal to 0.41 and 0.63 respectively. These constants have been fitted with experimental data of suspension systems. The drops in a liquid-liquid system need to behave similarly to solid spheres with non-deformable boundaries to apply the aforementioned framework. It must also be noted that any turbulence or pseudo-turbulence diffusion is not considered in the formulation of eq. 2.25. The mixture model in this form (eqs. 2.20, 2.22 and 2.25) is unable to predict the dynamics in polydisperse population of drops. This is a serious limitation as usually in liquid-liquid systems the drop size distribution extends to a wide range of sizes due to coalescence and breakup phenomena. Finally, eq. 2.14 can be added on the right-hand side of eq. 2.24 to take lift effects into account. The geometrical characteristics and boundary conditions of the CFD model are given in the Appendix B.

2.2.3 In-line separator model

Recently, it has been shown that the separation dynamics can be predicted relatively well in a horizontal pipe with a simple phenomenological one-dimensional model. The modelling framework is schematically illustrated in Fig. 2.5. Pereyra et al. (2013) implemented a model by Henschke et al. (2002) for batch settlers by transforming

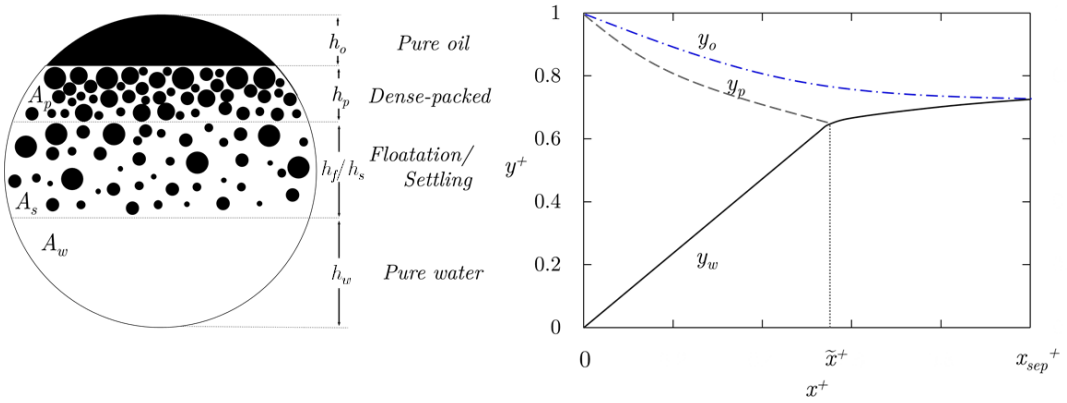

Figure 2.5: Horizontal pipe separator model illustrated for *o/w* dispersions. The subscripts o and w can be replaced with d and c for any two-phase mixture.

the separation time of the batch settler to a residence time of the mixture in the pipe. This time was computed by simply dividing the streamwise axial length of the pipe with the characteristic convective time x/u_m of the flow. The model is able to predict the drop concentration and the thickness of the continuous layers in the vertical direction and along the pipe by simply considering a modified settling/floatation velocity of the drops and two time-scales characterising drop-drop and drop-interface coalescence.

The main limitation of this model lies in the fact that the velocity field of the pipe and the drop concentration gradients are not coupled with the separation dynamics, contrary to Sec. 2.2.2. This model is also formulated with one average drop size and thus polydisperity is neglected, but changes in the drop size are allowed through a coalescence parameter, which has been fitted by Pereyra et al. (2013) for their system. Pérez (2005) developed a similar but more elaborate approach incorporating simplified PBE modelling.

2.2.3.1 Settling and floatation

An empirical model was developed by Pilhofer and Mewes (1979) to compute the vertical velocity of a swarm of drops in settling experiments. The model is valid for Archimedes numbers above 1 and dispersed phase fractions ranging between 0.06 and 0.55, where $Ar = \rho_c|\rho_c - \rho_d|d^3/\eta_c^2$. The vertical velocity for a swarm of drops can be then computed as

$$v_d = \frac{3\lambda\varphi_d\eta_c}{C_W\xi\left(1-\varphi_d\right)\rho_c d_p}\cdot\left[\left(1+Ar\frac{C_W\xi\left(1-\varphi_d\right)^3}{54\nu^2\varphi_o^2}\right)-1\right], \tag{2.27}$$

where the two settling parameters are equal to

$$\xi = 5\mathrm{K}_{\mathrm{HR}}^{-3/2}\left(\frac{\varphi_d}{1-\varphi_d}\right)^{0.45} \quad \text{and} \quad \nu = \left(\frac{1-\varphi_d}{2\varphi_d\mathrm{K}_{\mathrm{HR}}}\right)$$

where the Hadamard-Rybczynski factor, $\mathrm{K_{HR}}$, and the friction coefficient, C_W , are respectively equal to

$$\mathrm{K_{HR}} = 3\frac{\eta_c + \eta_d}{2\eta_c + 3\eta_d} \quad \text{and} \quad C_W = \frac{Ar}{6Re_\infty^2} - \frac{3}{\mathrm{K_{HR}} Re_\infty}.$$

The Re_∞ is the Reynolds number of a single settling drop in an infinitely expanded fluid. Henschke et al. (2002) recommended to use the presently well-established model by Ishii and Zuber (1979), instead of the model developed by Hu and Kinter (1955). Ishii and Zuber (1979) predict better the settling of drops with sizes in the range of 0.5 to $4\,\mathrm{mm}$, which are very important in the separation systems. According to Ishii and Zuber (1979) it can be written that

$$Re_\infty = 9.72\left[(1 + 0.01Ar)^{4/7} - 1\right].$$

From eq. 2.27 it is clear that the effect of neighbouring drops on the settling velocity is taken into account, similarly to the formulation of f_h. The viscosity of the mixture is considered in this model through a constant factor of $\mathrm{K_{HR}}$, which depends on the viscosity ratio of the dispersed and continuous phase. This behaviour contradicts eq. 2.18 type of correlations, which lead to infinite mixture viscosity for concentrations close to the maximum packing. The dependence on the concentration comes in through the ν parameter and is independent of the drop concentration. It needs to be noted that the local volume fractions are considered here instead of the in-situ volume fractions as in the mixture model of the previous Section. It follows that the evolution of the continuous layer of oil in a settling *w/o* dispersion or water in a floating *o/w* dispersion (cf. Fig. 2.5) expands linearly with x and can be written as

$$\frac{\mathrm{d}h_c}{\mathrm{d}x} = \frac{v_d x}{u_m}, \tag{2.28}$$

where v_d is computed from eq. 2.27 and h_c is the thickness of the pure water layer, which is equivalent to its height y_c when $y = 0$ is considered for the bottom of the pipe.

2.2.3.2 Separation of two-phase mixture

Following the predictions by Hartland and Jeelani (1988), the development of the pure layer thickness of the dispersed phase is

$$\frac{\mathrm{d}h_d}{\mathrm{d}x} = \frac{2\varepsilon_I d_{32,I}}{3\tau_I}, \tag{2.29}$$

assuming that the interface is flat and all drops on it have the same diameter $d_{32,I}$. The d_{32} is the Sauter mean diameter of the drops and can be computed as

$$d_{32} = \frac{\sum_{i}^{N_d} \left(d_i^3\right)}{\sum_{i}^{N_d} \left(d_i^2\right)}. \tag{2.30}$$

It can be further assumed that the local in-situ dispersed phase volume fraction close to the interface level is $\varepsilon_I \approx 1$. Eq. 2.29 gives the rate of change of the pure oil layer in a floating *o/w* dispersion (Fig. 2.5). It is clear from eq. 2.29 that the development depends on a drop-interface coalescence time τ_I. As the concentration at the dense-packed region is very high, drop-drop coalescence is also expected to take place. The change of the drop diameter at the dense-packed region is given by Hartland and Jeelani (1988) as

$$\frac{\mathrm{d}\left(d_{32}\right)}{\mathrm{d}x} = \frac{d_{32}}{6\tau_d u_m} \tag{2.31}$$

with τ_d characterising the drop-drop coalescence time.

Eq. 2.28 and eq. 2.29 give respectively the thickness of the layers h_c and h_d. The prediction of the location of the dense-packed region h_p and hence the settling h_s or floatation h_f region thickness needs to be done in two steps for $x^+ < \tilde{x}$ and for $x^+ > \tilde{x}$ as shown in Fig. 2.5, where $\tilde{x}$ denotes the axial location where the settling/floatation stops. A mass balance is used at the cross-sectional area based on the thicknesses of the layers at each step by assuming linearity along the depth of the pipe cross-section. For $x^+ \leqslant \tilde{x}$ this balance gives according to Pereyra et al. (2013)

$$A_p = \frac{A_o\varphi_d - (1-\varphi_d)\,A_d}{\varepsilon_{p,1} - \varphi_d} \qquad \text{for} \quad x^+ < \tilde{x} \tag{2.32a}$$

$$A_p = \frac{A\varphi_d - A_d}{\varepsilon_{p,2}} \qquad \text{for} \quad x^+ > \tilde{x}, \tag{2.32b}$$

where A_p denotes the dense-packed region cross-sectional area, while φ_d is the input volume fraction of the dispersed phase and $\varepsilon_{p,1}$ and $\varepsilon_{p,2}$ are the in-situ volume fractions of the dispersed phase at the dense-packed region (taken equal to 0.9) before and after the inflection point $\tilde{x}$. A strong assumption in eq. 2.32(a) is that the dispersed phase volume fraction at the settling layer is equal to the input one at all times. For $x^+ > \tilde{x}$ the in-situ dispersed phase fraction can be computed as

$$\varepsilon_{p,2} = \varepsilon_I - \exp\left(-C_1\frac{x}{u_m} - C_2\right),$$

where C_1 and C_2 are determined on the basis of continuity so that $\varepsilon_{p,1} = \varepsilon_{p,2} = \tilde{\varepsilon}_p$ at the inflection point. This condition thus provides the following formulations

$$C_1 = \frac{\tilde{\varepsilon}_p^2 \chi}{(A\varphi_d - A_d)(\varepsilon_I - \varepsilon_{p,1})} \quad \text{and} \quad C_2 = -C_1 \frac{\tilde{x}}{u_m} - \ln(\varepsilon_I - \varepsilon_{p,1}),$$

where the χ stands for

$$\chi = \left[\frac{\partial A_p}{\partial h_p} \left(v_d + u_m \frac{\mathrm{d}h_d}{\mathrm{d}x} \right) - \frac{u_m}{\tilde{\varepsilon}_p} \frac{\partial A_d}{\partial h_d} \frac{\mathrm{d}h_d}{\mathrm{d}x} - u_m \frac{\partial A_p}{\partial h_d} \frac{\mathrm{d}h_d}{\mathrm{d}x} \right]_{x=\tilde{x}}.$$

The set of eqs. 2.28, 2.29, 2.31 and 2.32 comprise the phenomenological model for the in-line separation. The geometrical closures are provided in Appendix A. In the aforementioned equations, the coalescence times τ_I and τ_d are still unknown. For the calculation of these times, the contact areas between a drop and the interface and between two drops are needed. More information is provided in Sec. 2.3.1.

2.3 Interfacial dynamics

In this Section the focus is turned to describing the physics behind the mechanisms that can affect the drop size, namely coalescence and breakup. The fundamental dynamics of these two interfacial phenomena are described and applied in liquid-liquid systems. Information on the characterisation of drop populations will be given in the final Section.

2.3.1 Coalescence

The importance of coalescence between two liquid bodies in industrial applications was recently illustrated in the review by Kamp et al. (2017). It was first observed by Osborne Reynolds (1875, 1881), that when a drop is placed on a liquid-liquid interface of two immiscible liquids it will not coalesce immediately with its mother phase as a thin film separating the two bodies forms beneath the drop. Charles and Mason (1960a) described the interfacial shapes that the drop and the film can take, while also noted that the film slowly drains. This film drainage time was found to significantly depend on the fluid properties. Once the film has drained to an infinitesimal thickness (~ 10 µm), molecular forces are strong enough to cause a rupture on the film and generate a neck connecting the drop with its motherphase. Under the influence of the interfacial forces, the neck expands until the drop is fully merged only a few milliseconds later. The film drainage time and the neck expansion stage comprise the coalescence mechanism. It was found that for certain conditions and liquid pairs, a secondary drop can be generated as the neck expands – a phenomenon called partial coalescence (Charles and Mason 1960b). A recent review by Kavehpour (2015) explains these basic mechanisms. In what follows, the film drainage

velocity is investigated in the first Section and the neck expansion dynamics in the second Section.

2.3.1.1 Film drainage

It was shown in the phenomenological in-line separator model that coalescence times, the sum of film drainage and neck expansion time, between a drop and the interface and between two drops control the separation of liquid-liquid mixtures (eqs. 2.29 and 2.31 respectively). Henschke et al. (2002) describe the main characteristics that are involved in determining the coalescence time in dense-packed regions of mixtures. At high concentration, the drops tend to deform due to pressure exerted on them. Both Henschke et al. (2002) for batch settlers and Conan et al. (2007) for pipes, report a deformation of the drops at the dense-packed region, with the shape described as hexagons by the former and as pentagonal dodecahedra by the latter. This deformation causes a simultaneous increase of the contact area between the drops and a decrease of the medium area between the drops, which translates to higher values of packing.

Figure 2.6 illustrates the asymmetrical film drainage model described by Henschke (1994). He solved numerically the equations describing the drop deformation and derived the following empirical formulations for the geometrical parameters as

$$r_{F,d} = 0.030d\sqrt{1 - \frac{4.7}{4.7 + La}} \quad \text{and} \quad r_a = 0.5d\sqrt{1 - \frac{4.7}{4.7 + La}},$$

which are based on a Laplace number representing the ratio of the hydrostatic pressure resulting from the drop-packing height above the drop considered h_{py} and of the interfacial tension equal to $La = \Delta\rho g h_{py} d/\sigma$. During drop-interface coalescence, the aforementioned equation can be used with $r_{F,I} = r_{F,d}\sqrt{3}$. With this Laplace number though it was found that the packing height was overestimated and therefore Henschke (1994) modified it as $La = (\Delta\rho g/\sigma)^{0.6} h_{py}^{0.2} d$ by fitting the exponents to experimental data obtained from batch settling experiments.

Apart from the deformation of the drops (Fig. 2.6(a)), it is important to predict the rate the film drains. A lot of film drainage models exist depending on the deformation and the assumptions considered as have been reviewed by Frising et al. (2006) and Chan et al. (2011). Here, the formulations by Henschke et al. (2002) based on a dimple formulation as illustrated in Fig. 2.6(b) are considered. The film thickness presents a minimum at the edge of contact, while the drainage is also not symmetric on its rotational axis. This leads in asymmetrical film drainage (Fig. 2.6(b)), which results in higher drainage rates.[3] Asymmetric drainage takes place when the pressure forces $F_P = \sigma\pi r_F^2/r_a$ acting on the film are not centred with normalised displacement from the centre equal to $r_V^+ = r_V/r_F$, which is the case in dense-packed drop systems.

3. Symmetrical drainage was considered more in the past and was described as $\tau_d \propto r_{F,d}^m$, with the exponent m ranging from ~ 1.4 to 4.0 (Charles and Mason 1960a; Hartland 1981; Chen 1985).

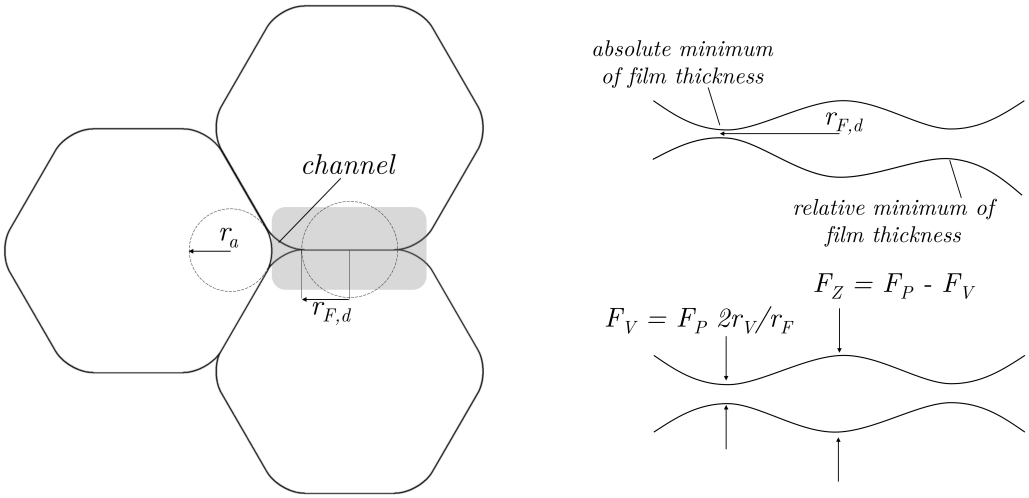

(a) Drop deformation leading to hexagons in the dense-packed region

(b) Asymmetrical film drainage

Figure 2.6: Film drainage process as described by Henschke et al. (2002).

The flow of the film is considered to take place along the horizontal axis of Fig. 2.6(b), where F_P can be divided into two contributions F_Z and F_V, as shown. The final solution is derived by superposition of the solutions of each case. Following Henschke et al. (2002) considerations, this gives drainage times for drop-interface and drop-drop coalescence respectively, as

$$\tau_I = \frac{(6\pi)^{7/6}\,\eta_c r_a^{7/3}}{4\sigma^{5/6}\mathrm{H}^{1/6} r_{F,I} r_V^+} \quad \text{and} \quad \tau_d = \frac{(6\pi)^{7/6}\,\eta_c r_a^{7/3}}{4\sigma^{5/6}\mathrm{H}^{1/6} r_{F,d} r_V^+}. \tag{2.33}$$

The Hamaker coefficient H is in the power of $1/6$ and thus its value does not significantly affect the results. According to Henschke et al. (2002) it can be fixed at $1 \cdot 10^{-20}$ N m, while the asymmetry parameter r_V^+ depends on the system and was fitted to the experimental curves by Pereyra et al. (2013) resulting in $r_V^+ = 0.007$. It must be noted that any effects of polydispersity are not considered in this model. These coalescence times can be used as closures for eqs. 2.29 and 2.31 of the in-line separation model of Sec. 2.2.3.

2.3.1.2 Neck expansion

Once the film drains to an infinitesimal thickness, the intermolecular forces become important and rupture the film, forming a connecting neck between the two coalescing bodies with a radius of r_n. The Young-Laplace pressure

$$\Delta P = \sigma \left(\frac{1}{R_{n,1}} + \frac{1}{R_{n,2}} \right) \tag{2.34}$$

controls the expansion dynamics of the neck, where $R_{n,1}$ and $R_{n,2}$ denote the principal radii of curvature with $R_n = R_{n,1} = R_{n,2}$ for spherical drops. On the rupture of the film, a singularity forms at the neck as its curvature is infinite at the point of

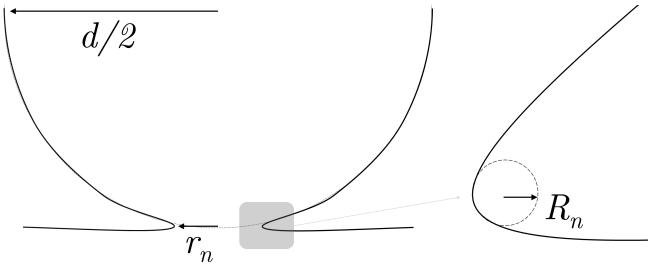

Figure 2.7: Schematic of the neck expansion mechanism during coalescence between a drop and an interface.

contact. A schematic illustration is presented in Fig. 2.7 describing the phenomenon of a drop of radius $a = d/2$ coalescing with a flat interface.

Motivated mostly by sintering and inkjet printing applications, a lot of work has been conducted to investigate drop-drop and drop-interface coalescence. Both numerical and experimental efforts have explored the neck expansion velocities, the curvature of the neck and the propagation of capillary waves. In Table 2.2 a list of works exploring the physical mechanisms during drop-drop and drop-interface coalescence is given. Studies focused only on partial coalescence dynamics have not been included (Kavehpour 2015; Zhang et al. 2015) along with studies exploring non-coalescence due to electrical effects (Ristenpart et al. 2009).

The neck expands rapidly during coalescence, presenting experimental limitations in the resolution of short times to investigate the $r_n(t)$ rates. Several experimental techniques have been implemented to acquire high spatial and temporal resolution in the measurements. From Table 2.2 it is clear that optical measurements are the norm, where the depth of field (DOF) is usually constrained by the camera system. High-speed imaging has been widely used, as it is easy to set up and can be used with a wide range of liquids. More elaborate efforts with LSCM and TLM (cf. footnote 6) can give images of very high spatial resolution of the order of 10^{-6} m, but can only reach recordings of 50 and 1 frame per second respectively and specific fluorescence dyes need to be introduced (Aarts et al. 2005; Aarts and Lekkerkerker 2008). X-ray imaging has provided recently the same high spatial resolution with time-resolved measurements of the order of 10^5 frames per second. PIV measurements both with volume illumination (bright-field PIV) (Chinaud et al. 2016; Nowak et al. 2017) and a laser plane (Mohamed-Kassim and Longmire 2004; Weheliye et al. 2017) have been used to obtain the velocity field during coalescence.

Interfacial tension drives the motion of the neck (as was shown by the Young-Laplace eq. 2.34) and viscous or inertial forces resist it. From dimensional analysis for short times and low Reynolds numbers, the viscous forces balance the interfacial forces, so that $Ca = \eta u_n/\sigma \sim 1$ (i.e. purely viscous Stokes regime), giving

$$r_n \propto \frac{\sigma}{\eta} t, \tag{2.35}$$

where η is the dynamic viscosity of the coalescing phase and σ is the interfacial

Table 2.2: Works investigating neck expansion dynamics during drop coalescence.

	Study[4]	Type[5]	Focus	Technique
Hopper (1990)	num.	d/d	neck velocity, curvature	
Eggers et al. (1999)	num.	d/d	neck velocity, curvature, interface shape	
Menchaca-Rocha et al. (2001)	both	d/d	neck velocity, curvature	imaging
Verdier and Brizard (2002)	exp.	d/d	neck velocity, flow field	PIV
Duchemin et al. (2003)	num.	d/d	neck velocity, curvature	
Gianotti and Nadim (2003)	num.	d/i	neck velocity, curvature (Hele-Shaw cell)	
Mohamed-Kassim and Longmire (2004)	exp.	d/i	neck velocity, wave propagation, flow field	PIV
Wu et al. (2004)	exp.	d/d	neck velocity	imaging
Aarts et al. (2005)	exp.	d/i	neck velocity	LSCM, TLM[6]
Thoroddsen et al. (2005)	exp.	d/d	neck velocity, curvature, wave propagation	imaging
Yao et al. (2005)	exp.	d/d	neck velocity, interface shape	imaging
Aryafar and Kavehpour (2006)	exp.	d/d	neck velocity during coalescence cascade	imaging
Yue et al. (2006)	num.	d/i	interface shape, flow field (viscoelastic fluids)	
Burton and Taborek (2007)	exp.	d/d	neck velocity (2D vs 3D)	imaging
Gilet et al. (2007)	exp.	d/i	neck velocity, curvature, wave propagation	imaging
Kapur and Gaskell (2007)	exp.	d/d	neck velocity	imaging
Thoroddsen et al. (2007)	exp.	d/d	neck velocity, curvature, wave propagation	imaging
Aarts and Lekkerkerker (2008)	exp.	d/i	neck velocity, interface shape	LSCM, TLM
Aryafar and Kavehpour (2008)	exp	d/i	neck velocity, wave propagation	imaging
Case and Nagel (2008)	exp.	d/d	neck velocity	electrical method
Fezzaa and Wang (2008)	exp.	d/d	neck velocity	x-ray imaging
Blanchette and Bigioni (2009)	num.	d/i	neck velocity, interface shape	
Blanchette et al. (2009)	both	d/i	neck velocity, curvature, interface shape, flow field	imaging
Kim and Longmire (2009)	exp.	d/d	flow field of colliding drops	PIV
Wang et al. (2009)	exp.	d/d	change in the surface area of the drops	imaging
Ortiz-Dueñas et al. (2010)	exp.	both	neck velocity, wave propagation, flow field	tomographic PIV
Eri and Okumura (2010)	exp.	d/i	neck velocity (Hele-Shaw cell)	imaging
Lai et al. (2010)	exp.	d/d	flow field of colliding drops on surface	PIV, tomographic LIF
Ata et al. (2011)	exp.	d/d	change in the surface area of the drops	imaging
Paulsen et al. (2011)	exp.	d/d	neck velocity, curvature	imaging, electrical[7]
Gac and Gradoń (2011)	num.	d/d	neck velocity	
Yokota and Okumura (2011)	exp.	d/i	neck velocity (Hele-Shaw cell)	imaging
Bordoloi and Longmire (2012)	exp.	d/d	flow field	tomographic PIV
Paulsen et al. (2012)	exp.	d/d	neck velocity, curvature	imaging
Sprittles and Shikhmurzaev (2012)	num.	d/d	neck velocity, curvature	
Thompson and Billingham (2012)	num.	d/d	neck velocity, curvature	
Gross et al. (2013)	num.	d/d	neck velocity, curvature	
Paulsen (2013)	exp.	d/d	neck velocity, curvature, interface shape	imaging,electrical
Paulsen et al. (2014)	exp.	d/d	neck velocity	imaging
Baroudi et al. (2015)	num.	d/d	neck velocity, interface shape, flow field	
Chen et al. (2015)	both	d/d	neck velocity, interface shape, flow field	imaging
Martin and Blanchette (2015)	num.	d/i	interface shape, flow field (surfactants)	
Mitra and Mitra (2015)	num.	d/d	neck velocity, interface shape	
Munro et al. (2015)	num.	d/d	neck velocity, interface shape	
Chinaud et al. (2016)	exp.	d/i	neck velocity, flow field (Hele-Shaw cell, surfactants)	imaging, BF PIV[8]
Lim et al. (2016)	exp.	d/i	neck velocity, curvature, interface shape	x-ray imaging
Lu et al. (2016)	num.	d/d	neck velocity, curvature, interface shape, flow field	
Nowak et al. (2016)	exp.	d/d	neck velocity, flow field (surfactants)	imaging, BF PIV
Wang et al. (2016)	exp.	d/d	neck velocity, interface shape	shadowgraphy
Nowak et al. (2017)	both	d/d	neck velocity, curvature, interface shape, flow field	imaging, BF PIV
Weheliye et al. (2017)	exp.	d/i	neck velocity, interface shape, flow field	PIV

tension of the coalescing and outer phase system. The velocity of coalescence is computed as $u_n = r_n/t$, which gives for an air-water system velocities close to ~ 70 $\mathrm{m\,s^{-1}}$. Eggers et al. (1999) predicted theoretically only logarithmic corrections to the aforementioned scaling argument as

$$r_n = 1 - \frac{1}{\pi}\frac{\sigma}{\eta} t \ln\left(\frac{\sigma}{\eta a}\right).$$

These corrections were not observed experimentally, while a proportionality constant was found approximately equal to unity for eq. 2.35 (Aarts et al. 2005; Thoroddsen

4. numerical study (num.) and experimental study (exp.).
5. drop-drop coalescence (d/d) and drop-interface coalescence (d/i).
6. laser scanning confocal microscopy (LSCM), transmission light microscopy (TLM).
7. an electrical method was implemented to capture the coalescence initialisation.
8. bright-field (volume illuminated) PIV measurements were conducted. The measuring plane was defined by the camera system.

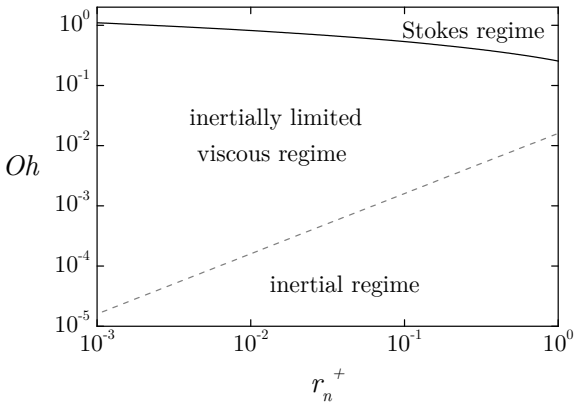

Figure 2.8: Boundaries of drop coalescence showing the limits of the viscous Stokes and inertial regimes in a two-dimensional geometry and for $\eta = 0.0084$ Pa s and $\sigma = 0.0316$ N m^{-1}.

et al. 2005; Yao et al. 2005). Paulsen et al. (2011) recorded smaller proportionality constants from their experiments.

The transition from viscous dominated dynamics to inertial happens at $Re \sim 1$ (Aarts et al. 2005) based on the neck expansion velocity and radius, but Thoroddsen et al. (2005) observed deviations from the linear scaling law of eq. 2.35 for higher $Re \gg 1$. According to Paulsen et al. (2012) the Stokes regime can be achieved when

$$Oh \propto \left| \ln\left(\frac{1}{8}\frac{r_n}{a}\right) \right| \left(\frac{r_n}{a}\right)^{-1/2},$$

where the Ohnesorge number is defined as $Oh = \eta/\sqrt{\rho\sigma a}$ with ρ being the density of the coalescing phase. For two-dimensional drops the same argument can be written as $Oh \propto |\ln(r_n/8a)|/\sqrt{4\pi}$. As described by Paulsen (2013) in detail there is a third regime linking the Stokes with the inertial regime. Specifically, these two regimes do not share a phase boundary, but are connected through an inertially-limited viscous regime, henceforth abbreviated as ILV. The transition to the inertial regime was found to take place at $r_n/a \propto Oh^2$ (Eggers et al. 1999; Aarts et al. 2005; Thoroddsen et al. 2005), but Paulsen et al. (2011) illustrated that $r_n/a \propto Oh$ describes the transition when the ILV regime is taken under consideration. These transition boundaries are plotted in Fig. 2.8 for $r_n^+ = r_n/a$.

When inertial effects dominate, it is not sufficient to set the Weber number $We = \rho u_n^2 r_n/\eta$ equal to unity, as the Capillary forces become equal to $\sigma a/r_n^2$ (Duchemin et al. 2003). By balancing the inertial to the capillary forces it results that

$$r_n \propto \left(\frac{\sigma a}{\rho}\right)^{1/4} t^{1/2}, \tag{2.36}$$

Duchemin et al. (2003) calculated theoretically a prefactor of 1.62, with Wu et al. (2004)

finding lower prefactors in their experiments and Paulsen et al. (2011) reporting prefactors ranging from ~ 1 to 3.

The curvature of the neck R_n (cf. Fig. 2.7) is dependent on the outer phase. Eggers et al. (1999) showed that in the absence of an outer fluid, the curvature is proportional to the neck as $R_n \propto r_n^3$, which agrees with the exact two-dimensional solution by Hopper (1990). When the viscosity of the outer phase increases then different dynamics are observed with $R_n \propto r_n^{3/2}$. For inertial dynamics Duchemin et al. (2003) developed a proportionality as $R_n \propto r_n^2$, which was also reported by Paulsen et al. (2011) and used as the characteristic length in the Reynolds number to predict the aforementioned regime boundaries by Lim et al. (2016). An exponential relation was shown in the experiments of Thoroddsen et al. (2005) in agreement with previous relations.

In drop-interface coalescence, Mohamed-Kassim and Longmire (2004) reported two capillary waves propagating – one along the horizontal axis and one inside the drop towards the top. The propagating velocity for the axial outward wave was reported at $2.6u_n$ and for the wave travelling inward towards the top of the coalescing drop at 1.9 and $2.3u_n$ for viscosity ratios of 0.14 and 0.33 respectively. It is clear that both waves travel faster than the neck. Blanchette and Bigioni (2006) described the significance of the capillary wave travelling to the top in the inertial regime and during partial coalescence. Nevertheless, Blanchette et al. (2009) later stated that capillary waves are not the only cause for the formation of secondary drops, as partial coalescence has also been observed in the viscous regime in the absence of waves.

Gilet et al. (2007) predicted the dispersion relationship for these waves assuming small wavelengths as $(\omega_l t_{ca})^2 = l^3/2$, where ω_l is the pulsation of mode $l = k \cdot a$, k is the wavenumber and t_{ca} is the capillary time $\sqrt{\bar{\rho} a^3/\sigma}$, where $\bar{\rho}$ is the average density of the coalescing and outer phase. The propagation time of the waves from the bottom to the top was found equal to $l^{-1/2}$. To take into account the effect of Bond number for surface-gravity waves Gilet et al. (2007) wrote

$$(\omega t_{ca})^2 = \frac{l}{2}\left(l^2 + Bo\right), \tag{2.37}$$

where

$$Bo = \frac{d^2 \Delta\rho g}{\sigma}, \tag{2.38}$$

and a significant fraction of the amplitude of the waves will be dissipated according to Blanchette et al. (2009) if

$$(ak)^{3/2} \frac{\pi\eta}{(\sigma\rho a)^{1/2}} \equiv (ak)^{3/2}\, \pi Oh = \mathcal{O}\{1\}. \tag{2.39}$$

2.3.2 Breakup

The drops of the dispersion in the pipe can deform and break under shear. When the velocity of the mixture is high, the interfacial tension forces cannot hold the spherical shape of the drops. The drops are stretched under the influence of the local shear gradients and eventually break up in two or more secondary drops. A critical modified Weber number can be written based on the shear gradient $We_{crit} = \eta_c \dot{\gamma} d_{max}/\sigma$ (Brauner 2003) and can predict the maximum size of a drop that can survive the flow in the pipe, i.e. when the interfacial forces will be able to counter the shear effects. It was found that the viscosity ratio $m = \eta_c/\eta_d$ plays a role in the dynamics. The critical Weber number, where breakup will start taking place for laminar conditions, increases for $m \ll 1$ (Acrivos and Lo 1978) as

$$d_{max} = 0.296 D \frac{\sigma}{\eta_c \dot{\gamma} D} m^{1/6}$$

For laminar pipe flow conditions it was previously shown that $\dot{\gamma} = 4u_m/D$ and it becomes clear that the Capillary number of the continuous phase $\eta_c u_m/\sigma$ plays a role in the phenomenon as

$$d_{max} = 0.074 D Ca_c^{-1} m^{1/6} \quad \text{for} \quad m \gg 1. \tag{2.40}$$

Brauner (2001) stated that for turbulent pipe flow, the regions where viscous shear is effective are small compared to the size of the drops and thus the dominant external stress is the dynamic pressure of turbulent eddies. Based on this argument, Kolmogorov (1949) and Hinze (1955) formulated a critical Weber number from a balance between the turbulent kinetic energy and the drop surface energy reading $\rho_c u'^2/2 \simeq 4\sigma/d_{max}$. The turbulent kinetic energy can be related to the mean rate of turbulent energy dissipation per unit mass of the continuous phase $\bar{e}$ as $u'^2 = 2\left(\bar{e} d_{max}\right)^{2/3}$, when the maximum drop size is between the Kolmogorov microscale $\ell_k = \left(\eta_c^3/\rho_c^3 \bar{e}\right)^{1/4}$ and the length scale of the energy containing eddies equal to $0.1D$ (Hinze 1959). From the aforementioned force balance it follows that $d_{max}\left(\rho_c/\sigma\right)^{3/5} \bar{e} \simeq 0.725$ with the constant obtained from fitting of experimental data. Kubie and Gardner (1977) assumed homogeneous and isotropic turbulence in the pipe and set $\bar{e} = 2fu^3/D$. It can therefore be written that

$$d_{max} = 0.55 D We_c^{-3/5} f^{-2/5} \quad \text{for} \quad \ell_k \ll d_{max} < 0.1D, \tag{2.41}$$

where f is the friction factor and the Weber number based on the continuous phase is $We_c = \rho_c u_m^2 D/\sigma$. Brauner (2001) wrote this formulation in a slightly different way by multiplying the right-hand side of (eq. 2.41) with $\left(\rho_m/\rho_c\left(1-\varphi_d\right)\right)^{-0.4}$ stemming from a variation in the formulation of the mean energy dissipation rate $\bar{e}$ in the pipe. This term can be considered approximately equal to unity for liquid-liquid dilute flows.

Eq. 2.41 is based on the assumption of a single drop in a turbulent field, thus it

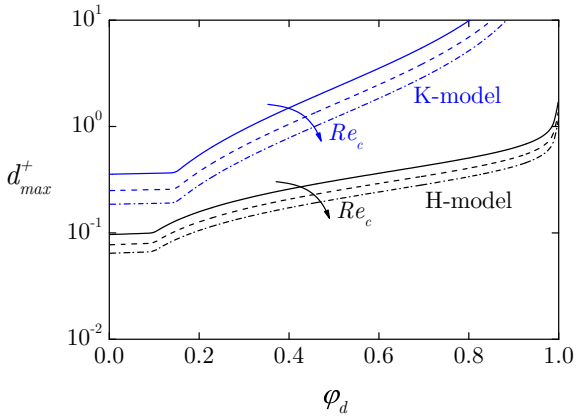

Figure 2.9: Maximum drop size predictions for a range of input dispersed phase fractions by eqs. 2.41, 2.42, 2.43 and 2.44 for $Re_c \in \{2300, 2800, 3300\}$ increasing with the arrow direction.

can only be applied in low drop concentration systems. At higher concentrations, coalescence takes place. Based on an energy balance between the turbulent kinetic energy of the continuous phase and the surface energy produced from the dispersed phase Brauner (2001) proposed a different formulation to describe these systems as

$$d_{max} = 2.22 D C_H^{3/5} We_c^{-3/5} f^{-2/5} \left(\frac{\rho_m}{\rho_c\,(1-\varphi_d)}\right)^{-2/5} \left(\frac{\varphi_d}{1-\varphi_d}\right)^{0.6}, \tag{2.42}$$

with C_H a constant of $C_H = \mathcal{O}\{1\}$. The same restrictions apply for eq. 2.42 as eq. 2.41 in regards to the maximum drop size allowed. For liquid-liquid pipe flows the maximum drop size is then found by taking the highest value between the two equations as $d_{max} = \max$ [eq. 2.41, eq. 2.42]. Eqs. 2.41 and 2.42 are called the H-model. By using eq. 2.2 for Re_c, the maximum drop size is illustrated in Fig. 2.9 for a range of input dispersed phase volume fractions.

Hughmark (1971) suggested that for drops larger than the scale of the energy containing eddies (i.e. $d > 0.1D$), the dynamic pressure due to the turbulent field should be evaluated based on the fluctuating turbulent velocity, which in pipe flow is of the order of the friction velocity, $\left(u'^2\right)^{1/2} \propto u^* = \left(\tau_{wall}/\rho_c\right)^{1/2} = u_m\,(f/2)^{1/2}$. According to Kubie and Gardner (1977), a maximum drop size for dilute systems is given by

$$d_{max} = 1.38 D We_c^{-1} f^{-1} \quad \text{for} \quad d_{max} > 0.1D. \tag{2.43}$$

For dilute systems $\rho_c \simeq \rho_m$, but for higher drop concentrations the wall shear stresses τ_{wall} now need to be written by taking into account the mixture density. Brauner (2001), based on the same energy balance as for eq. 2.42, concluded that the maximum drop size in dense systems can be written in the following form when the drops are larger than the length scale of the energy containing eddies

$$d_{max} = 8 D C_K We_c^{-1} f^{-1} \frac{\rho_c}{\rho_m} \left(\frac{\varphi_d}{1-\varphi_d}\right), \tag{2.44}$$

with C_K a constant of $C_K = \mathcal{O}\{1\}$. Eqs. 2.43 and 2.44 are called the K-model. When $d_{max} > 0.1$ the maximum drop size is then computed by taking the $d_{max} =$ max [eq. 2.43, eq. 2.44]. The predictions are plotted in Fig. 2.9 for different Reynolds numbers.

In this Chapter, the main theory concerning the separation and flow characteristics of liquid-liquid dispersions was described, illustrating the mechanisms that need to be accounted for to predict the behaviour of the unstable dispersed flows. A simplified mechanistic model was developed, which is based on batch settlers (vessel separators) and can predict the evolution of the characteristic layers of a separating liquid-liquid dispersion assuming an average drop size. To investigate the velocity field during the segregation of the drops, a CFD model based on the mixture approach is also developed, which is able to capture the drop motion in laminar Poiseuille flow, assuming a single mean size and rigid drop interfaces. The literature concerning the theory is reviewed and the state of the art formulations are considered for the modelling approaches.

Although several works have explored liquid-liquid dispersed flows, the literature survey of this Chapter demonstrates a lack of combined measurements of the drop size, phase volume fractions and velocities, that can provide an insight to the complex properties of unstable and concentrated dispersions. As discussed before, at such conditions apparent local density and viscosity effects are important, while drop-drop and drop-interface coalescence phenomena can significantly influence the flow structure. For this reason, the next Chapter will examine the new facilities employed and the new experimental methods developed to understand flow transitions and dispersion dynamics through simultaneous characterisation of drop sizes, volume fractions and velocity fields at a range of flow conditions. The detailed and local measurements combined with the modelling approaches aim to provide a novel perspective of concentrated and spatially developing dispersed pipe flows and reveal the underlying physical mechanisms.

Chapter 3

Experimental Methods

The scope of this Chapter is to provide details on the experiments conducted in this project. The facilities utilised and the experimental techniques developed are discussed in the next two Sections respectively, while in the last Section an overview of the experiments performed in each experimental setup is provided.

3.1 Systems and fluids

The experiments in the present work are conducted in three systems. In this Section, the details on the two flow-loops to study dispersed pipe flows and on a confined system to study coalescence are given. Information in regards to the fluids studied is also provided.

3.1.1 Pilot-scale flow loop

The initial experiments in this work studying the separation properties and flow characteristics of dispersed flows take place in a two-phase pilot-scale flow loop. The organic phase is a low viscosity model oil (Exxsol D140) and the aqueous phase is tap water. The properties of the two liquids are shown in Table 3.1. The experiments are conducted at ambient laboratory temperature of 20($\pm$2)^{o}C . The properties of the Exxsol oil are reported according to the supplier. The interfacial tension σ was measured with a drop shape analyser (Krüss DSA100) with the pendant drop method, while the refractive indices n with a refractometer (Abbe 5 Bellingham & Stanley). Each phase is stored in a separate tank as shown in Fig. 3.1. The tanks are made of fibreglass and have a capacity of approximately $0.9\ \mathrm{m}^3$, while each tank is connected to a centrifugal pump. A recycle stream is used to regulate the flow to the test section. The suction and recirculation discharge ports of the tanks have been placed in such a way to increase circulation and heat dissipation.

Table 3.1: Liquid properties of the pilot scale flow loop at 20^{o}C

Liquid	Phase	ρ $\mathrm{kg\,m^{-3}}$	η $\mathrm{Pa\,s}$	σ $\mathrm{N\,m^{-1}}$	n $-$
Water	Aqueous	998	$0.9 \cdot 10^{-3}$	0.0329	1.333
Exxsol D140	Organic	828	$5.5 \cdot 10^{-3}$		1.459

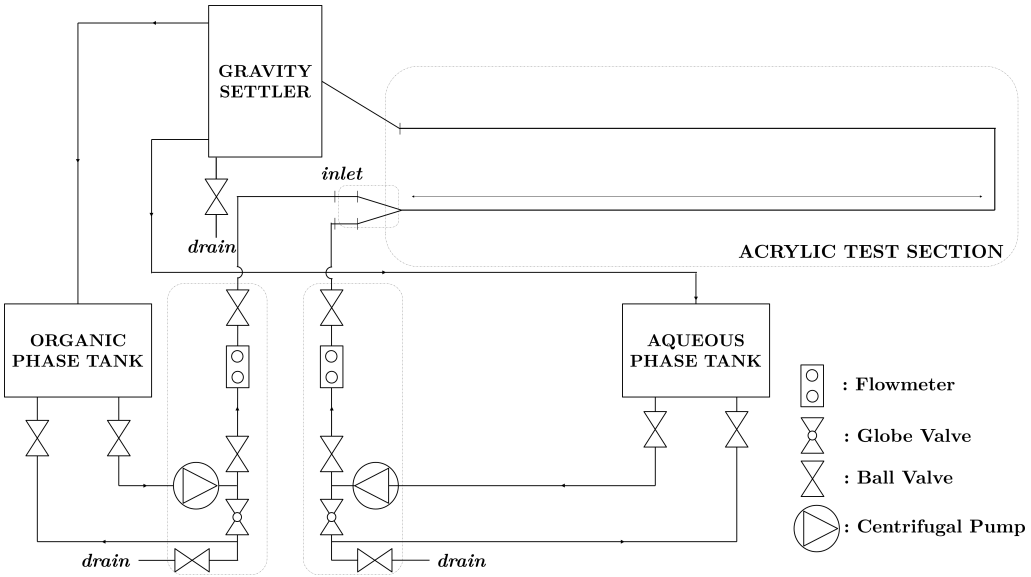

Figure 3.1: Schematic of the flow loop system.

Two Flowserve 2K40-25-250 centrifugal pumps are used to introduce the liquids to the test section. The pumps have motors of variable speed that can reach up to ∼3000 rpm. The power of the pumps is 18.5 kW and is supplied by two three-phase Santerno Sinus Penta inverters. The total dynamic head for each pump is approximately 96 m with a capacity in the range of 0.35 to 20 $\mathrm{m^3\,h^{-1}}$. The flow rates are digitally controlled by Coriolis mass flow meters (Proline Promass 80E by Endress & Hauser) with an accuracy of 0.2% as estimated by the supplier. The Coriolis flow meters can provide continuous measurements of the density of the liquids and indicate any possible temperature or separation issues. The liquids are transferred through 41 mm ID PVC pipes to the test section as shown in Fig. 3.1. A globe valve is used to regulate the recycle stream, while ball valves are installed at different sections of the flow line to allow the isolation of certain sections.

The liquids are introduced to the Perspex acrylic test section through an inlet configuration. The test section is a horizontal 37 mm (±0.3 mm) ID and ∼ 15 m length circular pipe as shown in Fig. 3.1. It comprises of two 7 m long legs connected via two U-bends of 75 mm radii of curvature and one 1 m section. Each leg is composed of spools of various lengths to accommodate different arrangements of the instruments. All instruments are placed in the front leg to avoid any disturbance of the flow by the bends (Collins and Knudsen 1970). The two liquids enter a 0.8 $\mathrm{m^3}$ gravity separator. A DC 9201/SS/PPL KnitMesh coalescer is installed vertically close to the entrance to enhance separation of the two immiscible liquids. A detailed description of its method of operation has been provided by Ngan (2011).

The inlet section, where the two liquid phases meet, is very important and can have an effect on the spatial configuration of the phases downstream. To minimise any mixing taking place between the two liquids, a Y-shaped junction can be used as illustrated in Fig. 3.2(a). The aqueous heavier phase joins through the bottom

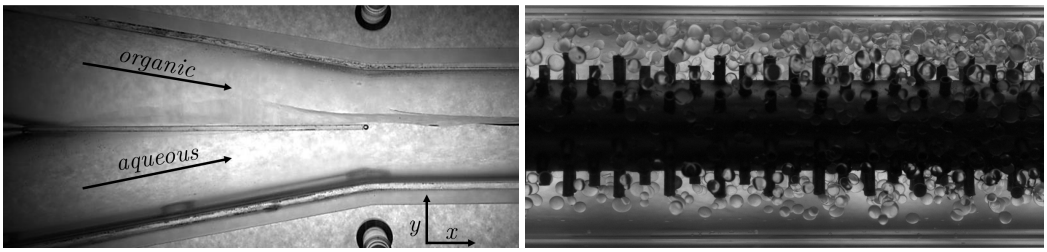

(a) Y-shaped inlet (b) Multi-nozzle inlet

Figure 3.2: Inlet configurations of the pilot-scale flow loop facility.

of the inlet and meets the organic lighter phase at the top. Some disturbance is expected close to the inlet, followed by the formation of small amplitude waves. For low and approximately equal flow rates of both phases, the waves tend to dampen downstream due to viscous effects. For higher flow rates, stronger waves can be generated from the Kelvin-Helmholtz instability (KHI) induced by high velocity gradients at the interface of the two liquids (Barral 2014). These interfacial waves can cause the formation of ligaments, which can break and generate drops causing a flow pattern transition. This mechanism has been recently explored experimentally in liquid-liquid pipe flows by (Al-Wahaibi and Angeli 2007; Barral and Angeli 2014; Park et al. 2016).

As discussed in Chapter 1, the focus in this project is placed on studying the flow characteristics and separation properties of unstable dispersions. Enhanced mixing needs to be introduced at the inlet section to generate kinetically unstable dispersed flow conditions that will separate downstream. A specially designed multi-nozzle inlet is utilised for the experiments in this facility. As shown in Fig. 3.2(b), the dispersed phase, in this case the organic phase, is introduced through more than a thousand stainless steel nozzles ($N_{nozzle} = 1056$) of 1 mm ID and 1.65 mm OD. The nozzles are 7 mm apart with alternating lengths of 2 and 4 mm to avoid coalescence taking place between drops of two neighbouring nozzles. The nozzles are placed at the outer periphery of a stainless steel 12.5 mm ID and 15 mm OD tube of 0.5 mm length located at the core of the pipe cross-section as shown in Fig. 3.2(b).

The number of nozzles has been selected so that the flow area of the nozzles for the dispersed phase is close to the annulus flow area of the continuous phase – presently giving a ratio of ~ 0.93. A similar inlet system was used by Conan et al. (2007). The authors chose the number of nozzles, so that the velocities in each one are kept below $3\ \mathrm{m\,s^{-1}}$ in the range of flow rates needed, to avoid pulverisation and the drop formation results from either ligament or jet breakup at the exit of the nozzles. In the work by Conan et al. (2007), the nozzles were set in a co-flow arrangement with the continuous phase flow, while in the current work the nozzles are set perpendicularly, in a cross-flow arrangement to enhance breakup. The main reason for using the multi-nozzle inlet in the present work, lies in the fact that dispersed flow conditions are generated at lower velocities and thus allow higher residence times in the pipe, which can result in higher separation along the axial streamwise

direction. Dispersed flow conditions are also generated for a wider range of phase fractions, as there is control on the continuous and the dispersed phase, contrarily to the drop formation in the Y-shaped inlet from the KHI. Finally, narrow drop size distributions are expected at the initial axial locations, as the drop formation mechanism is similar for all the nozzles. More details on the measurements in this facility are given in Chapter 4.

3.1.2 Matched refractive index flow loop

Further experiments are conducted in a second flow loop. This facility is designed so that the two immiscible liquids share the same refractive index to allow for accurate optical measurements in dense dispersions. As shown previously, the refractive index of Exxsol oils (organic phase) is relatively high at 20°C with $n_{20} > 1.440$, while the refractive index of tap water (aqueous phase) is equal to $n_{20} = 1.333$. It is possible to increase the refractive index of the aqueous phase by introducing glycerol to it. However, a significant amount of glycerol would be needed to match the refractive index of an Exxsol oil, as shown by Morgan et al. (2012), where an $\sim 82\%$ w/w glycerol/water mixture was needed. High levels of glycerol can cause entrapment of gas bubbles in the mixture, as was the case in the aforementioned work. The refractive index of air is approximately equal to unity and can cause significant light diffraction during optical measurements.

To avoid this problem in this work, a low viscosity silicone oil is used for the organic phase instead – with a refractive index of $n_{20} = 1.396$. To match this refractive index, glycerol is introduced in the aqueous phase at a relatively low concentration of ∼52% w/w. The properties of the liquids used are shown in Table 3.2. To distinguish between the liquids and better track the interface, a small amount of Rhodamine 6G dye was added in the aqueous phase. Rhodamine B-coated PMMA particles with a density of $\sim 1200\ \mathrm{kg\,m^{-3}}$ and a size ranging from 1 to 20 µm were used as tracers in the aqueous phase. A recent detailed review on the selection of fluids and solids for matched-refractive index experiments is given by Wright et al. (2017).

The schematic of the flow loop facility is very similar to that of Fig. 3.1. The liquids are stored in plastic tanks of approximately $0.16 \cdot 10^{-3}\ \mathrm{m^3}$ volume. Each tank is connected to a centrifugal pump (Procon Sandtex) of constant motor speed. Contrarily to the variable motor speed pumps of the previous flow loop facility, a recycle loop and valves are needed for each pump to regulate the flow rate. Two variable area flow meters are used for each flow line for low and high flow rates respectively. The final capacity lies in the range of 0.04 to 0.13 and from 0.13 to

Table 3.2: Liquid properties of the matched refractive index flow loop at 20°C

Liquid	Phase	ρ $\mathrm{kg\,m^{-3}}$	η $\mathrm{Pa\,s}$	σ $\mathrm{N\,m^{-1}}$	n –
Glycerol/Water	Aqueous	1146	$8.4 \cdot 10^{-3}$	0.0316	1.396
Silicone oil	Organic	913	$4.6 \cdot 10^{-3}$		

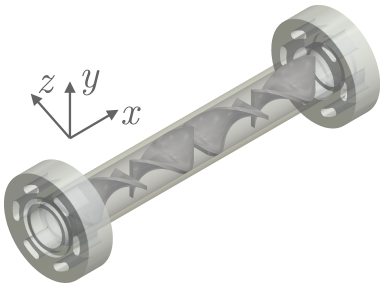

Figure 3.3: Pipe spool with a helical static mixer of 4 elements.

1.62 $\mathrm{m^3\,h^{-1}}$ for each flow meter. The flow meters are calibrated for their respective liquid phase. PVC $26\ \mathrm{mm}$ ID pipes with globe and ball valves are used for the liquid transfer of the liquids to the inlet section.

The test section used in the current experiments is a $26\ \mathrm{mm}$ ID Perspex acrylic circular pipe of $\sim 8.5\ \mathrm{m}$ length. Two horizontal legs of $4\ \mathrm{m}$ each are connected via two U-bends. As in the aforementioned facility, variable length spools are used and the measurements are conducted in the front leg of the flow loop. The gravity separator has a capacity of $0.22\ \mathrm{m^3}$, which allows the liquids to be fed back to their respective tanks. Short runs are very important in this rig, in order to allow enough time for separation of the fluids, but also to avoid any temperature changes induced by the pumps working at constant motor speed.

The liquids enter the test section through a Y-shaped junction (Fig. 3.2(a)), with the lighter organic phase coming from the top and the aqueous heavier phase from the bottom. As the goal remains to generate dispersed flow conditions at low velocities, enhanced mixing at the inlet needs to be introduced. For this reason, the two liquids pass through a 6-element helical static mixer (JLS International) of alternating mixing elements, where each element is set perpendicularly at a 90º angle to its adjacent elements. Thorough axial and radial mixing is provided from the mixer by dividing the main flow into two equal streams as the mixture passes each element. The number of divisions increases as $2^{N_{elements}}$, where $N_{elements}$ is the number of elements of the mixer. The total mixing length is $265\ \mathrm{mm}$. A shorter 4-element design of the mixer is illustrated in Fig. 3.3. Various flow patterns are observed with this flow configuration, which depend on the mixture velocity and input oil fractions – defined as

$$u_m = \frac{Q_o + Q_w}{A} \quad \text{and} \quad \varphi_o = \frac{Q_o}{Q_o + Q_w}, \tag{3.1}$$

where Q_o and Q_w are the volumetric flow rates of the organic and aqueous phase respectively and A is the pipe cross-sectional area. Detailed discussion on the results from the experiments of this facility are provided in Chapter 5.

3.1.3 Hele-Shaw cell

Additional experiments are also conducted in a confined system, to investigate further the coalescence mechanism and more specifically the neck expansion dynamics

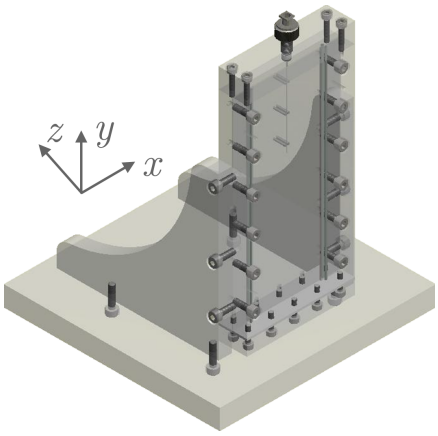

Figure 3.4: Hele-shaw cell with drop formation nozzle.

in the initial stages of coalescence. As discussed in Sec. 2.3.1.2, the neck expansion is a quick phenomenon and includes various length-scales. A Hele-Shaw (1898) cell is a quasi-two-dimensional cell comprised of two parallel plates with a thin gap Δz and is used to study in detail the aforementioned coalescence dynamics. A CAD design of the cell is presented in Fig. 3.4. Two-dimensional flows in porous media can be modelled with flows in a Hele-Shaw cell (Saffman and Taylor 1958). The average velocity of a viscous fluid flowing in the space between the plates is

$$\boldsymbol{U} = -\frac{\Delta z^2}{12\eta}\nabla P + \rho \boldsymbol{g}, \tag{3.2}$$

which is identical to Darcy's law for motion in a porous medium with a $\Delta z^2/12$ permeability. When $\Delta z \to 0$, for steady-state and uniform flow, the velocity component along the depth of the cell can be neglected $w = 0$, while the velocity in the plane of measurement can be assumed to depend only on the z direction. Under these assumptions, it can be written that $\nabla \cdot \boldsymbol{U} = 0$ and the two velocity components u and v along the x and y respectively can be averaged along the depth z.

Due to the interfacial symmetry in drop-drop coalescence, the film ruptures at approximately the closest point where the drops are placed. However, in this work drop-interface is studied, where the rupture can take place at various positions along the depth of the system (Mohamed-Kassim and Longmire 2004). Studying the coalescence mechanism in a Hele-Shaw cell allows to localise the film rupture point and study the early times of the neck expansion. Eri and Okumura (2010) and Yokota and Okumura (2011) have similarly both used a Hele-Shaw cell to study these dynamics. In this work, the Hele-Shaw cell is made from two Perspex acrylic plates of a few millimetres thickness and are separated by a distance $\Delta z \sim 1.25$ mm with spacers of homogeneous thickness. The plates have a length of $\Delta x = 80$ mm and a height of $\Delta y = 140$ mm. A nozzle, made from stainless steel of 0.5 mm ID, is introduced from the top and placed in the middle of the cell to allow for the formation of the drop, as shown in Fig. 3.4. A small valve was placed at the bottom of the cell to regulate the static pressure and keep the organic-aqueous interface as flat as possible.

To initialise the experiments, the cell is first filled with the lighter organic phase, while the aqueous phase is introduced next, in order to guarantee that the oil is wetting the walls along the whole cell. Enough time is given to the system until separation takes place, i.e. the aqueous phase goes to the bottom of the cell and the organic rises at the top. Aqueous drops are generated with a syringe pump (KDS Scientific) connected to the nozzle. The drops are surrounded by air when generated, to avoid any effects from additives present in the organic phase and allow the same volume of drops on every run. The drops have an ellipsoidal shape on the plane of measurement, while their thickness is smaller than the depth of the cell, as the oil phase is wetting the walls. The drops are left to settle at the liquid-liquid interface until they coalesce. An infinitesimal amount of ink is added to the aqueous phase to allow the distinction between the two phases and better capture the interface properties. The interface appeared on the images with a thickness of 1 pixel or about $10\ \mu\mathrm{m}$. Additional $10\ \mu\mathrm{m}$ silver-coated glass tracer particles with a density of $\sim 1400\ \mathrm{kg\,m^{-3}}$ are introduced in the aqueous phase to allow for PIV measurements.

3.1.3.1 Addition of surface active agents

Two different sets of liquids are used for the experimental runs in the Hele-Shaw cell. Firstly, the effect of a non-ionic surface active agent Span 80 (with a density of $990\ \mathrm{kg\,m^{-3}}$ and a molar weight of $428.6\ \mathrm{g\,mol^{-1}}$ at 20°C) is explored in a refractive index matched system of 82% w/w glycerol/water and Exxsol D80. Span 80 is soluble in the organic phase, with an HLB index of 4.3. Four surfactant concentrations in the organic solution are prepared by diluting an initial dense solution to the appropriate level. The solutions are then put in an ultrasound bath for $\sim 15\ \mathrm{min}$ at $45\ \mathrm{kHz}$ to homogenise the mixtures. The experiments are conducted at the laboratory ambient temperature of $22(\pm 2)$°C. The properties of the liquids are presented in Table 3.3.

The interfacial tension values of Table 3.3 are measured with the pendant drop method (Krüss DSA100). Following the Gibbs adsorption equation for a non-ionic surfactant, the surface excess Γ can be written as

$$\Gamma = -\frac{1}{\tilde{R}\mathcal{T}}\frac{\mathrm{d}\sigma}{\mathrm{d}\ln c},$$

Table 3.3: Liquid properties of the surfactant Span 80 study in the Hele-Shaw cell at 22°C

Phase	Liquid	ρ $\mathrm{kg\,m^{-3}}$	η $\mathrm{Pa\,s}$	n $-$	Span 80 w/w	σ $\mathrm{N\,m^{-1}}$
Aqueous	Glycerol/Water	1210	54×10^{-3}			
Organic	Exxsol D80	804	1.75×10^{-3}	1.443	0	26.7×10^{-3}
					2×10^{-5}	21.1×10^{-3}
					1×10^{-4}	18.3×10^{-3}
					1.5×10^{-4}	13.2×10^{-3}
					2×10^{-4}	9.6×10^{-3}

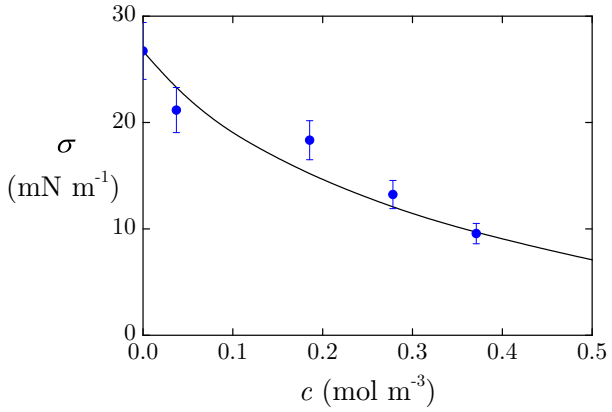

Figure 3.5: Interfacial tension values of the organic phase for different Span 80 concentrations. The continuous line is plotted from eq. 3.3.

where $\tilde{R}$ is the universal gas constant, $\mathcal{T}$ is the temperature and c is the molar concentration of the surfactant in the bulk. According to the Langmuir adsorption isotherm, the surface excess is related to the concentration of surfactant in the bulk as

$$\Gamma = \frac{\Gamma_\infty K_L c}{1 + K_L c},$$

where Γ_∞ is the adsorption capacity and depends on the minimum surface area occupied by an adsorbed surfactant molecule, while K_L is the ratio between the adsorption and desorption rate constants.

Combining the two aforementioned equations and integrating, it can be written that

$$\sigma = \sigma_0 - \tilde{R}\mathcal{T}\Gamma_\infty \ln\left(1 + K_L c\right), \tag{3.3}$$

which is known as the surface equation of state (EOS) correlating interfacial tension with the concentration of surfactant with σ_0 being the interfacial tension of the pure system with no surfactant. As Giribabu and Ghosh (2007) discuss, eq. 3.3 is valid for concentrations below the critical micelle concentration (CMC) of the corresponding surfactant, while they found from their experiments for a Span 80 in a mineral oil-water system that $\Gamma_\infty = 4.42\times10^{-6}\,\mathrm{mol\,m^{-2}}$ and $K_L = 10\,\mathrm{m^3\,mol^{-1}}$. Eq. 3.3 is plotted together with the experimental data in Fig. 3.5 and good agreement is found.

3.1.3.2 Addition of shear-thinning liquids

The second run of coalescence experiments in the Hele-Shaw cell handles the effects of shear-thinning fluids at the neck dynamics. For all cases, coalescence between an aqueous drop and its pool is studied, while the outer bulk phase is a low viscosity silicone oil. For comparison purposes with the flow loop facility, the same liquids as before are used – given in Table 3.2. The aqueous phase is a mixture of glycerol/water in a 52% w/w ratio to match their refractive indices. As in the previous

Section, the same amount of ink and tracer particles are introduced in the aqueous phase, to distinguish the interface and to accommodate for PIV measurements. The interfacial tension of the liquids is measured with a Krüss K100C instrument equipped with a Du Noüy ring here instead of the pendant drop method. The coalescence is studied between pairs of liquids with the same rheological properties. A Newtonian and three non-Newtonian solutions are employed as the coalescence phase in individual experimental runs.

Each of the non-Newtonian solutions contains a different concentration of xanthan gum, i.e. 500, 1000 and 2000 ppm respectively. No change in the density, interfacial tension and refractive index of the fluid was measured with the addition of xanthan gum. It is a rigid polymer and is soluble in aqueous solutions. Xanthan gum powder provided by Sigma-Aldrich is used. The solutions are prepared by first mixing distilled water with the xanthan gum powder by continuously stirring to avoid agglomeration. Once all the polymer is dissolved, the appropriate amount of glycerol is added and the stirring is continued until a homogeneous mixture is achieved. To avoid biodegradation of the polymer, the solutions are used immediately after production. No other liquid is investigated for the bulk phase, as Paulsen et al. (2014) found no significant effect on the early stages for different viscosity ratios of the bulk and coalescing phase.

An Advanced Rheometric Expansion System (ARES TG-42, TA Instruments) is used to study the rheological behaviour of the solutions. All measurements are carried out at 20^{o}C, while the rheometer has a Couette geometry with a bob of 16.5 mm ID, 17 mm cup size and a 0.05 mm gap. The rheological properties of the non-Newtonian solutions under investigation for the three xanthan gum concentrations are illustrated in Fig. 3.6. It is clear that all three solutions present shear-thinning behaviour and thus the well established Carreau model (eq. 3.4) is used to describe the data (Tam and Tiu 1989), as shown by the continuous curves in the Figure. The Carreau model is written as

$$\hat{\eta}(\dot{\gamma}) = \eta_{\infty} + (\eta_0 - \eta_{\infty})(1 + (\hat{\lambda}\dot{\gamma})^2)^{\frac{\hat{n}-1}{2}} \tag{3.4}$$

where $\hat{\eta}$ is the effective shear viscosity dependent on the shear rate $\dot{\gamma}$, η_0 and η_{∞} are the zero and infinite shear rate viscosity respectively, while $\hat{\lambda}$ denotes the relaxation time and $\hat{n}$ the power index of the model. The fitted parameters $\hat{\lambda}$ and $\hat{n}$ for the three concentrations, namely 500, 1000 and 2000 ppm are 13.9, 0.48; 27.2, 0.31 and 18.4, 0.25 respectively. Eq. 3.4 serves as a master equation able to predict the local viscosity of each solution based on the shear profile.

While the shear-thinning properties of xanthan gum aqueous solutions have been well established in the literature for a wide range of concentrations, temperatures and shear rates, it has been shown that at high concentrations they can also illustrate viscoelastic behaviour (Tam and Tiu 1989). The first stages of the coalescence can be well described as an extensional flow on the lateral direction of the main

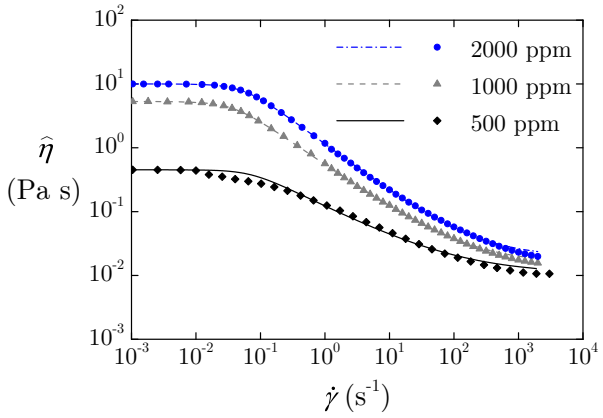

Figure 3.6: Rheological curves of shear-thinning solutions. The lines represent the fitted Carreau model to the data from eq. 3.4.

vertical flow. For this reason, the strain profile of the flow and the elastic properties of the solutions can prove of interest to understand the characteristics of coalescence between non-Newtonian fluids. It needs to be mentioned that the viscoelastic properties of xanthan gum solutions are quite weak, so typical rheometers are not able to accurately compute them. Thurston (1981) and Thurston and Pope (1981) illustrated through filament stretching experiments in a tube and in conjunction with theoretical models, how the oscillatory flow viscoelasticity of aqueous solutions of 125 to 1000 ppm xanthan gum is strongly dependent upon the amplitude of the shear, as well as the frequency. It was shown that an increase in concentration does not change the general character of the shear rate dependence, but the elastic component increases rapidly with concentration. Flow focusing microfluidic devices have also been used to correlate the effects of elasticity to an exponential filament thinning rate, when a viscous solution is stretched by an external immiscible fluid (Khagram et al. 1985; Arratia et al. 2008). However, in this work the viscoelastic characteristics of the solutions are not considered.

3.2 Techniques and data analysis

In this Section, a detailed description of the techniques implemented in this work is provided. The principles behind conductivity, tomography and laser-based diagnostics are discussed along with their application to the present experiments.

3.2.1 Conductivity

Several techniques have been implemented throughout the years based on the conductivity/impedance difference of the two liquids under investigation. As already discussed in Chapter 2, conductivity probes can provide information on the wetting phase and interface height (Edomwonyi-Otu and Angeli 2015), on interfacial waves (Barral and Angeli 2014) and most relevant to this work on drop size (Lovick and

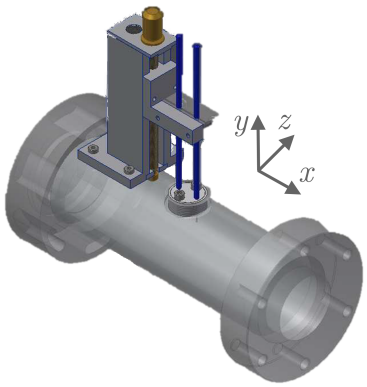

Figure 3.7: Pipe spool of dual-conductance probe with sensors.

Angeli 2004a; Ioannou et al. 2005; Ngan et al. 2011). Tomography systems have also been implemented. Ngan (2011) used an ERT system to study liquid-liquid flows, Schümann et al. (2016a) an x-ray system, while Hewakandamby et al. (2014) and Prasser et al. (2005) used wire-mesh sensors for gas-liquid flows.

3.2.1.1 Dual-conductance probe

A dual-conductance probe (DCP) is developed in the present work and implemented in the pilot-scale flow loop of Sec. 3.1.1. Its working principle is similar to the dual-impedance probe (Angeli and Hewitt 2000b), but works with direct current instead. The circuit is based on the work of Zhai et al. (2016). The probe records the conductivity at two locations close to each other. With rigorous signal analysis, it can measure the local in-situ phase fractions and the chord lengths of the drops.

Figure 3.7 illustrates a CAD drawing of the pipe spool with the probe as used in the pilot-scale flow loop, where three DCP are placed at three axial locations downstream the inlet of the test section. A traversing mechanism with the two sensors is placed on the top of each pipe spool. This accommodates for the vertical displacement of the sensors inside the pipe to record various locations on the y axis. The distance between the two sensors is equal to $\Delta x = 5$ mm. The sealing of the holes, where the two sensors penetrate the pipe spool, is done with PTFE tape and o-rings, to guarantee that no leaks take place as the flow passes through the probe. The sensors are rigid coaxial wires that have an inner and outer electrode separated by insulation. An outer layer of insulation with heat-shrink is also provided to avoid any sipping of water to the sensor. As water, oil and air (during shut-down) are in contact with the sensor tips, possible damage and corrosion to the sensors can take place, which can in turn lead to noise in the recorded signal. For this reason, new wires are installed before the start of each experimental run.

The use of direct current can cause possible polarisation effects at the sensor region. To avoid such effects, the circuit is designed based on a saturation amplification technology. The operation of the circuit works as follows. When the sensors are immersed in the water phase, the signal conditioning circuit outputs a high voltage,

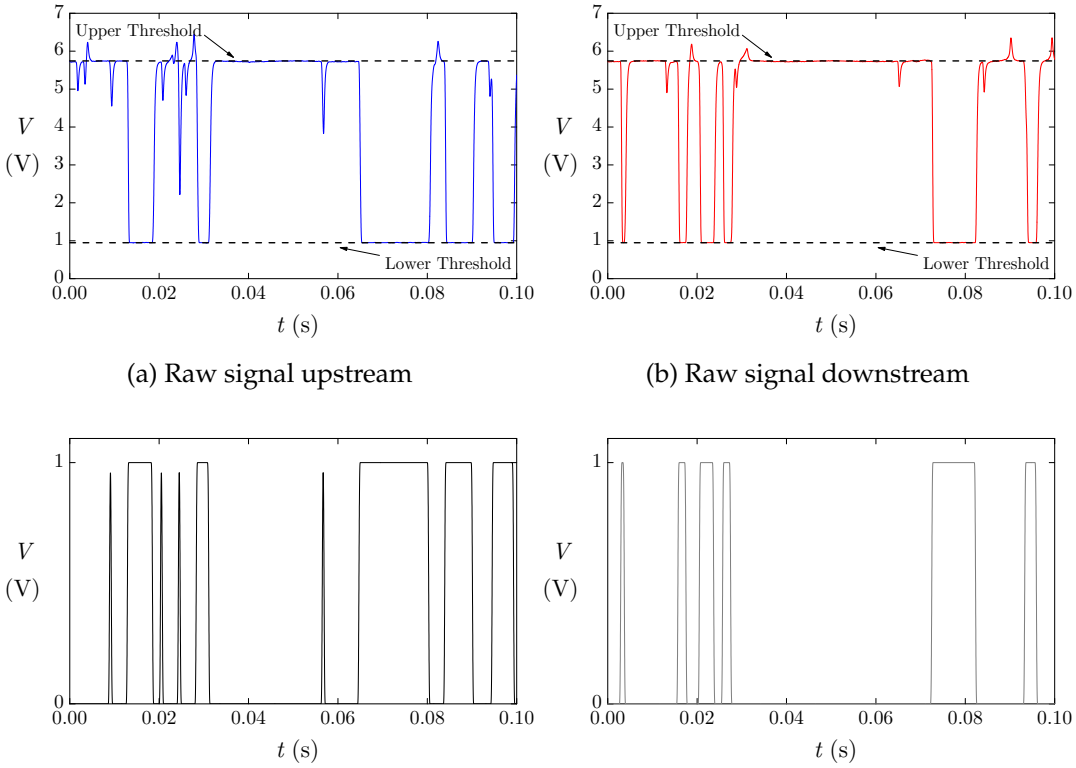

(a) Raw signal upstream

(b) Raw signal downstream

(c) Square signal upstream

(d) Square signal downstream

Figure 3.8: Raw and square wave signals from both the upstream and downstream sensor for an *o/w* flow.

as the conductivity is high. The opposite behaviour is recorded when the sensor tips are immersed in oil, i.e. oil drop passing through them. When a drop is covering the tip, the connection between the inner and outer electrode is broken and the circuit outputs low voltage instead. The raw signals are recorded by LabView. To acquire statistically meaningful results, the acquisition frequency of the sensor is set at 5 kHz and a sampling time of $T = 10$ s is selected. Depending on the flow condition and pipe axial and vertical measuring location, at least a few hundred drops are recorded with each sample.

A typical signal recorded is presented in Figs. 3.8(a) and (b) for the upstream and downstream sensor respectively in a duration of 100 ms. The signals are recorded during an *o/w* dispersed flow. As the water is the continuous phase, the voltage V recorded is at the maximum allowable threshold of the circuit ~ 5.8 V. When an oil drop covers the sensor tip, then the voltage recorded rapidly dips to the lowest allowable value of ~ 0.9 V. These limits have been adjusted from the components of the circuit together with two threshold filters – one high and one low as shown in Figs. 3.8(a) and (b). Any voltage recorded outside of this range is filtered. The raw signals can be then transformed to binary square wave signals, where the value of 1 denotes the presence of a drop.

As can be seen in Figs. 3.8(a) and (b), a few small peaks can be present at the

Table 3.4: Slope filter configuration for the raw signals.

Condition	Outcome (V)
$j > j_{crit}$	$V(t_{i+1}) = 1$
$j < -j_{crit}$	$V(t_{i+1}) = 0$
$-j_{crit} \leqslant j \leqslant j_{crit}$	$V(t_{i+1}) = V(t_i)$

signal that might not necessarily correspond to a drop, but possible noise from conductivity fluctuations in the surrounding area of the tip. Two main methods have been used in the literature to distinguish between the noise and the drops. First, Welle (1985) used a "double threshold" algorithm in gas-liquid flows to transform the raw signals to square wave signals. Several works with this technique have been conducted in liquid-liquid flows (Zhai et al. 2012; Zhai et al. 2016). In this work, a slope filter is used instead to distinguish between the noise and the drops, based on the work of Hu (2006).

For the upstream sensor $V_1(t)$, the slope filter j is equal to

$$j = \frac{V_1(t_{i+1}) - V_1(t_i)}{t_{i+1} - t_i}. \tag{3.5}$$

When the slope is higher than a set critical slope, $j_{crit}(> 0)$, the sample collected on time t_{i+1} is assigned a value of 1. If j is lower than $-j_{crit}$, the sample collected on time t_{i+1} is set to 0. If j ranges from $-j_{crit}$ to j_{crit}, then the value of the sampling time t_{i+1} is kept at the same value as the previous one (0 or 1). From the square wave signal, the oil volume fraction is calculated from the time the probe indicates oil (signal equal to 0) over the total time of the experiment. This behaviour is summarised in Table 3.4. The critical value of the slope is set based on the noise levels recorded in pure oil flow and ranges from $0.031 \leqslant j_{crit} \leqslant 0.115\ \mathrm{V\,s^{-1}}$. From the application of the filters, the square wave signals of Figs. 3.8(c) and (d) are obtained for the upstream and downstream sensor respectively. The in-situ oil volume fraction ε_o from each square wave signal can be computed by diving the total samples where drops are present (i.e. have the value of 1) by the total number of samples (50,000).

From the square wave signals acquired from both sensors the drop chord lengths can also be measured. The principle behind the computation lies in the assumption that a drop passing through the upstream sensor, will continue in the same direction and pass through the downstream sensor as well. This assumption holds true for the drop concentrations explored. When the drop passes through both sensors, a spike in their signals is recorded, but with a time delay τ_{delay}. This time delay is quasi-constant for all drops, assuming that all of them travel with approximately the same axial velocity. It can be computed by cross-correlating the two signals as

$$\mathcal{R}_{V_1,V_2}(\tau_{delay}) = \lim_{T\to\infty} \frac{1}{T} \int_0^T V_1(t) V_2\left(t + \tau_{delay}\right) \mathrm{d}t, \tag{3.6}$$

where $\mathcal{R}_{V_1,V_2}$ is the cross-correlation function of the signals of the upstream and

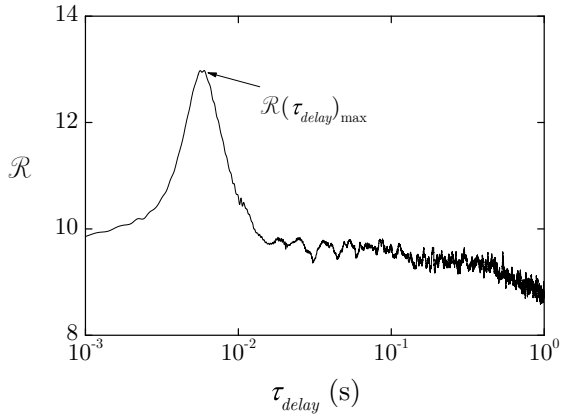

Figure 3.9: Cross-correlation (eq. 3.6) result between the upstream and downstream sensor of the DCP.

downstream sensors V_1 and V_2 respectively. Figure 3.9 illustrates the cross-correlation result of the signals of Figs. 3.8(c) and (d). A distinct peak (maximum of $\mathcal{R}$) is taken as the τ_{delay}. The primary to secondary peak ratios of the correlations are found satisfactory with values over 1.10 for all cases considered. The time-averaged axial velocity of the drops $\langle u_d \rangle$ can be then computed as the ratio of the distance of the sensors and the time delay from the cross-correlation giving $\langle u_d \rangle = \Delta x / \tau_{delay}$, where $\Delta x = 0.005$ for all the experiments.

The drop chord lengths can be obtained by multiplying each corresponding peak in the square wave with $\langle u_d \rangle$. It is important to note that the drops sizes recorded are not the drop diameters, but the drop chord lengths. However, for the purposes of this work they will be treated as equal. The minimum drop size that can be recorded is based on the coaxial wire dimensions, sampling frequency and the maximum drop velocity and was computed approximately equal to $200\ \mu\mathrm{m}$. The signals from both sensors can be used to acquire the drop sizes, but the upstream sensor is found to give more accurate results, which can be caused by disturbances induced by the wake of the upstream sensor to the downstream one. To evaluate the repeatability of the measurements, several runs are carried out with different coaxial wires of the same dimensions for $u_m = 0.5\mathrm{m\,s^{-1}}$ and $\varphi_o = 0.60$. The Sauter mean diameters, computed from eq. 2.30, deviate less than $\pm 18\%$ from the mean, with the upstream and downstream electrode giving a constant variation on top of the previous relative uncertainty of approximately $\pm 10\%$. As expected, the downstream sensor was capturing $\sim 30\%$ less drops compared to the upstream one, for samples $N_d = \mathcal{O}\{10^3\}$. It was found that the Sauter mean diameter of a sample of about 400 drops deviates from a sample of about 500 drops by less than 3%, while both sample sizes are statistically sufficient for 95% confidence levels at 7% margins of error.

For dilute enough cases, the DCP can be compared against drop size measurements conducted with high-speed imaging. It is noteworthy, that the d_{32} computed from the DCP are $\sim 10\%$ higher than those measured directly from the images. This

differencemight be higher, considering that the DCP measures chord lengths, which are by definition smaller (or equal) to the drop diameters measured from the images. However, it must be noted that the DCP measures only the drops in the middle plane of the pipe, while the drops measured in the images correspond to drops along the whole pipe depth with a bias towards the outer wall. As higher drop sizes are expected in the middle of the pipe (Bourdillon et al. 2016), this relative difference between the two methods is justified. Nevertheless, the overall experimental uncertainty of the DCP can be estimated at $\sim 30\%$ and the difference between the two methods falls within this range.

3.2.1.2 Electrical resistance tomography

To compare the results from the DCP, an electrical resistance tomography (ERT) system is used in the pilot-scale flow loop of Sec. 3.1.1 with the multi-nozzle inlet (oil dispersed) – also in three axial locations downstream the inlet of the test section. The ERT system allows the acquisition of the in-situ phase fractions in the pipe cross-sectional area. Previous studies have implemented this method (Holden et al. 1998; Bolton et al. 2007), which can also be extended to acquire the velocity profiles (Zhu et al. 2015), when two sets of sensors are utilised and placed close to each other. The ERT system in this work has one sensor consisting of 16 electrodes, placed in the periphery of an acrylic pipe spool of 37 mm ID (i.e. same as the test section). Each electrode is made from stainless steel and has an approximate diameter of 2 mm. Coaxial wires are soldered on each electrode and they are then connected to a p2000 unit by Industrial Tomography Systems. A single earth electrode is required – placed in a short axial distance from the measurement electrodes. Raw signals are recorded and post-treated with the ITS p^{+} software. A linear back projection (LBP) reconstruction algorithm is used to transform the grid from the sensor to the pipe cross-section, while Maxwell (1881) equation, given by

$$\varepsilon_d = \frac{2\kappa_c + \kappa_d - 2\tilde{\kappa} - \dfrac{\tilde{\kappa}\kappa_d}{\kappa_c}}{\tilde{\kappa} - \dfrac{\kappa_d}{\kappa_c}\tilde{\kappa} + 2\left(\kappa_c - \kappa_d\right)}, \tag{3.7}$$

is used to transform the conductivities to local in-situ phase fractions of the dispersed phase ε_d, where κ is the conductivity of either the continuous or the dispersed phase and $\tilde{\kappa}$ is the reconstructed measured conductivity given from the LBP.

The Exxsol oil (dispersed phase) conductivity for these experiments is very low and $\kappa_d \approx 0$ can be safely considered. Equation 3.7 can be for this reason reduced to $\varepsilon_d = \left(2\kappa_c - 2\tilde{\kappa}\right) / \left(\tilde{\kappa} + 2\kappa_c\right)$. The conductivity of the water (continuous phase κ_c) is contrarily relatively high, as salts are naturally present in the tap water used. A reference conductivity tomogram is taken when the pipe is completely filled with water. This calibration is performed before each experimental run to accommodate slight variations in the salt concentration of the water and provide better accuracy

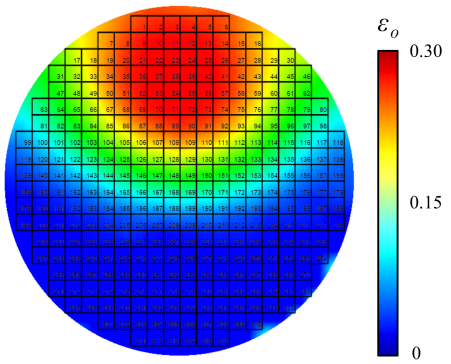

Figure 3.10: Typical tomogram acquired at the pilot-scale flow loop with the multi-nozzle inlet for $u_m = 1.0\mathrm{m\,s^{-1}}$ and $\varphi_o = 0.15$ at $x^+ = 25$.

in the performance of the Maxwell equation. The time-averaged ERT measurements are computed from 50 frames acquired over a time-span of $10\ \mathrm{s}$. The spatial resolution of the ERT 16-electrode system is $\sim 1.5\ \mathrm{mm}$.

An instantaneous ERT tomogram acquired at the pilot-scale flow loop facility with the multi-nozzle inlet is shown in Fig. 3.10 for $u_m = 1.0\ \mathrm{m\,s^{-1}}$ and $\varphi_o = 0.15$ at $x^+ = 25$. The grid of the 316 local conductivities obtained with the 16 electrode sensor is superimposed on the tomogram. A smoothening function is applied through the ITS p$^+$ software. This option allows the user to smooth the tomogram into a perfect circular image by integrating the edges of each grid box. It is important to note that this method does not provide finer results nor is an additional reconstruction scheme.

Quick closing valves (QCV) are used in the pilot-scale flow loop at 80 equivalent pipe diameters downstream the multi-nozzle inlet $x^+ = 80$. At that location an overall in-situ oil volume fraction $\bar{\varepsilon}_o$ can be acquired from the QCV, the ERT and DCP. While $\bar{\varepsilon}_o$ is simple to compute in the pipe cross-section from both the QCV and the ERT, the same is not true for the DCP, as the measurements are conducted on a vertical plane instead. To compare with the other methods, the cross-section is split in horizontal segments with each segment having the volume fraction measured at the middle plane. A similar method has been used by Schümann et al. (2016b) to extrapolate drop size results of an FBRM probe measuring in the middle plane, to the whole pipe cross-sectional area. Fig. 3.11 illustrates the comparison of the QCV, the DCP and the ERT for seven flow conditions. The measurements shown for the ERT and DCP are both time and spatially averaged $\langle\bar{\varepsilon}_o\rangle$ as discussed in the previous paragraphs.

In horizontal liquid-liquid dispersed flows, the slip in the streamwise direction x is very small, so $\varphi_o \approx \langle\bar{\varepsilon}_o\rangle$ is expected. From Fig. 3.11 it is clear, that the ERT system underpredicts the concentration of oil in the pipe cross-section for the whole range of input oil volume fractions. Most notably, for $\varphi_o = 0.60$ the deviation reaches almost 100%. This limitation stems from the sensor arrangement and the application of Maxwell's equation in dense systems. The low spatial resolution of the ERT ($\mathcal{O}\{1\}$

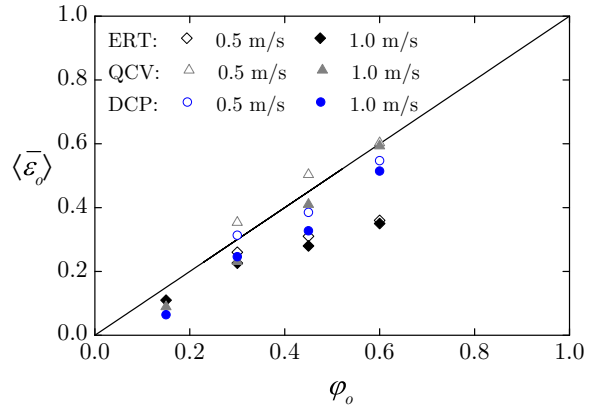

Figure 3.11: Mean in-situ oil volume fraction $\langle \bar{\varepsilon}_o \rangle$ measured from the ERT, the QCV and the DCP for different *o/w* flow conditions at $x^+ = 80$ downstream the multi-nozzle inlet.

mm) can also possibly affect the measurements. Nevertheless, the drop size does not seem to affect the behaviour of the ERT, as very close $\langle \bar{\varepsilon}_o \rangle$ are obtained for both mixture velocities at the same φ_o, in spite of the fact that different drop sizes are expected to be generated from the nozzles.

The QCV seem to adequately represent the measurements in Fig. 3.11. Some deviations might be due to flow pattern changes along the pipe, especially at the lower mixture velocity. If a separate layer of the dispersed oil phase forms, then higher oil concentrations are expected in the pipe cross-section. The DCP seems to follow the trends measured with the QCV with a mean deviation of about 20% lower than the QCV . The discrepancies can be caused by possible drops present in the system that either avoid the DCP or are too small ($d < 200$ µm) and fall below the measuring spatial resolution of the probe. Another reason can be the bias in the spatial averaging of the DCP by computing the in-situ oil fraction in the whole pipe cross-section, which assumes the same concentration of oil along the whole depth z.

3.2.2 Optical flow diagnostics

Optical measurements have been extensively implemented in the investigation of liquid-liquid pipe flows. High-speed imaging with volume illumination, where the measuring field is constrained by the depth of field (DOF) of the camera, can provide valuable qualitative results and has been used in the majority of cases to study flow structures (Trallero et al. 1997; Angeli and Hewitt 2000a; Shi and Yeung 2017). Zhai et al. (2017) combined the visualisations with statistical methods to acquire drop size measurements. Recent advancements in optical laser-based diagnostics (as discussed by Adrian and Westerweel (2011) and Westerweel et al. (2013)) have enabled measurements in a wide range of volume phase fractions and in more complex flow environments, where a laser plane defines the measuring field. Augier et al. (2003) implemented PLIF and PIV/PTV measurements in a vertical pipe. Wegmann and Rohr (2006) paved the way in horizontal flows and many have followed since (Liu

et al. 2006; Conan et al. 2007; Pouplin et al. 2011; Morgan et al. 2012; Chinaud et al. 2017). Nevertheless, certain challenges still remain in large-scale facilities and at high dispersed phase fractions (Wright et al. 2017). This Section will describe the measuring principles of these optical techniques and discuss their capabilities and limitations in their application to the experimental systems of the present work.

For the implementation of any optical technique in pipes of circular cross-section, a visualisation rectangular box is needed to avoid any diffraction of the light to the curved geometry. The material of the box and its contents need to ideally match that of the pipe. According to Snell-Descartes' law of diffraction between two media with different refractive indices it can be written that

$$\frac{\theta_1}{\theta_2} = \frac{u_{light,1}}{u_{light,2}} = \frac{\lambda_1}{\lambda_2} = \frac{n_1}{n_2}, \tag{3.8}$$

where θ is the angle of incident light measured from the normal of the boundary between the two media, n the refractive index of the medium, while u_{light} and λ are respectively the velocity and the wavelength of the light in the respective medium. The visualisation boxes in this work are made from Perspex acrylic with a refractive index $n = 1.495$ – same as the pipe material. The box is then filled with pure glycerol with $n = 1.473$ to match as closely as possible the refractive index of the acrylic and minimise light diffraction. This difference in the refractive indices does not illustrate any complications in the light reaching the pipe cross-section. The ratio of the incident light angles computed from eq. 3.8 is very close to unity ~ 1.05.

3.2.2.1 Volume illumination imaging

For dense dispersed flows, high-speed imaging with volume illumination can provide useful qualitative information. In this work, high-speed images are acquired in the pilot-scale flow loop of Sec. 3.1.1. A camera and a backlight system are placed on the desired transparent pipe section where the measurements are taking place, i.e. $x^+ = 25$, 70 and 135. These locations are very close to the DCP and ERT spools. For these measurements, two LED backlights are used in an angle to avoid shadows and improve image quality with more homogeneously distributed light. Light diffusing white paper, placed behind the visualisation boxes, is also used for that reason. The DOF of these measurements is decided by the optical system of the camera, namely the sensor and the lens attached. A Photron FastCam SA1.1 equipped with a 100 mm Tokina macro lens is used. The shutter speed is kept high enough to capture the interfaces of the drops as sharp as possible and both the shutter speed and the aperture are adjusted, so that the sensor receives enough light and the DOF is as small as possible. The acquisition frequency varies between 1 to 5.4 kHz, depending on the flow condition under investigation. The resolution is kept at 1024×1024 pixels[2].

1. The laser-based PLIF, drop size and PIV/PTV methods have also been described in detail in Voulgaropoulos and Angeli (2017).

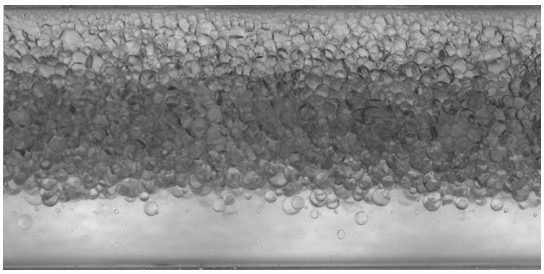

(a) Raw grayscale image

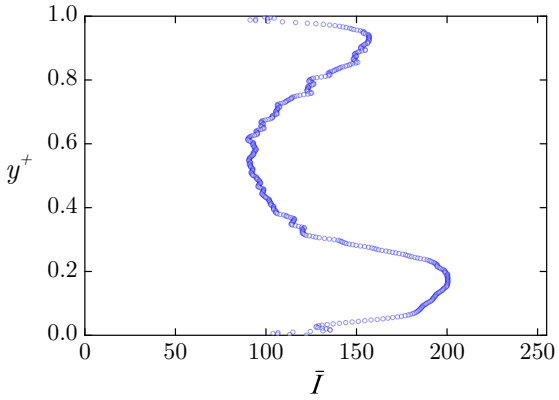

(b) Pixel intensities

Figure 3.12: Typical image and the respective axially averaged pixel intensity $\bar{I}$ profile acquired at the pilot-scale flow loop with the multi-nozzle inlet for $u_m = 0.5\,\mathrm{m\,s^{-1}}$ and $\varphi_o = 0.60$ at $x^+ = 25$.

A typical image is presented in Fig. 3.12(a) acquired at the pilot-scale flow loop at $x^+ = 25$ downstream the multi-nozzle inlet. The velocity is kept low $u_m = 0.60$ $\mathrm{m\,s^{-1}}$, and the phase fraction high $\varphi_o = 0.60$. This creates a very dense-packed layer in the middle of the pipe. The axially averaged grayscale pixel intensities, $\bar{I} \in [0,\ 255]$, are shown in Fig. 3.12(b). Despite the efforts for homogeneous lighting of the background, it can be seen that the pure water layer at the bottom of the pipe does not have the same $\bar{I}$. The curvature of the pipe can be the underlying cause for this effect.

Information on the flow patterns can be obtained from the acquired grayscale images, but at this drop concentration and with this imaging system it is very difficult to produce any quantitative information on the in-situ oil volume fraction profile. Drop size measurements from the captured images would also be very difficult to be conducted accurately, even with a relatively small DOF. There is a drop size stratification across the depth of the pipe cross-section, and thus the measurements would be biased towards the outer pipe wall as discussed in the previous Section. When the refractive indices of the pair of liquids are close, then a dye is commonly added in one of the two phases (Pérez 2005; Zhai et al. 2017; Shi and Yeung 2017). The dye can aid the distinction of the different flow structures.

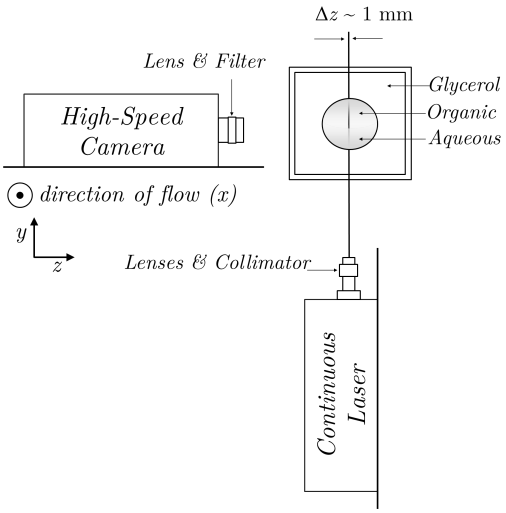

Figure 3.13: Schematic illustration of the optical laser-based measurements conducted at the matched refractive index flow loop downstream the static mixer at $x^+ = 15$ and 135.

3.2.2.2 Planar laser induced fluorescence

Contrarily to high-speed imaging with volume illumination, planar laser induced fluorescence measurements take place on a thin illuminating plane/sheet, emitted from a laser. In this work, PLIF measurements are conducted in the matched refractive index flow loop of Sec. 3.1.2 at $x^+ = 15$ and 135 downstream the inlet mixer. Eq. 3.8 shows that even small variations of the refractive indices of the two-phase mixture, can cause strong optical diffraction of the laser light, which would result in optical distortion and hence inaccurate measurements. Especially at high drop concentration, where the number of interfaces is very high, it is found experimentally that any difference in the refractive indices of the two liquids needs to be kept lower than $\Delta n < 0.001$. At higher values, shadows can appear and image clarity significantly drops.

The experimental setup for these measurements is shown in Fig. 3.13. A diode-pumped solid-state green continuous laser system (Laserglow Technologies) is placed vertically below the pipe. The emitting wavelength of the laser is $\lambda = 532$ nm and its output is set at 3000 mW. The laser beam generated in the middle of the pipe is transformed to a sheet in the axial direction of the flow with the aid of a concave lens. In these measurements, the measuring field is defined by the illuminating system and not the imaging system. It is thus important to decrease the laser plane thickness as much as possible, in order to conduct measurements at a quasi-two-dimensional area and avoid any effects from the stratification of the volume fraction and out of plane velocity. The laser thickness is reduced at the focusing plane with the use of a collimator to about 1 mm, which is below $\Delta z^+ < 0.04$ of the pipe diameter. The laser sheet alignment is conducted with the help of a graticule target with printed dots of known distances placed inside an oil filled pipe section.

A Phantom v1212 (Vision Research) high-speed camera is placed on the side of the pipe perpendicular to the visualisation box to record the flow. Frequencies up

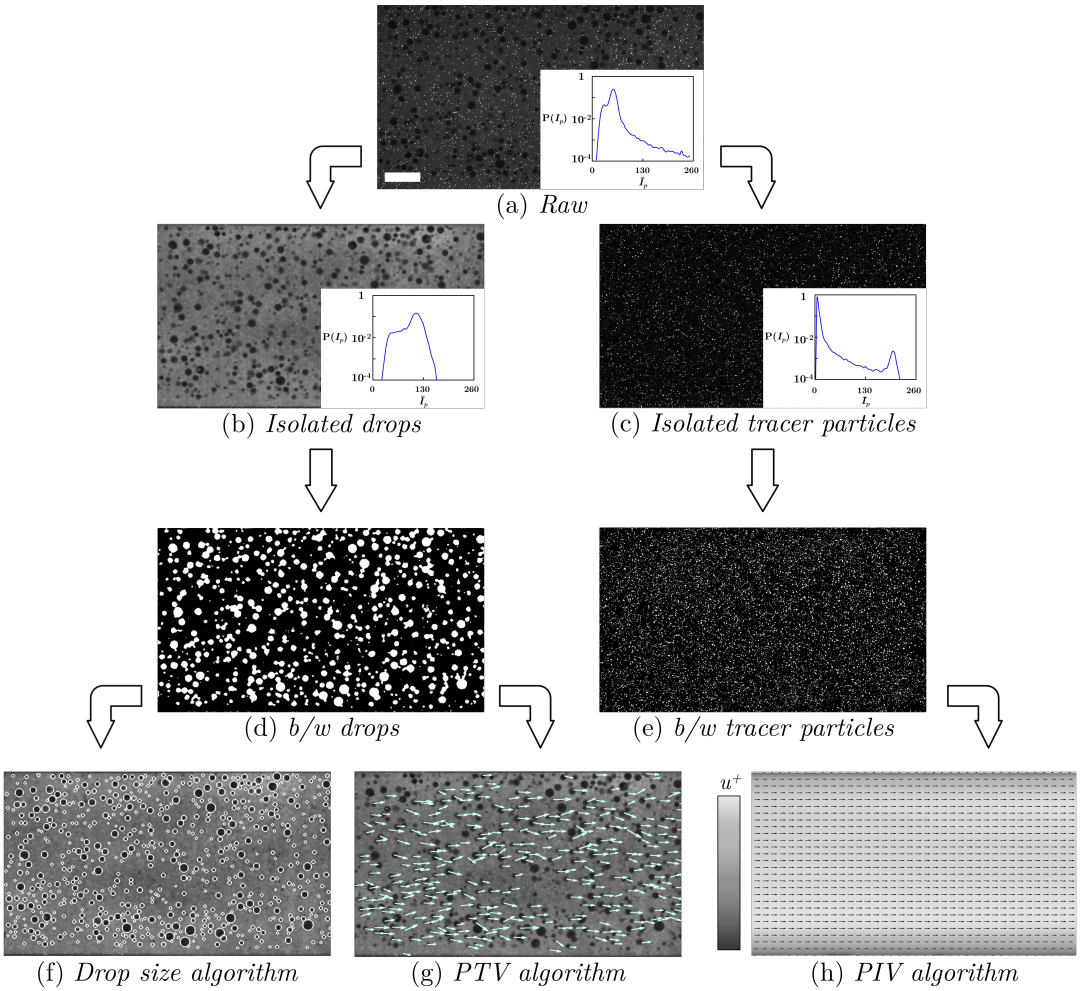

Figure 3.14: The image processing followed from a raw PLIF image to acquire information on the in-situ phase fractions, the drop size, together with the velocities of the dispersed and the continuous phase. The scale bar in (a) has a length of 5mm.

to 4 kHz are used at a 1280 by 800 pixels^2 resolution and 1280 by 440 pixels^2 after cropping for the area of interest, resulting in a final spatial resolution of 16.9 px/mm. The shutter speed is set at 95 µs, to allow enough light to reach the sensor, but at the same time avoid blurring due to the displacement of the particles while the shutter is kept open. A Tokina 100 mm macro lens is used here as well, but in conjunction with a high pass (> 580 nm) filter attached to it to eliminate any spurious light or reflections of the laser on the pipe frame. As shown in Fig. 3.13, the visualisation box is filled with pure glycerol for the reasons explained in Sec. 3.2.2.1. However, in laser plane measurements the refractive index of the solids is not very important as the incident angle of the laser plane is kept at 90° to the normal of the visualisation box. From eq. 3.8 no diffraction will take place for any ratio of refractive indices. In practice though, small deviations in the angle are possible, thus it is good practice to closely match the refractive indices of all media when possible.

A typical raw grayscale image acquired at $x^+ = 15$ downstream the static mixer for $u_m = 0.48\ \text{m}\,\text{s}^{-1}$ and $\varphi_o = 0.14$ is shown in Fig. 3.14(a). The dark regions denote

the oil drops, while the bright regions denote the continuous aqueous phase containing the fluorescent Rhodamine 6G dye. The bright spots are the tracer particles for the PIV measurements that will be discussed in a further Section. In the inset of Fig. 3.14(a) the respective number probability histograms $\mathrm{P}(I)$ are shown for the image. Each pixel has an intensity of $I \in [0,\, 255]$. Three peaks can be distinguished in the plot. The lower one represents the pixels of inside the oil drop, that have the lowest intensity $I \sim 30$ as the oil only absorbs the light from the laser. The second and highest probability peak stands for the pixels covering the background continuous phase. Their intensity is higher at $I \sim 55$ as a small concentration (~ 0.02ppm) of Rhodamine 6G dye is present. One last peak at $I \sim 230$ can be seen with a very small probability. It stands for the signal of the tracer particles.

The goal is to obtain information on the phase fraction profiles, the drop size distribution and as will be described in Sec. 3.2.2.3 obtain the velocity of the dispersed and the continuous phase. For all these methods, image analysis needs to be conducted. In this work, the image treatment methods are applied through MATLAB functions and algorithms. The image processing steps on the images of Fig. 3.14(left side) is described below.

In-situ phase fractions To accurately acquire the in-situ oil volume fraction profiles ε_o, the signal from the tracer particles needs to be removed from the images and the light needs to be homogenised to better distinguish between the aqueous and the organic phase. As a first step, a median filter is applied to the image in local spatial neighbourhoods of 5×5 pixels (Huang et al. 1979). The filter replaces each pixel in a neighbourhood matrix of elements $p_{i,j}$ with its median value (i.e. the most central value), where $i, j \in [1, \ldots, 5]$ are indices describing the elements of the neighbourhood matrix in the x and y direction respectively.

As a second step, contrast-limited adaptive histogram equalisation (CLAHE) is applied to the image. As is also clear from the probability histograms of the inset of Fig. 3.14(a), the images obtained are not well contrasted with a large number of pixels occupying only a small portion of the available range of intensities, with a $\mathrm{P}(I) > 0.95$ of pixels having an intensity in the range of $I \in [20, \ldots, 70]$. The principle in CLAHE is to stretch the dynamic range of the pixel values in such a way that the lighter pixels may turn still lighter, while the comparatively darker pixels may be still darkened (Acharya and Ray 2005). This enhances the clarity of the image by better differentiating between the organic and aqueous phases. More details on the mathematical formulation of this transformation are given by Zuiderveld (1994). The resulting image is shown in Fig. 3.14(b), where now the same number of pixels have spread in a range of intensities of almost double the size compared to before with $I \in [40, \ldots, 130]$.

In this work, the goal is not to record the concentration of dye in each pixel as only two values are of interest. Whether the pixel is part of the organic or the aqueous phase. Thus, to obtain better results, the image of Fig. 3.14(b) is binarised as

shown in Fig. 3.14(d). In liquid-liquid flows Morgan et al. (2012) used a global threshold for the binarisation, based on the mean intensity of each image. Augier et al. (2003) divided their images in 100×100 pixels^2 windows inside which the gray level histograms were measured. They detected the most frequent gray level corresponding to the fluorescent dye and that allowed them to set the local gray level limit under which the occurrence of the dispersed phase is detected. A similar method is applied in this work in the binarisation, by using locally adaptive thresholding, where a threshold value is computed for each pixel using the local mean intensity around neighbourhoods of $1/8^{\text{th}}$ of the size of the image. The sensitivity parameter is needed and set a-priori based on the flow condition. A post-treatment method of the binarised image is then used to remove any artifacts (Yanowitz and Bruckstein 1988). Several binarisation and post-treatment methods have been evaluated by Trier and Taxt (1995).

The column that correponds to the axial location of interest is then selected from the binarised image/matrix. As time-averaged results are needed, over 4000 frames are averaged to acquire the final in-situ oil volume fraction $\langle \varepsilon_o \rangle$ profiles. The number of frames (N_{frames}) to average is selected based on the estimated time-scales of the slowest phenomena taking place in the pipe. It is found that after ~ 2000 frames no significant change is recorded in the mean μ_{ε_o} and standard deviation s_{ε_o} of the in-situ oil fraction for five representative vertical positions along the pipe diameter, separated by $\Delta y^+ = 0.25$. The results are shown in Fig. 3.15 and confirm the argument that over $N_{frames} > 2000$ no considerable effect is observed in the statistics. The mean of the in-situ oil volume fraction is computed as

$$\mu_{\varepsilon_o} = \frac{1}{N_{frames}} \sum_{i=1}^{N_{frames}} \varepsilon_{o,i} \tag{3.9}$$

and the standard deviation as

$$s_{\varepsilon_o} = \sqrt{\frac{1}{N_{frames} - 1} \sum_{i=1}^{N_{frames}} (\varepsilon_{o,i} - \mu_{\varepsilon_o})^2}. \tag{3.10}$$

The final measured time-averaged in-situ volume oil fraction profile is shown in Fig. 3.16. Some local fluctuations $\mathcal{O}\{10^{-2}\}$ are observed in the profile and can possibly be attributed to the time-averaging. To avoid this noise in the profile, a smoothing Savitzky-Golay filter is applied. Successive sub-sets of adjacent data points are fitted with a low-degree polynomial by the linear least squares method. The number of neighbouring data points is selected based on the flow configuration. Care needs to be given in the regions with high in-situ phase fraction gradients, e.g. close to the pipe walls for homogeneous dispersions.

Drop size Several efforts have been conducted in the literature to develop an algorithm to accurately detect the drop trajectories and measure their size. Blaisot

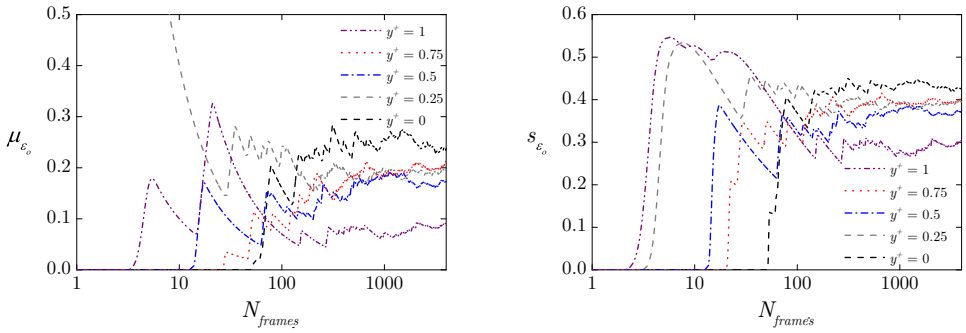

(a) Change of mean over the number of averaged frames.

(b) Change of standard deviation over the number of averaged frames.

Figure 3.15: The change of the low order statistics during time-averaging of the in-situ oil volume fraction profiles for a homogeneous *o/w* dispersion in the matched-refractive index flow loop.

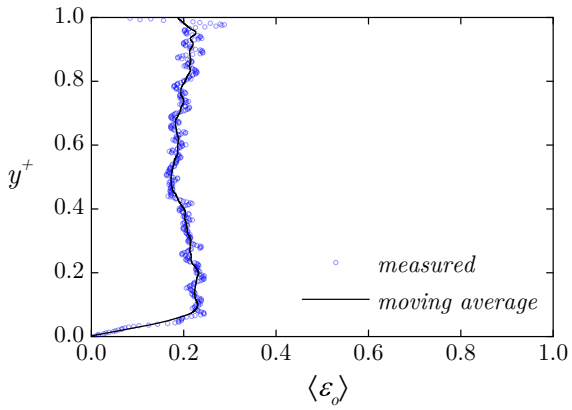

Figure 3.16: Time-averaged in-situ volume oil fraction obtained with PLIF for a homogeneous *o/w* dispersion in the matched-refractive index flow loop for $\varphi_o = 0.21$.

and Yon (2005) developed a method able to measure drop sizes of fuel sprays from high-speed images. Due to a wide imaging DOF, many drops appeared blurred (unfocused) on their images and therefore a correction to the apparent size of the unfocused drops was employed. As non-spherical drops were present, a computational method was applied by taking the second derivative of the filtered gray level function (local curvatures) to detect the boundaries of the contours of the drops. Castanet et al. (2013) developed an approach based on a Laplacian of the Gaussian method, which detects the outline of the drops, measures their size and tracks their trajectories in time and space. The method was applied in the secondary drops generated from drops impacting onto a heated surface. Similar experiments were conducted by Guildenbecher et al. (2014) by measuring the same parameters for the secondary drops produced from a drop impacting on a thin film and were captured in the three-dimensional space with digital in-line holography. For vertical gas-liquid flows, Lau et al. (2013) developed an image processing algorithm (based on watershedding the image) to measure the drop sizes of clustered bubbles using the criteria of a shape

factor. The algorithm was validated in a Hele-Shaw column. The method was later used by Zhai et al. (2017) in a liquid-liquid vertical sampling tube.

However, in all these works the dispersed volume fraction was either kept very low ($\varphi_d = \mathcal{O}\left\{10^{-2}\right\}$) or the experiments were conducted in quasi-two-dimensional channels with φ_d still only reaching 0.12. The main limitation is that all these works used imaging with volumetric illumination. In this work, drop sizes in very high dense dispersions are possible, as the measuring plane is defined by the thin laser plane, and thus any overlapping of drops even when local values of ε_d reach the values of the maximum possible packing (ε_{max}) are avoided. It needs to be underlined that due to the quasi-two-dimensional measurements, the drop chord lengths are measured instead of the drop sizes, similarly to the DCP of Sec. 3.2.1.1.

The image of Fig. 3.14(d) can be further used to measure the sizes of the drops (Voulgaropoulos and Angeli 2017). An algorithm is developed based on the *imfindcircles* function of MATLAB to capture the circular contours of the drops. The drops can deform under certain conditions and lose their spherical shape. In this work, it can be assumed that most drops have circular shape. Clift et al. (2005) predicted the shape of drops in free motion, based on the drop Reynolds number Re_d and Bond number Bo. The drop Reynolds number is defined based on the drop diameter and the convective flow of the pipe as $Re_d = \rho_c d u_m/\eta_c$ and $Bo = g\Delta\rho d^2/\sigma$. For the majority of cases $Re_d = \mathcal{O}\left\{10^2\right\}$ and $Bo = \mathcal{O}\left\{10^{-1}\right\}$ hold true, and thus spherical drops are expected. However, as discussed in Sec. 2.3.1.1, the drops at very high local dispersed phase fractions $\varepsilon_d \to \varepsilon_{max}$ are expected to slightly deform.

A Circular Hough Transform (CHT) algorithm, based on the pixel intensity gradients, is used for finding circular contours in an image. The parametric circular equations are written as

$$x = \mathcal{C}_{x,i} + a\cos\vartheta \quad \text{and} \quad y = \mathcal{C}_{y,i} + a\sin\vartheta, \tag{3.11}$$

where $\mathcal{C}_x$ and $\mathcal{C}_y$ are the x and y spatial coordinates of the centre of the circle i with radius a, while ϑ is the angle sweeping $\vartheta \in [0, \ldots, 360]$ to trace the perimeter of the circle. A search function then locates which pixels fall on the perimeter of circles, working in a three parameter space $(\mathcal{C}_x, \mathcal{C}_y, a)$. A result of the algorithm is shown in Fig. 3.14(f).

For some conditions with regions of high local dispersed phase fractions, a binarisation on two sensitivity levels is needed to better capture the boundaries of certain drops that appear less clear, i.e. their intensity is closer to the intensity of the surrounding continuous phase. This procedure is shown in Fig. 3.17 with a characteristic image where this phenomenon happens. Figures 3.17(a) and (b) illustrate the drop detection at the two sensitivity levels selected. From Fig. 3.17(c) it can be seen that some drops are detected from both sensitivity levels. A simple overlapping filter is applied to discard any doubles from the low sensitivity level when $\delta < \beta$, with

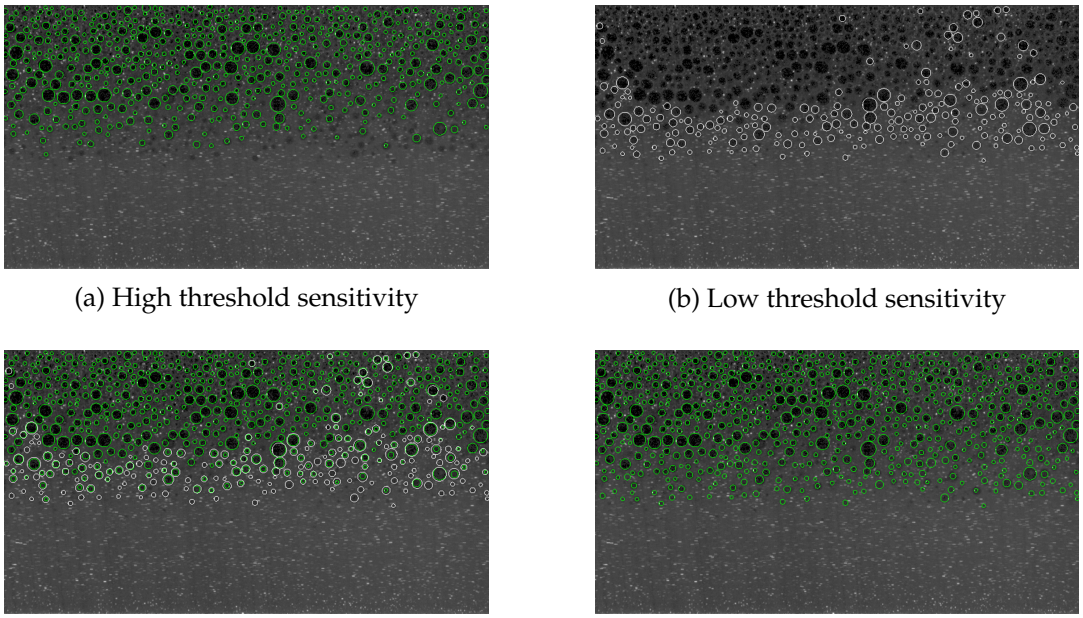

(a) High threshold sensitivity

(b) Low threshold sensitivity

(c) Combined

(d) Overlapping filter of eq. 3.12

Figure 3.17: Drop size measurement algorithm for an o/w dispersion in the matched-refractive index flow loop.

$$\delta = \sqrt{(\mathcal{C}_{x,i} - \mathcal{C}_{x,i+1})^2 + (\mathcal{C}_{y,i} - \mathcal{C}_{y,i+1})^2} \quad \text{and} \quad \beta = a_i + a_{i+1} - \hat{\beta}, \tag{3.12}$$

where δ is the distance between two centres of circles and $\hat{\beta}$ is a parameter set equal to 1 pixel.

As was done with the in-situ dispersed phase volume fractions, the same statistical analysis is needed for the drop size measurements in order to get statistically meaningful results. According to Angeli and Hewitt (2000b) at least 350 drops are needed in the distribution in order to include drops with higher sizes that have a lower probability to appear. In Fig. 3.18(a) the drop size distributions are shown for the o/w flow condition of Fig. 3.17. For this distribution a bin size of 0.25 mm is used. The colourbar denotes the number of drops used to generate the respective distribution. The present results are in accordance with the aforementioned observation, where the drop size distribution does not change when the number of drops used is $N_d > 600$.

To make more quantitative comparisons, the change in the Sauter mean diameter[2] d_{32} with the number of averaged drops is shown in Fig. 3.18(b), which is computed from eq. 2.30. A change of less than 1% is recorded for $N_d > 600$. In the inset of Fig. 3.18(b) the low order statistics (mean and standard deviation) are presented as well. The mean diameter of the drop population μ_d stabilises relatively sooner than the d_{32} with 1% recorded for $N_d > 100$ during the time-averaging. This difference compared to the d_{32} is because the d_{32} is more biased towards higher sizes and

2. As mentioned previously, both the DCP and PLIF are only able to measure drop chord lengths, which do not necessarily correspond to drop diameters.

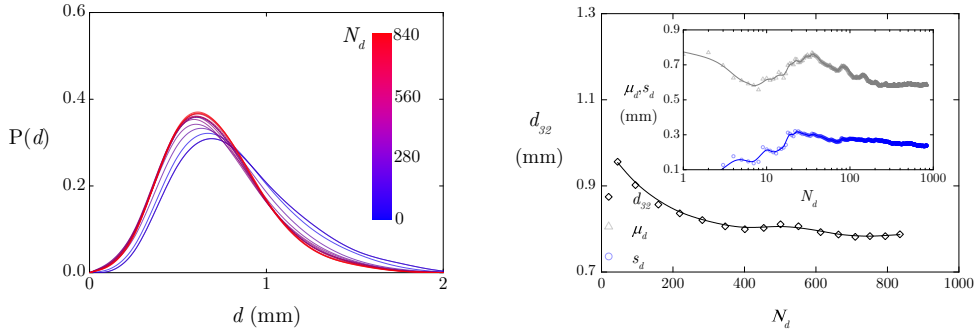

(a) Change of distribution over the number of averaged drops.

(b) Change of low order statistics over the number of averaged drops.

Figure 3.18: The change of the low order statistics during time-averaging of the in-situ oil volume fraction profiles for a homogeneous *o/w* dispersion in the matched refractive index flow loop.

thus certain large drops that may appear for larger sample numbers still affect it, while the μ_d is practically affected equally for all drop sizes. The standard deviation of the drop sizes s_d follows the same trend as the mean and is practically unaltered for $N_d > 100$. From Fig. 3.18, it can be concluded that relatively accurate results can be obtained for the low order statistics for low number of samples, but to obtain more detail in the population of drops through the d_{32} or the distributions, a higher number of samples is needed.

Finally, it is important to note that the MATLAB algorithm is tested against manual measurements in the same images for a few flow conditions. For the manual measurements, the two axes of the drops are measured (assuming ellipsoidal shapes) and the equivalent diameters are computed as $d_{equiv} \approx 1.55 A_d^{0.625}/S^{0.25}$, where the drop area is $A_d = \pi d_x d_y/4$ and the perimeter $S_d \approx 2\pi \left(1/2 \left((d_x/2)^2 + (d_y/2)^2\right)\right)^{1/2}$, with d_x and d_y being the two axes of the drops. The deviations between the MATLAB and manual measurements gave relative deviations below 10% for various flow conditions. The absolute uncertainty for the MATLAB method is ± 2 pixels or ± 0.12 mm, while for the manual method ± 2 pixels for each axis measured, which translates to an absolute uncertainty of ± 0.16 mm in the equivalent diameter of a drop.

3.2.2.3 Particle image/tracking velocimetry

Information on the velocity field of the aqueous phase, which contains the tracer particles can be obtained with particle image velocimetry. PIV is an extension of flow visualisation of the PLIF method described before, where the mean displacement of tracer particles between two images is measured to give quantitative information on the velocity fields. When a sufficient number of tracers are present in the image, statistical methods are employed to track the displacement of small groups of particles. As Adrian and Westerweel (2011) describe, the most common approach is to perform space-time cross-correlation of the particles lying in small square regions

(interrogation windows) with dimensions $\mathcal{W}$ in the pair of images. The most likely displacement vector $\Delta\boldsymbol{X}$ is evaluated in each of these interrogation windows, by a two-dimensional cross-correlation calculation (similar to eq. 3.6) between the first image $I_1(\boldsymbol{X}) = I(\boldsymbol{X}, t)$ and the second one $I_2(\boldsymbol{X}) = I(\boldsymbol{X}, t + \Delta t)$ as

$$\mathcal{R}_{I_1,I_2}(\Delta\boldsymbol{X}) = \int_{\mathcal{W}} I_1(\boldsymbol{X}) I_2(\boldsymbol{X} + \Delta\boldsymbol{X}) \mathrm{d}\boldsymbol{X} \tag{3.13}$$

The most probable particle displacement in the two-dimensional plane of measurement $\boldsymbol{X} = (x, y)$ is given by the maximum (peak) of $\mathcal{R}$ in the $\boldsymbol{X}$-plane. It follows that the velocity components in the plane can be computed by dividing the displacement by the time difference between the two images as $\boldsymbol{U} = \Delta\boldsymbol{X}/\Delta t$ or $(u, v) = (\Delta x/\Delta t, \Delta y/\Delta t)$ for the two-dimensional measurements.

The tracer particles need to exactly follow the streamlines, not alter the flow or fluid properties and not interact with each other, which realistically might not always be the case (Westerweel 1997). For the first requirement, the Stokes number of the particles St_p is computed as the ratio of the relaxation time of the particles and the Kolmogorov time scale, as

$$St_\mathrm{p} = \frac{\tau_\mathrm{p}}{\tau_k} \quad \begin{cases} \tau_\mathrm{p} = \dfrac{\rho_\mathrm{p} d_\mathrm{p}^2}{18\eta_c} \\ \\ \tau_k = \left(\dfrac{\eta_c}{e}\right)^{1/2} \end{cases}, \tag{3.14}$$

where ρ_p and d_p are the density and size of the tracer particles correspondingly. Contrary to eq. 2.19, in which the computation of the Stokes number for the drops is based on the main convective time scale of the flow D/u_m, the Kolmogorov time scale needs to be used for the tracer particles in eq. 3.14 instead, as it characterises the smallest time scale in the flow. As stated in Sec. 3.1.2 for the matched refractive index flow loop, rhodamine B-coated PMMA particles are used in the aqueous phase with a size of 1 to 20 µm and a density very close to that of the aqueous phase, giving $St_\mathrm{p} = \mathcal{O}\{10^{-2}\}$ for the flow conditions investigated. For $St_\mathrm{p} \ll 0.1$ any tracing accuracy errors are less than 1% (Tropea and Yarin 2007). Furthermore, no considerable change in the fluid properties is recorded with the addition of the tracers, as the concentration is kept low. For the same reason, interaction between the tracers is not expected.

As shown from the cross-correlation eq. 3.13, the signal of the tracer particles needs to be distinct. Nevertheless, the background is split in two intensity levels during dispersed flows (drops and continuous phase) as shown in the histogram of Fig. 3.14(a). This difference in the illumination levels of the background can add noise in the intensity peaks of the cross-correlation causing noise-to-peak ratios to increase (the coordinates of the peaks will remain the same). To avoid this effect, the tracer signal is isolated. A typical image treatment procedure is illustrated in the right-hand side of Fig. 3.14. The image of Fig. 3.14(b) is subtracted from Fig. 3.14(a)

as a first step. This transformation acts as a high-pass filter giving Fig. 3.14(c). As shown in the respective histogram plot in the inset, two peaks are present. The peak at very low intensity values now reflects both the drop and background, while the peak of the tracer particles remains at approximately the same intensity levels. In Fig. 3.14(c) some tracer particles appear brighter than the rest. The light scattering intensity of the particles depends significantly on their size and form. One order of magnitude increase of the particle radius can result in 10^6 higher intensity of scattering (Im et al. 2007). To homogenise the signal of the tracer particles and further avoid any background heterogeneity in the illumination, the images are then binarised in a similar way as before at one sensitivity level to give images as Fig. 3.14(e), which are used for the cross-correlation ultimately giving the velocity field of Fig. 3.14(h).

As two-dimensional measurements are conducted, it is important to consider any effects due to local velocity gradients at the scale of the interrogation window, as the transverse (z direction) out of plane motion of the particles due to shear can generate erroneous results during the cross-correlation stage (Westerweel 2008). The stratification of the velocity in the depth of the laser plane ($\Delta z \approx 1$ mm) is estimated below 5% of the maximum velocity, when the assumption of a parabolic profile on the transverse direction is made. The errors coming from this transverse motion are very low.

A discrete Fourier transformation (DFT) algorithm is used in this work, by calculating the correlation matrix in the frequency domain using fast Fourier transformation (FFT). For this method, Westerweel et al. (1997) advise to run several passes of the DFT on the same dataset, in order to keep the background noise in the correlation matrix low and provide high spatial resolution in the final vector map, together with a high dynamic velocity range and an optimal signal to noise ratio. Especially in the presence of drops, the number of tracer particles in each interrogation window inevitably decreases as the concentration of the drops increases. The rule of thumb is that the number of particles N_p in each interrogation window needs to range from $5 - 8$ to use PIV. For this reason, a three-pass DFT is used with an initial interrogation window starting from 64×64 pixels^2. The area of this interrogation window is larger than the typical drop areas observed in the experiments and thus enough particles are allowed in each window. For most flow conditions, the drops have diameters smaller than $0.1D$, while the interrogation window during the first iteration is approximately equal to $\sim 0.15D$.

Figure 3.19(a) illustrates the DFT interrogation windows used in two superimposed images with the tracers isolated. The same case as Fig. 3.14 is shown – recorded in the matched refractive index flow loop. Starting from the whole field of view, the interrogation windows decrease from 64×64 to 32×32 and 16×16 pixels^2 respectively. A 50% vector interpolation overlap is used at each DFT step to give a final vector grid of 8 pixels^2. The white pixels show the tracers in the first image $I_1(\boldsymbol{X}, t)$, while the tracers in the second image $I_2(\boldsymbol{X}, t + \Delta t)$ of the cross-correlation pair are shown with green. A clear displacement towards the right (x)

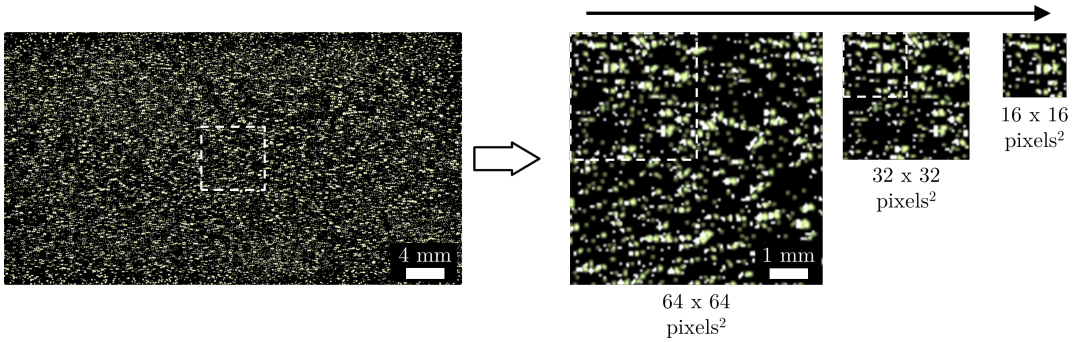

(a) Interrogation windows procedure of the iterative DFT. The white pixels denote the tracer particles in frame t and the green pixels the tracer particles in the $t + \Delta t$ frame.

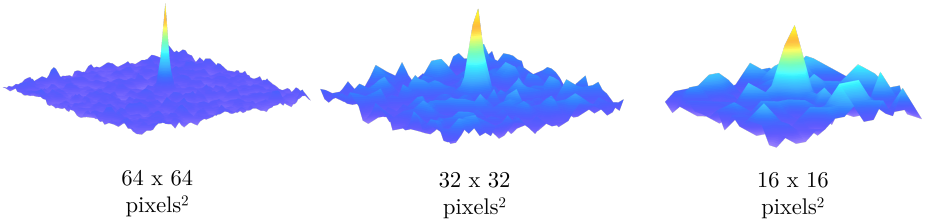

(b) Correlation functions (eq. 3.13) computed during the DFT iterations.

Figure 3.19: Iterative DFT correlation procedure for the PIV measurements for a typical image.

direction is shown, where the main convection takes place. Even in the smallest interrogation window $N_\mathrm{p} \gg 1$ holds, while the displacement is kept at about a quarter of the window.

In Fig. 3.19(b) the correlation functions for the three iterations are illustrated. The correlation peak in the first pass is characterised by very high signal to noise ratios and the peak is located towards the direction of the flow. The correlation peak of the second pass is almost in the centre of the correlation function, because of pre-shifting the correlation windows according to the first pass. The second correlation peak is lower than the one of the first pass, as a smaller window is chosen. The same trend holds for the third and final pass. It should be mentioned that the signal to noise ratios decrease with each step in the expense of higher number of PIV vectors in the flow field. The primary to secondary peak ratio was kept over 1.5 for all computations. The peaks of the cross-correlation $\mathcal{R}$ are fitted with a Gaussian function to the correlation matrix intensity (shown in Fig. 3.19(b)). As Nobach and Honkanen (2005) state, in the absence of excessive motion blur, it is sufficient to use only the directly adjacent vertical and horizontal pixels, resulting in a two times a 3-point fit, and evaluate the x and y axes separately. This method allows the acquisition of subpixel precision in the velocities computed.

In regions of higher concentrations of the dispersed phase, it is possible that not

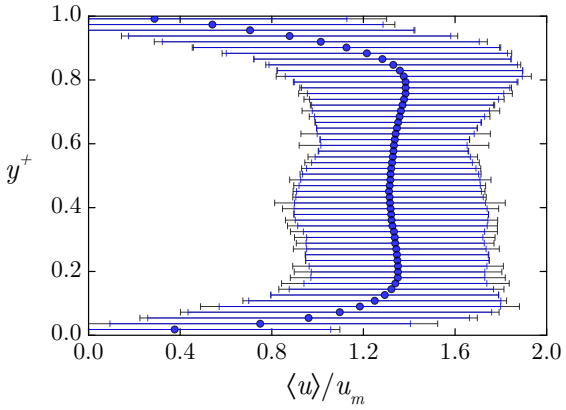

Figure 3.20: Time-averaged velocity profile obtained with PIV for a homogeneous *o/w* dispersion in the matched-refractive index flow loop. The bars denote the standard deviations before (black) and after (blue) the post-processing of the vectors.

enough tracers are present in an interrogation window. To reduce such errors, post-treatment was employed to filter out these velocities from the instantaneous velocity fields. Several local and global vector validation methods have been used in PIV measurements (Westerweel and Scarano 2005). In this work, an initial filter is applied by plotting the axial, u, versus the vertical, v, velocity component from all interrogation windows of all captured frames for one condition and by manually selecting appropriate limits. This filter is a simple way to roughly neglect false vectors outside of the range of validity. In the second stage, each velocity component of each interrogation window is compared with a lower and upper threshold t_l and t_h respectively, giving

$$t_l = \bar{U} - \hat{t} \cdot s_{\bar{U}} \quad \text{and} \quad t_h = \bar{U} + \hat{t} \cdot s_{\bar{U}}, \tag{3.15}$$

where $\hat{t}$ is a parameter that determines the strictness of the filter and $s_{\bar{U}}$ is the standard deviation of the magnitude of the spatially averaged velocity vector $\bar{\boldsymbol{U}}$ (Thielicke and Stamhuis 2014).

The outlier velocities are removed and the missing vectors are then replaced with the local mean values computed in the neighbourhood of 3×3 interrogation windows. In most cases, the mean velocities computed before and after the post-treatment deviate less than 1%, except for the first correlation box adjacent to the pipe walls, where the difference is about 30%. Similarly to the previous Section, 4000 frames or more are averaged to acquire the time-averaged velocity profiles of both $\langle u \rangle$ and $\langle v \rangle$. The standard deviations before (black) and after (blue) the vector post-treatment are shown for the same flow condition at two axial measuring locations, $x^+ = 15$ and 135 in Fig. 3.20 for the normalised streamwise velocity. As high concentrations of drops will lead inevitably to higher uncertainties, care needs to be taken when interpreting the velocities in such regions. Discussion on the interpretation of these results will follow in Chapter 5.

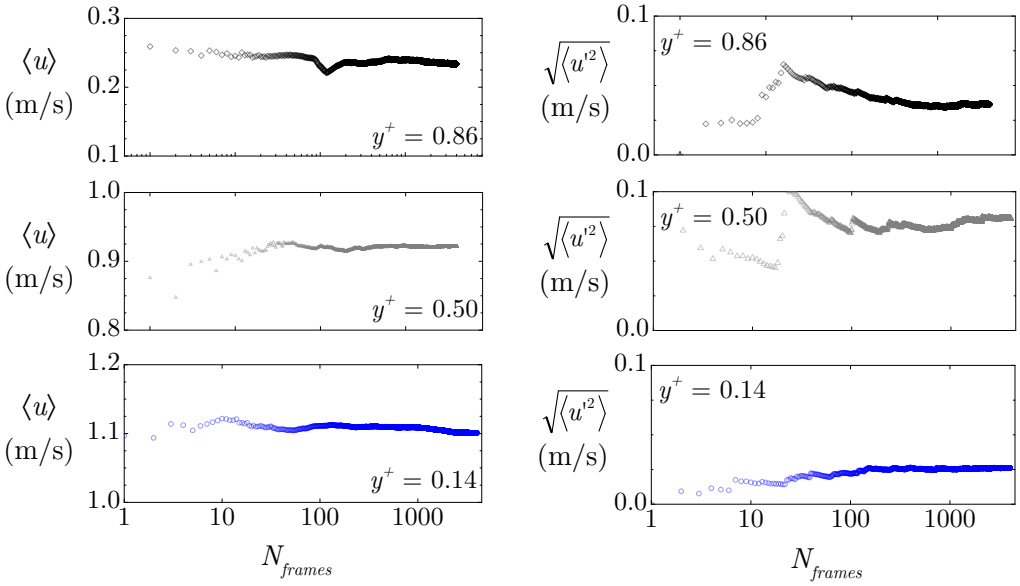

(a) Change of axial velocity over the number of averaged profiles.

(b) Change of axial fluctuating velocity over the number of averaged profiles.

Figure 3.21: The change of the mean value during time-averaging of the axial velocity and axial fluctuating velocity component for a segregated *o/w* dispersion in the matched refractive index flow loop for three vertical locations.

A comparison of the time-averaging process between the axial velocity and the axial fluctuating velocity at three vertical pipe locations in a segregated *o/w* dispersion with a pure aqueous layer at the bottom computed from PIV follows. The three locations $y^+ = 0.86, 0.50$ and 0.14 correspond to measurements at the dense-packed, floatation and pure aqueous layer and are shown in Fig. 3.21. The axial velocities at all three locations, shown in Fig. 3.21(a), converge adequately for $N_{frames} > 1000$ with relative differences of the order of $\mathcal{O}\{10^{-2}\}$, while they decrease to $\mathcal{O}\{10^{-5}\}$ for $N_{frames} > 3000$.

As the fluctuating velocities are of lower magnitude, stronger absolute deviations from the final mean are expected during the time-averaging as shown in Fig. 3.21(b). Nevertheless, the relative differences are similar to the axial velocities and convergence is reached. As expected, the intensity of the root-mean-square (RMS) of the fluctuating axial velocity component $\sqrt{\langle u'^2 \rangle}$ is higher in the dilute layer, where coherent quasi-turbulent structures are generated in the wakes of the drops as discussed in Sec. 2.1.2.3.

When the density of the tracers in the field of view is not sufficiently high, particle tracking velocimetry (PTV) can be used instead of PIV. PTV tracks the displacement of individual objects in time. In the experiments in the matched refractive index flow loop, the velocity of the individual drops can be computed. The drops are isolated in the image, as shown in 3.14(d), similarly to the drop size algorithm described before. The PTV algorithm used in this work for these computations was developed by Brevis et al. (2011). The algorithm is based on integrated cross-correlation (CC)/relaxation computations, which provide flexibility in the analysis

of images with different concentration of drops and at different flow conditions. The CC algorithm cross-correlates a reference matrix of the initial frame, based on a drop signal, with the interrogation matrices centred at each of the candidate drops of the subsequent frame. The cross-correlation with the highest coefficient represents the drop motion. The relaxation method (RM), originally implemented by Baek and Lee (1996) for turbulent flows, is a statistical approach to find the largest displacement probability of a drop within a pre-select area around it.

The drop size distributions at certain flow conditions illustrate high polydisperity and thus not all of them can be tracked on the same run. The detection algorithm used was developed by Takehara and Etoh (1998) and is structured on the Gaussian mask technique, where an input drop detection size is needed. Detailed information on the PTV algorithm is given by Brevis et al. (2011). The vector validation stage is comprised of similar methods as those of the PIV described in the previous paragraphs. A range of velocities is chosen in a u-v plot, and a local median filter is applied as in eq. 3.15. The individual velocities of the drops can be illustrated in a vector field as Fig. 3.14(g).

Finally, a similar approach to the PIV measurements described before, is followed for the velocity field measurements in the Hele-Shaw cell for the coalescence experiments. As discussed in Sec. 3.1.3, it can be assumed that $w = 0$ in the system. For this reason, simple volumetric illumination instead of a laser plane can be used for the PIV, with the DOF for the measurements defined by the camera and lens system as discussed also in Sec. 3.2.2.1, which was estimated at approximately 0.5 mm. This technique is called bright field particle image velocimetry (BF PIV). The errors are very low with $St_{\mathrm{p}} \ll 0.01$ for the highest time-scales in the coalescence by considering both the viscous and inertial time-scales of Sec. 2.3.1.2. The variation of the velocity in the depth of field is estimated at 25% of the maximum velocity, assuming a parabolic velocity profile along the z direction, so the relative correlation errors are estimated to be very low $\ll 1\%$.

3.3 Application

This Section serves as a summary to show which techniques, probes and liquids are used in each experimental setup, as described before in this Chapter. The experimental techniques implemented in the three systems are shown in Table 3.5, while the set of liquids together with any additives introduced to help with the techniques or manipulate the physical properties of the system are shown in Table 3.6.

Table 3.5: Summary of the techniques applied in each experimental system.

	pilot-scale flow loop	**matched refractive index flow loop**	**Hele-Shaw cell**
Conductivity:	DCP, ERT	-	-
High-speed imaging:	volumetric illumination	planar illumination, PLIF	volumetric illumination
High-speed PIV/PTV:	-	planar illumination	volumetric illumination, BF PIV

Table 3.6: Summary of the liquids along with any additives investigated in each experimental system.

	pilot-scale flow loop	**matched refractive index flow loop**	**Hele-Shaw cell**
Aqueous:	water	52% w/w glycerol/water	82% & 52% w/w glycerol/water
Organic:	Exxsol D140	silicone oil	Exxsol D80 & silicone oil
Dye:	-	fluorescent Rhodamine 6G	blue ink
Tracer Particles:	-	Rhodamine B-coated PMMA	silver-coated glass
Surfactant & Polymer:	-	-	Span 80 & Xanthan Gum

The DCP is used to measure the local volume fractions with overall relative uncertainties of about 20%, as estimated from the comparisons with the QCV and ERT measurements for a range of conditions and mixture velocities. The DCP also provides local measurements of the drop chord lengths, with an estimated relative uncertainty of less than 30%, despite the smaller deviations recorded when compared to direct drop size measurements from high-speed images. As discussed previously, the probe is unable to capture drops with a size smaller than $200\ \mu\mathrm{m}$, due to the geometrical properties of the coaxial wires. It is also possible that some small drops are filtered out from the high pass filter applied to remove the noise from the signal.

The PLIF measurements are able to provide time and space resolved measurements of the in-situ dispersed phase volume fraction very accurately for regions of pure liquids (below 1%), but the uncertainties in the regions of drops can even reach values of 30%. The main source of error, as discussed before, stems from the sensitivity of the adaptive binarisation algorithm. The error bias is amplified in dense regions, due to the presence of the drop interfaces. The PLIF measurements can also provide drop chord length measurements by using an automated algorithm, which carries an absolute uncertainty of ± 2 pixels or $\pm 0.12\ \mathrm{mm}$, imposed by the resolution of the images. Deviations between the automated and manual measurements gave deviations below 10%. While it is difficult to quantify the PIV/PTV errors, based on the computation of the Stokes number for the tracer particles for the smallest timescales considered, the relative uncertainties should be below 1%. However, for the PIV measurements and in the presence of drops inside the correlation windows, the standard deviations increased significantly. A comparison between PTV and PIV measurements showed differences below 10% (Voulgaropoulos and Angeli 2017), which is considered as the mean relative uncertainty of the PIV measurements.

In the pilot-scale flow loop, high-speed imaging is conducted at the inlet and three axial locations downstream, namely $x^+ = 25$, 70 and 135. The visualisations can provide qualitative information on the flow pattern transitions. The DCP and ERT sensors are placed close to the three imaging axial locations and conductivity measurements are performed. The ERT can give quantitative data on the distribution of the phases, while the DCP can measure drop size measurements and record the layer heights. The liquids used in this facility are a model oil Exxsol D140 and tap water.

Laser-based diagnostics are utilised in the matched refractive index flow loop,

where high-speed PLIF and PIV/PTV are conducted. The measuring field is defined by a thin laser sheet at the middle of the pipe. Information on the spatial configuration of the phases, the drop size and the velocity field are obtained. To conduct the measurements at high dispersed phase fractions, a mixture of glycerol/water is used to match the refractive index of a low viscosity silicone oil. A fluorescent dye and particles are used in the system to distinguish between the phases and allow PIV measurements respectively.

In the final experimental setup, coalescence is studied in a confined system. Bright field PIV with volume illumination is used with the measuring plane defined by the DOF of the camera and lens. Two different oils are used, a very low viscosity model oil Exxsol D80 and a silicone oil of slightly higher viscosity. The aqueous phases are a mixture of glycerol/water to match the refractive index of the respective organic phase. Blue ink is used to distinguish between the phases, while tracer particles are used to allow for the velocity field measurements. The effect of a non-ionic surfactant (Span 80) is studied in the Exxsol D80 system, while xanthan gum is introduced in the silicone oil. The use of the additives can help understand how surface active agents and complex fluids, which are commonly naturally present in the liquids of the systems in the oil and gas industry, can affect the coalescence mechanism.

Chapter 4

Separation Properties

In this Chapter the findings generated by the initial experiments conducted at the pilot-scale flow loop are discussed. A detailed description of the setup is provided in Sec. 3.1.1, while the techniques applied are discussed in Secs. 3.2.1 and 3.2.2.1. The goal of these experiments is to study kinetically unstable dispersions generated artificially through a multi-nozzle inlet. The focus is placed on understanding the separation properties by exploring the layer and drop size evolution downstream. The applicability of a phenomenological model developed for batch settlers is also investigated.

The conditions studied in detail with the DCP in this facility are summarised in Table 4.1, where $Q_m = Q_o + Q_w$. Two different mixture velocities and four input dispersed phase volume fractions are tested. The mixture Reynolds numbers are computed based on the mixture velocity and properties as shown in eq. 2.3. The density and viscosity are computed from eqs. 2.17 and 2.18 respectively for $\varepsilon_{max} = 0.90$. This high value of maximum packing will be discussed in Section 4.3. Due to polydisperity of the dispersions and especially in the presence of surfactants in the oil used in this system, higher values of packing are expected compared to the random packing value of 0.64 for monodisperse spheres. It must be noted that the Re_c are of the order of $\mathcal{O}\{10^4\}$, when ignoring the local effects of the dispersed phase. However, as dense dispersions are investigated, such effects are important. As it is clear from Table 4.1, most conditions are in the turbulent regime even when considering the Re_m.

Table 4.1: Conditions investigated with the DCP at the pilot scale flow loop at three axial measuring locations.

Q_m ($\mathrm{m^3\,s^{-1}}$)	u_m ($\mathrm{m\,s^{-1}}$)	φ_o	Re_m
0.56×10^{-3}	0.52	0.30	8331
0.56×10^{-3}	0.52	0.45	4361
0.56×10^{-3}	0.52	0.60	1751
1.12×10^{-3}	1.04	0.15	27529
1.12×10^{-3}	1.04	0.30	16662
1.12×10^{-3}	1.04	0.45	8722
1.12×10^{-3}	1.04	0.60	3503

4.1 Generation of dispersions

To generate the unstable dispersions at low mixture velocities, the multi-nozzle inlet of Fig. 3.2(b) is employed. Similar systems have been used by Galinat (2005) for vertical and Conan (2007) for horizontal liquid-liquid flows. The Exxsol D140 oil is introduced through the nozzles, while tap water flows in the annulus of the inlet. The initial drop size distribution depends on the drop formation dynamics at the nozzles. The velocity of the oil inside the nozzles is the primary reason controlling the final drop size, while the velocity of the continuous phase can also play a role. The velocity of the oil inside each nozzle can be found by dividing the oil flow rate with the total area of the nozzles as

$$u_{nozzle} = \frac{4Q_o}{N_{nozzle}\pi D_{nozzle}^2}, \tag{4.1}$$

based on the area of the cross-section of each cylindrical nozzle with a diameter $D_{nozzle} = 1$ mm and $N_{nozzles} = 1056$. With Q_o ranging from 0.17×10^{-3} to 0.67×10^{-3} $\mathrm{m^3\,s^{-1}}$, the velocities in each nozzle u_{nozzle} are in the range of 0.20 to 0.81 $\mathrm{m\,s^{-1}}$. The respective Reynolds number inside the nozzles are then $Re_{nozzle} = \mathcal{O}\{100\}$. Similarly, the velocity of the annulus region $u_{annulus}$ of the continuous phase can be computed by considering the annular area around the stainless steel tube and the flow rate of the water.

Some typical visualisations acquired with high-speed imaging are illustrated in Fig. 4.1 for three different flow conditions at two axial locations along the inlet – $x^+ = 0$ marks the end of the inlet section, while x^+ is the normalised axial distance x/D. In Figs. 4.1(a) and (b) it can be seen that an increase of the u_{nozzle} increases the drop size. The drops will detach when the buoyancy force is stronger than the interfacial tension. By comparing Figs. 4.1(a) and (c) it is clear that the annulus velocity of the continuous phase can change the dynamics of the drop formation. The drops detach faster due to the cross-flow, resulting in drops of smaller size.

For the seven different cases explored in detail in this study, the sizes recorded from the high-speed images for samples of ~ 200 drops are shown in Fig. 4.2. The Sauter mean diameters (eq. 2.30) are plotted. The data follow a decreasing trend with $u_{annulus}$. The neck or ligament breakup takes place sooner with increasing $u_{annulus}$, as the deformation due to the shear generated by the continuous phase velocity becomes stronger. A similar trend was observed in the vertical arrangement by Galinat et al. (2005), with a co-flow of the continuous phase instead of cross-flow as in this case.

For low velocities inside the nozzle, the diameter of the drops that form can be computed based on a simple force balance between the buoyancy and the interfacial force. This balance is described by the Bond number, $Bo = D_{nozzle}^2 \Delta\rho g/\sigma$ (similarly to eq. 2.39) at the periphery of the nozzle. According to Galinat (2005) it can be

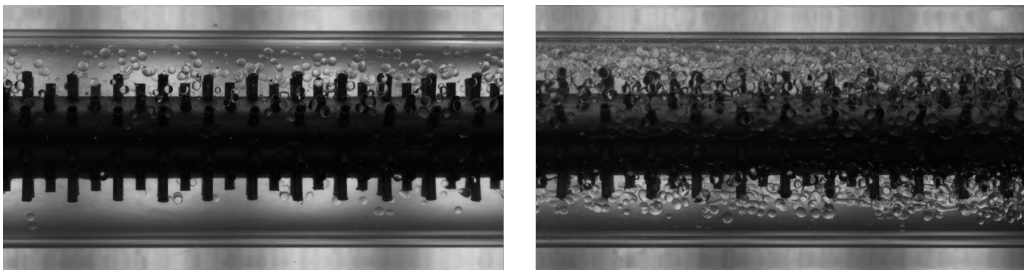

(a) $u_{nozzle} = 0.20\,\mathrm{m\,s^{-1}}$ and $u_{annulus} = 0.44\,\mathrm{m\,s^{-1}}$
$u_m = 0.52\,\mathrm{m\,s^{-1}}$ and $\varphi_o = 0.30$

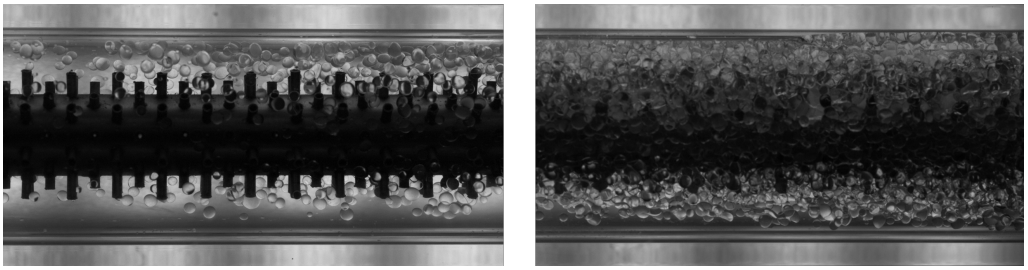

(b) $u_{nozzle} = 0.41\,\mathrm{m\,s^{-1}}$ and $u_{annulus} = 0.25\,\mathrm{m\,s^{-1}}$
$u_m = 0.52\,\mathrm{m\,s^{-1}}$ and $\varphi_o = 0.60$

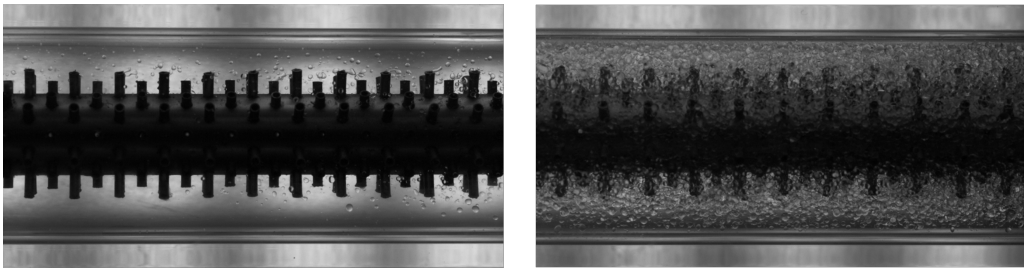

(c) $u_{nozzle} = 0.20\,\mathrm{m\,s^{-1}}$ and $u_{annulus} = 1.06\,\mathrm{m\,s^{-1}}$
$u_m = 1.04\,\mathrm{m\,s^{-1}}$ and $\varphi_o = 0.15$

Figure 4.1: High-speed images acquired at $x^+ = -10$ (left) and $x^+ = -4$ (right) for three flow conditions.

approximated to $d/D_{nozzle} = (6/Bo)^{1/3}$ or

$$d = \left(\frac{6\sigma D_{nozzle}}{g\Delta\rho}\right)^{1/3} \tag{4.2}$$

for a spherical drop. Sadhal et al. (2012) adjusted the right hand side of eq. 4.2 with a correcting factor to account for the liquid remaining at the nozzle after the detachment. However, for the current system it is neglected, as it was found to be below $0.1\,\mathrm{mm}$. Surprisingly, eq. 4.2 does not depend on the velocity inside the nozzle and for the current fluids gives $d = 4.9\,\mathrm{mm}$ (it is constant for all conditions), which is larger than the measured values of Fig. 4.2.

In the current experiments, the nozzles are in a cross-flow arrangement, which is found to significantly affect the breakup and hence the drop size distribution. Two mechanisms are observed in this work that describe the drop formation and

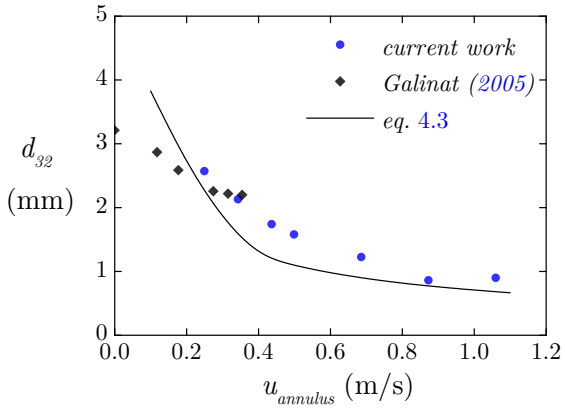

Figure 4.2: Sauter mean diameters of the drops recorded at the multi-nozzle inlet at $x^+ = -10$ for this study compared against the data by Galinat (2005) and eq. 4.3.

are affected by the velocity of the continuous phase in the annulus region $u_{annulus}$. They are presented in Figs. 4.3(a) and (b). In the first case of Fig. 4.3(a), the drop forms from breakup at the neck close to the nozzle region, which is typical for drops forming in an ambient fluid at rest. The drop grows towards the top of the pipe due to buoyancy, and the neck of the drop close to the nozzle decreases over time, until breakup takes place. The second mechanism was observed for high values of $u_{annulus}$. Similar dynamics are observed as in the aforementioned case, but the formation of a secondary drop also takes place. The drop stretches under the intense cross-flow and forms a ligament. It has been found that drop deformation and breakup of the ligament can generate secondary drops (Stone 1994), which will lead to higher polydisperity in the initial drop population of the dispersion.

Xu et al. (2005) developed a theoretical approach to describe the drop formation

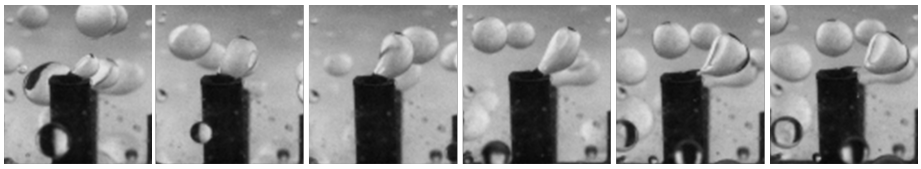

(a) Neck breakup at low continuous phase velocities, $u_{annulus} = 0.44\ \mathrm{m\,s^{-1}}$

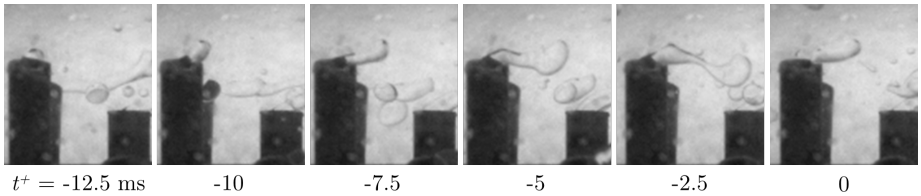

(b) Ligament breakup at high continuous phase velocities, $u_{annulus} = 1.06\ \mathrm{m\,s^{-1}}$.

Figure 4.3: Drop formation mechanisms observed at two continuous phase velocities for the same $u_{nozzle} = 0.20\ \mathrm{m\,s^{-1}}$

under cross-flow conditions based on a force balance at the drop. The interfacial tension force $F_\sigma = \pi D_{nozzle}\sigma$ keeps the drop together, with an opposite force stemming from the static pressure difference $F_P = F_\sigma D_{nozzle}/d$. The buoyancy and lift forces are written as $F_B = \Delta\rho g\pi d^3/6$ and $F_L = 0.761\tau_{wall}^{1.5}d^3\rho_c^{0.5}/\mu_c$. For this arrangement the wall shear stresses are computed as $\tau_{wall} = f\rho_c u_{annulus}^2/2$. For a spherical drop, the viscous drag force can be computed as $F_D = 3\pi d u_{annulus}\mu_c$. According to Xu et al. (2005) the following balance holds

$$F_\sigma D_{nozzle} = 2F_D d + (F_P + F_B + F_L)\, D_{nozzle}, \tag{4.3}$$

which is solved iteratively to give the drop size d. The resulting eq. 4.3 is plotted in Fig. 4.2 and compared against the experimental Sauter mean diameters. It can capture the trend in a satisfactory manner for the range of $u_{annulus}$ and Re investigated in this study.

The majority of drops observed in the experiments are spherical. The Bond number[1] for the drop can be computed as $Bo = g\Delta\rho d^2/\sigma = \mathcal{O}\{10^{-1}\}$ and the Reynolds number based on the continuous phase properties and drop size as $Re_d = \rho_c d u_m/\mu_c = \mathcal{O}\{10^2\}$. According to the empirical arguments of Clift et al. (2005), the drops have a spherical shape, except for the very large drops with $d > 5$ mm, where ellipsoidal shapes are expected.

4.2 Phenomenological observations

4.2.1 Flow pattern maps

As described in Sec. 2.1.1, several flow patterns can be observed during liquid-liquid horizontal pipe flows. When the Y-shaped inlet is used in the system, the flow patterns observed through high-speed imaging at $x^+ = 135$ are shown in Fig. 4.4. The water is introduced from the bottom and the oil from the top to minimise any mixing taking place between the two when they meet. As expected for low mixture velocities, stratified flows (*ST*) are observed, while drops appear close to the interface level for higher velocities. The drop generation, caused by the Kelvin-Helmholtz instability, results in dual-continuous structures downstream the pipe. When the velocities are high enough and the input oil volume fraction φ_o relatively low, water is the continuous phase and the oil is dispersed. When the mixture velocities are kept low, the turbulent levels are not high enough to keep the drops dispersed homogeneously and gravity leads to segregation and *o/w & w* patterns.

The dispersed flow categorisation of this work is presented in Fig. 4.5 and illustrates the different sub-categories of *o/w* and *w/o*. When segregation of oil drops has taken place then the term *o/w & w* is used instead. The flow patterns shown in Figs. 4.5(d) and (e) can be considered *DC* flow patterns. Nevertheless, in this work, Fig.

1. also referred to as Eötvös number

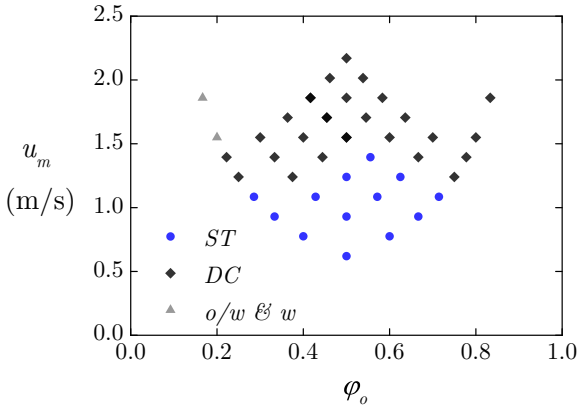

Figure 4.4: Flow pattern map for the Y-shaped inlet for a range of input oil fractions φ_o and mixture velocities u_m.

4.5(d) is categorised as *o/w & w & o* to underline the generation of a continuous layer of the oil (dispersed phase). This transition is very important as some portion of the oil wets the wall in contrast to water-continuous dispersed flows. It also signals the last transition towards separated flows, which is the ultimate goal of this study. The *o/w & w/o* structures are similar to *ST*, but are characterised by high pressure gradients, as both oil and water layers are dispersions.

When the multi-nozzle inlet is used and the oil flows through the nozzles (as shown in Fig. 4.1), drops of oil are expected even at low mixture velocities and for a wide range of input oil fractions, contrary to the Y-shaped inlet of Fig. 4.4. The flow structures at dense dispersions are difficult to quantify solely from the high-speed images and thus an ERT system is also employed. As the goal of this study is the development of the dispersions downstream the inlet, the flow pattern maps are investigated at the beginning ($x^+ = 25$) and end of the pipe ($x^+ = 135$) downstream the multi-nozzle inlet. The flow pattern maps at these two locations are plotted in Figs. 4.6(a) and (b) respectively.

For low velocities, *o/w & w & o* dispersions are observed in the first axial measuring location. The oil drops generated by the nozzles coalesce rapidly at the top of

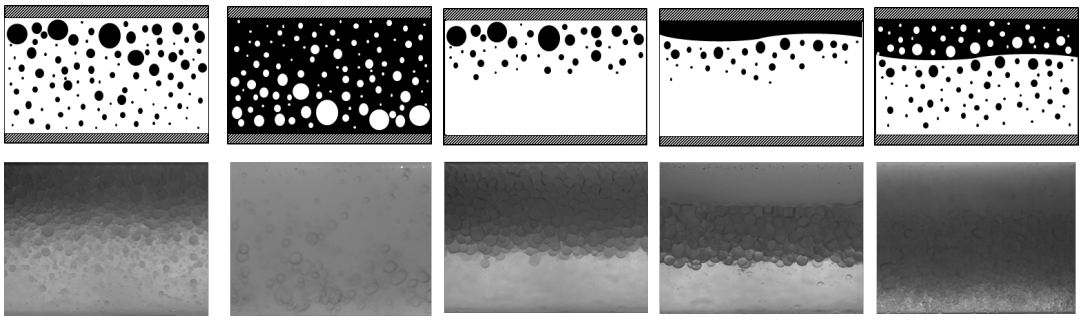

(a) *o/w* (b) *w/o* (c) *o/w & w* (d) *o/w & w & o* (e) *o/w & w/o*

Figure 4.5: Schematic representation and respective typical high-speed image of the dispersed flow patterns observed in this work.

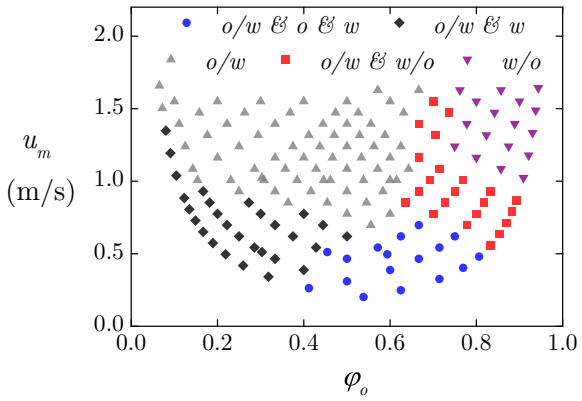

(a) Flow pattern map at $x^+ = 25$

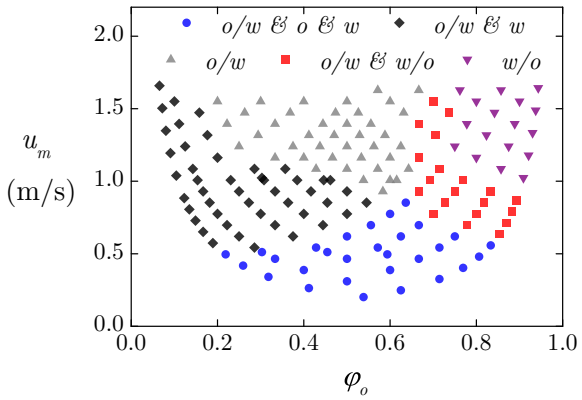

(b) Flow pattern map at $x^+ = 135$

Figure 4.6: Flow pattern maps at two axial locations downstream the multi-nozzle inlet obtained from high-speed images and conductivity tomograms.

the pipe and form a continuous layer of the dispersed phase. A continuous layer of water is also observed at the bottom of the pipe – mainly due to the buoyancy forces acting on the drops. As the flow develops, *o/w & w & o* dispersions are present at higher mixture velocities and input oil fractions. This development is caused by the coalescence of the drops as they flow along the pipe. If the flow patterns were investigated at longer lengths, e.g. $x^+ \gg 200$, *ST* flows are expected according to Fig. 4.4, where minimum mixing is induced at the inlet. This separation of the phases depends on the residence time of the dispersion inside the pipe. As the measurements in this work are conducted in the front-leg of the flow loop, the residence times are limited to the order of $t_{res} = \mathcal{O}\{10\}$ for the mixture velocities investigated.

Due to the enhanced mixing induced by the multi-nozzle inlet, homogeneous *o/w* dispersions appear for lower mixture velocities and a wider range of flow rates, as shown in Fig. 4.6(a) at $x^+ = 25$. As the dispersions flow, the drops segregate and a drop free layer of water forms at the bottom. This transition from *o/w* to *o/w & w* can be noted when comparing Figs. 4.6(a) to (b). Interestingly, *DC* (or equivalently *o/w & w/o*) appear at high input oil fractions. Finally, phase inversion takes place right

at the inlet section when high enough mixture velocities are used together with high input oil fractions. This transition does not change as the dispersions flow along the pipe.

4.2.2 General characteristics

In this work, the transition from *o/w* to *o/w & w* and from *o/w & w* to *o/w & w & o* is of interest as discussed in Chapter 1. For this reason, the conditions of Table 4.1 are carefully chosen to be studied in detail in order to acquire quantitative characteristics of these two transitions. Figure 4.7(a) presents a case of the *o/w* to *o/w & w* transition for $u_m = 1.04\ \mathrm{m\,s^{-1}}$ and $\varphi_o = 0.15$. Drops of oil have floated towards the top, forming a drop-free water layer at the bottom. Even at this high velocity, the dispersive inertial forces are not strong enough to keep the dispersion homogeneous. Typical images captured at $x^+ = 135$ from the bottom of the pipe are also shown. As the depth of field is kept quite sharp (DOF ≈ 10 mm) and placed in the middle of the vertical direction, it is clear that the drops still floating at the bottom are mainly close to the middle plane $z^+ \sim 0.5$, rather than close to the pipe side walls.

Figures 4.7(b) illustrates the generation of a continuous layer from coalescence of the oil drops at the top for $u_m = 0.52\ \mathrm{m\,s^{-1}}$ and $\varphi_o = 0.30$. This signals a flow pattern transition from *o/w & w* to *o/w & w & o*. A thin layer of pure oil has formed

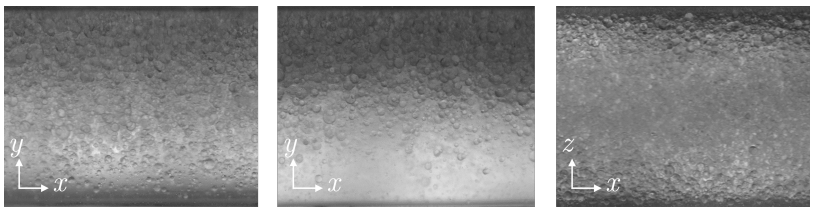

(a) $u_m = 1.04\ \mathrm{m\,s^{-1}}$ and $\varphi_o = 0.15$

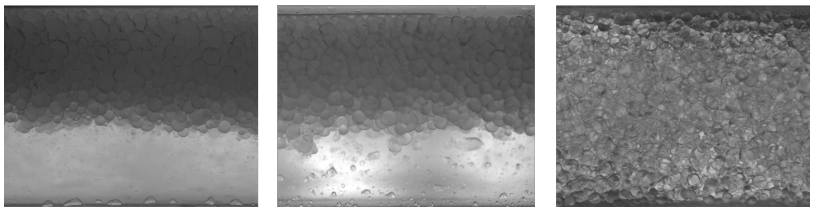

(b) $u_m = 0.52\ \mathrm{m\,s^{-1}}$ and $\varphi_o = 0.30$

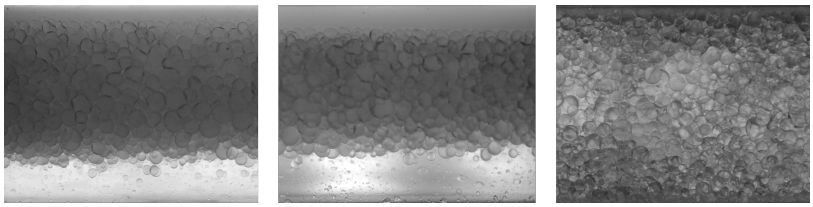

(c) $u_m = 0.52\ \mathrm{m\,s^{-1}}$ and $\varphi_o = 0.60$

Figure 4.7: High-speed images acquired at $x^+ = 25$ (left) and $x^+ = 135$ (middle, right) for three flow conditions. (a) Transition from *o/w* to *o/w & w* and (b) from *o/w & w* to *o/w & w & o* and (c) oil layer evolution.

at the top. Fig. 4.7(c) illustrates the increase of the thickness of this oil layer at the top of the pipe along the streamwise direction x, due to coalescence of drops with the interface. Visualisations at the bottom (right-hand side of the Figure), illustrate a stratification of size, with larger drops close to the middle. Nevertheless, it is clear that more thorough analysis needs to be conducted to quantify these characteristics. For this reason, the following Sections will focus on the results acquired using the DCP.

4.3 Layer evolution

A DCP is placed at three axial measuring locations, namely $x^+ = 15, 80$ and 150. Measurements are taken for every $\Delta y^+ = 0.054$ in the vertical direction. The seven conditions of Table 4.1 are studied, resulting in a total of ~ 400 measurements for the DCP. In this Section, the layer development is investigated. The layer height definitions are shown for a *o/w* dispersion in Fig. 2.5. They are also shown in Fig. 4.8 for completeness, for the *o/w* dispersions studied in this Chapter. A pure water drop free layer is defined when the DCP is not able to capture any drops $\varepsilon_o = 0$. It should be mentioned though that very small drops can avoid the sensors as discussed in Sec. 3.2.1.1. The floatation layer is defined from the vertical point where drops are detected until dense-packing is recorded, i.e. $0 < \varepsilon_o < 0.9$. The dense-packed layer is then valid from $0.9 \leqslant \varepsilon_o < 1$ and it follows that the pure oil layer is defined at the regions where the in-situ oil fraction becomes equal to unity.

Pérez (2005) defined the dense-packed layer boundary at $\varepsilon_p = 0.75$ (close to the random packing of spheres), while Schümann et al. (2016b) at $\varepsilon_p = 0.80$. (Pereyra et al. 2013) followed the formulation of Henschke et al. (2002) for batch settlers and set the dense-packed layer at $\varepsilon_p = (\varphi_o + 1)/2$. In this work the boundary is set at $\varepsilon_p = 0.90$, as discussed by Conan et al. (2007), who found that the integrated momentum balance of the continuous phase agreed with their pressure drop measurements despite the presence of the drops. These high in-situ oil fraction values are justified

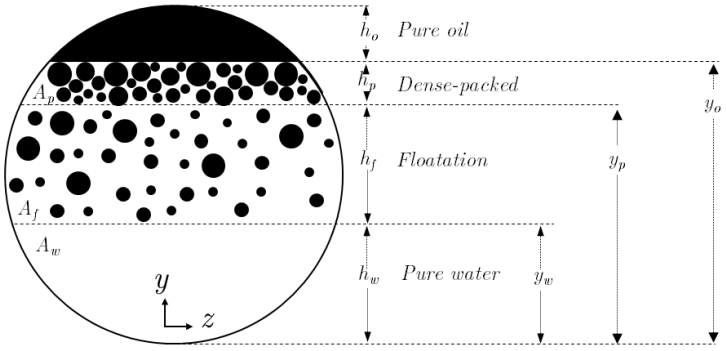

Figure 4.8: Schematic illustration of the spatial configuration of a separating dispersion with the notation of the different layers.

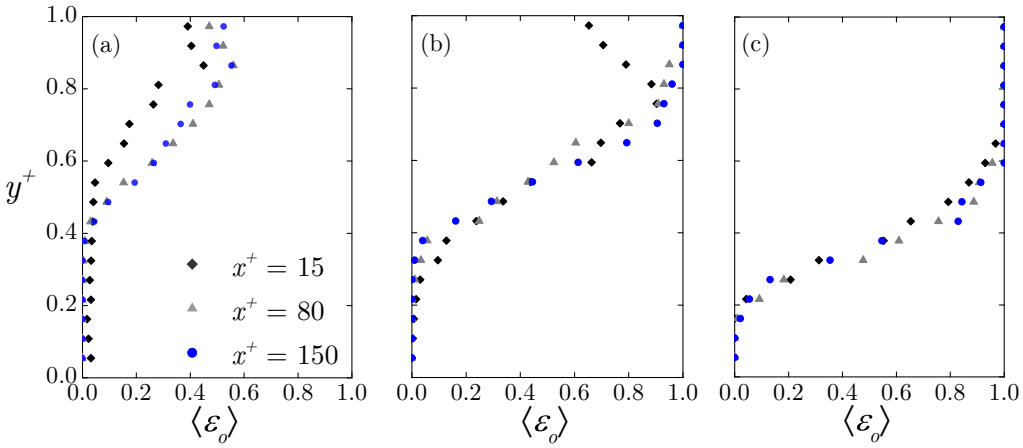

Figure 4.9: Time-averaged in-situ volumetric oil fraction profiles obtained from the DCP for three flow conditions and three axial locations. (a) $u_m = 1.04\,\mathrm{m\,s^{-1}}$ and $\varphi_o = 0.15$, (b) $u_m = 0.52\,\mathrm{m\,s^{-1}}$ and $\varphi_o = 0.30$ and (c) $u_m = 0.52\,\mathrm{m\,s^{-1}}$ and $\varphi_o = 0.60$.

due to polydisperity of the system, which is inevitable in liquid-liquid flows (Pouplin et al. 2011). Specifically for this system, the low velocities investigated allow for increased coalescence dynamics, that can in turn result in high variance in the drop size distributions. Conan et al. (2007) found that the vertical velocity component at this phase fraction tends to zero $v_d \to 0$ and any floatation or settling has stopped.

The vertical time-averaged in-situ oil fraction profiles $\langle \varepsilon_o \rangle$ obtained from the DCP for $\Delta t = 10$ s are shown in Fig. 4.9 for the same flow conditions as in Fig. 4.7 and for three axial measuring locations $x^+ = 15$, 80 and 150. The profiles are smoothed with a moving average filter to better illustrate the trends. In Fig. 4.9 homogeneous dispersed flow is observed for $u_m = 1.04\,\mathrm{m\,s^{-1}}$ and $\varphi_o = 0.15$, which is in accordance with the visualisations. The drop-free water layer at the bottom of the pipe slightly increases as the flow develops $x^+ \to 150$; however, the differences fall within the 20% uncertainty of the phase fraction from the DCP. A slight decrease of the in-situ oil fraction is observed close to the top wall for all three locations. Lift forces are stronger close to the walls in a cylindrical pipe and can push larger drops away from the walls. Similar behaviour has been recorded by Ekambara et al. (2008) in gas-liquid and by Ngan (2011) in liquid-liquid pipe flows. Interestingly, the same dip in the concentration of the dispersed phase close to the walls has also been recorded both in experiments and simulations with non-deformable solid spheres (Kaushal and Tomita 2007; Tiwari et al. 2009; Yan and Koplik 2009).

This decrease of ε_o close to the top wall is more pronounced in Fig. 4.9(b) at $x^+ = 15$. In the same Figure, a transition from an *o/w & w* to an *o/w & w & o* pattern is taking place as the dispersion flows. A pure oil forms at the top of the pipe due to coalescence of drops. This transition can also be observed in the relevant visualisations of Fig. 4.7(b). As the concentration in the bottom of the dense-packed layer, rather than close to the wall, is higher, the development of the pure oil layer does not start close to the pipe wall. Conan (2007) illustrates this mechanism in his dissertation. The formation of the continuous oil layer at the top was captured with

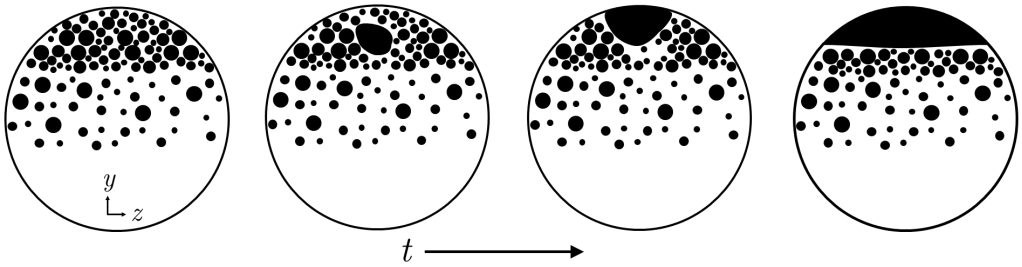

Figure 4.10: Schematic illustration of the evolution of the dispersion structure from *o/w & w* to *o/w & w & o* pattern. The transition in time reads from left to right.

high-speed PLIF experiments in the middle plane of the pipe for unstable dispersions. This mechanism is shown schematically in Fig. 4.10. A blob of oil drops coalesces in the middle of the dense-packed layer. Mainly due to buoyancy, it floats towards the top and starts wetting the walls, while more drops start coalescing with it and eventually form a continuous oil layer.

Figure 4.9(c) shows the in-situ phase fraction profiles recorded for $u_m = 0.52$ $\mathrm{m\,s^{-1}}$ and $\varphi_o = 0.60$. The higher input dispersed phase fraction, compared to Fig. 4.9(b), causes the generation of the pure oil layer at the top. This generation is also clear right from the inlet section as shown in the visualisation of Fig. 4.1(b) at $x^+ = -4$ for the same flow condition. Larger drops are generated from the nozzles, which are susceptible to stronger buoyancy and enhanced coalescence dynamics. As the dispersion flows along the pipe, the oil continuous layer thickness is increased as more drops coalesce with it. Notably, no change in the pure water layer is observed at the bottom, as stratification has already taken place for $x^+ < 15$. The early segregation of the drops can be attributed to higher viscosities in the floatation layer, which result in lower turbulence levels and thus quicker floatation velocities.

To better quantify the spatial evolution of the characteristic layers that form and develop, the time-averaged height of the dense-packed layer $\langle y_p^+ \rangle$ and of the pure oil layer $\langle y_o^+ \rangle$ (normalised with the pipe diameter D) along x^+ are shown in Figs. 4.11(a) and (b) respectively for the conditions of Table 4.1. For the low mixture velocity cases, $u_m = 0.52$ $\mathrm{m\,s^{-1}}$, the dense-packed layer height decreases with the input dispersed phase fraction. This behaviour is expected as more volume of oil is present for higher φ_o and the maximum packing value is reached at lower values of y^+. As the mixture velocity increases the packing of drops happens at higher y^+, as dispersive forces are stronger and floatation is less pronounced. As the dispersions flow along the pipe, the height of the packed layer gradually decreases with more drops gradually floating towards the top. This behaviour is more dominant for the low mixture velocity cases $u_m = 0.52$ $\mathrm{m\,s^{-1}}$, where the residence time is higher $t_{res} \approx 10.7$ s compared to the $u_m = 1.04$ $\mathrm{m\,s^{-1}}$ cases with $t_{res} \approx 5.3$ s. The residence time is computed simply as $t_{res} = \Delta x / u_m$. Nevertheless, high stratification of the velocity is expected, since the viscosity in the dense-packed layer will be lower due to local effects, and thus the residence time of the packed region will be even higher.

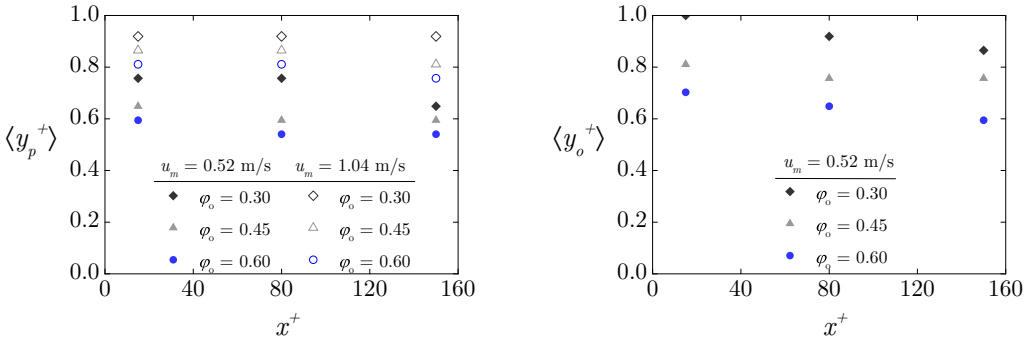

(a) Time-averaged dense-packed layer height

(b) Time-averaged continuous oil layer height

Figure 4.11: Spatial development of the characteristic layer heights as the dispersion flows along the pipe.

Figure 4.11(b) illustrates the time-averaged pure oil layer heights recorded. A continuous layer of oil was recorded only at the low mixture velocity cases, in accordance with the flow pattern maps of Fig. 4.6. To identify this layer height, careful treatment and analysis of the data follows, as fluctuations due to waves or larger drops can influence it. Time-averaging of the profiles provides the layer height where $\varepsilon_o = 1$, but is biased towards higher values of y^+ for the aforementioned reason. As also observed in the visualisations of Fig. 4.7(b) and (c), as the input oil fraction increases, so does the pure oil layer height. This behaviour can be attributed to larger drops generated at the nozzles, which float faster and coalesce easier. The decrease of the pure oil layer height along x^+ (higher thickness h_o) is also shown in the Figure, but the resolution of the probe (incremental measurements every $\Delta y^+ = 0.054$) on the y^+ direction and the only three measurements along x^+, do not allow to obtain a slope of a fitted curve with confidence.

The dynamics of the packing are buoyancy dominated and depend on the density difference of the fluids and the drop size. The Buoyancy number Bu has found wide use in gravity dominated low-Reynolds number particulate and suspension pressure-driven flows for predicting separation lengths and other flow characteristics (Norman et al. 2005; Yan and Koplik 2009). Bu is defined as the ratio of gravity to inertial effects and can be written for horizontal flows as

$$Bu = \frac{|\rho_d - \rho_c| g d_{32}^2}{18 \eta_c u_m}. \tag{4.4}$$

It is clear that the Buoyancy number is practically a ratio of the vertical velocity (computed as the settling/floatation velocity of the drops from eq. 2.12) over the axial mixture velocity. Figure 4.12 presents the dense-packed layer heights recorded at different axial lengths plotted against the respective Buoyancy numbers. It is clear that a linear trend exists between Bu and the time-averaged $\langle y_p^+ \rangle$, showing the strong dominance of gravity in the separation of the phases. The same effect of the packing dynamics due to the mixture velocity is also discussed by Conan et al. (2007). They

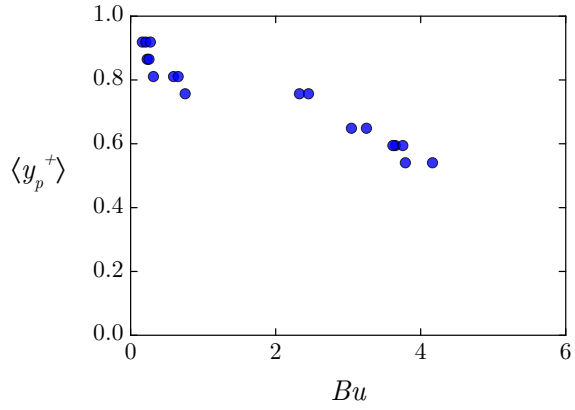

Figure 4.12: Spatial development of the time-averaged dense-packed layer height recorded at different Buoyancy numbers with the DCP.

introduce a modified Froude number Fr, where $u_m/\sqrt{gd_{32}}$ is related to the packed layer height in a power of $1/4$.

4.4 Drop size evolution

To better quantify and understand the aforementioned trends, a detailed study of the drop sizes present in the pipe follows. The drop sizes (chord lengths) recorded in a time interval of $\Delta t = 10$ s for each axial and vertical location of the probe are analysed.

4.4.1 Drop size distributions

Figure 4.13(a) shows a histogram for a representative case of drop size distribution. Sturges' rule (Scott 2009) can be applied to determine the number of bins N_{bins} to use in the histograms as

$$N_{bins} = 1 + 3.322\,(\log_{10} N_d)\,. \tag{4.5}$$

As explained before, in the present experiments N_d varied from a few hundred to a few thousand drops for each measurement giving $N_d = \mathcal{O}\{10\}$. An ad-hoc value of 0.5 mm is used instead for the bin size, which is found to represent the distributions adequately, provides a similar number of bins as eq. 4.5 and it is constant for all conditions. The detail of the histograms increases with smaller bin size, but deviations can occur if the number of drops in the population is not high enough, since some bins are left with an inadequate number of drops.

It has been found that the drop size distribution in liquid-liquid systems does not follow a normal distribution. The Rosin and Rammler (1933) distribution has been found to describe the drop size distributions in liquid-liquid flows well (Karabelas 1978). Angeli and Hewitt (2000b) used a modified Rosin-Rammler distribution given

by

$$\mathrm{CDF}_{Rosin-Rammler}(d) = 1 - \exp\left(-2.995\left(\frac{d}{d_{95}}\right)^{p_{RR}}\right), \tag{4.6}$$

where the diameter of the 95$^{\text{th}}$ percentile d_{95} was used together with a fitted parameter p_{RR} ranging from 2.1 to 2.9. More recent efforts have implemented log-normal distributions to capture the positive skewness usually present in liquid-liquid systems (Augier et al. 2003; Lovick and Angeli 2004a). It is clear from both Figs. 4.13(a) and (b), that the log-normal distribution captures very well most of the range of drop sizes for the current experiments as well. Nevertheless, the log-normal distribution is found to be slightly biased towards higher probabilities of the larger drops.

The probability density functions and cumulative distribution functions of the drop size distributions $\mathrm{PDF}(d)$ are computed for log-normal distributions (Whittaker and Watson 1996) as

$$\mathrm{PDF}_{log-normal}(d|\mu_d, s_d) = \frac{1}{d s_d \sqrt{2\pi}} \exp\left(\frac{-\left(\ln d - \mu_d\right)^2}{2 s_d^2}\right) \tag{4.7}$$

$$\mathrm{CDF}_{log-normal}(d|\mu_d, s_d) = \frac{1}{2}\left[1 + \mathrm{erf}\left(\frac{\ln d - \mu_d}{s\sqrt{2}}\right)\right], \tag{4.8}$$

where the error function erf is computed as

$$\mathrm{erf}(d) \equiv \frac{2}{\sqrt{\pi}} \int_0^d e^{-\tilde{d}^2} \mathrm{d}\tilde{d} \tag{4.9}$$

with $\tilde{d}$ being the transformation variable of d for the integration. The log-normal distributions are based on the fact that $\log(d)$ will be distributed normally. While the mean μ and variance s of a population are computed from eqs. 3.9 and 3.10 respectively, the mean $\hat{\mu}$ and variance $\hat{s}$ of a log-normal distribution can be computed

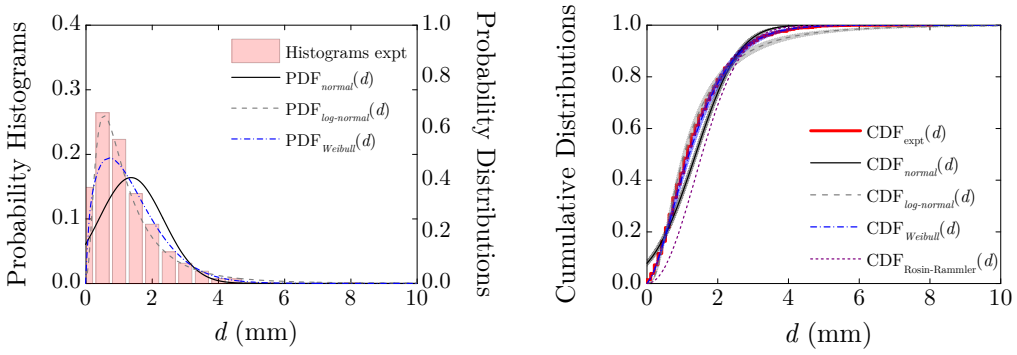

(a) Histogram and PDFs (b) CDFs

Figure 4.13: Drop size distributions for $u_m = 1.04\ \mathrm{m\,s^{-1}}$ and $\varphi_o = 0.45$ at $x^+ = 150$ and $y^+ = 0.86$

as

$$\hat{\mu} = \exp\left(\mu + s^2/2\right) \tag{4.10}$$

$$\hat{s} = \exp\left(2\mu + s^2\right)\left(\exp\left(s^2\right) - 1\right). \tag{4.11}$$

The less-known Weibull distribution can also illustrate well the positive skewness (Fig. 4.13), but has found limited use in liquid-liquid dispersions as discussed by Zhou and Kresta (1998). For the sake of comparison with other works only log-normal distributions are used in the present work hereafter.

A stratification of drop size is expected along the vertical direction of the pipe. Bourdillon et al. (2016) showed in their numerical simulations that the size of the dispersed drops is expected to increase with the direction of buoyancy. Figure 4.14 shows the drop size histograms $\mathrm{P}(d)$ together with the probability density functions of the drop size $\mathrm{PDF}(d)$ for three flow conditions at $x^+ = 15$. Three vertical positions are chosen for each flow condition, namely $y^+ = 0.43$, 0.54 and 0.65 to have an adequate number of drops for the different spatial configurations for the three flow conditions. The size distributions for $u_m = 1.04\ \mathrm{m\,s^{-1}}$ and $\varphi_o = 0.30$ are very narrow (Fig. 4.14(a)), as very small drops are generated at the multi-nozzle inlet for this condition. Both from the histograms and the PDFs, it can be seen that larger drops are present along the vertical pipe height y^+. The probability to find bigger sizes increases and the PDFs become flatter. This trend can be justified by the floatation dynamics of the dispersed phase, where higher size drops will have a stronger vertical motion towards the top and thus they segregate faster – as can also be predicted from eq. 2.12.

For homogeneous dispersed flows with the same input oil fraction, but a lower mixture velocity $u_m = 0.52\ \mathrm{m\,s^{-1}}$, larger drops are expected due to the drop formation at the inlet as described in Sec. 4.1. By comparing Figs. 4.14(a) and (b), this behaviour is clear for the three vertical locations chosen. Finally, larger drops are observed when the input oil fraction is increased to $\varphi_o = 0.60$ at Fig. 4.14(c), because of the smaller $u_{annulus}$ at the inlet. The generation of the pure oil layer at the top does not seem to affect this argument. Notably, for this case, the $\mathrm{PDF}(d)$ for $y^+ = 0.54$ presents smaller drop sizes than $y^+ = 0.43$. This behaviour is due to the small variation in the histograms between the two vertical locations and cannot necessarily be attributed to the spatial configuration of the dispersion. It lies within the estimated uncertainty of the drop size measurements from the DCP.

The log-normal CDFs are shown in Fig. 4.15 for the same three flow conditions and vertical locations at $x^+ = 15$. Similar trends are observed with higher slope CDFs computed with increasing y^+. Notably, the 95% confidence intervals also become wider with increasing vertical height. Both the d_{95} and the d_{max} can be easily extracted from the aforementioned Figure. The d_{max} does not seem to be much affected with the vertical height y^+ for $u_m = 1.04\ \mathrm{m\,s^{-1}}$ and $\varphi_o = 0.30$ in Fig. 4.15(a). However, a significant increase is found for the lower mixture velocity cases in Figs.

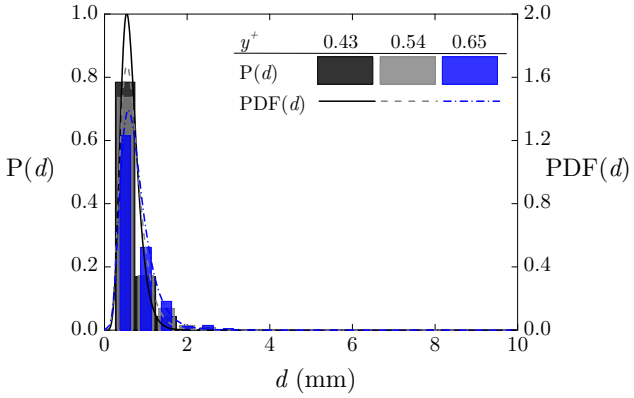

(a) $u_m = 1.04\,\mathrm{m\,s^{-1}}$ and $\varphi_o = 0.30$

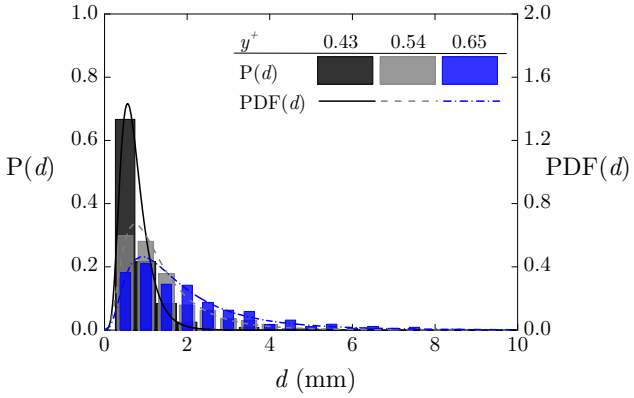

(b) $u_m = 0.52\,\mathrm{m\,s^{-1}}$ and $\varphi_o = 0.30$

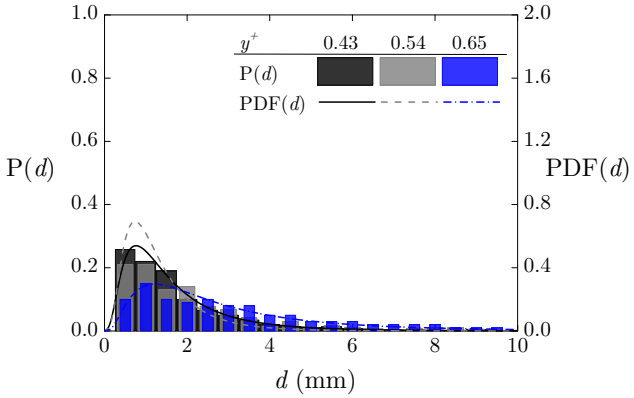

(c) $u_m = 0.52\,\mathrm{m\,s^{-1}}$ and $\varphi_o = 0.60$

Figure 4.14: Number probability histograms and probability density functions of eq. 4.7 of the drop size distribution for three flow conditions and three vertical locations and $x^+ = 15$.

4.15(b) and (c). It is also interesting to note that the d_{max} seems to change by an order of magnitude when decreasing the mixture velocity from $u_m = 1.04\,\mathrm{m\,s^{-1}}$ to

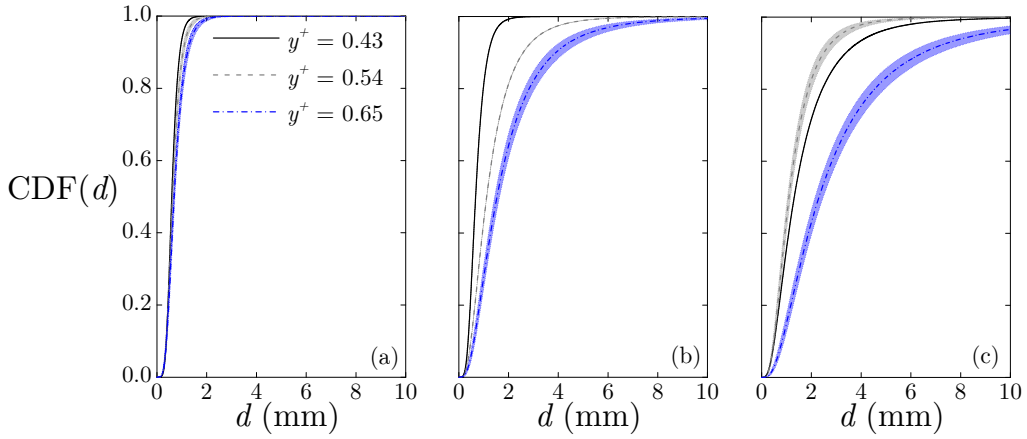

Figure 4.15: Cumulative distribution functions of eq. 4.8 for three flow conditions (a) $u_m = 1.04\,\mathrm{m\,s^{-1}}$ and $\varphi_o = 0.30$, (b) $u_m = 0.52\,\mathrm{m\,s^{-1}}$ and $\varphi_o = 0.30$ and (c) $u_m = 0.52\,\mathrm{m\,s^{-1}}$ and $\varphi_o = 0.60$, at $x^+ = 15$ and three vertical locations y^+.

$u_m = 0.52\ \mathrm{m\,s^{-1}}$ for the same input oil fraction $\varphi_o = 0.30$ (Figs. 4.15(a) and (b)). More thorough investigation on the physical mechanisms that can affect the d_{max} of the population will take place in the following Section.

The evolution of the drop size distributions are illustrated in more detail in the contour plots of Fig. 4.16. Two input oil fractions $\varphi_o = 0.30$ and 0.60 are investigated for the same mixture velocity $u_m = 1.04\,\mathrm{m\,s^{-1}}$. The number probabilities of the drop sizes are plotted for all the vertical measurement locations y^+ and the three axial x^+. As floatation of the oil drops towards the top takes place, the number of drops measured at the bottom for $\Delta t = 10$ seconds decreases with axial length and so does the accuracy of these measurements. Nevertheless, the measurements are shown for completeness. At the last axial location $x^+ = 150$ and $\varphi_o = 0.30$, no drops were recorded below $y^+ < 0.2$.

For $x^+ = 15$ and low input oil fraction in Fig. 4.16(a) the drop size distribution is very narrow, with very high probabilities $\mathrm{P}(d) > 0.8$ found at low drop sizes $d < 1$ mm. This trend holds along the vertical direction, with slightly larger drops observed at $y^+ > 0.8$. As the dispersion evolves along x^+ (Fig. 4.16(c) and (e)), the drop size distributions at the upper part of the become wider with sizes reaching $d = 3$ mm, but with low probabilities $\mathrm{P}(d) < 0.1$. The drop increases with y^+. Interestingly, for this flow condition two peaks are present at the last two axial locations for $y^+ \sim 0.8$ in Figs. 4.16(c) and (e), where the drop size decreases before it increases back for $y^+ > 0.9$. This behaviour can be attributed to lift and buoyancy forces together with wall effects and drop-drop interactions.

At the higher input oil fraction φ_o, an almost homogeneous drop size distribution, similar to the case of $\varphi_o = 0.30$, is observed at the initial axial measuring location (Fig. 4.16(b)). Some segregation has already taken place at the higher input oil fraction, with slightly higher probabilities for smaller drops close to the bottom of the pipe. This can be attributed to the larger drops generated at the inlet and thus stronger buoyancy forces that push the larger drops of the distribution towards the

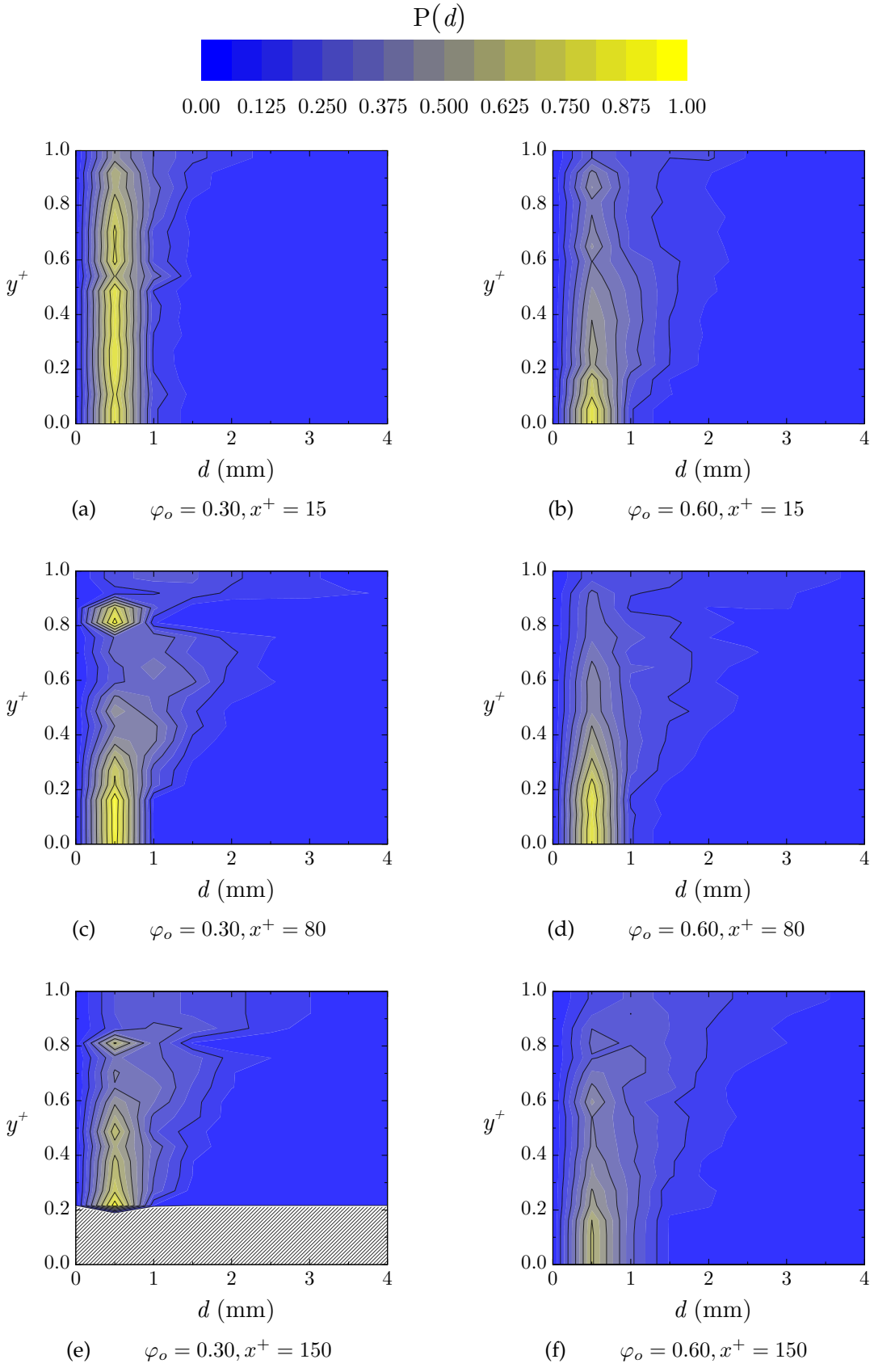

Figure 4.16: Number probability contour plots of the drop size distributions for three axial locations for two input oil fractions at the same $u_m = 1.04\,\mathrm{m\,s^{-1}}$.

Table 4.2: Descriptive statistics of the drop size distributions of Fig. 4.17.

		x^+	mean	standard deviation	skewness	kurtosis
$u_m = 0.52\ \mathrm{m\,s^{-1}}$	$\varphi_o = 0.30$	15	1.49	1.26	2.12	9.20
		80	1.59	1.30	2.02	8.55
		150	2.35	1.91	1.46	4.87
	$\varphi_o = 0.45$	15	1.72	1.52	1.94	7.51
		80	2.02	1.67	1.70	6.17
		150	2.27	1.76	1.54	5.37
	$\varphi_o = 0.60$	15	1.73	1.52	1.92	7.46
		80	1.75	1.51	1.91	7.43
		150	1.90	1.49	1.79	6.91
$u_m = 1.04\ \mathrm{m\,s^{-1}}$	$\varphi_o = 0.15$	15	0.73	0.37	1.45	6.70
		80	0.82	0.46	1.44	6.32
		150	0.89	0.52	1.56	7.44
	$\varphi_o = 0.30$	15	0.75	0.36	1.40	6.40
		80	1.06	0.75	2.12	10.90
		150	0.96	0.63	1.97	10.06
	$\varphi_o = 0.45$	15	0.81	0.46	1.68	8.13
		80	0.78	0.43	1.63	7.79
		150	1.00	0.66	1.99	10.15
	$\varphi_o = 0.60$	15	1.04	0.77	2.23	11.64
		80	1.14	0.92	2.33	11.79
		150	1.20	0.88	2.15	10.68

top. Similarly to the lower input oil fraction, higher drop sizes are present towards the top of the pipe as the flow develops along x^+ as shown in Figs. 4.16(d) and (f). When comparing Figs. 4.16(e) and (f), it becomes clear that the higher input oil volume fraction has increased the drop size along the pipe vertical direction with wider distributions recorded.

To obtain a global picture of the size distributions for the seven conditions investigated with the dual-conductance probe, the log-normal probability density functions are computed from eq. 4.7. The skewness and kurtosis together with the lower order statistics of each distribution are presented in Table 4.2, while the distributions are shown in Fig. 4.17. The sub-figures from top to bottom follow the same indexing of the conditions as the rows of Table 4.1.

While the Sauter mean diameter will be discussed in the following Section it can be seen in Table 4.2 that in the majority of cases the mean and standard deviation both increase with axial distance x^+. More specifically, it can be written that $\mu_d \propto s_d$ with excellent agreement even for a proportionality constant equal to 0.78 (regression coefficient), giving a coefficient of determination $\mathcal{R}^2 = 0.933$. The skewness of a distribution shows the asymmetry of the data around the mean and is computed

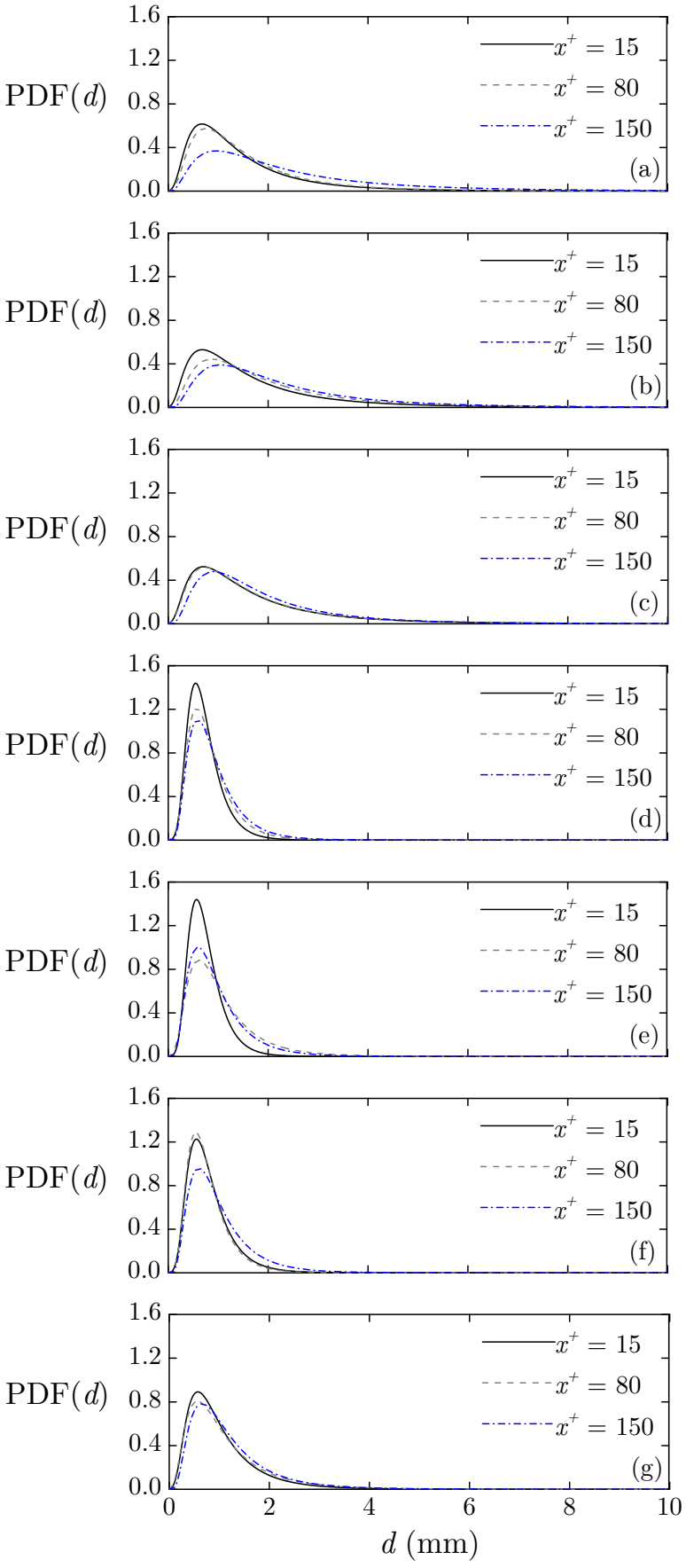

Figure 4.17: Probability density functions of eq. 4.7 for the conditions of Table 4.1 (same order as the rows of the Table).

as the third moment

$$\text{skewness} = \sum_{i}^{N_d} \frac{(d_i - \mu_d)^3}{N_d s_d^3}. \tag{4.12}$$

All the skewness values are above 1, denoting a strong asymmetry (positive). It can also be seen that the skewness decreases with axial length, but no concrete argument can be determined for linking it with the input oil fraction or mixture velocity. It is possible that other effects at the inlet can be controlling the skewness. The strong asymmetry is also present in Fig. 4.17 for all the cases considered in this study. It can also be seen that the conditions at $x^+ = 150$, where coalescence effects are more pronounced, are more symmetric.

The kurtosis can also be used to study these distributions. The definition of kurtosis remains ambiguous in the literature. While some argue that it is the degree of peakedness of a distribution, it has been recently discussed that it better illustrates the combined weight of the tails relative to the rest of the distribution. In this work, this translates to the effect of the number of larger drop sizes present in the distribution. It is computed similarly to eq. 4.12 as the fourth moment

$$\text{kurtosis} = \sum_{i}^{N_d} \frac{(d_i - \mu_d)^4}{N_d s_d^4}. \tag{4.13}$$

The very high positive values measured in the present experiments show the applicability of the log-normal distributions, which are capable of capturing the long tails of the distributions as shown in Fig. 4.17.

4.4.2 Mean drop size

The goal of this Section is to link the characteristic drop sizes, i.e. Sauter mean d_{32} and maximum diameter d_{max}, of the drop populations of each case with certain physical mechanisms. This can allow more concrete arguments to be made in regards to the phenomena taking place in the pipe compared to the more empirical observations of the previous Section.

It has been found that in liquid-liquid systems in stirred tanks, a direct proportionality between the Sauter mean diameter and the maximum diameter of the dispersed phase exists. This proportionality has also been tested in both gas-liquid (Azzopardi and Hewitt 1997) and liquid-liquid pipe flows (Angeli and Hewitt 2000b; Brauner 2003; Ioannou et al. 2005; Schümann et al. 2016b) with good agreement as

$$d_{32} = k_d d_{max}, \tag{4.14}$$

where k_d is the proportionality constant that can take values in the range of 1.5 to 3 as has also been recently reviewed by Schümann et al. (2015).

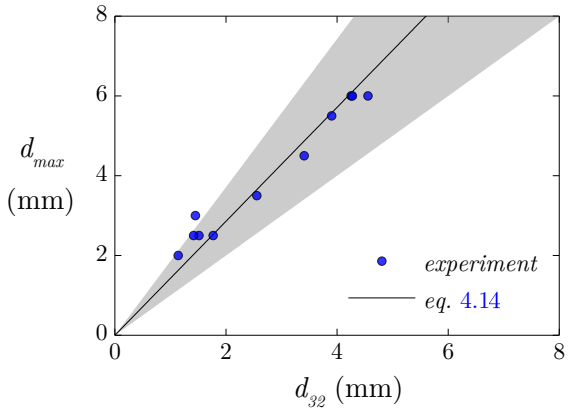

Figure 4.18: Experimental values of the Sauter mean d_{32} and maximum diameters d_{max} recorded in the experiments with the DCP. Eq. 4.14 is plotted with 70% of confidence intervals.

For the current experiments the maximum diameters d_{max} have been computed according to Angeli and Hewitt (2000b), where the 95$^{\text{th}}$ percentile of the overall distribution is considered for the maximum diameter, i.e. $d_{max} \equiv d_{95}$. It should also be mentioned that the drop sizes shown are based on the chord length measurements of the DCP. While the d_{max} will practically stay unaffected, an increase in the d_{32} values is expected when considering drop sizes from chord lengths (Hu et al. 2006). Figure 4.18 illustrates that the same proportionality holds for the current system. The slope of the curve is fitted with $k_d = 1.43$. The uncertainties for both the d_{max} and d_{32} are estimated at 30% along the whole range of drop size. To illustrate the deviation of the experiments from eq. 4.18 a 70 % confidence interval is plotted and shown by the grey area in Fig. 4.18.

A thorough empirical approach has been established in the literature to predict the maximum drop size that can survive breakup from the local shear gradients. For laminar flow condition eq. 2.40 predicts maximum drop sizes of $2D$ for the higher mixture velocity, which are significantly over the experiments. Breakup can also happen due to the turbulent eddies as discussed in Sec. 2.3.2. From Table 4.1 shown earlier, the Re_m based on the mixture properties do not seem to reach turbulent conditions as $Re_m < 2300$ for most cases considered. However, the Re_c based on the continuous phase properties are of the order of $\mathcal{O}\{10^4\}$, which indicate turbulent flow conditions. An effort to use the empirical models of Sec. 2.3.2 follows.

The maximum drop sizes recorded in the current experiments are for dense dispersions (with concentrations $\varphi_o > 0.10$) and range in sizes below and above the turbulent fluctuating length scale of $0.1D$. For these reasons, eqs. 2.42 and 2.44 need to be respectively considered. Both these equations are plotted in Fig. 4.19(a) and (b) together with the experimental data of the respective maximum diameters d_{max}. While the trend seems to be captured, the coefficients are computed as $C_H = \mathcal{O}\{10\}$ and $C_K = \mathcal{O}\{10^{-2}\}$, which indicates that both models are unable to predict the experiments well as they are far from the order of unity that Brauner and Ullmann

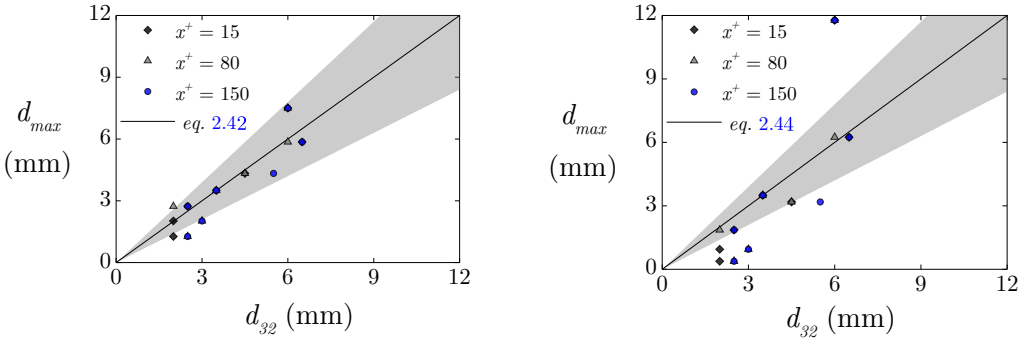

(a) $u_m = 1.04\ \mathrm{m\,s^{-1}}$ and $\varphi_o = 0.30$ (b) $u_m = 1.04\ \mathrm{m\,s^{-1}}$ and $\varphi_o = 0.30$

Figure 4.19: Experimental d_{max} values compared against (a) eq. 2.42 and (b) eq. 2.44. The equations are plotted with 70% of confidence intervals.

(2002) discuss. This can be attributed to the suppressed turbulent levels due to the presence of the dispersed phase, which increases the local viscosity values and does not allow breakup to take place. It is also possible that the intense coalescence between the drops affects the results, together with the development length of the flow that needs to be considered. As small drops are generated from the nozzles, t_{res} might not be enough to reach the d_{max} predicted from the correlations.

It is clear from the discussion of the previous paragraphs that any development effects need to be considered. Figure 4.20 depicts the experimental d_{32} obtained along the normalised streamwise length x^+ for the two mixture velocities for the whole range of input oil fractions tested. The contour lines are plotted every 0.125 mm. The higher mixture velocity exhibits smaller drop sizes compared to the lower

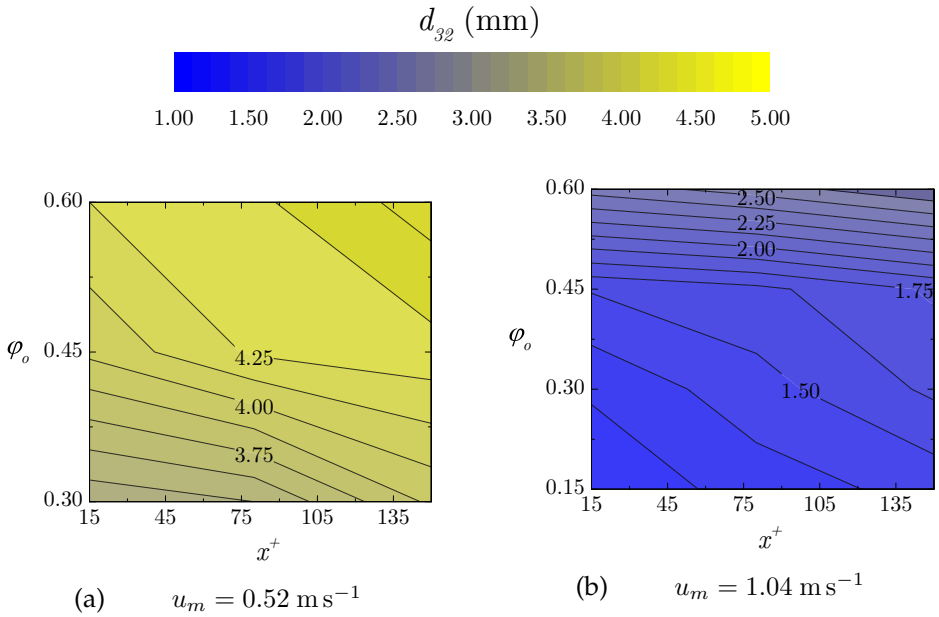

(a) $u_m = 0.52\ \mathrm{m\,s^{-1}}$ (b) $u_m = 1.04\ \mathrm{m\,s^{-1}}$

Figure 4.20: Contour plots of Satuer mean d_{32} measured from the DCP as the flow develops along x^+ for the conditions investigated. Contour lines are plotted every 0.125 mm

mixture velocity as discussed previously and it is now clearly illustrated in Fig. 4.20(b). The Sauter mean diameter increases along the pipe and with the input oil fraction φ_o. This behaviour takes place even for the $u_m = 0.52\ \mathrm{m\,s^{-1}}$ cases, where a continuous oil layer of drops forms at the top of the pipe as was shown in Fig. 4.11(b). Comparing Fig. 4.20 to Table 4.2, a similar trend of the Sauter mean diameters can be observed for the mean values of the distributions.

4.5 Pipe separator

Apart from the detailed characterisation of the dispersed flows conducted in the horizontal test section of the pilot-scale facility, another important objective of this work is to predict the separation properties of these dispersions, as discussed in Chapter 1. The test section can act as a horizontal pipe separator (Pérez 2005) and the phenomenological model described in Secs. 2.2.3 and 2.3.1.1 can be used to predict the layer development and the drop coalescence rates. More specifically, the evolution of the normalised height of the water continuous layer y_w^+, the dense-packed layer y_p^+ and the oil continuous layer y_o^+ are computed together with the Sauter mean diameter d_{32} present at the dense-packed layer of the dispersion.

The main assumption of the model lies in the fact that the velocity field inside the pipe is neglected. As the velocities at the dilute layer can reach high values (and possibly turbulent conditions), the floatation of the drops could be affected. For this reason, a coefficient of the order of unity is introduced in the floatation dynamics eq. 2.27, to take into account such effects. This value is set ad-hoc and is the same for all the experiments of this study. Considering that the velocities at the dense-packed layer will be very small due to the high drop concentration, it is safe to assume that the coalescence rates are not affected by the flow field and can be assumed similar to batch settlers.

Furthermore, monodisperse drop populations are considered. This can have a significant effect on the floatation, as the drops will float at different rates. Nevertheless, the Sauter mean diameter has been shown to well capture the mean floatation (Pilhofer and Mewes 1979). It is also important to assume clear interfaces with no particles or surfactants present to be able to apply the asymmetrical film drainage model of Henschke et al. (2002) described in Sec. 2.3.1.1. The coalescence parameter is set at $r_V^+ = 0.007$ according to the horizontal pipe separation predictions by Pereyra et al. (2013). In the dilute layer of the dispersion, no coalescence takes place, while the phase fraction is assumed to be the same as the input φ_o. Archimedes numbers are computed $Ar = \mathcal{O}\{10\} > 1$ and the input oil fractions are in the range of validity suggested by Henschke et al. (2002).

Six conditions are presented in Fig. 4.21 to illustrate the effect of the input oil fraction and of the mixture velocity of the dispersion. The initial conditions are given for the measurements at $x^+ = 15$. A description of the phenomena predicted for the low mixture velocity $u_m = 0.52\ \mathrm{m\,s^{-1}}$ follows. The drops start floating at the

top of the pipe and the water continuous layer y_w^+ increases with a constant slope as predicted by eq. 2.27. Similar dynamics are observed among the different input oil fractions φ_o, with a lower initial water layer height computed as the φ_o increases. The dense-packed layer height y_p^+ decreases until it meets the water continuous layer at $\tilde{x}$. Floatation has stopped at this axial location and all the drops are located in the dense-packed layer. Coalescence between two drops and between drops and the interface cause an increase of the mean drop size and a decrease in the height of the oil continuous layer y_o^+ (or simply increase in its thickness h_o). As the initial drop sizes are relatively large due to the generation method of the dispersions, the dynamics of y_o^+ are developing quasi-linearly.

While only three measurements are conducted along the axial length of the pilot-scale flow loop (due to space limitations of the lab), the model is able to predict the evolution of the characteristic layers of the dispersions as they flow along the pipe. Interestingly, the drop size evolution is also captured well with $r_V^+ = 0.007$, which was fitted for a system with similar properties by Pereyra et al. (2013). Despite the high uncertainty bars of the experiments with $\sim 20\%$ for the layer heights and $\sim 30\%$ for the drop sizes, the mechanisms are captured to an adequate degree by the phenomenological model.

For the higher mixture velocity $u_m = 1.04\ \mathrm{m\,s^{-1}}$ slightly different trends are observed. The drop sizes generated are smaller for these conditions and thus the floatation takes place over longer axial distance x^+. The dense-packed layer height y_p^+ decreases as its thickness h_p increases when increasing the input oil fraction φ_o. The coalescence of the drops with the pure oil layer at the dense-packed layer seems to take place faster than the floatation, so the dense-packed layer follows practically the same trend as the pure oil layer. The oil layer evolution is no longer linear and its slope decreases with x^+. Disagreement between the experiments and predictions is found for low axial lengths, as in the experiments no continuous layer is measured until $x^+ \sim 150$ for the higher mixture velocity and the range of input dispersed phase fractions tested. The model, however, predicts that drop-interface coalescence will take place from the first time-step. In reality, drops colliding at the walls together with lift forces pushing the drops at the opposite direction of gravity close to the top wall can hinder the generation of the pure oil layer, especially if the turbulent dispersive forces are also considered.

The total separation x_{sep} in solid-liquid suspension flows can be predicted according to Nott and Brady (1994) as

$$x_{sep} \sim \frac{3}{32\,\mathrm{d}(\varphi_d)} \frac{D}{2} \left(\frac{D}{d}\right)^2, \tag{4.15}$$

where $\mathrm{d}(\varphi_d)$ is a non-dimensional diffusion coefficient and can be set as $3/32\mathrm{d}(\varphi_d) \approx \mathcal{O}\{1\}$. Norman et al. (2005) simply used the hindered settling of eqs. 2.12 and 2.13

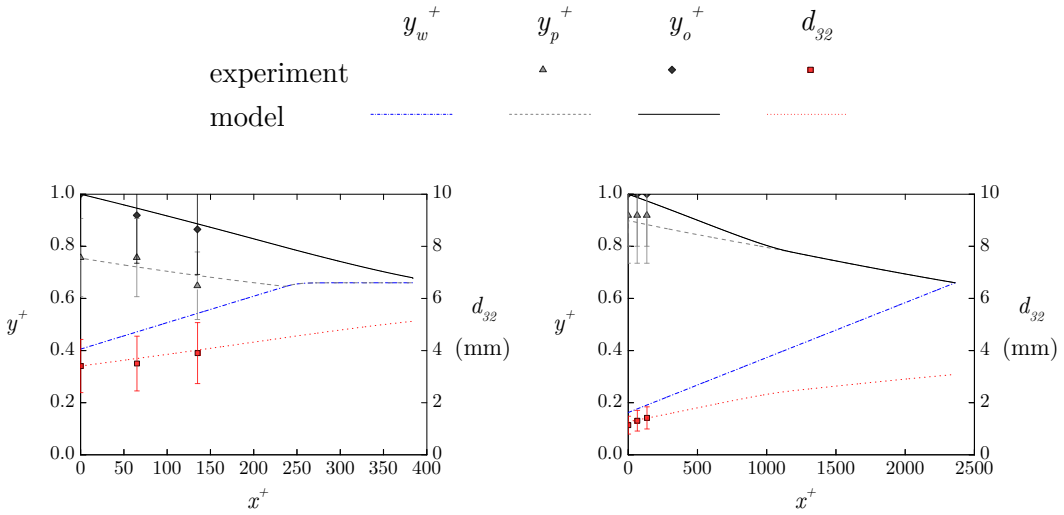

(a) $u_m = 0.52\,\mathrm{m\,s^{-1}}$, $\varphi_o = 0.30$

(b) $u_m = 1.04\,\mathrm{m\,s^{-1}}$, $\varphi_o = 0.30$

(c) $u_m = 0.52\,\mathrm{m\,s^{-1}}$, $\varphi_o = 0.45$

(d) $u_m = 1.04\,\mathrm{m\,s^{-1}}$, $\varphi_o = 0.45$

(e) $u_m = 0.52\,\mathrm{m\,s^{-1}}$, $\varphi_o = 0.60$

(f) $u_m = 1.04\,\mathrm{m\,s^{-1}}$, $\varphi_o = 0.60$

Figure 4.21: Prediction of the evolution of the characteristic layers of the dispersed flows and of the Sauter mean diameter in the horizontal test section of the pilot-scale flow loop facility.

giving

$$x_{sep} \sim \frac{D u_m}{v_t f_h(\varepsilon_d)},$$

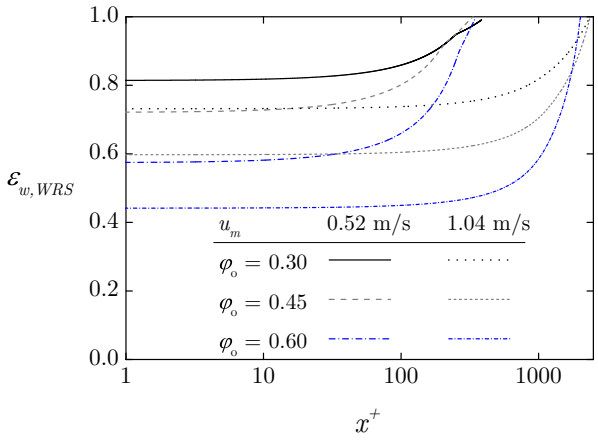

Figure 4.22: The in-situ water volume fraction in the water-reach stream over the normalised axial distance as computed by eq. 4.17 for six conditions conducted at the pilot-scale flow loop.

which can be written based on the Bu number as

$$x_{sep} \sim \frac{D}{2d^2 Bu} \frac{1}{f_h(\varepsilon_d)}. \tag{4.16}$$

However, this relation gives more accurate results when gravity is the main dominant force with $Bu \gg 1$, which is not true for the dispersed flows of the present experiments. Also, eqs. 4.15 and 4.16 are developed for suspensions and do not consider change in the drop size as the mixture flows along the pipe due to coalescence.

The phenomenological separation model can be employed instead to find the separation length. The total separation of the two phases in the oil-water system can be computed as the location x^+_{sep}, where the pure water layer y^+_w meets the pure oil layer y^+_o. A complete separation of the phases usually requires an impractically long length in liquid-liquid systems. Shorter lengths of horizontal pipe separators can be used to achieve water knockout from the pipe. Pereyra et al. (2013) proposed accordingly a different criterion, considering the length required for achieving a desired water fraction in the water-reach stream (x_{WRS}) as

$$\varepsilon_{w,WRS} = \frac{A_w + (Q_{w,WRS}/Q_m A - A_w)(1 - \varphi_o)}{Q_{w,WRS}/Q_m A}, \tag{4.17}$$

where $\varepsilon_{w,WRS}$ is the volumetric fraction of water present in the water-reach stream, $Q_{w,WRS}/Q_m$ is the fraction of the mixture flowing in the water-rich stream, which can be written as $Q_{w,WRS} = u_m (A - A_o - A_p)$ and $Q_m = Q_o + Q_w = u_m A$. In Fig. 4.22, $\varepsilon_{w,WRS}$ is plotted against the normalised axial development length for the conditions investigated in the pilot-scale flow loop. As previously discussed, the separation length for the higher mixture velocity is significantly higher. The length chosen for a separator can be determined based on the in-situ water fraction. When $\varepsilon_{w,WRS}$ reaches a desired water concentration, e.g. $\varepsilon_{w,WRS} \sim 0.96$ (Pereyra

Table 4.3: Separation lengths predicted from the phenomenological model and simple theorems of suspension flows.

u_m		model x^+_{WRS}	model x^+_{sep}	eq. 4.15 x^+_{sep}	eq. 4.16 x^+_{sep}
$0.52\ \mathrm{m\,s^{-1}}$	$\varphi_o = 0.30$	6.8	14.2	1.5	1.5
	$\varphi_o = 0.45$	6.2	12.4	1.1	2.7
	$\varphi_o = 0.60$	8.7	12.9	1.0	8.2
$1.04\ \mathrm{m\,s^{-1}}$	$\varphi_o = 0.30$	77.7	87.4	11.1	22.0
	$\varphi_o = 0.45$	82.5	87.7	7.8	37.9
	$\varphi_o = 0.60$	72.1	74.7	3.0	50.1

et al. 2013), x^+_{WRS} will be much smaller than x^+_{sep} (as shown in Fig. 4.22), which can optimise the spacing needs in the design of separation facilities.

Table 4.3 summarises the separation lengths predicted by eqs. 4.15 (Nott and Brady 1994) and 4.16 (Norman et al. 2005) for suspension flows together with the predictions of the phenomenological model by Pereyra et al. (2013), based on the final separation length where the oil and water curves meet x_{sep} and the axial length x_{WRS} where $\varepsilon_{w,WRS} = 0.96$ (according to eq. 4.17). It is clear that both eqs. 4.15 and 4.16 are significantly underpredicting the separation length. This is because the Bu numbers are of the order of 1 and because the interfacial phenomena are neglected. The drops reaching the top of the pipe will need finite time to coalesce and full separation to take place as predicted by the film drainage time between a drop and an interface in the model as τ_I. Also the equation of Pilhofer and Mewes (1979) used in the phenomenological model is adjusted with a coefficient to better capture the inertial effects that can hinder the floatation velocities of the drops and better reflect the conditions investigated.

In this Chapter, the drop size distributions and the separation properties of the liquid-liquid dispersed pipe flows generated from a multi-nozzle inlet were investigated with high-speed imaging, an ERT system and a DCP able to measure local volume fractions and drop chord lengths. Higher size drops were measured in the direction of buoyancy. The distributions became flatter along the axial flow direction due to drop-drop coalescence. The maximum drop sizes recorded along the pipe revealed that breakup did not take place. A one-dimensional phenomenological model transformed from batch settlers is used to capture the main mechanisms that take place during the oil-water separation in pipe flow. While good agreement is found for the range of conditions investigated, it is important to test it against other oil-water systems to explore how the asymmetrical film drainage parameter r_V affects these predictions. It is also clear that the velocities at the floatation water

continuous layer are very high and inertial effects cannot be neglected and only accounted for with a simple coefficient. Finally, the model assumes an average mean size, which does not consider the different floatation velocities and coalescence times that would take place in a population of drops. The next Chapter focuses on the first step of the separation and specifically discusses the drop motion dynamics and how the velocity profile changes inside the pipe as the drop segregate along the flow direction.

Chapter 5

Flow Characteristics

Further investigation of the evolving dispersed flows has been carried out in the matched refractive index flow loop. The technical details of the flow loop and the liquids were given in Sec. 3.1.2. As the refractive index of both phases is matched, higher detail can be obtained on the phenomena taking place in the middle plane of the pipe cross-section, as high-speed PLIF and PIV/PTV measurements allow the acquisition of the in-situ local phase fractions and drop sizes alongside the velocity fields of both phases at two axial locations $x^+ = 15$ and 135 downstream the mixer. A thorough discussion on the details of the aforementioned techniques and their uncertainties was provided in Secs. 3.2.2.2 for the PLIF and Sec. 3.2.2.3 for the PIV measurements respectively. The goal of this Chapter is to explore the flow characteristics of the dispersions and how they are affected by the segregation taking place downstream the inlet. A CFD model is developed and solved numerically using the finite element method (FEM) to compare with the experimental findings of the drop concentration and velocity inside the pipe, and fuel the discussion on the significance of the physical mechanisms.

The dispersions are generated in this facility from a static mixer placed after a Y-shaped inlet where the two liquids meet. Due to the mixing taking place, there is less control on the flow patterns developing and the drop size distributions produced. Over forty conditions are investigated for a wide range of flow rates and input phase fractions. The mixture velocities u_m used in the current experiments are relatively low in the range of 0.1 to 1 $\mathrm{m\,s^{-1}}$ and combined with the high viscosity of both phases (Table 3.2), result in Reynolds numbers based on the mixture properties Re_m ranging from about a hundred to a few thousand. The mixture properties are used as described in Sec. 2.2.2 together with eqs. 2.17 and 2.18 to compute the density and viscosity of the mixture correspondingly. For the present experiments, it was found that the maximum in-situ phase fraction can reach values up to $\varepsilon_{max} = 0.74$ before phase inversion takes place and a flow pattern transition occurs as shown in Sec. 2.1.1.3.

5.1 Generation of dispersions

5.1.1 Flow downstream the mixer

As discussed in Sec. 3.1.2 the dispersions are generated through a helical static mixer of six elements as shown in Fig. 3.3. Despite the low Reynolds numbers of the conditions investigated, the mixer can disturb the local velocity field at the initial length of the test section. The single phase vertical profiles of the time-averaged streamwise velocity $\langle u \rangle$ of the water gave good agreement between the two axial measuring locations $x^+ = 15$ and $x^+ = 135$. The Reynolds numbers tested, covered the laminar regime, with small deviations from the parabolic profile $u/u_{max} = 1 - 4(y^+ - 0.5)^2$ recorded only at the initial measuring location and for the higher Reynolds numbers $Re > 1000$. The vertical direction y^+ is normalised with the pipe diameter D with $y^+ = 0$ denoting the bottom of the pipe. The development length for the Reynolds numbers investigated in the present experiments is of the order of $\mathcal{O}\{10\}D$ and thus some development effects are expected at the initial measuring axial location at $x^+ = 15$.

The fluctuations of both velocity components are computed from the PIV measurements, to investigate closer the effects of the mixer on the flow. The vertical profiles of the product of the time-averaged fluctuations $\langle u'v' \rangle$, which can be directly related to the Reynolds stress $\rho_c \langle u'v' \rangle$, are plotted in Fig. 5.1. They are also measured for single-phase flow of water and at the same two axial measuring locations $x^+ = 15$ and 135. At $Re = 250$ in Fig. 5.1(a) the fluctuations are insignificant at both axial locations, suggesting laminar flow. However, the fluctuations at $x^+ = 15$ for $Re = 1205$ become stronger but remain practically 0 at $x^+ = 135$ (Fig. 5.1(b)). This behaviour shows that the mixer slightly affects the flow at the initial measuring location, but its effect is not propagated downstream. At the highest Reynolds number tested, Re $= 2451$ in Fig. 5.1(c), similar fluctuations are measured at both axial locations, typical of fully developed turbulent flow.

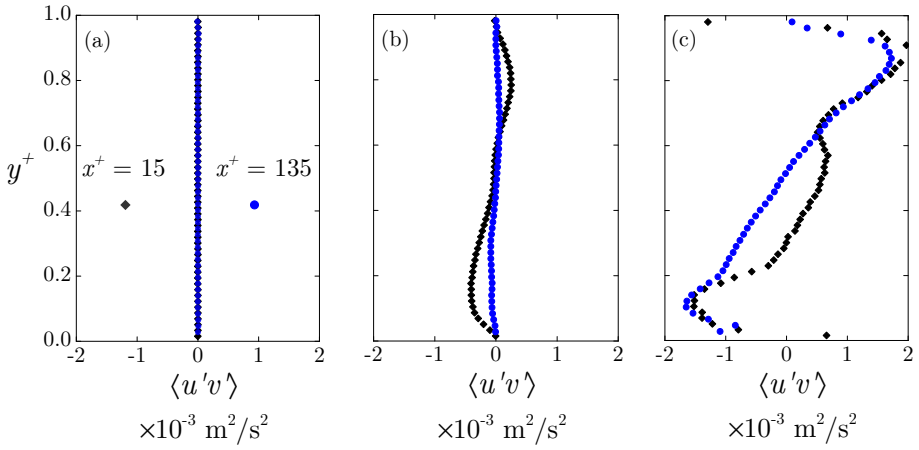

Figure 5.1: Vertical profiles of the normalised time-averaged fluctuations at the two axial measuring locations for (a) $Re = 250$, (b) $Re = 1205$ and (c) $Re = 2451$.

5.1.2 Drop size spectra

Generation of dispersed flows in static mixers has been investigated thoroughly in the past (Theron and Le Sauze 2011) and also discussed in the recent review by Ghanem et al. (2014). The interest in this work lies in helical static mixers, where the mixing elements direct each phase radially towards the pipe walls and back to the center. A uniform turbulent shear field is generated in the mixer that quickly disperses the immiscible liquids and produces a narrow drop size distribution. Characterising the drop size distributions is the focus of this Section.

For helical static mixers, Middleman (1974) first developed a correlation for turbulent conditions to predict the Sauter mean diameter based on the Weber number $We = \rho_c u_m^2 D/\sigma$ and the friction factor as

$$d_{32} \propto DWe^{-0.6} f^{-0.4}, \tag{5.1}$$

which is equivalent to eq. 2.41. Based on the approximation by Bird et al. (1960) that $f \sim Re^{-1/4}$ for $Re > 3000$, Middleman (1974) wrote eq. 5.1 as $d_{32} \propto We^{-3/5} Re^{1/10}$. A few years later, Chen and Libby (1978) correlated their experimental data by taking into account the viscosity ratio $m = \eta_c/\eta_d$ writing that

$$d_{32} = 1.14 DWe^{-0.75} m^{-0.18}. \tag{5.2}$$

In accordance with previous efforts, Berkman and Calabrese (1988) developed the following correlation

$$d_{32} = 0.49 DWe^{-0.6} \left(1 + 1.38 \mathrm{Vi} \left(\frac{d_{32}}{D}\right)^{0.33}\right)^{0.6}, \tag{5.3}$$

where Vi is a viscosity group computed as $\mathrm{Vi} = (\eta_d u_m/\sigma)\,(\rho_c/\rho_d)^{1/2}$. More recent work has been developed for different types of mixers, which are not suitable to this work as the dispersions in this work are generated through a helical design very similar to a Kenics mixer.

The Sauter mean diameters computed in the present work at the initial axial measuring location downstream the helical static mixer, $x^+ = 15$, are shown in Fig. 5.2. Detailed information on the drop size measurements from the PLIF images is provided in Sec. 3.2.2.2. Equation 5.1 seems to well predict the Sauter mean diameters measured in the pipe. A coefficient of determination $\mathcal{R}^2 = 0.982$ is computed based on a fitting of the proportionality constant with the LAR method. The drops with $d_{32} > 4$ mm or $u_m < 0.30\ \mathrm{m\,s^{-1}}$ were not considered in the fitting. At low velocities, coalescence is expected to be strongly dominant and already have taken place between $x^+ = 0$ and 15.

Eqs. 5.2 and 5.3 do not seem to match the results well. They seem to significantly underpredict the drop sizes in the pipe. As mentioned, coalescence is dominant in this system and can have an effect on the drop sizes measured. By assuming a

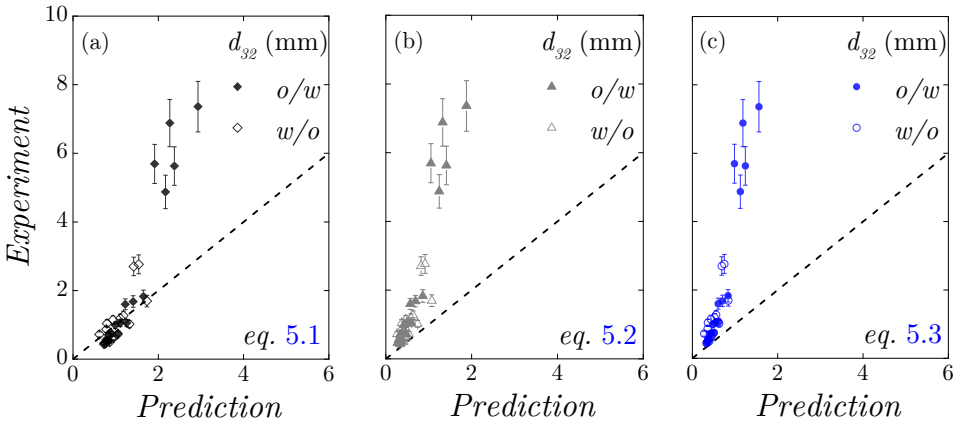

Figure 5.2: Comparison of the experimental Sauter mean diameters recorded at $x^+ = 15$ with three different literature correlations (a) eq. 5.1, (b) eq. 5.2 and (c) eq. 5.3.

proportionality constant of ~ 2 for both eqs. 5.2 and 5.3, the data collapse very well with the predictions with $\mathcal{R}^2 > 0.95$.

Dense dispersions are considered in the current work with $\varphi_d > 0.10$. The rate of surface energy production of the dispersed phase due to coalescence is proportional to the rate of turbulent energy supply by the continuous phase. Eq. 5.1 was adjusted by Brauner (2001) with the ratio of the dispersed and continuous phase fractions $(\varphi_d/(1-\varphi_d))^{3/5}$, finally giving

$$d_{32}^{+} \propto \mathrm{We}^{-3/5} f^{-2/5} \left(\frac{\rho_m}{\rho_c(1-\varphi_d)}\right)^{-2/5} \left(\frac{\varphi_d}{1-\varphi_d}\right)^{3/5}, \tag{5.4}$$

for $d_{32}^{+} = d_{32}/D$. Fig. 5.3 shows good agreement between the experiments and predictions.

Notably, the aforementioned correlations are developed based on the Sauter mean diameter and not the maximum diameter, while the theory of Sec. 2.3.2 handling the breakup in a pipe turbulent field is developed based on the d_{max}. It is true that a

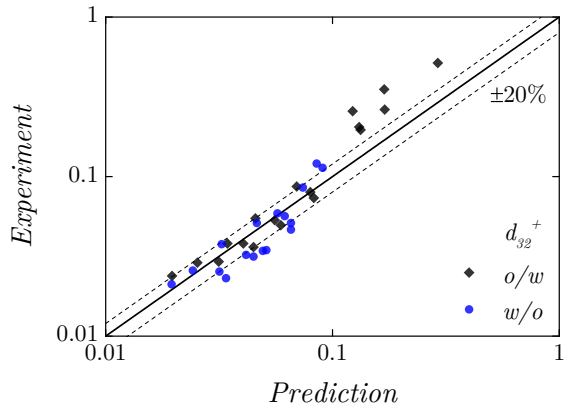

Figure 5.3: Comparison of the experimental Sauter mean diameters recorded at $x^+ = 15$ with the predictions of eq. 5.4.

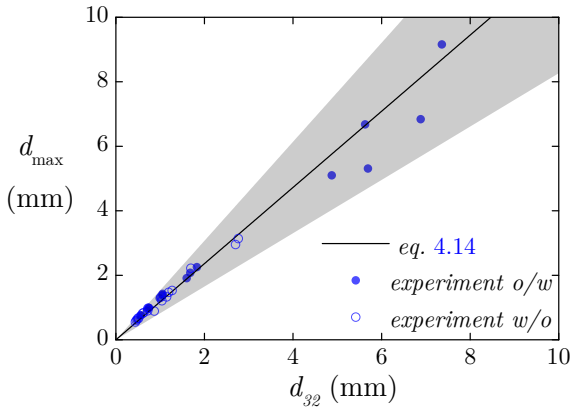

Figure 5.4: Experimental values of the Sauter mean d_{32} and maximum diameters d_{max} recorded in the experiments from the PLIF. Eq. 4.14 is plotted with 70% of confidence intervals.

proportionality between the d_{32} and the d_{max} has been found in both pipe flow (as discussed for Fig. 4.18) and static mixers (Berkman and Calabrese 1988; Lemenand et al. 2003; Yamamoto et al. 2007) allowing the extension of the theory for the d_{32}.

To test this argument for the current experiments, the Sauter mean diameters (chord lengths) recorded at $x^+ = 15$ are plotted against the maximum diameters $d_{max} \equiv d_{95}$ (as defined in Chapter 4) in Fig. 5.4. Equation 4.14 provides the slope of this curve, which for the current experiments is $k_d \approx 1.18$ with $\mathcal{R}^2 = 0.974$. The 70% confidence intervals are also plotted for k_d. The experiments collapse very well to eq. 4.14 illustrating the close link between the maximum and Sauter mean diameter. Interestingly, the slope k_d is found lower than expected from the range reported by Schümann et al. (2015). The lower value can mostly be attributed to strong coalescence dynamics that increase the Sauter mean diameters already at $x^+ = 15$.

5.2 Phenomenological Characteristics

5.2.1 Flow structure development

The two immiscible liquids enter the static mixer in a stratified manner, with the lighter oil at the top and the heavier water at the bottom of the pipe. In all cases studied, dispersions have formed at the exit of the mixer, which tend to segregate further downstream. Figure 5.5 illustrates typical high-speed PLIF images obtained for reppresentative flow conditions at two axial locations, namely at $x^+ = 15$ and 135. Figures 5.5(a)-(c) present cases of oil in water dispersions *o/w*, while Figs. 5.5(d)-(f) present cases of water in oil dispersions *w/o*. The water contains the fluorescent dye and the PIV tracer particles, and appears white in the images, while the oil appears black.

For the water continuous cases (Figs. 5.5(a)-(c)), the dispersions at the outlet of the mixer at $x^+ = 15$, appear uniformly spread in the pipe. As the dispersions

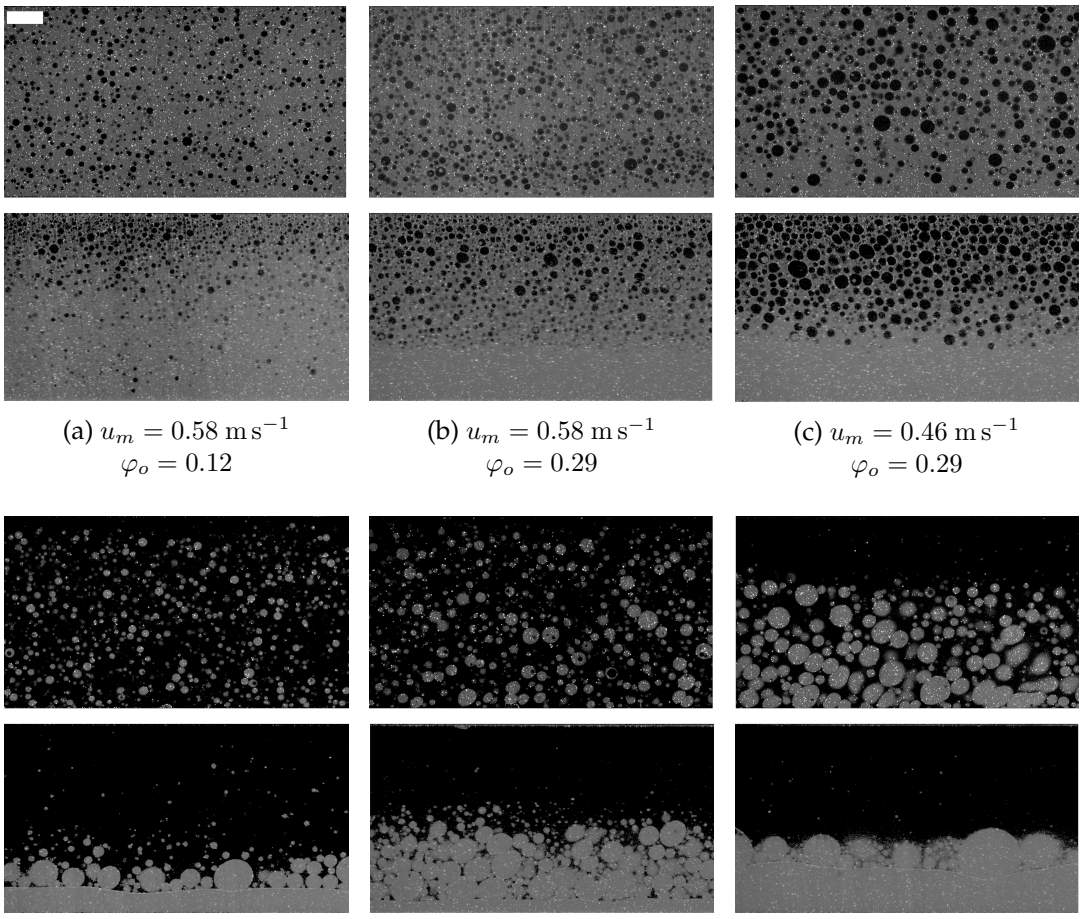

(a) $u_m = 0.58\ \mathrm{m\,s^{-1}}$ $\varphi_o = 0.12$ (b) $u_m = 0.58\ \mathrm{m\,s^{-1}}$ $\varphi_o = 0.29$ (c) $u_m = 0.46\ \mathrm{m\,s^{-1}}$ $\varphi_o = 0.29$

(d) $u_m = 0.58\ \mathrm{m\,s^{-1}}$ $\varphi_o = 0.88$ (e) $u_m = 0.58\ \mathrm{m\,s^{-1}}$ $\varphi_o = 0.71$ (f) $u_m = 0.40\ \mathrm{m\,s^{-1}}$ $\varphi_o = 0.71$

Figure 5.5: PLIF images acquired for a few typical flow conditions investigated downstream the static mixer at $x^+ = 15$ (top) and $x^+ = 135$ (bottom). The scale bar is $5\ \mathrm{mm}$ long.

evolve, the oil drops start to segregate, and a clear aqueous phase layer appears at the bottom of the pipe. This is less pronounced in the case of $u_m = 0.58\ \mathrm{m\,s^{-1}}$ and $\varphi_o = 0.12$, where the initial population contains some very small drops which settle very slowly and are still present close to the bottom of the pipe at $x^+ = 135$. Drop re-entrainment might also be taking place, affecting the smaller drops in this spatial configuration (Conan et al. 2007). Apart from the stratification of the oil fraction, a stratification of drop size also occurs with distance, with larger drops located near the upper part of the pipe.

Quite different dynamics are observed for the oil continuous *w/o* cases of Figs. 5.5(d)-(f), obtained for the same mixture velocities and dispersed phase volume fractions. In the oil continuous dispersions, larger drops are generated by the mixer, compared to the water continuous dispersions – as also predicted by eq. 5.1. For the lower mixture velocity case (Fig. 5.5(f) top) the drops have already started to segregate at $x^+ = 15$, and a clear oil layer is visible at the top of the pipe. In all cases, at the downstream location $x^+ = 135$, a clear water layer has developed at the bottom

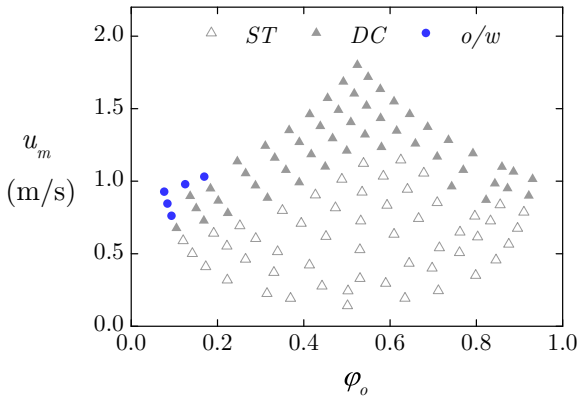

Figure 5.6: Flow pattern map for the Y-shaped inlet (without the static mixer) for a range of input oil fractions φ_o and mixture velocities u_m.

of the pipe. This suggests that the segregated drops coalesce to form the continuous layer.

Similarly to Sec. 4.2.1, categorising the observed flow patterns from the images, can illustrate the transition boundaries between them and how they shift with axial length. A wider range of flow patterns is recorded with the static mixer in the current experiments than was observed in Fig. 4.5 with the multi-nozzle inlet, as there is now less control on the continuous and dispersed phase of the dispersion. As discussed in Sec. 2.1.1.3, phase inversion can take place in static mixers at very low values of $\varphi_o \sim 0.5$ according to Tidhar et al. (1986).

To study the effect of the static mixer, the flow pattern map at $x^+ = 135$ is first plotted without it, for a range of mixture velocities u_m and input oil volume fractions φ_o in Fig. 5.6. The flow patterns recorded are obtained from just the Y-shaped inlet instead, by minimising any mixing at the inlet of the pipe. The characterisation was conducted based on observations from the PLIF images. As the measurements are planar and in the middle of the pipe, the distinction between the different patterns was relatively simple to conduct without any image analysis needed.

It is clear from Fig. 5.6, that even at relatively high mixture velocities of $1\ \mathrm{m\,s^{-1}}$, stratified (*ST*) conditions are observed for the majority of input oil fractions without the mixer. Dual-continuous (*DC*) patterns start developing when the input oil fraction is decreased, finally giving dispersed *o/w* dispersions for $\varphi_o < 0.2$. Interestingly, the heavier water (aqueous phase) disperses relatively harder in the lighter oil, as was also the case for the system of liquids of the pilot-scale flow loop and shown in Fig. 4.4. It seems that the viscosity ratio, which in the present experiments is about $\eta_w/\eta_o \approx 1.8$ compared to the $\eta_w/\eta_o \approx 0.2$ of the previous system, does not play a dominant role in the preferential dispersion. However, it must be noted that in the current experiments, the fluorescent dye and the tracer particles are introduced in the water phase and they can affect these dynamics as discussed by De Malmazet et al. (2015).

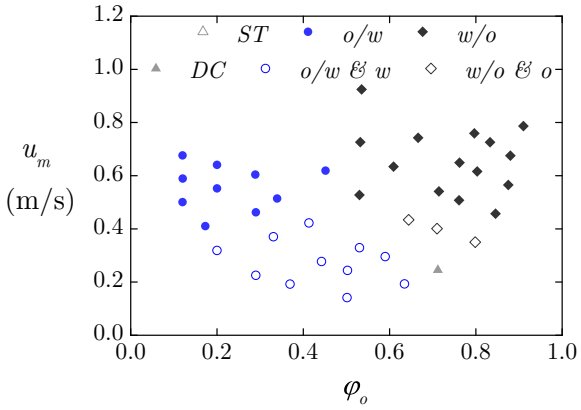

(a) $x^+ = 15$

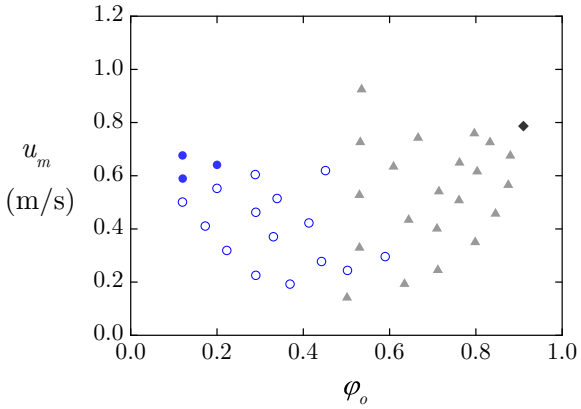

(b) $x^+ = 135$

Figure 5.7: Flow pattern maps at two axial locations downstream the static mixer obtained from PLIF images.

The different flow patterns obtained with the static mixer at the two axial measuring locations are illustrated in Figs. 5.7(a) and (b) for the two axial measuring locations respectively. Phase inversion takes place at $\varphi_d \sim 0.5$ – characteristic of static mixers. For both axial locations, all the patterns observed when the mixer is present are dispersed, while at the same conditions without the mixer the flow is stratified with no drops present. The patterns generated by the mixer are not stable and should separate downstream provided the test section is long enough

As can be seen from Fig. 5.7 at the initial axial location $x^+ = 15$, homogeneously dispersed flow (either oil or water continuous) can be achieved for $u_m \gtrsim 0.5\ \mathrm{m\,s^{-1}}$. At the same conditions further downstream at $x^+ = 135$ (Fig. 5.7(b)), the drops have segregated and a clear drop-free layer of the continuous phase forms. In the water continuous dispersions however, a layer of the initial dispersed phase has also formed and the pattern becomes dual continuous flow (DC).

5.2.2 Drop size evolution

The drop size (cord length) distributions of both the *o/w* and *w/o* dispersions and their change with axial location are discussed in this Section. In Fig. 5.8 the probability histograms $\mathrm{P}(d)$ are plotted for the flow conditions of Fig. 5.5 together with the corresponding PDFs computed from eq. 4.7 for both types of dispersions. A constant bin size is used for the histograms equal to 0.25 mm, which is found to describe accurately most of the conditions and illustrates in enough detail the characteristics of each distribution. The log-normal density distributions are found to represent well the majority of cases.

The distributions for the *o/w* dispersions in Fig. 5.8(a) are narrow with most of the drops smaller than 1 mm. As the input concentration of the drops in the pipe increases, so does their size along with the probability to find large drops. Nevertheless, the distributions remain relatively narrow. When the mixture velocity decreases the distribution becomes wider, with a significant decrease in the number of small drops. The energy in the mixer for lower mixture velocities is not enough to break up the drops.

For the *w/o* dispersions in Fig. 5.8(b), the trends are similar, but the distributions

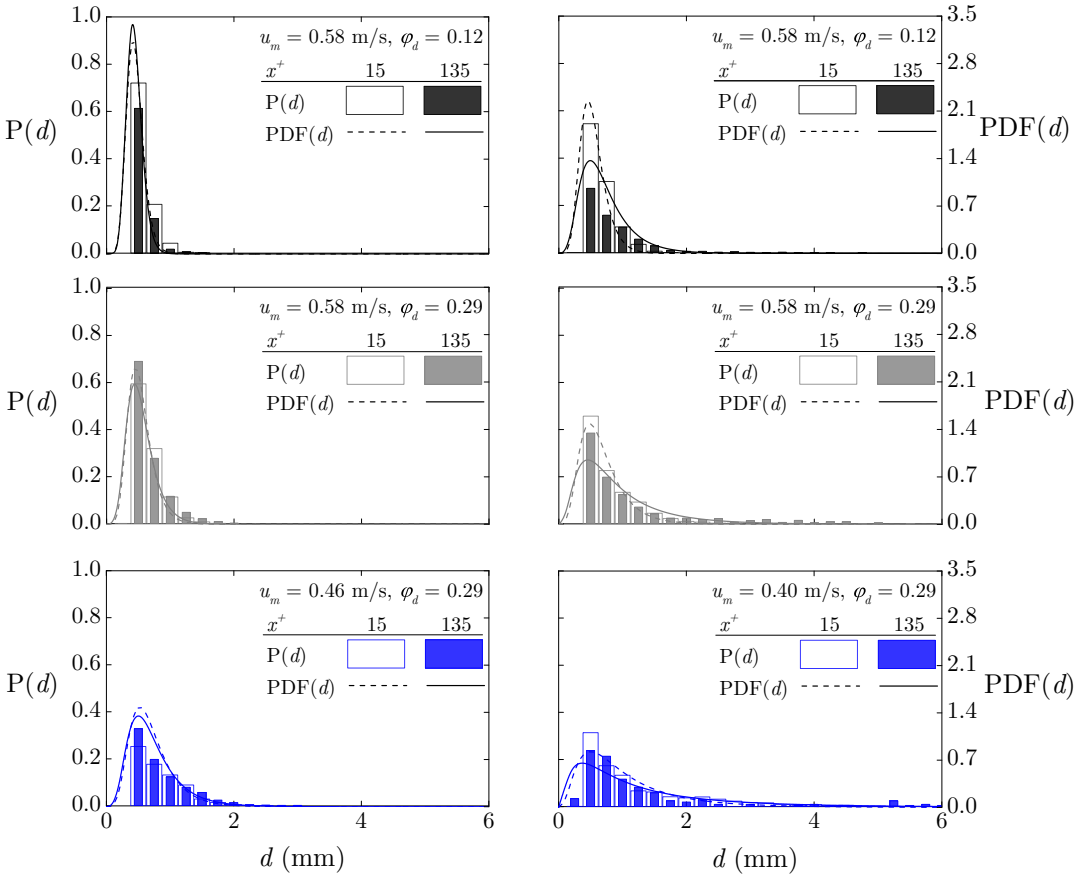

(a) *o/w* dispersions (b) *w/o* dispersions

Figure 5.8: Probability histograms and probability density functions for the flow conditions of Fig. 5.5 for both *o/w* (left) and *w/o* (right) dispersions.

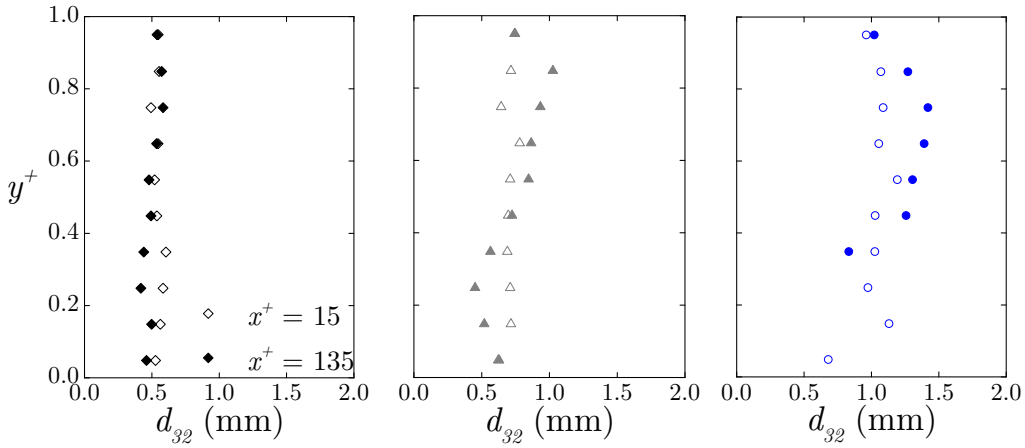

(a) *o/w* dispersions

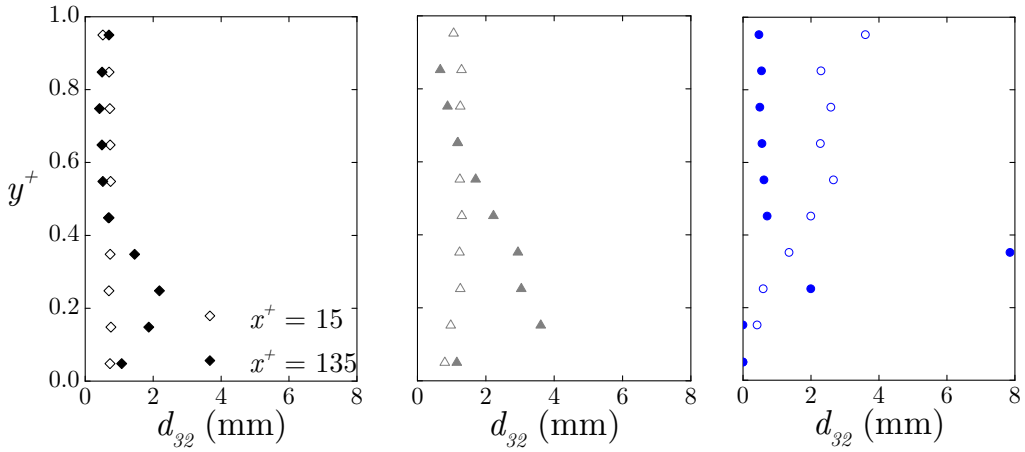

(b) *w/o* dispersions

Figure 5.9: Vertical profiles of the Sauter mean diameter for the flow conditions of Fig. 5.5 for both *o/w* and *w/o* dispersions, with $u_m = 0.58\ \mathrm{m\,s^{-1}}$ and $\varphi_d = 0.12$ (left), $u_m = 0.58\ \mathrm{m\,s^{-1}}$ and $\varphi_d = 0.29$ (middle) and $u_m = 0.46\ \mathrm{m\,s^{-1}}$ ($0.40\ \mathrm{m\,s^{-1}}$ for the *w/o* case) and $\varphi_d = 0.29$ (right). The open symbols are for $x^+ = 15$ and the solid for $x^+ = 135$

are in general wider than in the *o/w* dispersions. The difference in the distributions for the same flow conditions stems from the friction factor in the static mixer. For the oil continuous dispersed flows less frictional losses are expected, as the lower viscosity of the oil gives higher Reynolds numbers. From eq. 5.1 it is clear that less friction translates to higher drop sizes generated by the mixer for this type of dispersions, giving wider distributions that develop downstream.

In general, the drop size distributions for both the *o/w* and *w/o* dispersions become wider downstream the pipe indicating coalescence between drops. Together with the results of the previous Chapter, this behaviour is a strong affirmation for the phenomenological model that predicts a simultaneous increase in both the drop size and the thickness of the continuous layer formed from the dispersed phase.

The variations of the average Sauter mean drop diameters along the vertical directions for the same conditions are presented for both axial locations in Figs. 5.9(a)

and (b) for the *o/w* and *w/o* dispersions respectively. To calculate the averages, the vertical distance is split in 10 equal horizontal segments of $\Delta y^+ = 2.6$ mm, and the d_{32} for each segment is computed. The number of drops averaged in each segment is always $N_d > 200$.

For the *o/w* dispersions in Fig. 5.9(a), the drop size is almost uniform along the vertical direction at $x^+ = 15$. There is a change of the profile at $x^+ = 135$ – especially for the high volume fraction or low mixture velocity, which reflects the segregation of the drops seen in the PLIF images of Fig. 5.5. Interestingly, a slight dip of the drop size is recorded near the top in all cases, which is attributed to lift forces close to the pipe walls. Lift forces act stronger on the larger drops. From the equation of lift velocity (eq. 2.14), it can be written that $u_L \propto d^3$, which justifies the aforementioned argument. As discussed in Sec. 2.2.2, the lift coefficient is significantly higher closer to the pipe walls (Matas et al. 2009), leading to the resulting trend.

Figure 5.9(b) shows the *w/o* cases. The dispersions are relatively homogeneous at the initial axial location for the high mixture velocity. In the case of $u_m = 0.46$ $\mathrm{m\,s^{-1}}$ and $\varphi_d = 0.29$, the segregation of the drops has already occurred and the mean drop sizes are higher in the lower part of the pipe. A continuous layer of the aqueous phase forms further downstream. The drop size is found to increase close to the formed interface, and high gradients in the average drop size profiles occur, as also shown in the PLIF images of Fig. 5.5. The drop size in *DC* patterns has been investigated in detail by Lovick and Angeli (2004a), finding the same behaviour.

5.3 Flow field

The *o/w* dispersions are considered in more detail. For these mixtures, the oil remains the dispersed phase along the pipe and the results can be compared against the numerical simulations. In the simulations it is assumed that drops are monodispersed and their size does not change with axial location, i.e. no breakup or coalescence takes place. The experiments showed that the Sauter mean diameters for the *o/w* dispersions only varied by 200 µm between the two measurement locations, which is very close to the experimental uncertainty of ± 116 µm. With these sizes the drop Stokes number is well below unity for all conditions investigated, allowing the use of the mixture model in the numerical simulations. More details in regards to the discretisation method of the FEM, the geometry used and the initial and boundary conditions of the CFD model are given in Appendix B.

The hydrodynamic interactions at high dispersed phase volume fractions can also lead to shear-induced diffusion. The shear rate in Poiseuille flows varies across the pipe and thus the stress field is not homogeneous. Due to this reason, it has been established that neutrally buoyant suspended particles migrate towards the central region of the pipe and the local volume fraction becomes an increasing function of the distance from the wall (Yeo and Maxey 2011). For the present case, the dispersed phase also has a density difference with the continuous medium as $\rho_d/\rho_c \approx 0.80$. The

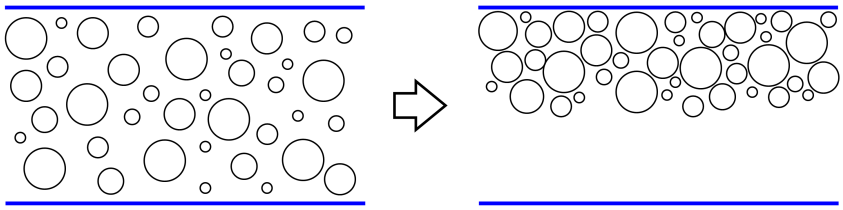

Figure 5.10: Schematic illustration of the *o/w* segregating dispersions along the pipe.

dynamics remain similar, but with the addition of the gravity force exerted on the dispersed phase, which produces a net migration towards the direction of buoyancy.

The flow conditions of *o/w* dispersions investigated both experimentally and numerically are presented in Table 5.1. The range of velocities varies from $u_m = 0.40$ $\mathrm{m\,s^{-1}}$ to 0.58 $\mathrm{m\,s^{-1}}$ and the input oil volume fractions varied from $\varphi_o = 0.12$ to 0.36. For these flow conditions, homogeneous *o/w* dispersions are formed at the inlet, while at $x^+ = 135$ segregation of the drops occurs giving *o/w & w* patterns as illustrated schematically in Fig. 5.10. PLIF images at the two axial locations for three typical cases of Table 5.1 were already illustrated in Figs. 5.5(a)-(c). The Reynolds number based on the mixture properties and velocity ranges from $Re_m = 500$ to 1462, while the Reynolds number based on the continuous phase properties and velocity, Re_c (with $u_c \simeq u_m$), is slightly higher, with values ranging from $Re_c = 1405$ to 2072. In both cases, the flows are lower than the transitional regime to turbulent conditions of ~ 2000 and thus turbulence can be ignored in the simulations.

Previous numerical studies have investigated the local flow dynamics and dispersed phase motion for segregating suspension flows (e.g. studies of Norman et al. (2005) and Yan and Koplik (2009)), but the literature in liquid-liquid systems is very limited. Ngan (2011) implemented a Eulerian-Eulerian approach to capture the dynamics of turbulent homogeneous dispersed flows in a horizontal pipe, where only comparisons of the in-situ dispersed phase fraction were made.

5.3.1 Development and characteristic scales

In the simulations it is assumed that the drops are uniformly distributed in the pipe. This assumption is supported by the experimental findings as shown in Fig. 5.9.

Table 5.1: Flow conditions investigated in detail and compared with the CFD simulations.

u_m ($\mathrm{m\,s^{-1}}$)	φ_o	d^+	$\mathrm{Re_m}$	Bu	$\mathcal{L}^+$
0.40	0.17	0.040	840	0.042	20.1
0.46	0.12	0.029	1157	0.045	38.8
0.46	0.29	0.045	610	0.018	38.1
0.53	0.24	0.028	881	0.030	81.4
0.53	0.36	0.039	500	0.014	86.1
0.58	0.12	0.021	1462	0.008	75.0
0.58	0.29	0.030	767	0.016	128.9

Shear-induced migration occurs due to inhomogeneities in the number of collisions the drops experience, due to shear and concentration gradients (Phillips et al. 1992) as explained in Sec. 2.2.2. This migration leads the drops from regions of high to low shear and high to low concentrations. The velocity for shear-induced migration scales as $\dot{\gamma}D$ and the time as $D^2/\left(\dot{\gamma}a^2\mathcal{D}\right)$ for a characteristic length scale of D, where $\dot{\gamma}$ is the shear rate, $\mathcal{D}$ is the diffusion coefficient and a is the drop radius. Fully developed flow is expected after a distance of $\mathcal{O}\{(D/a)^2\, D\}$ (Morris and Brady 1998), which in the current system is of the order of $\mathcal{O}\{10^2 D\}$ for drops with radii ranging from approximately $a = 270$ µm to 520 µm.

As the drops are susceptible to buoyancy forces, the segregation will be faster and the diffusion estimate can serve as the upper limit. It can be seen from the high-speed PLIF images that segregation has already taken place for the polydisperse experimental system at $x^+ = 135$ for most cases examined. The local in-situ oil fraction can be computed with less than 20% experimental error. The experimental time-averaged in-situ oil volume fractions across the pipe diameter D are computed as

$$\langle\bar{\varepsilon}_o\rangle = \frac{1}{D}\int_0^D \varepsilon_o(y)\mathrm{d}y. \tag{5.5}$$

To compare the results between the two-dimensional CFD simulations, the in-situ oil volume fraction of the simulations is normalised so that the flow is conserved and $\int_0^D \varepsilon_o u_c \mathrm{d}y$ is satisfied as described by Morris and Brady (1998). For the simulations, steady-state is considered with $\varepsilon_o = \langle\varepsilon_o\rangle$.

Inspired by suspension flows (Hampton et al. 1997; Semwogerere et al. 2007), an evolution parameter E_p for the oil volume fraction is introduced to quantify the development length, and is defined as

$$E_p\left(x\right) = \frac{1}{D}\int_0^D \left|\frac{\langle\varepsilon_o(x,y)\rangle}{\langle\bar{\varepsilon}_o(x,y)\rangle} - \frac{\langle\varepsilon_{o,0}(y)\rangle}{\langle\bar{\varepsilon}_{o,0}(y)\rangle}\right|\mathrm{d}y, \tag{5.6}$$

where $\varepsilon_{o,0}$ and $\bar{\varepsilon}_{o,0}$ are the initial local and spatially averaged across the pipe diameter D in-situ oil volume fractions. It follows that $\varphi_o \equiv \langle\bar{\varepsilon}_{o,0}\rangle$ and $E_p(x) = 0$ for a homogeneous dispersion along y.

The evolution parameter computed for the simulations for eight axial locations along the pipe is plotted for four conditions of Table 5.1 against the normalised axial distance in Fig. 5.11. The evolution parameter increases asymptotically and reaches a plateau. Hampton et al. (1997) fitted the rate of growth of E_p with x to an exponential function (continuous and dashed lines in the Figure) written as

$$E_p\left(x^+\right) = a_1\left[1 - \exp\left(a_2 x^{+0.8}\right)\right] + a_3, \tag{5.7}$$

where a_1, a_2 and a_3 are fitting parameters computed from the least-squares method

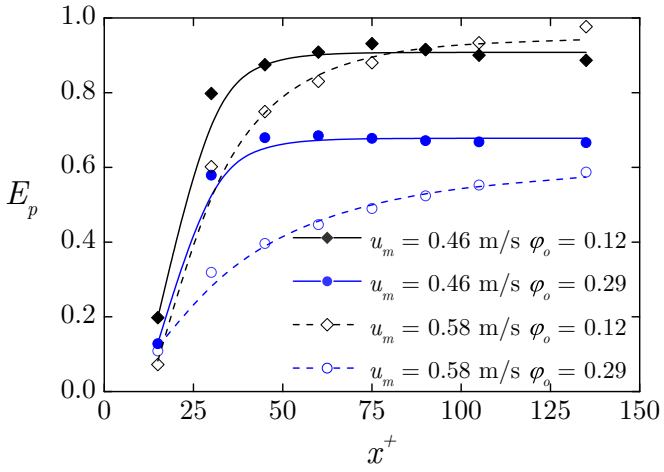

Figure 5.11: Evolution parameter computed from eq. 5.6 from the simulation results and fitted with eq. 5.7 for four typical flow *o/w* conditions.

with $a_2 < 0$. The coefficient a_3 should be equal to zero in order to denote the homogeneous profile in the beginning of the pipe, but takes small values instead to better describe the experimental data.

From the evolution parameter, the entrance length L, defined as the axial location where the evolution parameter reaches 95% of its asymptotic value $E_p^{\infty} = a_1 + a_3$, can be found as $E_p\left(x^+\right) = a_1\left(1 - \exp\left(-x^+/L\right)\right) + a_3$ (Semwogerere et al. 2007). The entrance length then is

$$L = \left\{ \frac{1}{a_2} \ln\left[0.05 \left(1 + \frac{a_3}{a_1} \right) \right] \right\}^{1/a_4} \tag{5.8}$$

with $a_4 \simeq 0.6$. The normalised development lengths $L^+ = L/D$ computed from the oil concentration profiles are $L^+ < 135$ and less than the length of the test section.

From Fig. 5.11 it can be seen that the evolution parameter decreases with increasing input oil volume fraction and mixture velocity. However, shorter development lengths are observed for lower mixture velocities, as can be seen from Table 5.1. Similar behaviour has been reported recently by Abbas et al. (2017) for *o/w* dispersed flows with smaller drop sizes than in this study with $a = \mathcal{O}\{10^{-5}\}$ m.

5.3.2 Volume fraction profiles

For neutrally buoyant drops, simple Suspension Balance Models (SBM) (Zarraga et al. 2000) can be implemented to predict the concentration profile of the dispersed phase. These models are deduced from the local momentum balance at steady-state and assume a Newtonian behaviour of the mixture. They have been found to give relatively good results in *o/w* emulsions, but for relatively small drops so that any buoyancy effects are not considered (Abbas et al. 2017). In the present case, gravity plays a dominant role in the final shape of the profiles as the size of the drops is

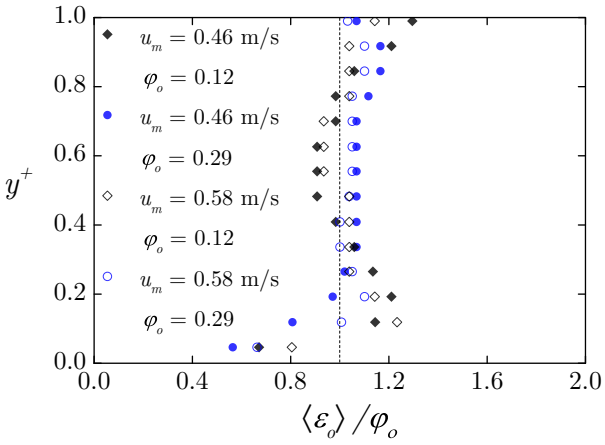

Figure 5.12: Ratios of the vertical in-situ oil volume fraction profile over the input oil volume fraction obtained with PLIF for four typical *o/w* flow conditions at $x^+ = 15$.

one order of magnitude higher than the experiments by Abbas et al. (2017) (having a similar density ratio between the two phases), while shear-induced migration also affects them.

The effect of gravity and shear-induced migration on the motion of the drops and the development of the concentration profiles along the pipe is studied. The vertical profiles of the experimental time-averaged in-situ oil volume fractions are extracted from the PLIF images. This analysis can provide quantifiable information on the distribution of the two phases and help the comparisons with the CFD model. As discussed previously, the dispersions generated from the static mixer are assumed to be homogeneously distributed along the vertical pipe direction in the beginning. This argument is tested in the experiments by plotting the vertical profiles of the time-averaged in-situ oil volume fractions $\langle \varepsilon_o(y) \rangle$ divided by the respective input oil fractions φ_o at the measuring location close to the static mixer, as shown in Fig. 5.12 for four typical conditions of Table 5.1 at $x^+ = 15$.

As can be seen, at the initial measuring location, the ratios of ε_o/φ_o are very close to unity, and the dispersion is almost homogeneous, particularly in the middle of the pipe. Some segregation has already taken place as can be seen from the lower values close to the bottom of the pipe ($y^+ < 0.2$) and from the higher values near the top ($y^+ > 0.8$). The profiles are affected by the input oil volume fraction, but they may also be affected slightly by the flow field close to the static mixer. The CFD simulations are initialised using a homogeneous profile $\varepsilon_o(y) = \varphi_o$ at $x^+ = 0$ for all conditions investigated.

For the same conditions, the experiments are compared against the CFD simulations at $x^+ = 135$ in Fig. 5.13. The simulated profiles agree reasonably well with the experimental ones and show asymmetric profiles where drops have accumulated at the upper part of the pipe leacing a clear water layer at the bottom (*o/w & w* pattern). These findings are in agreement with the visualisations of Fig. 5.5. Similar characteristics are observed for relatively higher mixture velocities and Reynolds numbers

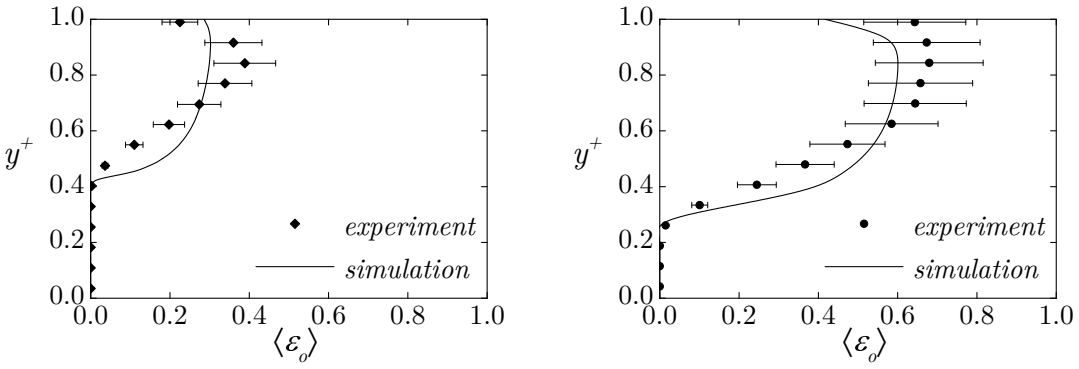

(a) $u_m = 0.46\ \mathrm{m\,s^{-1}}$ and $\varphi_o = 0.12$

(b) $u_m = 0.46\ \mathrm{m\,s^{-1}}$ and $\varphi_o = 0.29$

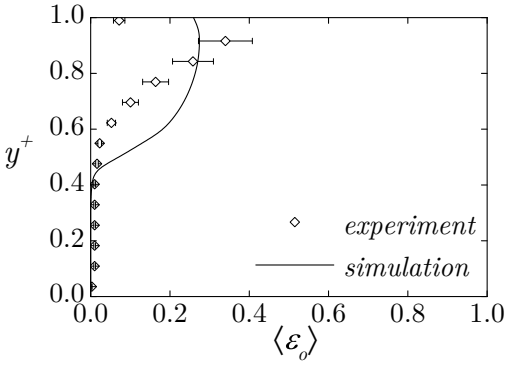

(c) $u_m = 0.58\ \mathrm{m\,s^{-1}}$ and $\varphi_o = 0.12$

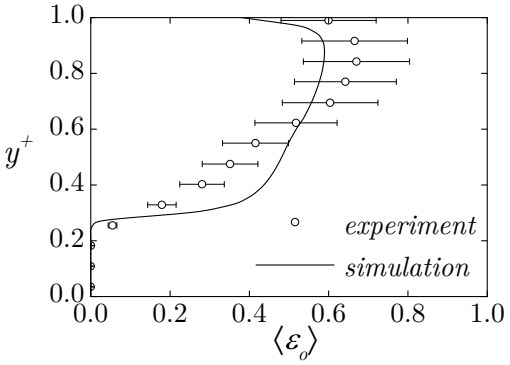

(d) $u_m = 0.58\ \mathrm{m\,s^{-1}}$ and $\varphi_o = 0.29$

Figure 5.13: Vertical profiles of the in-situ oil volume fraction obtained from the PLIF experiments and the CFD simulations for four typical *o/w* flow conditions at $x^+ = 135$.

in the experiments of Conan et al. (2007).

The height of the clear water layer decreases with increasing input oil fraction and is predicted accurately, with absolute deviations from the experiments of $\Delta y^+ < 0.05$. Small differences are only seen for $u_m = 0.58\ \mathrm{m\,s^{-1}}$ and $\varphi_o = 0.12$ (Fig. 5.5), with the simulations predicting a clear water layer. This difference may be attributed to the polydisperity of the mixture, which is not considered in the CFD model.

In the upper region of the pipe some deviations can be seen for most cases, especially at the lower input oil volume fractions of Figs. 5.13(b) and (d). While the shape of the profiles is similar for both simulations and experiments, the actual values at each measuring location y^+ can differ more than the 20% experimental uncertainty. This behaviour can be attributed to the shear-induced diffusion coefficients given in eq. 2.26 and set in the model in the drop transport eq. 2.25.

Finally, a decrease of the oil drop concentration very close to the wall is observed in all experiments (Fig. 5.13). This behaviour cannot be attributed to shear-induced migration, as the velocities at the top are very low, due to the high drop concentrations, which in turn give high local viscosity values (computed from eq. 2.18). A similar decrease in the profiles was reported by Ekambara et al. (2008) for gas-liquid and Ngan (2011) for liquid-liquid dispersed horizontal flows. In both these studies

a lift force was used to capture this trend in numerical models based on a Eulerian-Eulerian approach. In the current work, in which the mixture model is used, the lift force is accounted for by introducing a lift velocity in the slip formulation. According to Matas et al. (2009) for particulate flows in pipes, the lift velocity coefficient depends on the vertical pipe location and increases near the walls, while it is practically zero close to the pipe centre.

The decrease in the in-situ oil volume fraction close to the top wall is thus predicted as can be seen in Fig. 5.13, but some differences between the experiments and the simulations can be noted, with the numerical profiles having a steeper slope compared to the experimental ones. The simulations only consider an average drop size, and not the actual distributions found in the experiments (Fig. 5.9). The drops in the distribution with sizes smaller than the average size used in the simulations, experience a smaller lift force and hence increased concentration close to the wall, as the lift velocity is proportional to d^3. The dependence of lift velocity on size is reflected in the simulation results, since the case with the largest drop size (Fig. 5.13(b)), has the highest concentration slope close to the wall.

5.3.3 Streamwise velocity profiles

The streamwise velocity profiles measured experimentally and predicted numerically are also compared. For homogeneously dispersed liquid-liquid flows, parabolic profiles have been reported for input dispersed phase fractions below $\varphi_d < 0.5$ (Pouplin et al. 2011), while for higher concentrations the velocity profiles followed power-law shear-thinning characteristics (Conan 2007; Abbas et al. 2017). In the present work, the input oil volume fraction is low (Table 5.1), but it increases reaching local volume fractions above 0.5 when the drops segregate.

The transition from laminar to turbulent flow conditions in solid-liquid pipe flows cannot be simply characterised by a single phase or a mixture Reynolds number Re_m. Matas et al. (2003) found from experiments with neutrally buoyant particles that the critical Reynolds number for the transition depends on both the concentration of the dispersed phase and the particle to pipe diameter ratio. For the drop sizes considered in this work, the transition can happen either at Reynolds numbers lower than 2000 when φ_d is low, or at higher Re at increased φ_d. More recent and mainly numerical work has further considered the effect of concentration on the critical Re (Loisel et al. 2013; Yu et al. 2013; Lashgari et al. 2014; Abbas et al. 2017). For the current system where the drops stratify and there are concentration variations in a pipe cross-section, it is difficult to define a critical Re for the transition. For *o/w & w* dispersions, Conan et al. (2007) found that the velocities at the dense-packed layer drastically decrease, while the maximum of the velocity profiles is present in the drop-free water layer.

The time-averaged vertical profiles of the streamwise (axial) velocity component of the continuous water phase are plotted together with the simulation results in Fig. 5.14 for four typical flow conditions. The velocities are normalised with the

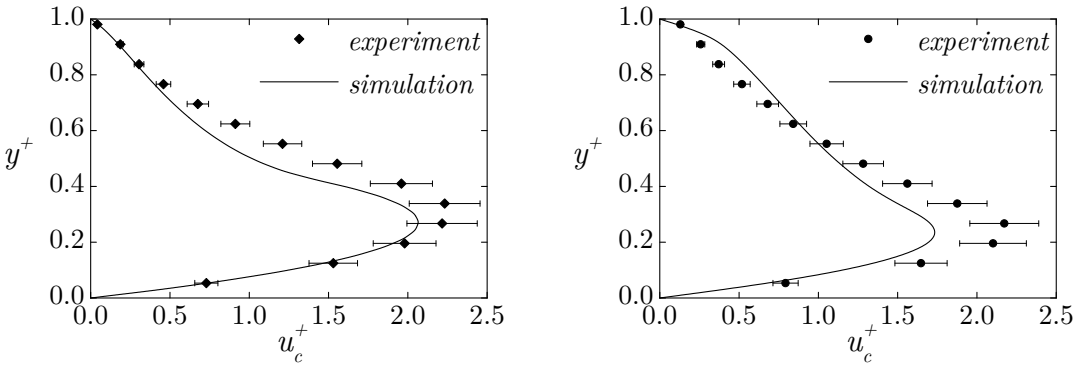

(a) $u_m = 0.46\,\mathrm{m\,s^{-1}}$ and $\varphi_o = 0.12$ (b) $u_m = 0.46\,\mathrm{m\,s^{-1}}$ and $\varphi_o = 0.29$

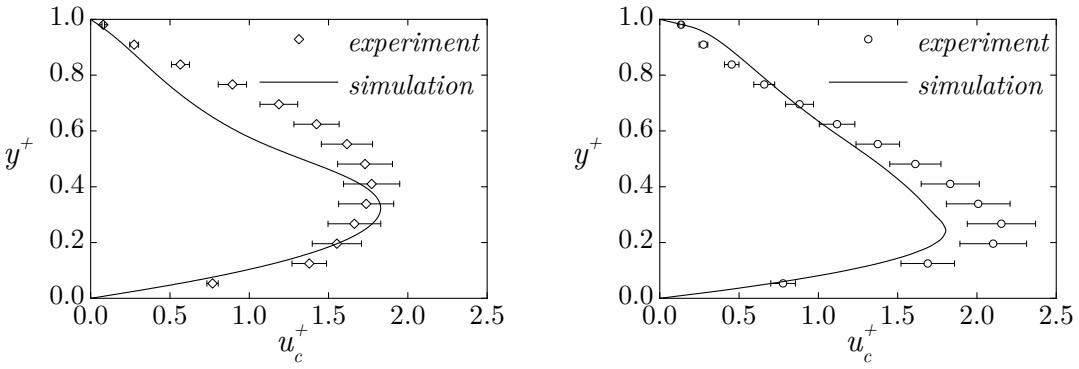

(c) $u_m = 0.58\,\mathrm{m\,s^{-1}}$ and $\varphi_o = 0.12$ (d) $u_m = 0.58\,\mathrm{m\,s^{-1}}$ and $\varphi_o = 0.29$

Figure 5.14: Vertical profiles of the streamwise velocity of the continuous phase obtained from the PIV experiments and the CFD simulations for four typical *o/w* flow conditions at $x^+ = 135$.

average mixture velocity $u_c^+ = Q_m/A$. At the beginning of the pipe, where the dispersions are homogeneous, Newtonian parabolic profiles are found experimentally and predicted from the simulations (not shown).

Good agreement is also found at $x^+ = 135$, within the mean relative 10% uncertainty considered for the measurements. The profiles are asymmetrical with low velocities at the upper part of the pipe, where the dispersion has become dense and high velocities in the clear water layer. The agreement between the experiments and the simulations illustrates that the use of a mixture viscosity in the model (eq. 2.2.2) can represent the phenomena taking place in the pipe and that the dispersion does in fact behave as a suspension of rigid solid spheres.

Some deviations are observed in the typical cases presented in Fig. 5.14, with the experiments presenting higher velocities at the clear water layer. These differences are not necessarily reflected in the in-situ oil volume fraction profile of Fig. 5.13. The higher deviations observed in Fig. 5.14(c) may be due to the presence of small drops close to the bottom of the pipe, which are not present in the simulations.

This Chapter provides detailed measurements with laser-based diagnostic tools at two axial pipe locations downstream a static mixer generating liquid-liquid dispersions. Fluctuations caused by the mixer are recorded for laminar flow conditions

for small axial lengths, but dissipate further downstream. The mixer is found to generate drops of size in accordance with the empirical formulations of the literature. Different flow patterns are recorded, and their development along x^+ is shown to depend on the initial size, dispersed phase volume fraction and mixture velocity. Higher drop sizes are recorded along the direction of buoyancy with a small dip close to the pipe walls – possibly caused by lift forces. The vertical drop concentration profiles showed a similar trend as the drops segregated towards the top. The packing of the drops induces local changes of the physical properties of the mixture, resulting in asymmetrical velocity profiles, with the maxima of the velocity located in the drop free layer. CFD simulations, solved with the FEM, predict well the experimental results by considering gravity, lift and shear-induced diffusion, which are found to be the dominant forces controlling drop motion in Poiseuille flow. It is concluded that the drops behave as suspensions of solid rigid spheres for the conditions investigated.

Chapter 6

Coalescence Dynamics

Interfacial phenomena during dispersed flows are crucial, as breakup and coalescence can have an impact on both the flow characteristics and the separation properties of the dispersions. Understanding these phenomena can help provide better predictions of the drop sizes distribution changes through population balance equation models. The methods behind these models have been reviewed in Liao and Lucas (2009) for breakup and Liao and Lucas (2010) for coalescence, while the recent review by Solsvik and Jakobsen (2015) portrays the latest developments in the field and underlines the need for better understanding.

The dispersed flows investigated in this work are for low velocities and thus drop breakup due to turbulent eddies can be considered negligible for most drop sizes and flow conditions examined, as Sec. 2.3.2 explains. However, the same case cannot be made for the coalescence between drops and between drops and an interface. As discussed in Sec. 2.3.1, film drainage takes place between neighbouring fluid bodies of the same liquid and if sufficient time is allowed coalescence takes place. This drainage time (discussed in detail in Sec. 2.3.1.1), is the driving force in the separation of immiscible liquid-liquid dispersions and is crucial in PBE routines. It has thus triggered lots of dedicated studies on the topic for Newtonian fluids (Klaseboer et al. 2000; Ramachandran and Leal 2016), with surfactants (Yeo et al. 2003), contaminants (De Malmazet et al. 2015) and even fluids with complex rheology (Goel and Ramachandran 2017).

In the present Chapter, the focus is placed on the first few milliseconds after film drainage has taken place and rupture of the interfaces has begun. It has been shown that very interesting dynamics develop after this singularity occurs, which can affect the separation of the liquids (Fezzaa and Wang 2008). As described in Sec. 2.3.1.2, a liquid bridge (neck) forms and connects the two coalescing bodies, while it quickly expands driven by the interfacial energy minimisation dynamics. In the present case, coalescence between a drop and a horizontal interface is investigated, which develops high pressure differences between the coalescing bodies (eq. 2.34). In the first Section, coalescence is studied during pipe flow, while in the next two Sections, the rigorous neck expansion characteristics are explored in a confined quasi-two-dimensional system to allow a more systematic investigation, where the addition of surface active agents and shear-thinning fluids is possible. Surfactants

can introduce local gradients of the interfacial tension along the interface and highly disrupt the expansion velocity and curvature of the neck, while polymers can induce local variations of the viscosity that influence the flow field around the singularity point.

6.1 From pipe flows to confined systems

As the velocities are kept low in both flow loop systems, coalescence between drops and between a drop and an interface are recorded as the dispersion flows along the pipe. This leads to the increase of drop size and the generation and evolution of a continuous layer of the dispersed phase. The planar measurements conducted with PLIF at the matched refractive index flow loop allow detailed measurements close to the coalescence point and can help unravel the underlying dynamics.

A time-lapse of the coalescence of an aqueous drop with the aqueous-organic interface is presented in Fig. 6.1 obtained in the matched refractive index flow loop. The flow is from left to right and the drop moves with a mean streamwise velocity of approximately $0.42\ \mathrm{m\,s^{-1}}$. The mixture velocity for this condition is $u_m = 0.46\ \mathrm{m\,s^{-1}}$. As explained in Table 3.6 and Chapter 5, the gray colour denotes the aqueous phase (i.e. mixture of 52% w/w glycerol/water and the ink), black the organic phase (i.e. low viscosity silicone oil) and white spots the PIV tracer particles. A large aqueous drop of $d^+ \simeq 0.2$ located close to the bottom of the pipe moves along the interface in the axial direction. At time $t = 0$ ms a relative motion of the tracer particles on the opposite direction of the stream can be distinguished, which can be interpreted as the initialisation of the coalescence. The measurement of the exact

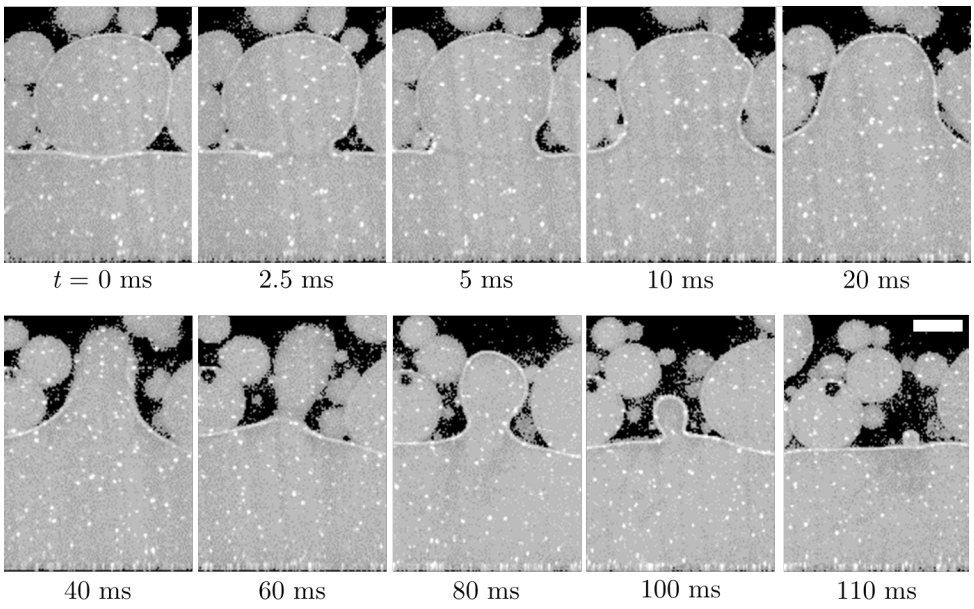

Figure 6.1: Ten time steps of a coalescing aqueous drop with an interface in the matched refractive index flow loop. The cross-flow is from left to right. The scale bar denotes $2\ \mathrm{mm}$.

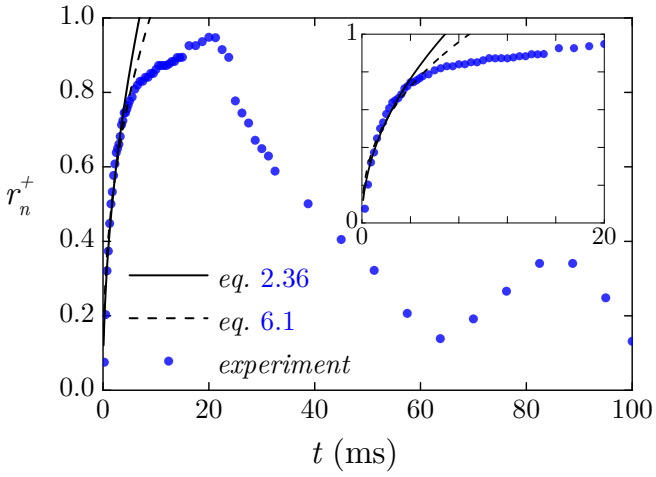

Figure 6.2: Normalised neck expansion over time for the coalescence event of Fig. 6.1. The continuous line is computed from eq. 2.36 by Eggers et al. (1999) and Duchemin et al. (2003), while the dashed line is computed from eq. 6.1 by Lim et al. (2016). The inset focuses on the data for the early times.

time that coalescence starts is limited by the acquisition frequency. In the current case, high-speed PLIF imaging is conducted at a 4 kHz frequency, which translates to an uncertainty of ± 0.125 ms.

During the coalescence, a small neck is formed linking the drop with the interface as explained in Sec. 2.3.1.2. Its size expands rapidly with a velocity of $u_n \sim 1\ \mathrm{m\,s^{-1}}$ at the initial time-steps of the present case, with the neck size starting from a few microns and reaching a few millimetres in a time of just $\Delta t = 2.5$ ms. The neck keeps expanding until it reaches a maximum at about 20 ms and then it decreases and the drop is fully merged with the bulk aqueous phase.

To quantify the neck expansion dynamics, the neck radius r_n normalised with the drop radius a (r_n^+) is plotted over the time in Fig. 6.2. A linear part trend exists for $t \lesssim 2.5$ ms. For asymmetrical coalescence, where the ratio of the radii of the coalescing bodies reaches ∞ (drop-interface case), both Aarts et al. (2005), Thoroddsen et al. (2007) and Lim et al. (2016) found similar dynamics in their experimental results for the early times during drop-interface coalescence with the neck reaching a threshold value for longer times and were in agreement with the Lattice Boltzmann simulations of Lim et al. (2017). At longer times, the neck radius drops significantly, reaches a minimum value and then repeats the whole trend with a lower threshold before completely coalescing with the interface.

While for longer times, the dynamics become complicated and no simple scaling argument exists, several authors have tried to establish the theory for the neck expansion at the early times. It must be noted that for all neck radii computed for this system and based on Fig. 2.8, coalescence takes place mainly in the inertial regime. Eggers et al. (1999) followed by Duchemin et al. (2003) wrote that for the inertial regime the dynamics scale as eq. 2.36. The cross-flow velocities in the pipe

are relatively low for the current case and no collisions are expected to take place at the dense-packed layer close to the interface in order to disrupt the mechanism. As shown in Fig. 6.2 the theory developed for confined systems matches relatively well the experiments in the pipe, where cross-flow is present. A proportionality constant equal to ~ 2 is used, which slightly deviates from the 1.62 found theoretically by Duchemin et al. (2003).

Recently, Lim et al. (2016) tried to extend the scaling law for the inertial regime for all systems independent of the size ratio of the coalescing bodies (symmetry of coalescence). Based on the inertial time $t_{iner} = \rho a^3/\sigma$ (Aarts et al. 2005), the neck expansion is proportional to

$$r_n^+ \propto (t/t_{iner})^{\xi}, \tag{6.1}$$

where ξ is a growth exponent equal to $1/2$ for symmetrical coalescence translating to the scaling of Eggers et al. (1999), or with a suggested value of $\xi \simeq 0.4$ from Lim et al. (2016) and Lim et al. (2017) for the extremely asymmetric case, which corresponds to the current experiment. It is clear from Fig. 6.2 that both eq. 2.36 and eq. 6.1 give relatively similar predictions.

High-speed PIV measurements are employed to also investigate the velocity field generated from the coalescence phenomenon. The velocity vectors are plotted for the same ten time-steps of Fig. 6.1 in Fig. 6.3. The streamwise velocity u_m is subtracted from the vectors to illustrate the underlying patterns. The interface boundary of the coalescing drop is schematically shown with a continuous line, while the length of the vectors represents their magnitude. The vorticity, defined as the curl of the velocity as

$$\boldsymbol{\omega} = \nabla \times \boldsymbol{U},$$

which simplifies to

$$\omega_z = \left(\frac{\partial v}{\partial x} - \frac{\partial u}{\partial y} \right) \tag{6.2}$$

assuming a two-dimensional flow, is also shown in Fig. 6.3 with the colour contours. The vorticity is estimated from the PIV measurements by computing the central second order differences of the velocity data. The method has been found to amplify the reported velocity errors (Westerweel et al. 2013), so care needs to be given in the quantitative interpretation of the vorticity contours.

At $t = 0$ ms, the interface has ruptured on the right side of the drop. Under the effect of interfacial tension, the formed neck between the drop and the interface is expanding axially. The maximum velocity of the expanding neck occurs at $t = 2.5$ ms. The axial velocities become symmetric on both sides of the drop at a later time step ($t = 20$ ms). The same behaviour has been described by Mohamed-Kassim and Longmire (2004) for a confined system without a cross-flow.

Gravity and Laplace pressure cause a strong downward motion of the aqueous phase from the drop to the bulk continuous phase. The combination of the axial

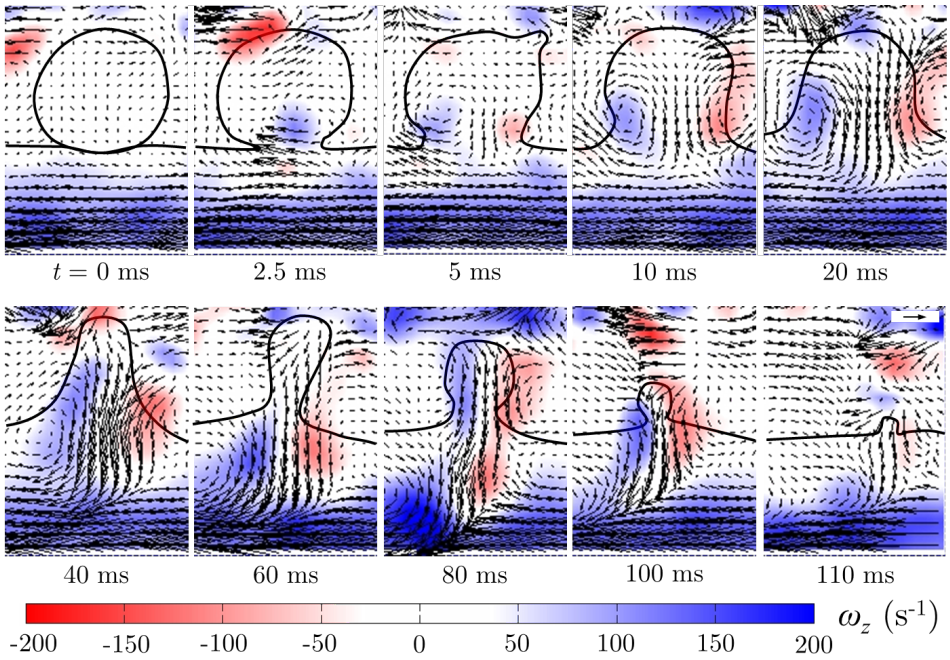

Figure 6.3: The instantaneous velocity fields denoted with black vectors and the vorticity illustrated with the colour contours are plotted during the coalescence of a drop for ten time steps. The interface has been plotted manually from the raw images to illustrate the approximate drop boundaries. The cross-flow is from left to right. The scale bar denotes 2 mm and the arrow length a velocity of $0.1\ \mathrm{m\,s^{-1}}$.

and the vertical motion generates two counterrotating vortices in the drop. Similar velocity and vorticity patterns have also been observed in stationary systems (Mohamed-Kassim and Longmire 2004; Weheliye et al. 2017). The neck expansion velocities reported in stationary systems are also similar to the one observed in this work. The adjacent drops would have an effect on the film drainage rate and the local flow fields, as discussed by Bordoloi and Longmire (2012) on the effect of neighbouring particles on drop coalescence. Chinaud et al. (2016) showed that two more counteracting vortices form in the bulk coalescing phase. However, the spatial resolution in the current experiments is not high enough to capture these vortices. At time $t = 40$ ms the neck decreases until $t = 60$ ms. Neck pinch off (partial coalescence) is overcome, and thus after $t = 80$ ms the drop continues to drain in the bulk homophase. The rate of decay is similar for both the vertical velocity component and the vorticity.

The vertical velocity component, v, and the vorticity, ω_z, profiles are shown in Figs. 6.4(a) and (b) respectively, for the same time steps shown in Figs. 6.1 and 6.3 at the rupture location $y^+ \simeq 0.20$ and after coalescence starts. As can be seen in Fig. 6.4(a) the absolute maximum of the vertical velocity increases as the coalescing drop moves along the pipe. The velocity v reaches the highest value for $x^+ = 134.9$ or $t = 40$ ms. Once the formed neck between the drop and the interface starts decreasing, as shown for t = 60 ms, the maximum v also temporarily decreases. At $t = 80$ ms, when the neck starts expanding again, the vertical velocity increases again before finally

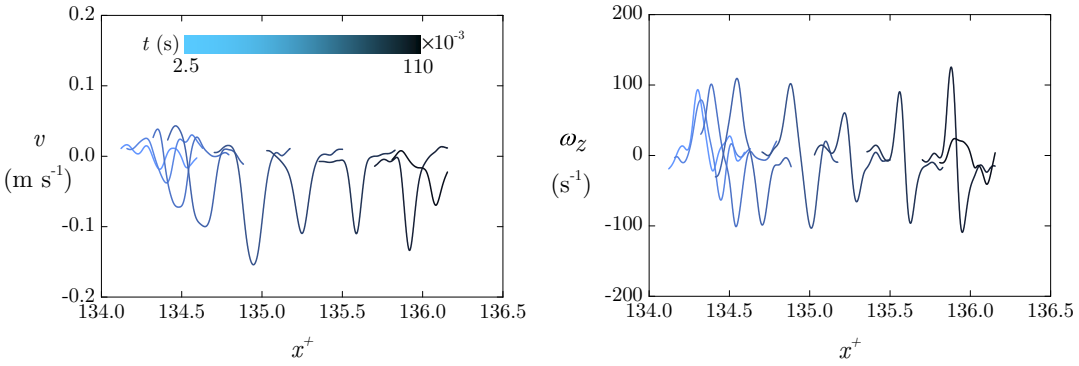

(a) vertical velocity component (b) relative vorticity

Figure 6.4: The horizontal profiles at the interface level $y^+ \simeq 0.2$ during the coalescence. The same time steps are plotted as Figs. 6.1 and 6.3 with $t \in [2.5,\ 110]$ ms (light to dark).

the whole drop joins the continuous phase and the local v peak decreases. A similar trend is observed in the vorticity shown in Fig. 6.4(b). Two vorticity peaks, one negative (from the counterclockwise vortex) and one positive (from the clockwise vortex), form at each time step, which increase as the neck expands in the initial time steps. This is followed by a temporary decrease, an increase and then a final decay of the vorticity. The profiles of v and ω_z seem to follow the neck expansion dynamics of Fig. 6.2.

It must be noted that the case discussed in this Section is a typical one, and covers the main important points observed in all cases. However, a more thorough investigation on the topic is needed, studying drop-drop and drop-interface coalescence, recording the neck expansion velocities and computing the velocity fields, for a wide range of drop sizes and possibly different liquids. In the current experiment, there is no control on these parameters, so arguing that the cross-flow velocity does not influence the dynamics would be speculative. As a final note, only one difference compared to the confined systems is observed. The highest point of the drop during the coalescence does not go below the interface level at any point during the coalescence. This finding contradicts the behaviour found in confined systems for a few viscosity ratios (Mohamed-Kassim and Longmire 2004), while this has only been recorded for systems with high surfactant concentrations (Weheliye et al. 2017). The dynamics of coalescence are investigated in more detail in confined systems in the next two Sections, focusing on the effects of surface active agents and complex fluids at the initial times.

6.2 Surfactant effects

In the current[1] and following Section, coalescence is studied in a confined system instead of a horizontal pipe, as it permits better control on the conditions and more flexibility on the selection of fluids and additives. This control in turn permits for

1. Results of this Section have also appeared in Chinaud et al. (2016).

more in depth analysis at isolated conditions. A Hele-Shaw cell is used, which is a quasi-two-dimensional cell made from two parallel acrylic plates placed in such a way to form a thin gap of $D \simeq 1.25$ mm and allows to localise the rupture point. More details on the setup are given in Sec. 3.1.3. The fluids used in the present experiments are Exxsol D80 and a 82% glycerol/water w/w mixture containing a blue dye.

As explained in Sec. 2.3.1, the interfacial tension forces are mainly driving the coalescence between two liquid bodies. For this reason, the goal of this Section is to investigate how local variations of the interfacial tension can have an effect on the dynamics of the neck expansion. To accomplish that, a surface active agent is introduced in the organic phase of the system at concentrations below the CMC value. The surface EOS is obtained and given in eq. 3.3, which provides a master equation linking the concentration of the surfactant to the interfacial tension of the system (Fig. 3.5). More details on the physical properties of the liquids and the nature of the surfactant are given in Sec. 3.1.3 and in Table 3.3.

Recent simulations by Martin and Blanchette (2015) revealed that the surfactant concentration along the interface is not uniform during coalescence and two peaks of concentration are located symmetrically on either side of the neck for the initial times. Unravelling the concentration of surfactant along the interface experimentally can be difficult, however, in the present Section the surfactant effect is illustrated with direct measurements of the neck expansion and comparisons of the dynamics against theoretical models. Moreover, the velocity field is measured with BF PIV, and the flow structures generated in the initial times are presented.

6.2.1 Neck expansion velocity

From the high-speed visualisations conducted, it is found that the presence of surface active agents modifies the geometry of the approaching interfaces compared to systems without surfactants. Raw images for droplet coalescence without surfactant 6.5(a) and with a $c = 1.5\,10^{-4}$ surfactant concentration 6.5(b) are used to illustrate the corresponding configurations. the schematic representations of the mechanisms (similar to Fig. 2.7), are demonstrated in 6.5 where the geometrical parameters relevant to droplet coalescence with and without a surfactant present in the oil phase are shown, assuming a two-dimensional configuration.

In the absence of a surface active agent, the radius of the neck r_n connecting the drop with the interface is located above the initial flat interface level during the whole coalescence process. The distance $2R_n$, separating the center of the neck from the initial interface height, corresponds to the local radius of curvature of the neck during the early stages of coalescence. A similar geometrical modelling has been used by Yokota and Okumura (2011) to describe the dynamics of droplet coalescence for different viscosity fluids in a Hele-Shaw cell. When a surfactant is present in the bulk phase the geometrical characteristics change. The addition of surfactant decreases the interfacial tension that keeps the interface flat which then tends to

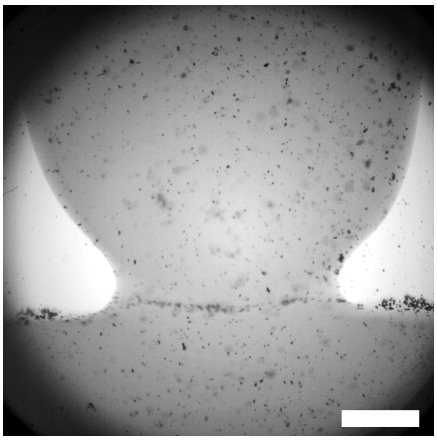

(a) Typical image without the surfactant

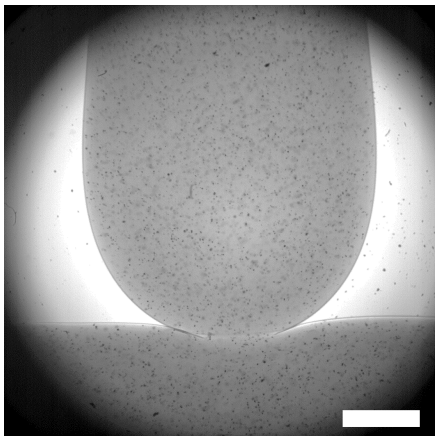

(b) Typical image for Span 80 at $c = 1.5\,10^{-4}$

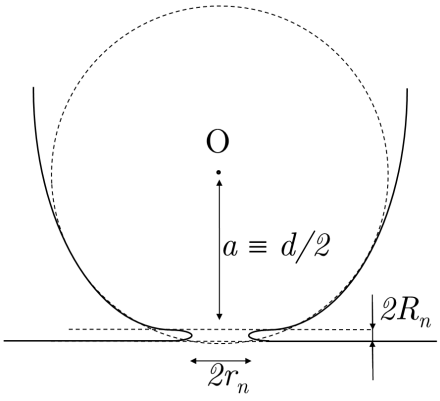

(c) Schematic illustration without Span 80

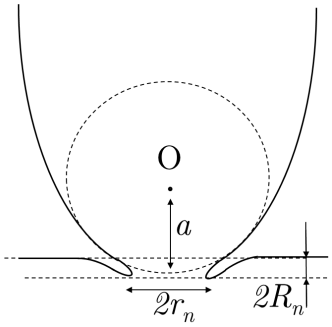

(d) Schematic illustration with Span 80

Figure 6.5: High-speed images and respective schematic illustration of the coalescence mechanism with and without the surfactant. The scale bars denote 2 mm.

deform under the approaching drop (Fig. 6.5(d)). In this case, the horizontal plane defined by the neck radius is located for a given time below the initial interface level. During the initial stages of neck rupture and until the neck reaches the initial interface height, the local radius of the neck curvature is not large enough to be detected by the current imaging system. In these stages the neck appears on the images as a curved line moving along the contact line between the drop and the lower phase.

To study the dynamics of coalescence, the evolution of the neck radius over time is recorded and shown in Fig. 6.6. The data follow a linear trend for short times, irrespective of the surfactant concentration. More importantly, this linearity continues for neck radii beyond the diameter of the cell D, which is in accordance with previous experiments in Hele-Shaw cell geometries (Eri and Okumura 2010; Yokota and Okumura 2011). This measured linear evolution of the neck with time indicates an almost constant interfacial tension value at least at the neck region during the initial stage. As eq. 2.35 is valid for the initial times and the viscosity of the solution

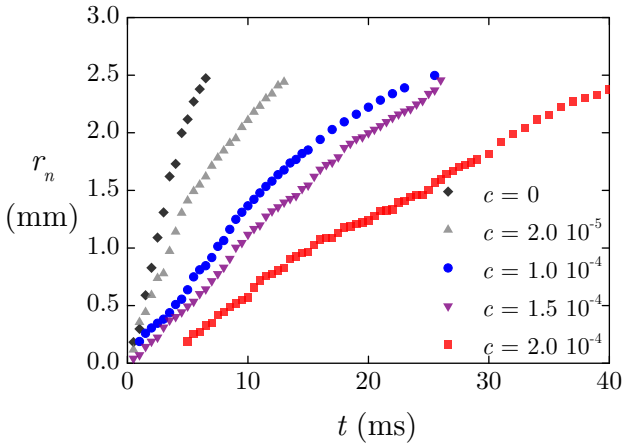

Figure 6.6: Neck radius evolution over time of a typical drop for different surfactant mass ratios.

is constant, the local interfacial tension values should also remain constant, suggesting that there is no variation of the surfactant concentration at the neck during this stage.

From the slopes of the lines in Fig. 6.6, the neck expansion velocities, u_n, can be calculated for the different surfactant concentrations. It should be noted that in Fig. 6.6 the data of only one typical drop coalescence event are shown for each concentration, but to produce the final dynamics many drops are used to obtain an average neck velocity for each concentration. The average neck velocity for the pure solution is $0.295\,(\pm 45\%)\ \mathrm{m\,s^{-1}}$. The deviation in the velocity is in fact much higher for the pure solutions compared to the surfactant ones (less than 10%) for two main reasons. The pure solutions have higher neck velocities compared to the surfactant ones, because they have higher interfacial tension which drives coalescence. With the image acquisition frequency used of $2\ \mathrm{kHz}$ only five images could be captured for pure solutions in the first regime compared to approximately 30 for the highest concentrated surfactant solution. Secondly, the pure system is more susceptible to dust present in the cell compared to the surfactant ones (De Malmazet et al. 2015), which can affect the final neck expansion velocity. Similar velocity deviations have also been reported by Eri and Okumura (2010), where the neck velocities ranged from 0.25 to $0.35\ \mathrm{m\,s^{-1}}$ for one set of liquids.

Two distinct regimes which describe the neck expansion during droplet coalescence have been identified in previous studies as discussed in Sec. 2.3.1. The first viscous regime occurs immediately after the neck ruptures and is limited to a short time range and the inertial regime happening at longer times. The transition from the first to the second regime takes place for $Re_n = \rho R_n u_n/\eta > 1$ based on the neck characteristics (Thoroddsen et al. 2005), while a third regime was recently observed by Paulsen et al. (2012) as explained in Sec. 2.3.1. Even though coalescence takes place in a quasi-two-dimensional cell, to model the neck dynamics in this first regime, the flow is considered three dimensional, as the neck is smaller than the

depth of the cell in the z direction (Eri and Okumura 2010; Yokota and Okumura 2011). Following these assumptions, a general scaling law holds true for neck diameters smaller than the diameter of the cell as $2r_n \leqslant D$. The non-dimensional Ohnesorge and Capillary numbers for this regime are respectively defined as

$$Oh = \frac{\eta}{\sqrt{\rho\sigma a}} \tag{6.3}$$

and

$$Ca = \frac{\eta u_n}{\sigma}, \tag{6.4}$$

with η and ρ representing the viscosity and density of the coalescing phase, and σ the interfacial tension between the two phases. The characteristic velocity in the Ca number is the neck velocity $u_n = \mathrm{d}r_n/\mathrm{d}t$, while the characteristic length scale for the Oh number is the drop radius, which controls the surfactant diffusion dynamics.

A linear scaling law applies in the viscous regime, where $Ca \approx 1$, expressed as $r_n(t) \propto D\,(t/t_{visc})$, where $t_{visc} = D\eta/\sigma$; this gives $u_n \propto \sigma/\eta$ (eq. 2.35), which for the initial stages is valid for three-dimensional as well as for two-dimensional geometries for neck diameters less than the cell depth (Burton and Taborek 2007). While this scaling law is well established for three-dimensional liquid-liquid coalescence, it is not well explored for two-dimensional cells. In two-dimensional cells, the proportionality constant, α, can be computed (Eri and Okumura 2010) as

$$\alpha = \frac{1}{2\pi}\left[\ln\left(\frac{8}{Re_n}\right) - 0.077\right], \tag{6.5}$$

giving

$$u_n = \alpha\frac{\eta}{\sigma}. \tag{6.6}$$

The proportionality constant corresponds to the drag coefficient of a cylinder in Stokes flow (Lamb 1932), and is found by considering the neck is locally cylindrically shaped with a length equal to the cell thickness D and a radius equal to the radius of curvature of the neck R_n. The constant α depends only on the local neck radius of curvature, which is small and can be considered constant for the initial times, and the neck velocity, which can be considered constant for each surfactant concentration – as shown in Fig. 6.5. For the early stages of coalescence, the maximum local neck radius of curvature is $R_n \sim 2$ pixels for all solutions, which in turn gives a value of approximately $R_n = 10\ \mu\mathrm{m}$. For the highest neck expansion velocity (pure solution) and the maximum radii of curvature, eq. 6.5 gives for a system without surfactant a theoretical value of $\alpha = 0.5$. The addition of surfactant can only decrease the neck expansion velocity and thus increase the theoretical value of α.

Using the linear law of eq. 6.6, the non-dimensional neck radius over the nondimensional time is plotted in Fig. 6.7(a). For the calculations, the surfactant concentration at the neck region c_n is taken equal to the bulk one c (Table 3.3). As shown

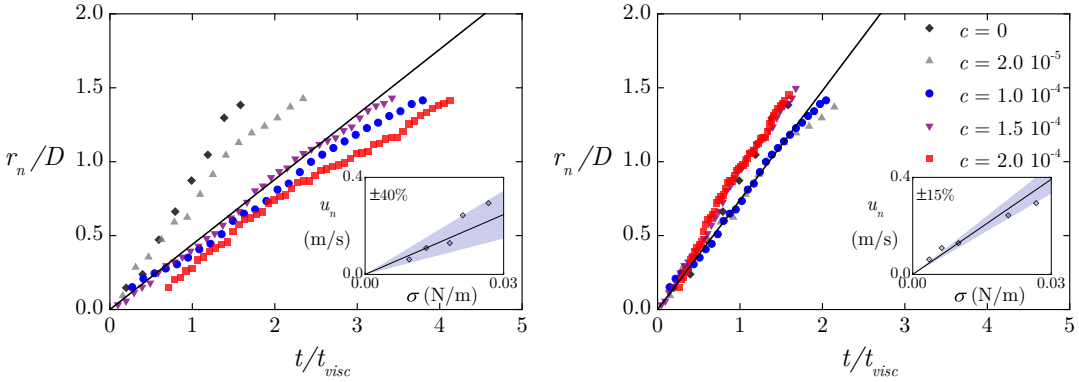

Figure 6.7: Neck radius evolution over the scaled time. The insets show the averaged velocities for the corresponding case with the continuous line representing the fitted slopes for (a) $\alpha = 0.4$ and (b) $\alpha = 0.7$.

in Fig. 6.7(a) the lines for the surfactant concentrated solutions clearly fail to collapse. The averaged neck velocities are also plotted against σ in the inset of Fig. 6.7(a) where it can be seen that the slope of the line ($\equiv \alpha$) is equal to 0.4 with a wide spread of data ($\sim 40\%$). This value is lower than the theoretical value for the pure solution ($\alpha = 0.5$) and cannot be correct as an increased surfactant concentration can only decrease the neck velocity and thus only increase α.

As described by Eggleton et al. (1999), certain physical processes controlling the diffusion and desorption or adsorption of the surfactants have to be considered to better explain their effect on the dynamics of coalescence. In the case of a droplet coalescing with a flat interface, mass transfer of the surfactants need to be taken into account. Dilution of the surfactant due to the interface dilatation can be ignored, since there is no growth of interface during coalescence. In addition, the mass transfer of surfactant from the bulk to the interface is negligible for low surfactant concentrations (below the CMC value). This is because mass transfer occurs mainly during the seeding time of the droplet, which is of the order of $\mathcal{O}\{10^2\}$ s, compared to the coalescence process which is of the order of $\mathcal{O}\{1\}$ s (Martin and Blanchette 2015).

The current system is characterised with $Oh = \mathcal{O}\{10^{-1}\}$, which in turn gives $Pe^{-1} \ll Oh$, with the Péclet number defined as

$$Pe = \frac{a^2}{\mathcal{D}_\Gamma \tau_\mathcal{D}}, \tag{6.7}$$

where $\mathcal{D}_\Gamma$ is the surface diffusivity coefficient and $\tau_\mathcal{D}$ is a typical time scale of diffusion (Eggleton et al. 1999). In similar conditions, Martin and Blanchette (2015) showed that for inert surfactant molecules, a peak of surfactant concentration appears at the neck during the coalescence process. They attributed this to the significant time difference between the typical time of surfactant diffusion and the time scale of the coalescence process. An interfacial tension gradient was computed along the interface away from the neck, but locally the interfacial tension was constant with

$c_n > c$.

According to the simulations by Martin and Blanchette (2015), a concentration of surfactant almost twice as that in the bulk fluid is expected during coalescence for the experiments presented here. From Fig. 3.5, the local interfacial tension values at the neck, can be found by doubling each bulk surfactant concentration. A new scaling curve can be thus produced, which is presented in Fig. 6.7(b). All curves now collapse in a single line, which suggests the local neck surfactant concentration is higher in the neck than in the bulk and $c_n \approx 2c$. Additionally, the new fitted slope of u_n versus σ obtained from the average neck velocity data and shown in the inset of Fig. 6.7(b) gives a value of $\alpha = 0.7$, with a small deviation $(\pm 15\%)$. This value is above the theoretical one for the pure solution ($\alpha = 0.5$) and captures the slower neck evolution with surfactants. A description of the findings of Sec. 6.2 is also provided in Chinaud et al. (2016).

6.2.2 Generation and advection of vortices

The results presented in this Section correspond to a typical drop for each surfactant concentration. Streamlines are computed from the velocity fields obtained by high-speed BF PIV measurements with $\Delta t = 0.5$ ms. For all the solutions implemented in this study, the hydrodynamics tend to exhibit the same pattern, despite the changes in the surfactant concentration in the organic phase. The moment the interface breaks and the coalescence singularity occurs, movement of the tracer particles close to the singularity can be observed. The measurement of the coalescence time starts from this point. However, at the very early stages of coalescence, the bursting tip appears as a continuous black line and velocity fields and the neck radius cannot be computed accurately. This behaviour is more pronounced at high surfactant concentrations and corresponds to a maximum of two frames. Consequently the first velocity field measurements are taken after 0.5 to 1 ms depending on the surfactant concentration.

Figure 6.8 shows streamlines for two different time steps corresponding to the linear first regime, where the effects of time and surfactant concentration are observed. The time steps chosen correspond to neck diameters of $r_n = 0.25$ and $r_n = 0.625$ mm or aspect ratios of $2r_n/D = 0.4$ and $2r_n/D = 1$, respectively. The velocity fields show the generation of two pairs of counter-rotating vortices. One pair is located inside the droplet above the initial interface level, while the other is formed in the bulk fluid below the interface level. The upper pair of vortices is denoted as UV and the lower pair as LV, with the clockwise rotation as "+" and the anticlockwise as "-". As the time increases, UVs are advected along the interface and towards the top of the droplet, while LVs are advected towards the bulk, but stay close to the interface.

Qualitatively, the size of the vortices seems to increase in the surfactant concentrated solution. By continuity of the velocity, this can be attributed to the fact that a larger part of the interface is moving. The velocities of advection of the pairs UV and

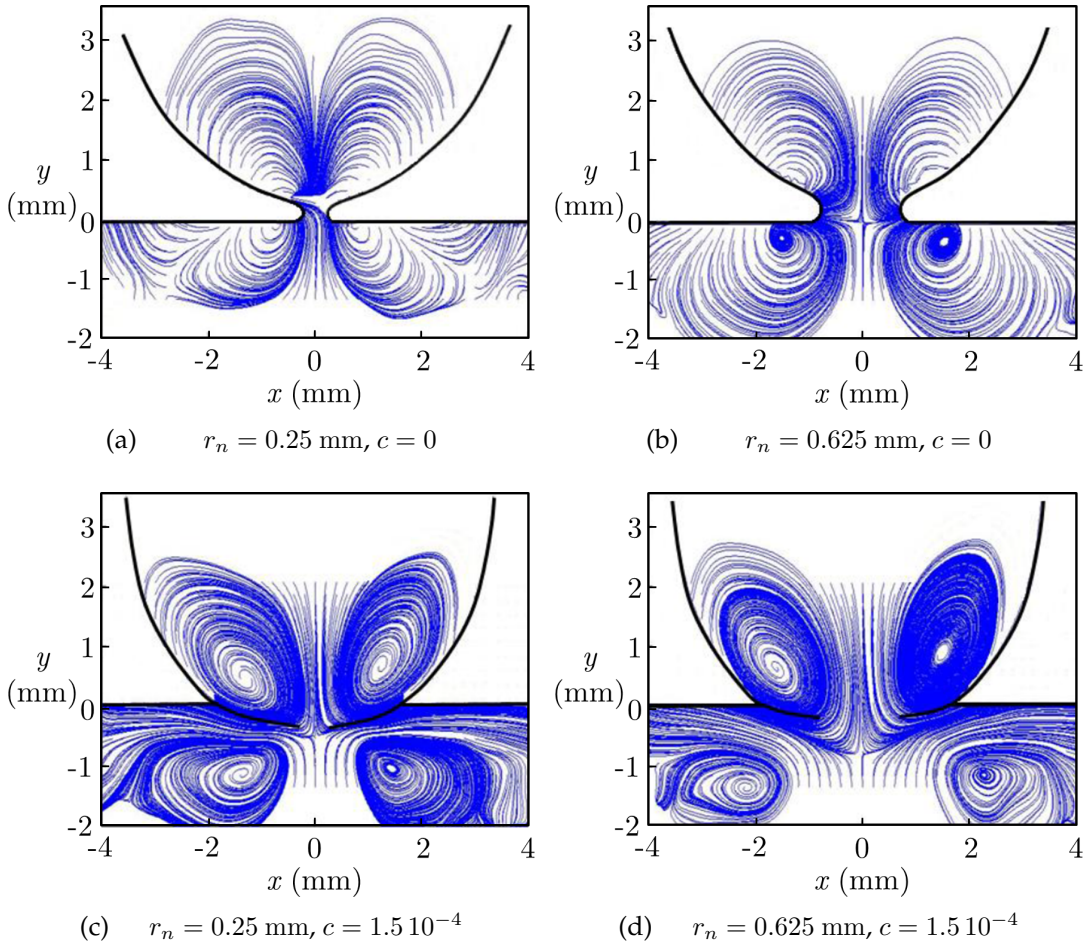

Figure 6.8: Streamlines at two different time steps for two cases with and without surfactant. The interface has been plotted manually from the raw images to illustrate the approximate drop boundaries.

LV are different and this behaviour can be observed, for example, in the asymmetry between UV- and LV+ from the initial horizontal interface level which increases over time (Fig. 6.5(d)). The generation of UV can be explained by considering that the expansion of the neck introduces two main flow velocities inside the droplet — one horizontal in the direction of the neck growth, and the other vertical with direction from the droplet to the bulk. These two components generate, respectively, UV+ and UV-. For the generation of LV, a similar reasoning can be applied. From the singularity point where the rupture occurs, two vertical flow movements (positive for UV and negative for LV) are generated. This results in significant pressure difference between this singularity point and the rest of the fluid, which drives the neck growth and the vertical velocity components.

From the high-speed BF PIV measurements conducted in this study, it is shown that the upward and downward vertical velocity components, both directed towards the singularity point, are of the same order of magnitude for very short times. Interestingly though, for longer times, the downward velocity becomes higher than the

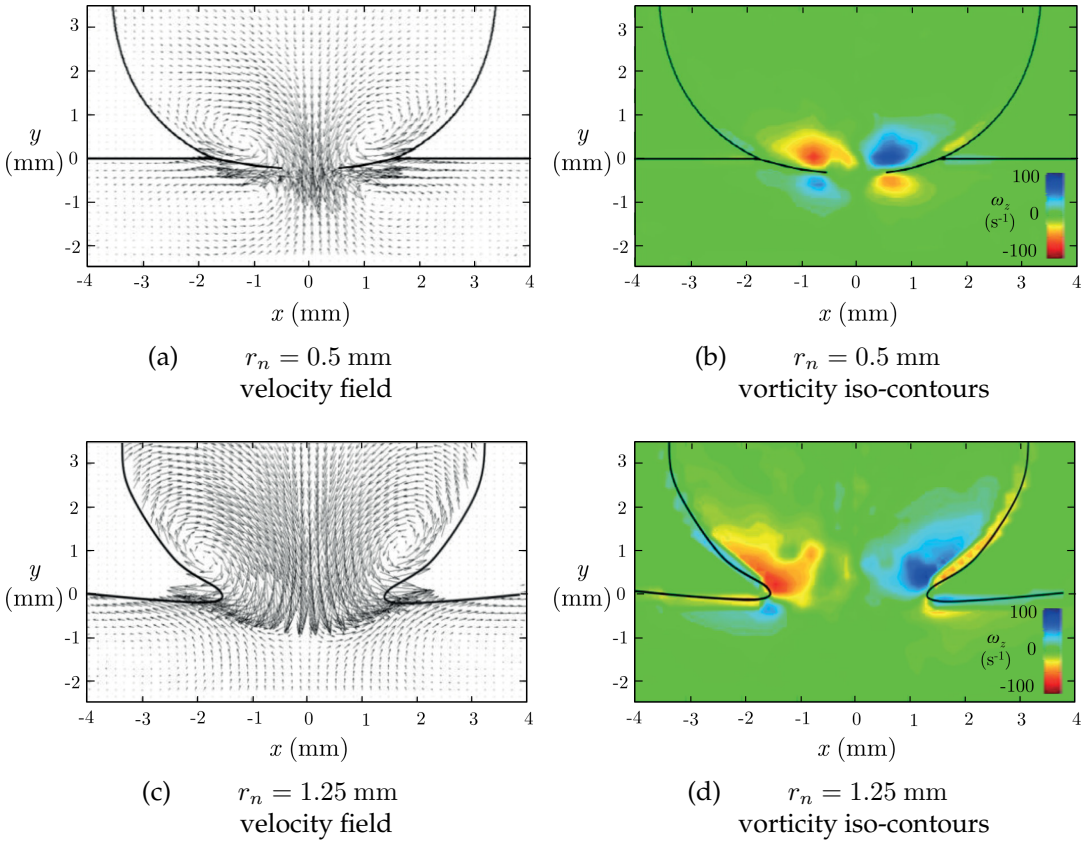

(a) $r_n = 0.5$ mm velocity field

(b) $r_n = 0.5$ mm vorticity iso-contours

(c) $r_n = 1.25$ mm velocity field

(d) $r_n = 1.25$ mm vorticity iso-contours

Figure 6.9: The velocity field and the corresponding vorticity iso-contours in the drop and bulk phase for a surfactant solution of $c = 1.5\,10^{-4}$ at two time-steps. The interface has been plotted manually from the raw images to illustrate the approximate drop boundaries.

upward as the coalescence progresses. Previous experimental efforts on the coalescence of three-dimensional droplets (Mohamed-Kassim and Longmire 2004; Weheliye et al. 2017) have not managed to capture these short time dynamics, but have illustrated a similar behaviour for the longer times.

For a given solution, LV and UV have different advection velocities which depend on the surfactant concentration. To quantify the velocity difference, vortices have been tracked. Figure 6.9(a) presents a typical velocity field for a surfactant concentration of $c = 1.5\,10^{-4}$, while Fig. 6.9(b) shows the corresponding vorticity ω_z iso-contours. It can be noticed that there is a slight deviation between the centres of the vortices and the location of the vorticity extrema. Figures 6.9(a) and (b) exhibit clearly that the vorticity iso-contours mainly match the internal corner of the vortex position which corresponds to the rotation occurring close to the singularity. It is worth noting that LV vanish as the end of the viscous regime is reached, as is shown in Figs. 6.9(c) and (d).

The tracking of the vortices depends on the complexity of the flow (Jeong and Hussain 1995) and in the present study the streamlines seem to indicate better the location of the centres of the vortices, rather than other computational methods. The centres of the vortices have been tracked manually at each time step by recording the position of the center of the core created by the streamlines with an accuracy of a

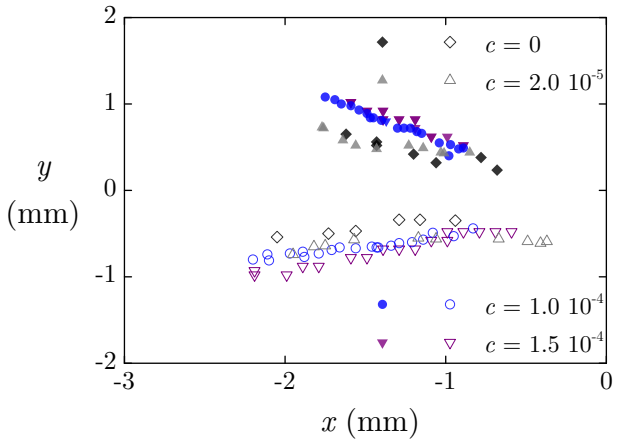

Figure 6.10: Spatial evolution for a constant time step in the x-y plane of the centres of the two vortices present on the left-hand side of the droplet within the viscous regime for different surfactant concentrations, UV- for $y > 0$ (solid symbols) and LV+ for $y < 0$ (open symbols).

corresponding PIV correlation box (± 0.16 mm). Figure 6.10 presents for one drop the spatial evolution in the x-y plane, of the centres of the two vortices on the left-hand side (UV- and LV+) for a constant time step within the viscous regime. The positive values of y correspond to the movement of UV, while negative to the movement of LV. The data have been rescaled by putting the origin of the frame in the position of the initial interface breaking point. This is because the breakage point does not always occur at the centre of the drop.

The presence of the surfactant tends to shift the trajectory of the UV vortices to the top of the droplet over time. As shown in Fig. 6.10, UV- tends to have a linear trend for all cases while the slope is increased at higher surfactant concentrations. The distance travelled over time for one drop for each concentration can be seen in Fig. 6.11 for the UV- (Fig. 6.11(a)) and LV+ (Fig. 6.11(b)) vortices respectively. The propagation seems to be linear, which indicates that the convection velocity of

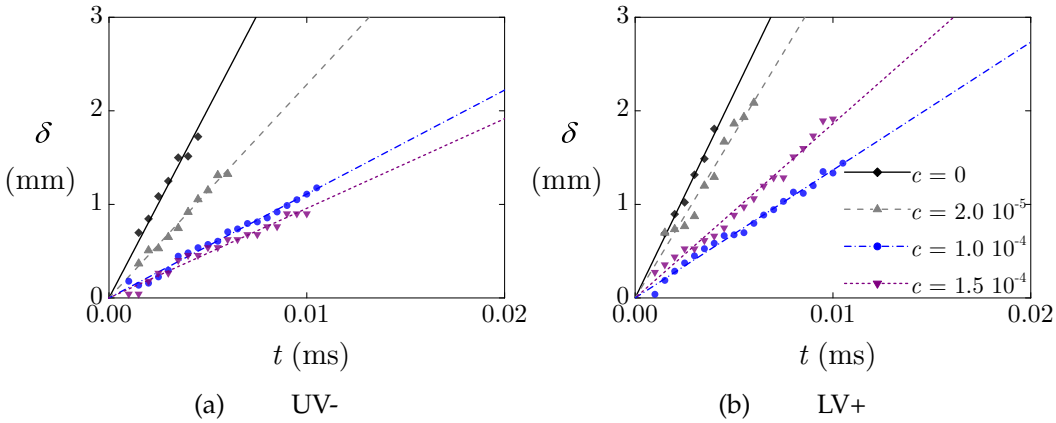

(a) UV- (b) LV+

Figure 6.11: Distance of the vortices travelled over time for a typical drop at different surfactant concentrations.

each vortex remains constant. For each solution, the velocity of advection of LV+ is always greater than the velocity of advection of UV-. This can be qualitatively explained by considering that UV is bounded by the aqueous-organic interface with a shape that depends significantly on the surfactant concentration. It can also be seen that for one drop the advection velocities of UV- are slightly lower than the corresponding neck velocities, while those of LV+ are higher; this is observed for all drops studied. The neck velocity appears to be the mean of the two counter-rotating vortices UV- and LV+ for each coalescing drop. The vortices generated by the rupture of the interface follow the neck dynamics for the viscous regime. The trajectories of the vortices plotted are only shown for time up to ~ 0.01 s, compared to Fig. 6.5, because at longer times the vortices collapse and the corresponding streamlines cannot be traced accurately.

6.3 Shear-thinning effects

It is clear from the previous Section that the viscosity of the liquids plays a dominant role in the initial time dynamics. While viscosity effects in Newtonian fluids have been extensively studied in both three-dimensional cells (Thoroddsen et al. 2005; Thoroddsen et al. 2007) and a Hele-Shaw cell (Eri and Okumura 2010), non-Newtonian effects, which are commonly encountered in oil and gas applications (Ghoumrassi-Barr and Aliouche 2016), have not been well explored. The simulations of Yue et al. (2006) illustrate how viscoelasticity delays the pinch-off for partial coalescence with the polymers resisting the stretching of the drop, while recent simulations of coalescence between two neighbouring drops by Sun et al. (2015) have shown how the shear-thinning behaviour can affect the vortex ring formation causing a jet-like mixing. Nevertheless, the dynamics close to the neck, the respective scaling laws and the velocity field for the initial times still remain ambiguous.

In this Section, the effect of a polymer introduced in the aqueous phase (52% w/w glycerol/water mixture containing a blue dye and the PIV tracer particles) is investigated in the same quasi-two-dimensional Hele-Shaw cell as in the previous Sec. 6.2 with high-speed BF PIV. A pure solution and three different xanthan gum concentrations are investigated in this study. Xanthan gum induces shear-thinning behaviour as illustrated in the master curve of Fig. 3.6 and is described well by the Carreau model of eq. 3.4. A low viscosity silicone oil is used as the organic phase. More information on the cell are given in Sec. 3.1.3 and for the fluids, which are the same as the fluids used in the matched refractive index flow-loop (results shown in Chapter 5 and Sec. 6.1, with their physical properties provided in Table 3.2).

The objectives are to understand how the apparent viscosity changes affect the neck expansion velocity and its curvature, along with effects on the velocity field inside the drop and near the neck region. Xanthan gum has a relaxation time of $\mathcal{O}\{10^{-2}\}$ s (Chow and Fuller 1984), while the experiment has characteristic times for the initial dynamics of interest of the order of $\mathcal{O}\{10^{-3}\}$ s. This behaviour provides in

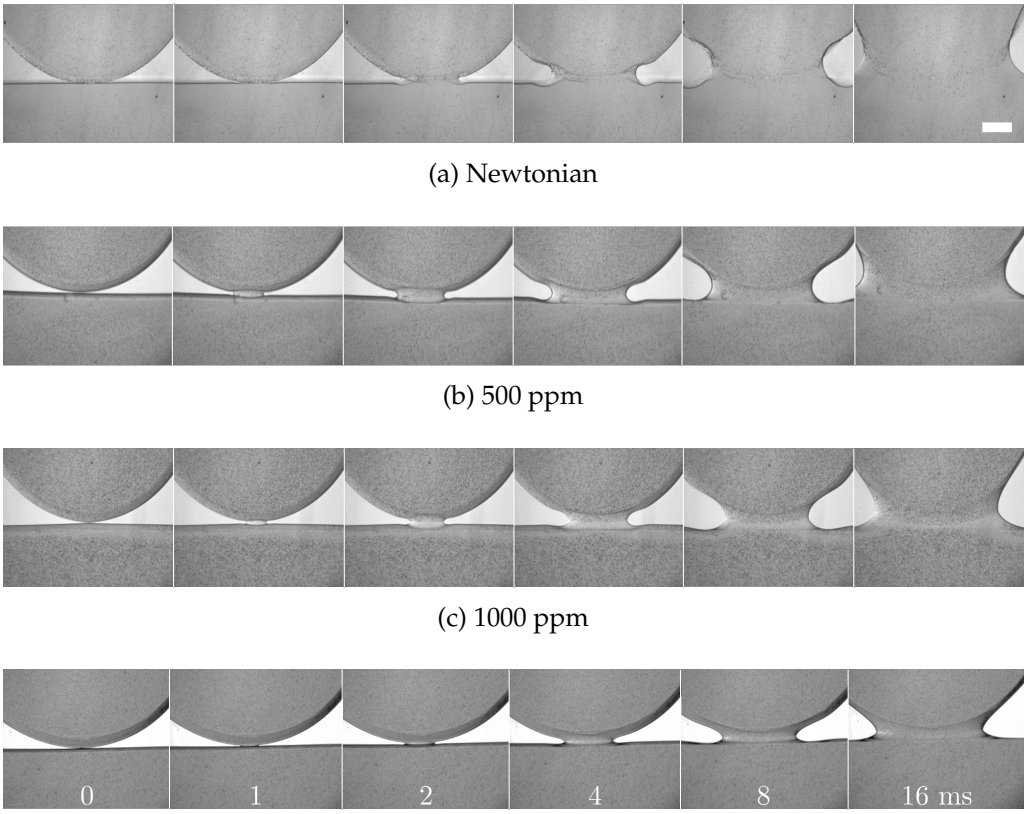

(a) Newtonian

(b) 500 ppm

(c) 1000 ppm

(d) 2000 ppm

Figure 6.12: Six time steps of an aqueous drop coalescing with an interface in the Hele-Shaw cell for four xanthan gum concentrations. The scale bar denotes 1 mm.

turn Deborah numbers as $De = \mathcal{O}\{10\}$, which translates to expected non-Newtonian behaviour of the polymer-containing aqueous phase. The long polymer chains of the xanthan gum take longer to align with the flow. Considering that the flow is complex with vortical structures generated from the singularity as shown in Fig. 6.8, the alignment of the polymer with the flow will be even more difficult to take place and thus shear-thinning effects are more likely close to the rupture point, rather than close to the interface.

6.3.1 Neck expansion and curvature

The neck evolution in time is portrayed in Fig. 6.12 for four xanthan gum concentrations through the acquired high-speed images. Image corrections are applied to homogenise the lighting between the cases. The time-steps of each frame are denoted in the bottom of the plot. The pancake-shaped drop (ellispoid squeezed between the two parallel plates of the Hele-Shaw cell) is resting at the undisturbed interface. Rupture happens and the neck begins to expand. A wave crest is also visible – mainly for the Newtonian case. As the xanthan gum concentration increases the expansion becomes slower and the curvature at the neck sharper. These same trends have also been reported for solutions in which the viscosity increased (Thoroddsen et al. 2005).

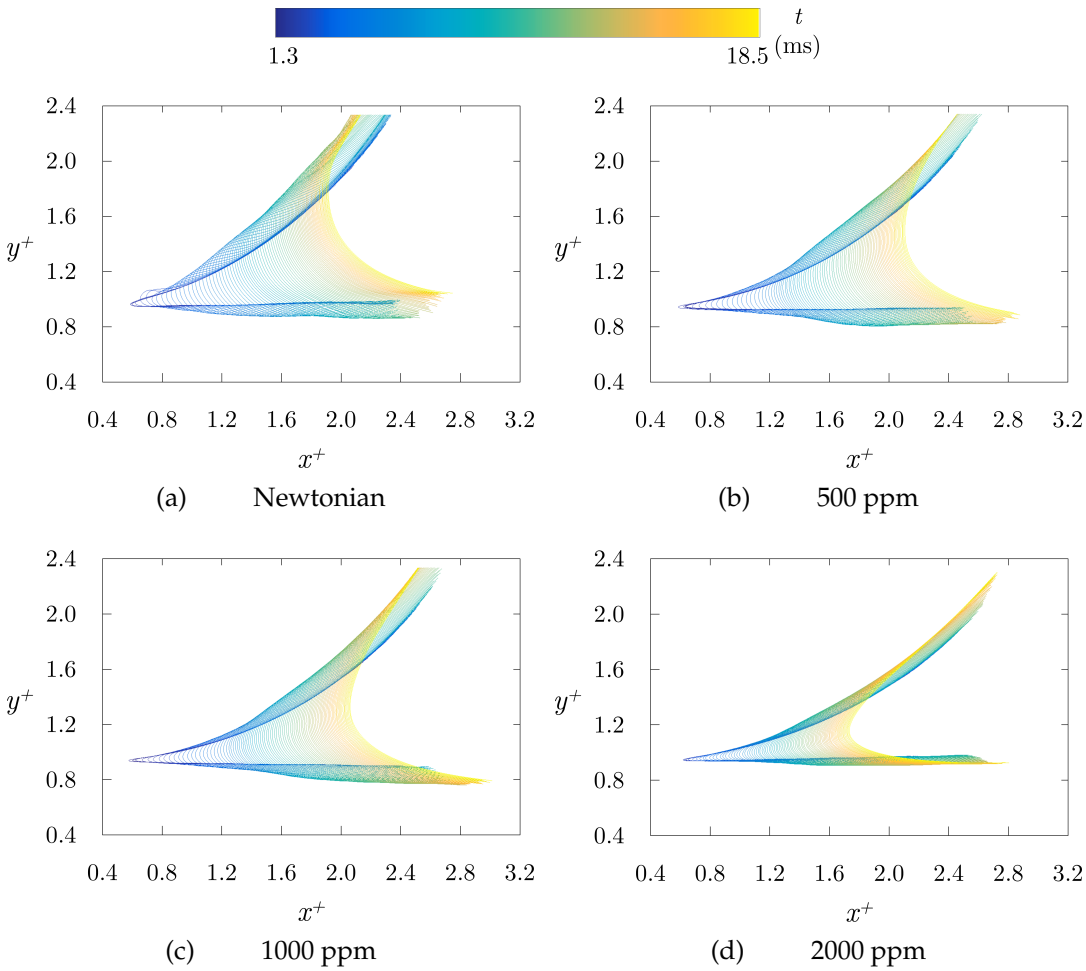

Figure 6.13: Time evolution of the interfacial shapes obtained with image analysis during the coalescence in the Hele-Shaw cell for the different xanthan gum concentrations. Only the right-hand side part of the drop is shown with $t \in [1.3,\ 18.5]$ ms (dark to light).

Image analysis is conducted to obtain the interface position during the early times of coalescence for the right-hand side of the drop for the four xanthan gum concentrations investigated. The final interface position and shape are plotted in Fig. 6.13. It becomes clear that as the coalescence advances, a capillary wave is formed and propagates along the interface, both at the drop and the bulk boundary. Qualitatively the waves are similar among the difference cases, with only a single crest visible from the primary wave. Further waves can possibly follow but are below the resolution of the imaging system. The amplitude of the waves increases with time and it has been found that this increase is due to the dispersion of the capillary wave with a phase velocity

$$u_{wave} = \sqrt{\frac{2\pi\sigma}{\lambda\Delta\rho}}, \tag{6.8}$$

where λ is the wavelength, while it has been found that the amplitude can be correlated with time as $\Delta y_{wave} \propto t^{2/3}$ (Keller and Miksis 1983). However, the focus of the present experiments is not on the wave characteristics.

To quantitatively discuss the trends observed from the images obtained, the neck

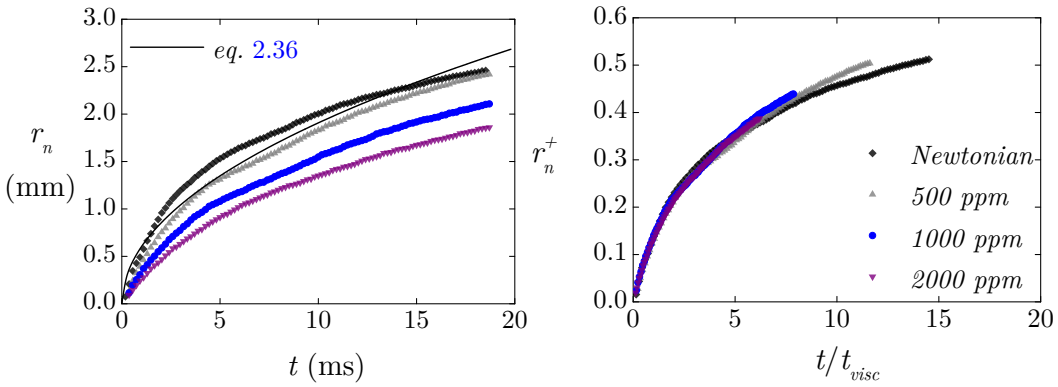

Figure 6.14: Neck radius evolution over time for the Newtonian and three shear-thinning solutions.

evolution is recorded for the initial times and is plotted for the different xanthan gum concentrations in Fig. 6.14. In Fig. 6.14(a) shows the evolution of the radius of the neck r_n over time t. It is clear that the linear expansion expected in the initial viscous regime is further limited to shorter times compared to the experiments of Sec. 6.2, due to the lower viscosity of the Newtonian solution. As explained in Sec. 2.3.1, the neck radius can be scaled as $r_n \propto t^{1/2}$ with eq. 2.36. It must be noted that although a proportionality coefficient is not used in the scaling relation, a relatively good agreement is found for these early times. It should be noted that no shear-thinning effect can be distinguished for the four different solutions, as the scaling of the $t^{1/2}$ dependence is validated and the viscosity is quasi-constant as the neck expansion advances.

While inertial effects are dominant (based on the Reynolds number of the neck), it is clear that the viscous forces still affect the neck expansion velocity, with a smaller r_n obtained with increasing xanthan gum concentration. For this reason, a viscous time, now defined as $t_{visc} = a\eta/\sigma$, is introduced and the normalised neck expansion $r_n^+ = r_n/a$ is plotted against t/t_{visc} in Fig. 6.14(b) for the four xanthan gum concentrations, where a is the drop radius. For the ellipsoidal shape the equivalent radius of the ellipses is taken as a with $a \approx 0.78 A_d^{0.625}/S^{0.25}$, where the drop area is $A_d = \pi d_x d_y/4$ and the perimeter $S_d \approx 2\pi \left(1/2 \left((d_x/2)^2 + (d_y/2)^2\right)\right)^{1/2}$, with d_x and d_y being the two axes of the ellipsoidal drop. The viscosity in the non-Newtonian solutions depends on the shear rate as shown in Fig. 3.6 and given by eq. 3.4.

For the scaling of t/t_{visc}, the viscosity at the infinite shear rate plateau is considered, based on the argument that the shear rate close to the interface, where the neck dynamics are of interest reaches its maximum values and thus it can be written that $t_{visc} = a\eta_\infty/\sigma$. It is clear from the collapse of the data in Fig. 6.14(b), that the hypothesis holds true. The argument of constant viscosity close to the neck is also stronger with the non-Newtonian solutions, following the dynamics of the Newtonian one.

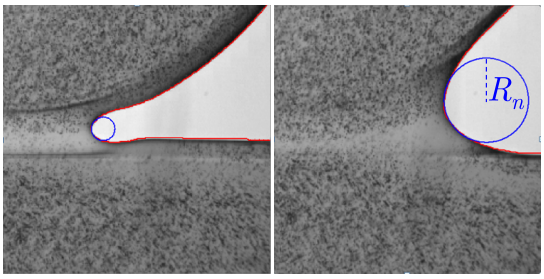

Figure 6.15: The interface (red line) tracking method fitting a fitted circular arc (blue line) at the neck for two time-steps of a typical coalescing drop in the Hele-Shaw cell.

For longer times $t/t_{visc} > 8$ deviations can be observed, that can be attributed to experimental error, uncertainties in the fitting of the coefficients of the Carreau model of eq. 3.4, or to the fact that the viscosity stops being constant close to the neck, and the expansion dynamics change.

The interface shape in the neck region is investigated in more detail by computing the local radii of curvature of the neck R_n. Due to the ambiguity in the measurements, the circular arc is fitted in a segment of the interface larger than $L > 20$ pixels using a Matlab code. The interface is extracted from the images, as shown previously in Fig. 6.13, and circular arcs are fitted close to the neck as shown in Fig. 6.15 by using

$$R_n = \frac{\left[\left(\frac{\mathrm{d}x}{\mathrm{d}L}\right)^2 + \left(\frac{\mathrm{d}x}{\mathrm{d}L}\right)^2\right]^{3/2}}{\left|\frac{\mathrm{d}x}{\mathrm{d}L}\frac{\mathrm{d}y^2}{\mathrm{d}^2L} - \frac{\mathrm{d}y}{\mathrm{d}L}\frac{\mathrm{d}x^2}{\mathrm{d}^2L}\right|}. \tag{6.9}$$

Two time-steps are presented, where the tracked interface is indicated with red and the circular arc with blue. The algorithm results were tested against manual measurements and showed good agreement. Slight deviations are expected at both small and large radii of curvature. The resolution of the images is kept at 86.6 pixels$/$mm for these measurements.

The resulting curvature evolution of the neck for the four different xanthan gum concentrations investigated is plotted in Fig. 6.16. A quasi-linear increase with time is recorded for all cases, with the curvature reaching asymptotically a threshold value. This value is different between the cases. This finding is consistent with the visualisations, where a sharper neck can be seen as the xanthan gum concentration increases. Similar behaviour has been reported in three-dimensional systems with Newtonian fluids of varying viscosity (Thoroddsen et al. 2007). This finding leads to building a stronger argument towards considering a quasi-constant viscosity at the neck region for the initial times despite the Deborah numbers above unity.

Interestingly, for the case of inviscid coalescence, Duchemin et al. (2003) found that the neck curvature should scale with $R_n \propto r_n^2$. In Fig. 6.16, the neck curvature normalised with the drop radius a is plotted against the square of the normalised neck radius. While the data do not collapse on the expected line, it is clear that they

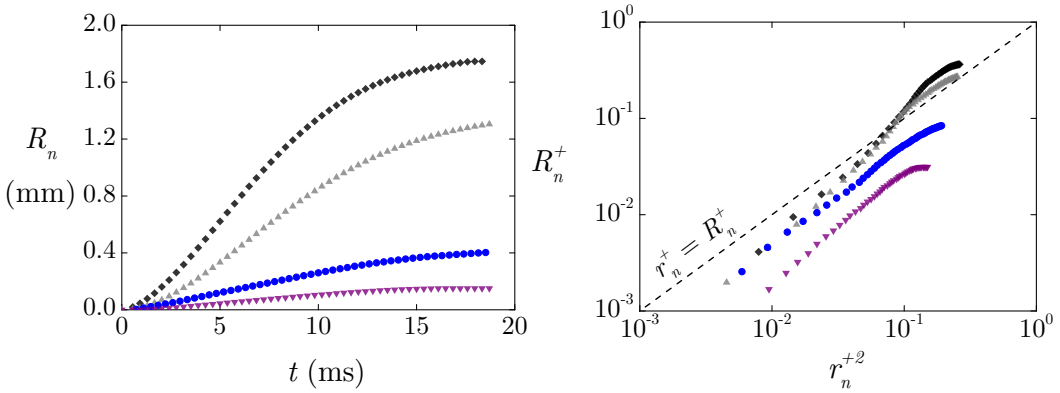

(a) Neck curvature over time (b) Scaling law

Figure 6.16: The neck curvature over time and the normalised curvature versus the square of the normalised neck for four xanthan gum concentrations.

still follow the same proportionality between the square of the neck radius and its curvature. The slope of the different xanthan gum concentrations remains approximately equal to unity. The different proportionality constants cannot be predicted from the scaling law and would need to be fitted to collapse the data.

It has been shown that the viscosity at the initial times and close to the interface can be considered quasi-constant, where the infinite shear rate viscosity η_∞ seems to describe well the scaling laws for the different xanthan gum concentrations. It remains to be seen, if the viscosity is also quasi-constant inside the drop for these initial times, and for this reason the velocity field close to the rupture point is investigated with BF PIV measurements.

6.3.2 Velocity field and local viscosity

Velocity measurements are conducted from the high-speed images with BF PIV, as explained in Sec. 3.2.2.3. The velocities of the aqueous phase (coalescing phase) are computed, as it contains the PIV tracers. The velocity fields computed are masked and the velocities inside the drop and in the bulk are only shown, while the interfacial boundaries are tracked and illustrated in the following Figures with continuous black lines. Good spatial resolution is achieved for these measurements, capturing well the length-scales of interest. However, deviations are expected close to the interface for the computations requiring gradients of any velocity component, i.e. computation of the magnitude of shear rate $\dot{\gamma}$ (eq. 2.21) and vorticity on the transverse plane ω_z (eq. 6.2).

Figure 6.17 illustrates the patterns formed after the rupture of the interface and the initialisation of the coalescence. The length of the arrows shows the magnitude of the velocities in the x-y plane and the contours give the vorticity on the z plane. As the neck expands, the strong horizontal motion of the neck along x, combined with the vertical motion towards the rupture point, lead to the formation of two counter-rotating vortices on each side of the drop. It has been shown that a vortex

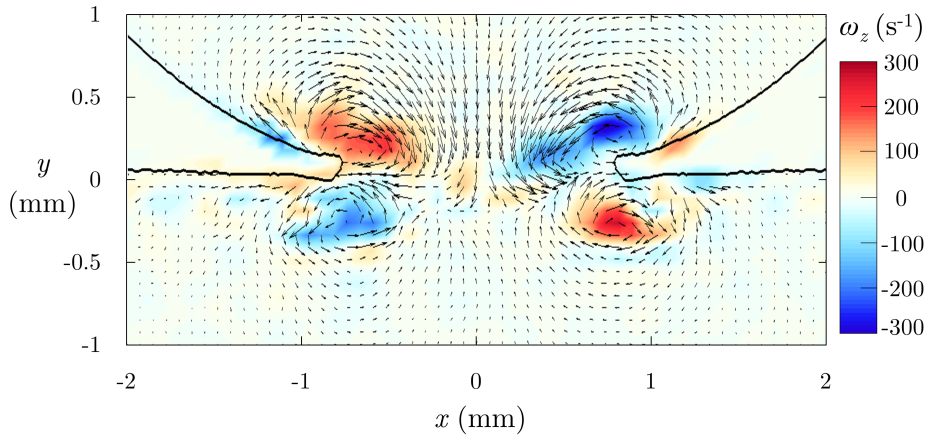

Figure 6.17: Velocity vector field and vorticity contours of a Newtonian drop coalescing in the Hele-Shaw cell.

ring is generated, travelling from the body of smaller radii of curvature, i.e. the drop, towards the body of larger radii of curvature, i.e. bulk aqueous phase (Mohamed-Kassim and Longmire 2004). However, for the cases investigated, it was found that a vertical motion from the bulk towards the rupture point also exists, which is in the same order of magnitude. This motion can be attributed to the fact that the rupture takes the form of a three-dimensional ring even in the Hele-Shaw cell for very short times $r_n < D/2$ and the strongest curvature determining the coalescence is the one towards the z direction along the diameter of the cell.

To better illustrate this ring formation, high-speed images of the very early stage are shown for different time-steps in Fig. 6.18. The images are recorded in an angle compared to the horizontal plane to better illustrate this effect. It becomes clear from the image at $t = 0.37$ ms that the rupture has a three-dimensional shape in the beginning and it is constricted by the walls of the cell at later times. The curvature along z is expected to be dominant and of similar magnitude for both the bulk and the drop, leading to a similar vertical motion towards the rupture point for both bodies. This vertical motion is observed for all the cases – independent of the xanthan gum concentration.

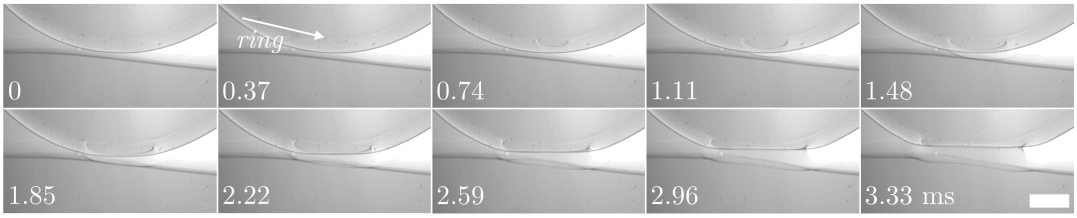

Figure 6.18: High-speed images obtained in a small angle to the horizontal plane to illustrate the three-dimensional ring formation at the early times of a coalescing drop in a Hele-Shaw cell. The scale bar denotes 1 mm.

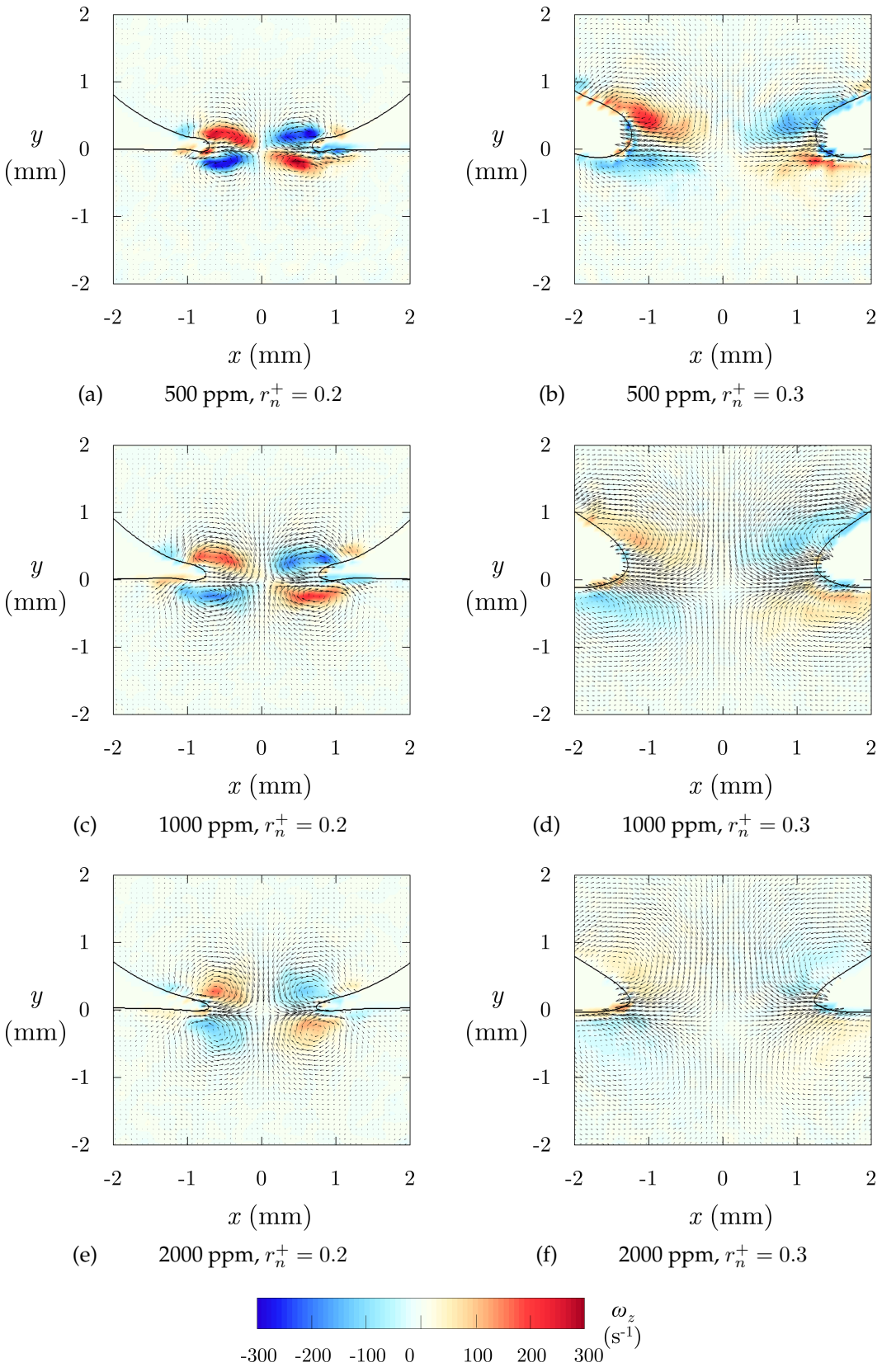

Figure 6.19: Velocity vector field and vorticity contours of a shear-thinning drop coalescing in the Hele-Shaw cell for three different concentrations and two neck radii.

The velocity field for the non-Newtonian cases is also computed for two time-steps, namely when the neck has reached a radius of $r_n^+ = 0.2$ and 0.3 relative to the radius of the coalescing drop. For the 500 ppm case, the velocity field is similar to to that of the Newtonian case as shown in Fig. 6.19(a). The vorticity reaches values of $\sim 300\ \mathrm{s}^{-1}$ and the velocities recorded present similar trajectories and magnitudes. However, as the concentration of xanthan gum is increased (Figs. 6.19(c) and (e)), the velocity magnitudes significantly drop, while also lower values of the vorticity are computed. However, the shape of the vortical structures remains qualitatively similar. The difference between the cases can be attributed to different apparent viscosity values in the region of the vortices. While the neck expansion dynamics scaled very well for an infinite viscosity (Fig. 6.14), the gradients of the velocities inside the drop are different when the xanthan gum concentration is increased.

At the second time-step of $r_n^+ = 0.3$ (Figs. 6.19(b),(d) and (f)), the vortices have still not collapsed, but are displaced towards the neck expansion direction and away from the rupture point. The magnitude of the velocities and the vorticity have decreased, while the centre of the vortices no longer corresponds to the maximum vorticity. The rupture point illustrates a velocity pattern typical for stagnation points, which stems from the neck motion and can provide low local pressures. Finally, a second vortical structure with an opposite rotation is present close to the four primary vortices, giving relatively high values of vorticity. This vorticity can be possibly attributed to the Capillary waves travelling along the interface. Below the crest of the waves, a circulation pattern is expected that can lead to curling of the velocity.

To further characterise the vortices and examine their rotational properties, the circulation in the area close to the vortices inside the aqueous drop are computed for the shear-thinning solutions. The circulation Γ_{ω_z} is linked to the vorticity as

$$\Gamma_{\omega_z} = \frac{1}{A_{\omega_z}} \int_{A_{\omega_z}} |\omega_z| \, \mathrm{d}A_{\omega_z}, \tag{6.10}$$

and it can be used to estimate the circulation in a finite area close to the vortex. A similar method has been used by Weheliye et al. (2017) by integrating over an area of ad-hoc vorticity (iso-contour). In this work, this area is taken for $|\omega_z| > 50\ \mathrm{s}^{-1}$, which provides sufficiently accurate measurements and for early enough times for all the different xanthan gum solutions.

The circulation values of the symmetric vortices are found very close (not shown here) and only the circulation of the vortex on the right-hand side and above the rupture point is illustrated in Fig. 6.20. The profiles are smoothed with a moving average filter to better illustrate the trends, while the respective uncertainties are shown with error bars. The circulation is highest in the very early steps of the coalescence and rapidly decreases as the neck expands. As the concentration of xanthan gum increases, the circulation of the vortices decreases until all three solution practically reach the same plateau, which indicates that the counter-rotating vortices have extended to their largest area for $t > 15$ ms.

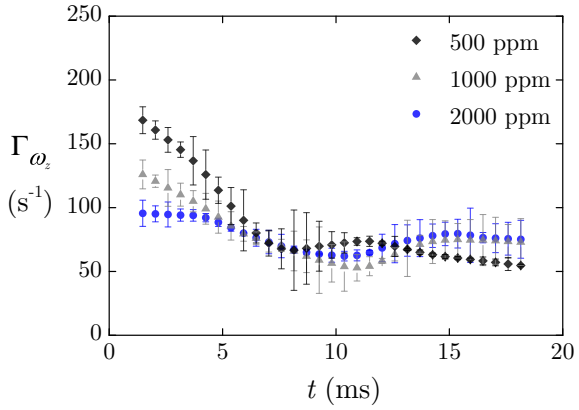

Figure 6.20: Circulation computed from eq. 6.10 for $|\omega_z| > 50$ s^{-1} for the right-hand side vortex inside the aqueous drop for the non-Newtonian solutions.

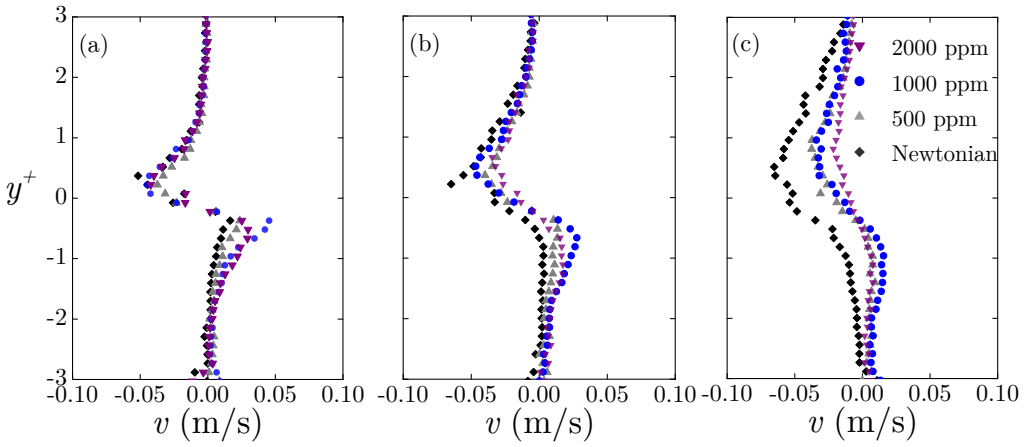

Figure 6.21: Vertical profiles of the vertical velocity component at $x = 0$ (centre-line of the rupture) for three time-steps when (a) $r_n^+ = 0.2$ (b) $r_n^+ = 0.3$ and (c) $r_n^+ = 0.4$.

The vertical profiles of the vertical velocity component $v(x, y)$ are plotted along the centre-line of the rupture ($x = 0$) in Fig. 6.21 for three different normalised neck radii r_n^+. Two peaks are clear close to the normalised with the cell thickness rupture point $y^+ = 0$, denoting the motion towards the singularity as described previously. The vertical velocities towards the top decrease at longer times, while the velocities towards the bottom remain quasi-constant during the time considered. It is clear that for the early times and the same neck radius, the vertical velocities are very similar for all the xanthan gum concentrations. This is very interesting, considering that the velocities inside the drop are very different among the cases as illustrated previously in Fig. 6.19.

To examine in more detail the shear-thinning effects, the magnitude of the shear rate computed from eq. 2.21 is shown in the contour plot of Fig. 6.22 for the x-y plane and the 1000 ppm solution. The time-step when the neck radius reaches $r_n^+ = 0.2$ is shown. A range of shear rates is present in the coalescing drop covering values as small as 1 s^{-1} and reaching values close to 1000 s^{-1}. The shear rate reaches its

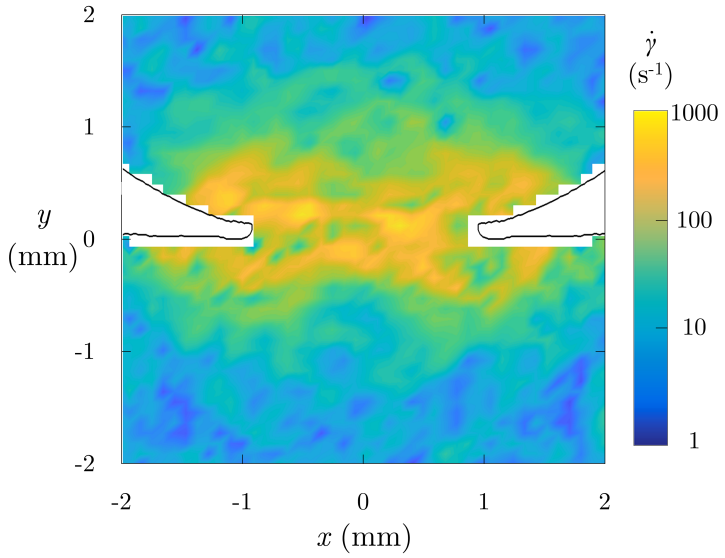

Figure 6.22: Shear rate magnitude contours computed from the BF PIV measurements and eq. 2.21 for 1000 ppm xanthan gum concentration and $r_n^+ = 0.2$.

maximum close to the rupture point and these values extend on both horizontal directions for each side of the drop and towards the leading neck. Low values of shear rate are recorded close to the centres of the vortices, with strong gradients of shear rate present. It is expected that shear-thinning effects are present in these regions, which can justify the differences recorded in the velocity fields of Fig. 6.19 and the circulation of the vortices of Fig. 6.20, for the solutions of different concentrations of xanthan gum.

By using eq. 3.4, a master curve connecting the shear rate magnitude with the local dynamic viscosity is obtained for the three non-Newtonian solutions. The shear rates computed from the BF PIV measurements can be translated to local viscosity values that can illustrate better the differences recorded in regions of high shear rate changes. The shear rate range computed is within the shear-thinning region of the xanthan gum solutions as shown in Fig. 3.6. The contours of the viscosity are presented in Fig. 6.23 for the three xanthan gum concentrations investigated and the same two time-steps as Fig. 6.19, namely for $r_n^+ = 0.2$ and 0.3.

For $r_n^+ = 0.2$, low values of the viscosity, almost reaching the Newtonian plateau, are present close to the neck region, independent on the concentration of xanthan gum. As shown in Figs. 6.23(a),(c) and (e), the viscosity is very low in the region close to the rupture point, while it increases almost two orders of magnitude a millimetre away. As coalescence progresses and the neck radius advances to $r_n = 0.3$ (Figs. 6.23(b),(d) and (f)), a region of intermediate viscosity ($\hat{\eta} = \mathcal{O}\{10^{-1}\}$) is formed surrounding the rupture region. Interestingly, the low viscosity close to the neck remains for the early times, which can explain why the scaling law for the neck radius in Fig. 6.14(b) is true, indicating a quasi-constant viscosity in time. Also, the assumption that the viscosity close to the neck can be considered equal to η_∞ is fair, since

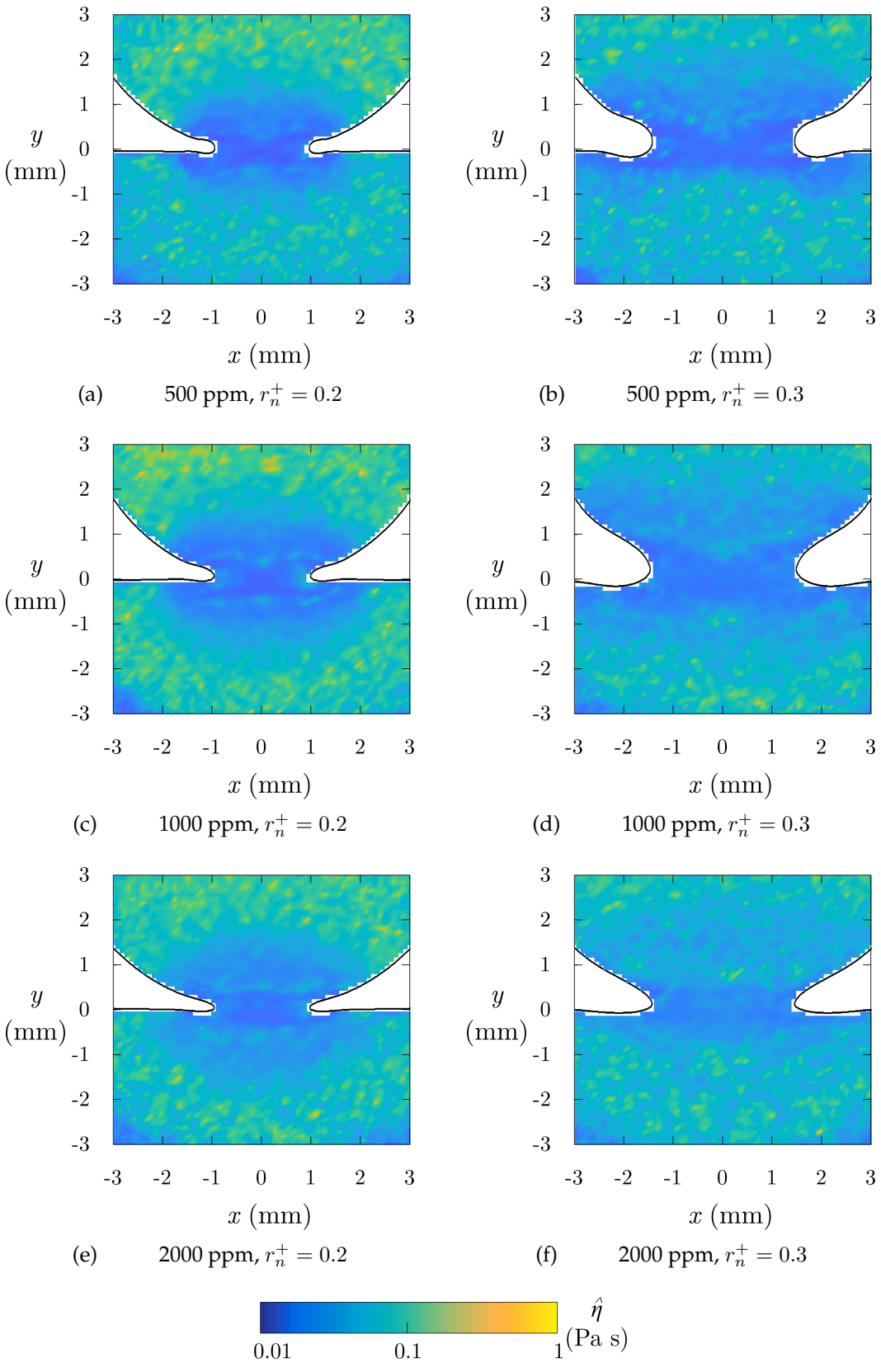

Figure 6.23: Contours of the effective local viscosity computed from eq. 3.4 and eq. 2.21 using the BF PIV measurements for the shear-thinning solutions at two time-steps.

the lowest values of viscosity are gathered close to the neck region, as can be seen from Fig. 6.23. In the region of the vortices, fluctuations of the local viscosity values are measured, while even orders of magnitude differences are computed between the varying xanthan gum concentrated solutions. The viscosity variations affect the circulation of the vortices and the vorticity values, by changing the gradients of the velocity close to their centre.

Generally, similar phenomena are observed for all solutions. The increase of xanthan gum delays the neck radius r_n expansion, in a manner that can be attributed to Newtonian behaviour, due to the high shear at the neck. The curvature at the neck R_n is also affected in an equivalent way, showing sharper neck shapes as the concentration of xanthan gum increases. The vortices formed differ between the cases, most notably for the higher xanthan gum concentrations. Both the vorticity and circulation are drastically decreased with the increase of the polymer concentration. The shear rate variations provide interesting patterns in the viscosity contours, with quasi-constant Newtonian-like behaviour close to the rupture, and high shear-thinning behaviour at the region of the vortices. The viscosity away from the rupture point reaches values close to 100 times the viscosity close to the neck.

In this Chapter, the dynamics of coalescence were explored in two systems. Firstly, a drop coalescing with the interface of a dual continuous liquid-liquid pipe flow is investigated with PLIF and PIV measurements. The neck radius is tracked in time for the whole coalescence phenomenon and scaling laws are able to capture the dynamics during the initial neck expansion. PIV measurements revealed a strong vertical motion from the drop towards the bulk, which generated two counteracting vortices on each side of the drop. This behaviour is in accordance with previous efforts for confined systems with no cross-flow.

Further drop-interface coalescence experiments were conducted in a Hele-Shaw cell, where the addition of surface active agents and polymers was explored. The neck expansion velocity was reduced when surfactants were present in the outer phase, while scaling laws revealed a higher concentration at the neck region than in the bulk. Interestingly, two counter-rotating vortices were generated on each side of the drop that had not been recorded experimentally before. The shape of the streamlines agreed well with simulations. As the surfactant concentration increased, the interface shape was deformed and the propagation direction of the vortices changed. When xanthan gum was added in the aqueous coalescing phase, the dynamics were significantly slowed down. Good agreement with scaling laws was found, when the infinite shear viscosity was taken for the neck velocity. Supported also by similar results for the neck curvature, it became clear that the dynamics of the neck were Newtonian for the xanthan gum concentrations investigated. Due to the shear rate gradients inside the coalescing drops, variations of viscosity affecting the resulting velocity fields were recorded.

Chapter 7

Conclusion

An overview of the main findings of this work along with their impact are discussed next. The conclusions from each Chapter are drawn and recommendations for further studies are suggested.

7.1 Final remarks

In this work, unstable concentrated dispersed liquid-liquid pipe flows were generated through enhanced inlet mixing for relatively low mixture velocities and their evolution along the pipe was studied. Both conductivity and optical measurements were utilised at several axial locations to acquire information on the phase fractions, drop size distributions and velocity changes. Different modelling approaches were used to predict the separation properties and flow characteristics of the dispersions.

In Chapter 2, the main literature was summarised, illustrating the need for detailed measurements and observations during spatially developing dispersed flows at high dispersed phase fractions. A mechanistic approach based on batch settlers was followed to formulate a model predicting the separation properties of dispersions in pipes. In order to capture the drop and continuous phase velocity inside the pipe, CFD numerical simulations were performed based on the mixture approach with a drop transport equation taking into account shear-induced diffusion, lift and gravity.

In Chapter 3, the characteristics of the two flow loops to study the evolution of the dispersed pipe flows, and of the Hele-Shaw cell to study coalescence were provided. The basic principles behind the experimental techniques were explained and their application to the present systems was illustrated. A detailed analysis was given on the signal treatment method followed for the DCP measurements, on the image analysis algorithms developed to obtain the phase fractions and the drop sizes, and on the methodologies used to acquire the local velocities of both phases.

In Chapter 4, the experiments conducted in the pilot-scale flow loop facility were presented. The dispersions were generated through a multi-nozzle inlet, which provided relatively narrow drop size distributions. It was shown that the cross-flow velocity was the main contributing factor for the final drop size distributions from the nozzles and the experimental data matched well with simple predictions based

on force balance at the nozzle. The flow structures developed were highly unstable for the lower mixture velocities, with changes in the flow patterns occuring downstream the inlet. Local measurements of the phase fractions showed an increase in the dense-packed layer thickness along the pipe that depended on the mixture velocity and input dispersed phase fraction. Drop size measurements at the three axial locations showed a growth of the drops as they flow, while breakup could be neglected. The coalescence model by Henschke et al. (2002) for batch settlers (vessel separators) provided good predictions for the separation of the dispersions in pipes, as the velocities close to the dense-packed layer are very low, due to enhanced local viscosity values.

In Chapter 5, the matched refractive index flow loop was investigated, where the dispersions were generated through a helical static mixer. For the higher velocity cases it was found that the flow field was affected by the mixer for only a few diameters downstream – these effects decayed soon due to viscous effects. The dispersions generated from the mixer illustrated narrow drop size distributions, which agreed well with literature correlations. Velocity profiles of oil in water dispersions revealed asymmetry as the floatation of the oil drops took place, with higher continuous phase velocities present at the drop-free layer. Lower velocities at the dense-packed layer indicate high apparent viscosity effects – very similar to suspension flows. Driven by these results, CFD simulations based on the mixture modelling approach were conducted. The dominant mechanism of drop separation was gravity, but shear-induced diffusion and lift were also both found to affect the motion of the drops. Agreement was found between the experiments and the simulations, establishing that dispersions behave as suspensions of solid rigid spheres – consistent with recent experimental findings (Pouplin et al. 2011; Abbas et al. 2017).

In Chapter 6, coalescence in the dual-continuous pattern in the pipe was shown between a drop and an interface. It was found that the dynamics of the neck expansion match the scaling laws for confined systems, while the velocity field presented similar structures to confined systems (Mohamed-Kassim and Longmire 2004). Further analysis was conducted in a Hele-Shaw cell, where the rupture point is localised and good resolution of the coalescence can be obtained. The addition of surface active agents in the coalescing phase induced a delay in the neck expansion. It was indirectly found by comparisons with scaling laws, that a higher concentration of surfactant was present close to the neck region, which agrees with recent simulations (Martin and Blanchette 2015). The interface deformed with the surfactants due to elasticity changes and the advection of the vortices was altered. Coalescence with shear-thinning fluids illustrated a quasi-constant viscosity at the neck for the early times. The high shear rates close to the neck presented an almost Newtonian behaviour of the solutions. However, the vortices inside the drop were significantly altered due to large viscosity changes, with lower values of the vorticity and circulation recorded, as the concentration of the polymer increased.

7.2 Future work and perspectives

The current work has taken upon some challenging tasks and answered some long-standing questions in regards to the behaviour of unstable liquid-liquid dispersions and the coalescence dynamics. It has also raised questions that cannot be currently answered – fuelling future endeavours in the field.

The main contribution from this work stems from the detailed measurements acquired in very complex multi-phase flow environments. Drop size measurements in the past have recorded very high uncertainties (Maaß et al. 2011; Schümann et al. 2016b) in similar systems. The DCP was able to capture well the drop sizes with uncertainties estimated at 30%. It would be interesting to use the DCP in different orientations, to study the drop size distributions in the cross-section, by considering three-dimensional effects. This will allow in depth comparisons with recent efforts on three-dimensional PBE models (Bourdillon et al. 2016).

The planar laser-based flow measurements, provided an insight on the flow in the middle plane of the pipe by matching the refractive index of the two liquids. However, stereo or volumetric measurements could provide more information on the velocity field along the transverse direction and also reveal non-Newtonian shear-thinning effects that can start appearing for high drop concentrations at the dense-packed region (Conan 2007).

Focusing on small-scale phenomena both experimentally and numerically can provide detailed information on the local flow characteristics. It was discussed in Sec. 2.1.2.3, that the drops can alter the turbulent levels in the continuous phase. Matas et al. (2003) illustrated that the transition to turbulence can either be delayed or advanced depending on the concentration and sizes of the drops. The interaction between drops and the flow field of the carrier phase remains unresolved (Maxey 2017). A dedicated study needs to be conducted by controlling the size and the concentration of the drops independently, and perform very high resolution measurements to capture the fluctuating motions of both phases. In laminar conditions, pseudo-turbulence can be expected due to the fluctuations in the wake of the drops. The buoyancy of the drops will increase the complexity of the problem.

The derived separation model based on batch settlers is a simple but physics-based approach, that is able to capture the main mechanisms appearing in the pipe. Its predictions can be further extended if a drop size distribution instead of a single mean drop size is considered, by incorporating PBE. Coalescence was found experimentally to also take place in the dilute layer of the dispersions, which the model in its present form neglects. Taking into account the hindrance of the vertical velocity due to the mean cross-flow can also drastically improve the current empiricism in the approach.

The CFD simulations performed, gave very good predictions of the macroscopic phenomena by capturing the motion of the drops due to gravity, lift and collisions induced from shear, concentration and viscosity gradients, when a single drop size

is considered. It would be interesting to see how a polydisperse drop population will affect shear-induced diffusion and lift dynamics will change. A recent effort was conducted by Marmet et al. (2017) for Poiseuille flows, but with Brownian simulations. Extending the current simulations to a three-dimensional model, able to capture the velocity field and the phase fraction in the pipe cross-section as it develops, could provide a better insight on the spatial configuration of the phases and the resulting velocity field. Considering non-Newtonian effects for the very high concentrated regions might also help improve current predictions.

As discussed in the last paragraph of Sec. 6.1, coalescence in pipe flow was not extensively studied in the present work, due to limitations in the cross-flow velocities, layer thickness and size of coalescing drops, as all these parameters were interchangeably linked. Isolating these effects can provide a better understanding and help improve modelling routines. Studying coalescence in confined systems for a wider range of surface active agents and polymers could provide a more in depth understanding of the effect of complex fluids, which are related for pipe flows, as they are usually naturally present in most industrial applications.

Not a single of the aforementioned tasks is a simple undertaking and should be by no means underestimated. Each one presents challenges of its own – both experimentally and numerically. However, the outcomes can significantly improve the current knowledge and overcome the present limitations in vexing issues of multiphase flows, especially for the oil and gas industry. While the recent efforts in flow assurance modelling lie mainly in two-fluid formulations, by employing separate momentum equations for each phase, current trends seem to shift towards powerful mixture models, able to tackle rudimentary issues such as hydrates and hydrodynamic slugs (Danielson 2012).

Appendix A

Geometrical Closures for the Separation Model

In this Appendix, the geometrical closures needed to transform the separation model from batch settlers by Henschke et al. (2002) to pipe flows with a circular cross-section are provided similarly to Pereyra et al. (2013). As the batch settler model is developed for a rectangular beaker, the heights of the dispersed and continuous phase computed respectively from eqs. 2.28 and 2.29 need to be translated to cross-sectional pipe areas.

The link between the heights of of the continuous phase h_c and of the dispersed phase h_d with their respective areas A_c and A_d are given by

$$A_c = \frac{D^2}{4}\left[\pi - \arccos\left(2\frac{h_c}{D} - 1\right) + \left(2\frac{h_c}{D} - 1\right)\sqrt{1 - \left(2\frac{h_c}{D} - 1\right)^2}\right] \tag{A.1}$$

$$A_d = \frac{D^2}{4}\left[\pi - \arccos\left(2\frac{h_d}{D} - 1\right) + \left(2\frac{h_d}{D} - 1\right)\sqrt{1 - \left(2\frac{h_d}{D} - 1\right)^2}\right]. \tag{A.2}$$

In order to compute χ in the model, the derivative of the area of the dispersed phase needs to be computed as

$$\frac{\partial A_d}{\partial h_d} = 2\sqrt{h_d\,(D - h_d)}. \tag{A.3}$$

The area of the dense-packed region is computed from the mass balance of eq. 2.32 and can be transformed to a respective height with the following similar formulation as

$$A_p = \frac{D^2}{4}\left[\pi - \arccos\left(2\tfrac{h_p+h_d}{D} - 1\right) + \left(2\tfrac{h_p+h_d}{D} - 1\right)\sqrt{1 - \left(2\tfrac{h_p+h_d}{D} - 1\right)^2}\right] - A_d \tag{A.4}$$

and the respective derivatives

$$\frac{\partial A_p}{\partial h_p} = 2\sqrt{(h_d + h_p)\,(D - h_p - h_d)} \tag{A.5}$$

$$\frac{\partial A_p}{\partial h_d} = 2\sqrt{(h_d + h_p)\,(D - h_p - h_d)} - 2\sqrt{h_d\,(D - h_d)}, \tag{A.6}$$

which are the final equations needed for the computation of χ and to close the separation model given in Sec. 2.2.3 and Sec. 2.3.1.1.

Appendix B

Geometrical and Boundary Characteristics of the Mixture Model

The mixture model developed and presented in Sec. 2.2.1 and Sec. 2.2.2 is solved numerically in COMSOL Multiphysics version 5.2a using the finite element method (FEM).

The geometry is built in a two-dimensional x-y plane, of height (axis of gravity) equal to the diameter of the pipe $\Delta y = D = 26$ mm and length of approximately $\Delta x = 150D$, to allow comparisons with the measurements at $x = 135D$ and at the same time avoid any outlet effects without significantly increasing the computational domain.

The mesh is generated by splitting the domain in quadrilateral elements. A grid study is conducted to find a suitable number of elements that provide accurate enough data, but keeping the computational cost down. Normalised velocity and in-situ dispersed phase fraction changes are investigated as the number of elements is altered. The results are shown in Fig. B.1 for a typical case. It is clearly shown that approximately a million elements are enough to provide the results with good accuracy.

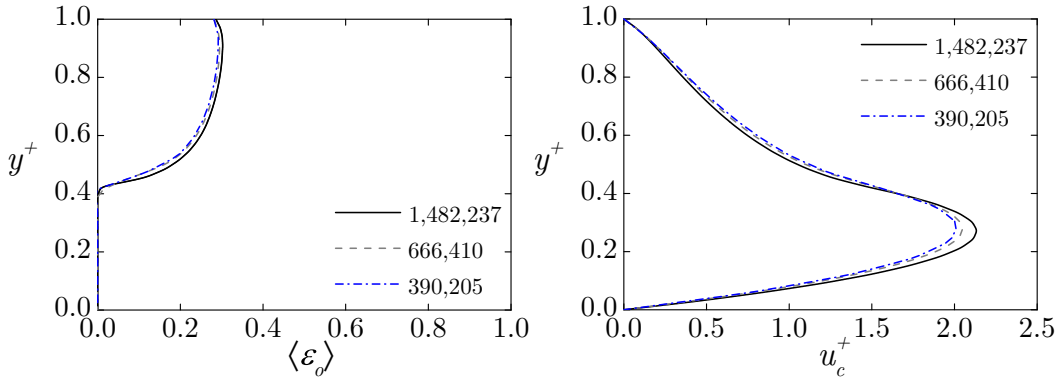

Figure B.1: Grid study illustrating the change in the vertical profiles of (a) the in-situ oil (dispersed phase) concentration and (b) the velocity of the continuous phase.

A numerical simulation of Poiseuille flow can be performed either by fixing the driving force (mean pressure gradient) or by keeping the mass flux constant. In the present simulations the latter approach is used. Constant velocity along y is prescribed at the inlet, equal to the mixture velocity u_m from each experimental case. The input dispersed phase fraction is constant along y (homogeneous) and the drop size is taken as the average d_{32} from the experiments. The properties of the liquids are given as measured. The no-slip condition is considered for the top and bottom walls and atmospheric pressure for the outlet.

Bibliography

Aarts, D. G.A. L., and H. N. W. Lekkerkerker. 2008. Droplet coalescence: drainage, film rupture and neck growth in ultralow interfacial tension systems. *Journal of Fluid Mechanics* 606:275–94.

Aarts, D. G.A. L., H. N. W. Lekkerkerker, H. Guo, G. H. Wegdam, and D. Bonn. 2005. Hydrodynamics of droplet coalescence. *Physical Review Letters* 95 (16): 164503.

Abbas, M., A. Pouplin, O. Masbernat, A. Liné, and S. Décarre. 2017. Pipe flow of a dense emulsion: Homogeneous shear-thinning or shear-induced migration? *AIChE Journal:* In press.

Acharya, T., and A. K. Ray. 2005. *Image processing: principles and applications.* John Wiley & Sons.

Acrivos, A., and T. S. Lo. 1978. Deformation and breakup of a single slender drop in an extensional flow. *Journal of Fluid Mechanics* 86 (4): 641–72.

Adrian, R. J., and J. Westerweel. 2011. *Particle Image Velocimetry.* 30. Cambridge University Press.

Al-Wahaibi, T., and P. Angeli. 2007. Transition between stratified and non-stratified horizontal oil–water flows. Part i: stability analysis. *Chemical Engineering Science* 62 (11): 2915–28.

Al-Wahaibi, T., and P. Angeli. 2008. Droplet size and velocity in dual continuous horizontal oil–water flows. *Chemical Engineering Research and Design* 86 (1): 83–93.

Angeli, P., and G. F. Hewitt. 2000a. Flow structure in horizontal oil–water flow. *International Journal of Multiphase Flow* 26 (7): 1117–40.

Angeli, P., and G. F. Hewitt. 2000b. Drop size distributions in horizontal oil-water dispersed flows. *Chemical Engineering Science* 55 (16): 3133–43.

Arirachakaran, S., K. D. Oglesby, M. S. Malinowsky, O. Shoham, and J. P. Brill. 1989. An analysis of oil/water flow phenomena in horizontal pipes. In *Spe production operations symposium.* Society of Petroleum Engineers.

Arratia, P. E., J. P. Gollub, and D. J. Durian. 2008. Polymeric filament thinning and breakup in microchannels. *Physical Review E* 77 (3): 036309.

Aryafar, H., and H. P. Kavehpour. 2006. Drop coalescence through planar surfaces. *Physics of Fluids* 18 (7): 072105.

Aryafar, H., and H. P. Kavehpour. 2008. Hydrodynamic instabilities of viscous coalescing droplets. *Physical Review E* 78 (3): 037302.

Asmolov, E. S. 1999. The inertial lift on a spherical particle in a plane Poiseuille flow at large channel Reynolds number. *Journal of Fluid Mechanics* 381:63–87.

Ata, S., R. J. Pugh, and G. J. Jameson. 2011. The influence of interfacial ageing and temperature on the coalescence of oil droplets in water. *Colloids and Surfaces A: Physicochemical and Engineering Aspects* 374 (1): 96–101.

Augier, F., O. Masbernat, and P. Guiraud. 2003. Slip velocity and drag law in a liquid-liquid homogeneous dispersed flow. *AIChE Journal* 49 (9): 2300–16.

Augier, F., P. Guiraud, and O. Masbernat. 2007. Fluctuating motion in a homogeneous liquid-liquid dispersed flow at high phase fraction. *Physics of Fluids* 19 (5): 057105.

Azzopardi, B. J., and G. F. Hewitt. 1997. Maximum drop sizes in gas-liquid flows. *Multiphase Science and Technology* 9 (2).

Baek, S. J., and S. J. Lee. 1996. A new two-frame particle tracking algorithm using match probability. *Experiments in Fluids* 22 (1): 23–32.

Balachandar, S., and J. K. Eaton. 2010. Turbulent dispersed multiphase flow. *Annual Review of Fluid Mechanics* 42:111–33.

Barkley, D. 2016. Theoretical perspective on the route to turbulence in a pipe. *Journal of Fluid Mechanics* 803.

Barmak, I., A. Gelfgat, H. Vitoshkin, A. Ullmann, and N. Brauner. 2016. Stability of stratified two-phase flows in horizontal channels. *Physics of Fluids* 28 (4): 044101.

Baroudi, L., S. R. Nagel, J. F. Morris, and T. Lee. 2015. Dynamics of viscous coalescing droplets in a saturated vapor phase. *Physics of Fluids* 27 (12): 121702.

Barral, A. H. 2014. Stratified wavy oil-water flows. PhD diss., University College London.

Barral, A. H., and P. Angeli. 2014. Spectral density analysis of the interface in stratified oil–water flows. *International Journal of Multiphase Flow* 65:117–26.

Belfort, G., R. H. Davis, and A. L. Zydney. 1994. The behavior of suspensions and macromolecular solutions in crossflow microfiltration. *Journal of Membrane Science* 96 (1-2): 1–58.

Berkman, P. D., and R. V. Calabrese. 1988. Dispersion of viscous liquids by turbulent flow in a static mixer. *AIChE Journal* 34 (4): 602–9.

Bird, R. B., W. E. Stewart, and E. N. Lightfoot. 1960. Transport phenomena. *New York:* 413.

Blaisot, J. B., and J. Yon. 2005. Droplet size and morphology characterization for dense sprays by image processing: application to the Diesel spray. *Experiments in Fluids* 39 (6): 977–94.

Blanchette, F., and T. P. Bigioni. 2006. Partial coalescence of drops at liquid interfaces. *Nature Physics* 2 (4): 254.

Blanchette, F., and T. P. Bigioni. 2009. Dynamics of drop coalescence at fluid interfaces. *Journal of Fluid Mechanics* 620:333–52.

Blanchette, F., L. Messio, and J. W. Bush. 2009. The influence of surface tension gradients on drop coalescence. *Physics of Fluids* 21 (7): 072107.

Bolton, G. T., M. Bennett, M. Wang, C. Qiu, M. Wright, K. M. Primrose, S. J. Stanley, and D. Rhodes. 2007. Development of an electrical tomographic system for operation in a remote, acidic and radioactive environment. *Chemical Engineering Journal* 130 (2): 165–69.

Bordoloi, A. D., and E. K. Longmire. 2012. Effect of neighboring perturbations on drop coalescence at an interface. *Physics of Fluids* 24 (6): 062106.

Bourdillon, A. C., P. G. Verdin, and C. P. Thompson. 2016. Numerical simulations of drop size evolution in a horizontal pipeline. *International Journal of Multiphase Flow* 78:44–58.

Brauner, N., and M. D. Maron. 1992. Stability analysis of stratified liquid-liquid flow. *International Journal of Multiphase Flow* 18 (1): 103–21.

Brauner, N., M. D. Maron, and J. Rovinsky. 1998. A two-fluid model for stratified flows with curved interfaces. *International Journal of Multiphase Flow* 24 (6): 975–1004.

Brauner, N. 2001. The prediction of dispersed flows boundaries in liquid–liquid and gas–liquid systems. *International Journal of Multiphase Flow* 27 (5): 885–910.

Brauner, N. 2003. Liquid-liquid two-phase flow systems. In *Modelling and experimentation in two-phase flow,* 221–79. Springer.

Brauner, N., and A. Ullmann. 2002. Modeling of phase inversion phenomenon in two-phase pipe flows. *International Journal of Multiphase Flow* 28 (7): 1177–204.

Bretherton, F. P. 1962. The motion of rigid particles in a shear flow at low Reynolds number. *Journal of Fluid Mechanics* 14 (2): 284–304.

Brevis, W., Y. Niño, and G. H. Jirka. 2011. Integrating cross-correlation and relaxation algorithms for particle tracking velocimetry. *Experiments in Fluids* 50 (1): 135–47.

Brinkman, H. C. 1952. The viscosity of concentrated suspensions and solutions. *The Journal of Chemical Physics* 20 (4): 571–71.

Burton, J. C., and P. Taborek. 2007. Role of dimensionality and axisymmetry in fluid pinch-off and coalescence. *Physical Review Letters* 98 (22): 224502.

Case, S. C., and S. R. Nagel. 2008. Coalescence in low-viscosity liquids. *Physical Review Letters* 100 (8): 084503.

Castanet, G., P. Dunand, O. Caballina, and F. Lemoine. 2013. High-speed shadow imagery to characterize the size and velocity of the secondary droplets produced by drop impacts onto a heated surface. *Experiments in Fluids* 54 (3): 1489.

Chakrabarti, D. P., G. Das, and P. K. Das. 2007. Identification of stratified liquid–liquid flow through horizontal pipes by a non-intrusive optical probe. *Chemical Engineering Science* 62 (7): 1861–76.

Chan, D. Y., E. Klaseboer, and R. Manica. 2011. Film drainage and coalescence between deformable drops and bubbles. *Soft Matter* 7 (6): 2235–64.

Charles, G. E., and S. G. Mason. 1960a. The coalescence of liquid drops with flat liquid/liquid interfaces. *Journal of Colloid Science* 15 (3): 236–67.

Charles, G. E., and S. G. Mason. 1960b. The mechanism of partial coalescence of liquid drops at liquid/liquid interfaces. *Journal of Colloid Science* 15 (2): 105–22.

Chen, J.-H., and G. M. Faeth. 2001. Continuous-phase properties of homogeneous particle-laden turbulent flows. *AIAA Journal* 39 (1): 180–83.

Chen, J.-D. 1985. A model of coalescence between two equal-sized spherical drops or bubbles. *Journal of Colloid and Interface Science* 107 (1): 209–20.

Chen, S. J., and D. R. Libby. 1978. Gas-liquid and liquid-liquid dispersions in a Kenics mixer. In *71st annual AIChE meeting*, 8–18.

Chen, Y., C. Shen, and G. P. Peterson. 2015. Hydrodynamics and morphologies of droplet coalescence. *Industrial & Engineering Chemistry Research* 54 (37): 9257–62.

Chinaud, M., V. Voulgaropoulos, and P. Angeli. 2016. Surfactant effects on the coalescence of a drop in a Hele-Shaw cell. *Physical Review E* 94 (3): 033101.

Chinaud, M., K. H. Park, and P. Angeli. 2017. Flow pattern transition in liquid-liquid flows with a transverse cylinder. *International Journal of Multiphase Flow* 90:1–12.

Choi, S. J., and W. R. Schowalter. 1975. Rheological properties of nondilute suspensions of deformable particles. *Physics of Fluids* 18 (4): 420–27.

Chow, A. W., and G. G. Fuller. 1984. Response of moderately concentrated xanthan gum solutions to time-dependent flows using two-color flow birefringence. *Journal of Rheology* 28 (1): 23–43.

Clift, R., J. R. Grace, and M. E. Weber. 2005. *Bubbles, drops, and particles.* Courier Corporation.

Collins, S. B., and J. G. Knudsen. 1970. Drop-size distributions produced by turbulent pipe flow of immiscible liquids. *AIChE Journal* 16 (6): 1072–80.

Conan, C. 2007. Etude expérimentale et modélisation des écoulements liquide-liquide en conduite horizontale. PhD diss., Institut National Polytechnique de Toulouse.

Conan, C., O. Masbernat, S. Décarre, and A. Liné. 2007. Local hydrodynamics in a dispersed-stratified liquid–liquid pipe flow. *AIChE Journal* 53 (11): 2754–68.

Cox, R. G., and S. K. Hsu. 1977. The lateral migration of solid particles in a laminar flow near a plane. *International Journal of Multiphase Flow* 3 (3): 201–22.

Danielson, T. J. 2012. Transient multiphase flow: past, present, and future with flow assurance perspective. *Energy & Fuels* 26 (7): 4137–44.

De Malmazet, E., F. Risso, O. Masbernat, and V. Pauchard. 2015. Coalescence of contaminated water drops at an oil/water interface: Influence of micro-particles. *Colloids and Surfaces A: Physicochemical and Engineering Aspects* 482:514–28.

Dodd, M. S., and A. Ferrante. 2016. On the interaction of Taylor length scale size droplets and isotropic turbulence. *Journal of Fluid Mechanics* 806:356–412.

Duchemin, L., J. Eggers, and C Josserand. 2003. Inviscid coalescence of drops. *Journal of Fluid Mechanics* 487:167–78.

Edomwonyi-Otu, L. C., and P. Angeli. 2015. Pressure drop and holdup predictions in horizontal oil–water flows for curved and wavy interfaces. *Chemical Engineering Research and Design* 93:55–65.

Eggers, J., J. R. Lister, and H. A. Stone. 1999. Coalescence of liquid drops. *Journal of Fluid Mechanics* 401:293–310.

Eggleton, C. D., Y. P. Pawar, and K. J. Stebe. 1999. Insoluble surfactants on a drop in an extensional flow: a generalization of the stagnated surface limit to deforming interfaces. *Journal of Fluid Mechanics* 385:79–99.

Einstein, A. 1906. Calculation of the viscosity-coefficient of a liquid in which a large number of small spheres are suspended in irregular distribution. *Ann. Phys. Leipzig* 19:286–306.

Ekambara, K., R. S. Sanders, K. Nandakumar, and J. H. Masliyah. 2008. CFD simulation of bubbly two-phase flow in horizontal pipes. *Chemical Engineering Journal* 144 (2): 277–88.

El-Hamouz, A. M., and A. C. Stewart. 1996. On-line drop size distribution measurement of oil-water dispersion using a par-tec m300 laser backscatter instrument. In *Spe annual technical conference and exhibition.* Society of Petroleum Engineers.

Eri, A., and K. Okumura. 2010. Bursting of a thin film in a confined geometry: rimless and constant-velocity dewetting. *Physical Review E* 82 (3): 030601.

Fezzaa, K., and Y. Wang. 2008. Ultrafast x-ray phase-contrast imaging of the initial coalescence phase of two water droplets. *Physical Review Letters* 100 (10): 104501.

Frising, T., C. Noïk, and C. Dalmazzone. 2006. The liquid/liquid sedimentation process: from droplet coalescence to technologically enhanced water/oil emulsion gravity separators: A review. *Journal of Dispersion Science and Technology* 27 (7): 1035–57.

Gac, J. M., and L. Gradoń. 2011. A two-dimensional modeling of binary coalescence time using the two-color lattice-Boltzmann method. *Journal of Aerosol Science* 42 (5): 355–63.

Galinat, S., O. Masbernat, P. Guiraud, C. Dalmazzone, and C. Noïk. 2005. Drop break-up in turbulent pipe flow downstream of a restriction. *Chemical Engineering Science* 60 (23): 6511–28.

Galinat, S. 2005. Etude expérimentale de la rupture de gouttes dans un écoulement turbulent. PhD diss., Institut National Polytechnique de Toulouse.

Garnier, C., M. Lance, and J. L. Marié. 2002. Measurement of local flow characteristics in buoyancy-driven bubbly flow at high void fraction. *Experimental Thermal and Fluid Science* 26 (6): 811–15.

Ghanem, A., T. Lemenand, D. Della Valle, and H. Peerhossaini. 2014. Static mixers: Mechanisms, applications, and characterization methods–A review. *Chemical Engineering Research and Design* 92 (2): 205–28.

Ghoumrassi-Barr, S., and D. Aliouche. 2016. A rheological study of xanthan polymer for enhanced oil recovery. *Journal of Macromolecular Science, Part B* 55 (8): 793–809.

Gianotti, D., and A. Nadim. 2003. Fluid drop coalescence in a Hele-Shaw cell. *Senior Thesis, Harvey Mudd College.*

Gilet, T., K. Mulleners, J.-P. Lecomte, N. Vandewalle, and S. Dorbolo. 2007. Critical parameters for the partial coalescence of a droplet. *Physical Review E* 75 (3): 036303.

Giribabu, K., and P. Ghosh. 2007. Adsorption of nonionic surfactants at fluid–fluid interfaces: importance in the coalescence of bubbles and drops. *Chemical Engineering Science* 62 (11): 3057–67.

Goel, S., and A. Ramachandran. 2017. The suppression of droplet-droplet coalescence in a sheared yield stress fluid. *Journal of Colloid and Interface Science* 492:199–206.

Grassi, B., D. Strazza, and P. Poesio. 2008. Experimental validation of theoretical models in two-phase high-viscosity ratio liquid–liquid flows in horizontal and slightly inclined pipes. *International Journal of Multiphase Flow* 34 (10): 950–65.

Grave, E. J., M. D. Olson, A. E. Menchaca, R. W. Westra, and M. R. Akdim. 2015. Performance testing of an inline electrocoalescer device with medium and heavy crudes. *Oil and Gas Facilities* 4 (05): 56–65.

Gross, M., I. Steinbach, D. Raabe, and F. Varnik. 2013. Viscous coalescence of droplets: A lattice Boltzmann study. *Physics of Fluids* 25 (5): 052101.

Guildenbecher, D. R., L. Engvall, J. Gao, T. W. Grasser, P. L. Reu, and J. Chen. 2014. Digital in-line holography to quantify secondary droplets from the impact of a single drop on a thin film. *Experiments in Fluids* 55 (3): 1670.

Habchi, C., T. Lemenand, D. Della Valle, and H. Peerhossaini. 2009. Liquid/liquid dispersion in a chaotic advection flow. *International Journal of Multiphase Flow* 35 (6): 485–97.

Hamad, F. A., and P. Ganesan. 2015. Effect of drops on turbulence of kerosene–water two-phase flow in vertical pipe. *International Journal of Heat and Fluid Flow* 56:152–59.

Hamad, F. A., B. K. Pierscionek, and H. H. Bruun. 2000. A dual optical probe for volume fraction, drop velocity and drop size measurements in liquid-liquid two-phase flow. *Measurement Science and Technology* 11 (9): 1307.

Hampton, R. E., A. A. Mammoli, A. L. Graham, N. Tetlow, and S. A. Altobelli. 1997. Migration of particles undergoing pressure-driven flow in a circular conduit. *Journal of Rheology* 41 (3): 621–40.

Han, Y. F., N. D. Jin, Z. Q. Yin, Y. Y. Ren, and Y. Gu. 2017. Measurement of oil bubble size distribution in oil-in-water emulsions using a distributed dual-sensor probe array. *Experimental Thermal and Fluid Science* 86:204–23.

Hanzevack, E. L., and G. D. Demetriou. 1989. Effect of velocity and pipeline configuration on dispersion in turbulent hydrocarbon-water flow using laser image processing. *International Journal of Multiphase Flow* 15 (6): 985–96.

Hanzevack, E. L., C. B. Bowers, and C.-H. Ju. 1987. Study of two-phase flow by laser image processing. *AIChE Journal* 33 (12): 2003–7.

Hartland, S. 1981. Coalescence in dense-packed gas/liquid and liquid/liquid dispersions. *Tenside Det* 18:178–89.

Hartland, S., and S. A. K. Jeelani. 1988. Prediction of sedimentation and coalescence profiles in a decaying batch dispersion. *Chemical Engineering Science* 43 (9): 2421–29.

Hele-Shaw, H. S. 1898. The flow of water. *Nature* 58 (1489): 33–36.

Henschke, M. 1994. *Dimensionierung liegender flüssig-flüssig-abscheider anhand diskontinuierlicher absetzversuche.* VDI-Verlag.

Henschke, M., L. H. Schlieper, and A. Pfennig. 2002. Determination of a coalescence parameter from batch-settling experiments. *Chemical Engineering Journal* 85 (2): 369–78.

Hewakandamby, B. N., A. U. Kanu, B. J. Azzopardi, and G. Kouba. 2014. Parametric study of churn flow in large diameter pipes. In *Proceedings of fourth asme joint us–european fluids engineering summer meeting. fedsm2014.*

Hinze, J. O. 1955. Fundamentals of the hydrodynamic mechanism of splitting in dispersion processes. *AIChE Journal* 1 (3): 289–95.

Hinze, J. O. 1959. Turbulence: An introduction to its mechanisms and theory. *Mechanical Engineering* 1396.

Holden, P. J., M. Wang, R. Mann, F. J. Dickin, and R. B. Edwards. 1998. Imaging stirred-vessel macromixing using electrical resistance tomography. *AIChE Journal* 44 (4): 780–90.

Hopper, R. W. 1990. Plane Stokes flow driven by capillarity on a free surface. *Journal of Fluid Mechanics* 213:349–75.

Hu, B. 2006. Experimental and theoretical investigations of phase inversion in liquid-liquid dispersions. PhD diss., University College London (University of London).

Hu, B., and P. Angeli. 2006. Phase inversion and associated phenomena in oil-water vertical pipeline flow. *The Canadian Journal of Chemical Engineering* 84 (1): 94–107.

Hu, B., P. Angeli, O. K. Matar, C. J. Lawrence, and G. F. Hewitt. 2006. Evaluation of drop size distribution from chord length measurements. *AIChE Journal* 52 (3): 931–39.

Hu, S., and R. C. Kinter. 1955. The fall of single liquid drops through water. *AIChE Journal* 1 (1): 42–48.

Huang, T., G. J. T. Yang, and G. Y. Tang. 1979. A fast two-dimensional median filtering algorithm. *IEEE Transactions on Acoustics, Speech, and Signal Processing* 27 (1): 13–18.

Hughmark, G. A. 1971. Drop breakup in turbulent pipe flow. *AIChE Journal* 17 (4): 1000–0.

Ibarra, R., C. N. Markides, and O. K. Matar. 2014. A review of liquid-liquid flow patterns in horizontal and slightly inclined pipes. *Multiphase Science and Technology* 26 (3).

Im, K.-S., K. Fezzaa, Y. J. Wang, X. Liu, J. Wang, and M.-C. Lai. 2007. Particle tracking velocimetry using fast x-ray phase-contrast imaging. *Applied Physics Letters* 90 (9): 091919.

Ioannou, K. 2006. Phase inversion theoretical and experimental investigations in oil/water dispersed flows in horizontal pipelines. PhD diss., University College London (University of London).

Ioannou, K., O. J. Nydal, and P. Angeli. 2005. Phase inversion in dispersed liquid–liquid flows. *Experimental Thermal and Fluid Science* 29 (3): 331–39.

Ishii, K., and H. Hashimoto. 1980. Lateral migration of a spherical particle in flows in a circular tube. *Journal of the Physical Society of Japan* 48 (6): 2144–55.

Ishii, M., and N. Zuber. 1979. Drag coefficient and relative velocity in bubbly, droplet or particulate flows. *AIChE Journal* 25 (5): 843–55.

Jeong, J., and F. Hussain. 1995. On the identification of a vortex. *Journal of Fluid Mechanics* 285:69–94.

Kalyon, D. M. 2005. Apparent slip and viscoplasticity of concentrated suspensions. *Journal of Rheology* 49 (3): 621–40.

Kamp, J., J. Villwock, and M. Kraume. 2017. Drop coalescence in technical liquid/liquid applications: A review on experimental techniques and modeling approaches. *Reviews in Chemical Engineering* 33 (1): 1–47.

Kapur, N., and P. H. Gaskell. 2007. Morphology and dynamics of droplet coalescence on a surface. *Physical Review E* 75 (5): 056315.

Karabelas, A. J. 1978. Droplet size spectra generated in turbulent pipe flow of dilute liquid/liquid dispersions. *AIChE Journal* 24 (2): 170–80.

Kaushal, D. R., and Y. Tomita. 2007. Experimental investigation for near-wall lift of coarser particles in slurry pipeline using γ-ray densitometer. *Powder technology* 172 (3): 177–87.

Kavehpour, H. P. 2015. Coalescence of drops. *Annual Review of Fluid Mechanics* 47:245–68.

Keller, J. B., and M. J. Miksis. 1983. Surface tension driven flows. *SIAM Journal on Applied Mathematics* 43 (2): 268–77.

Khagram, M., R. K. Gupta, and T. Sridhar. 1985. Extensional flow of xanthan gum solutions. *Journal of Rheology* 29 (2): 191–207.

Kim, J., and E. K. Longmire. 2009. Investigation of binary drop rebound and coalescence in liquids using dual-field PIV technique. *Experiments in Fluids* 47 (2): 263–78.

Klaseboer, E., J. P. Chevaillier, C. Gourdon, and O. Masbernat. 2000. Film drainage between colliding drops at constant approach velocity: experiments and modeling. *Journal of Colloid and Interface Science* 229 (1): 274–85.

Kolmogorov, A. N. 1949. On the breakage of drops in a turbulent flow. In *Dokl. Akad. Navk. SSSR*, 66:825–28. 5.

Krieger, I. M., and T. J. Dougherty. 1959. A mechanism for non-Newtonian flow in suspensions of rigid spheres. *Transactions of the Society of Rheology* 3 (1): 137–52.

Kubie, J., and G. C. Gardner. 1977. Drop sizes and drop dispersion in straight horizontal tubes and in helical coils. *Chemical Engineering Science* 32 (2): 195–202.

Lai, Y.-H., M.-H. Hsu, and J.-T. Yang. 2010. Enhanced mixing of droplets during coalescence on a surface with a wettability gradient. *Lab on a Chip* 10 (22): 3149–56.

Lake, L. W., and E. D. Holstein. 2007. Petroleum engineering handbook, Volume V (B) Reservoir engineering and petrophysics.

Lamb, H. 1932. *Hydrodynamics.* Cambridge university press.

Lance, M., and J. Bataille. 1991. Turbulence in the liquid phase of a uniform bubbly air–water flow. *Journal of Fluid Mechanics* 222:95–118.

Lashgari, I., F. Picano, W.-P. Breugem, and L. Brandt. 2014. Laminar, turbulent, and inertial shear-thickening regimes in channel flow of neutrally buoyant particle suspensions. *Physical Review Letters* 113 (25): 254502.

Lau, Y. M., N. G. Deen, and J. A. M. Kuipers. 2013. Development of an image measurement technique for size distribution in dense bubbly flows. *Chemical Engineering Science* 94:20–29.

Leighton, D., and A. Acrivos. 1987. The shear-induced migration of particles in concentrated suspensions. *Journal of Fluid Mechanics* 181:415–39.

Lemenand, T., D. Della Valle, Y. Zellouf, and H. Peerhossaini. 2003. Droplets formation in turbulent mixing of two immiscible fluids in a new type of static mixer. *International Journal of Multiphase Flow* 29 (5): 813–40.

Levich, V. G. 1962. *Physicochemical hydrodynamics.* Prentice hall.

Li, L., F. Popa, and B. C. Houchens. 2015. Mechanistic prediction of oil-water, two-phase flow in horizontal or near-horizontal pipes for a wide range of oil viscosities. In *Spe annual technical conference and exhibition.* Society of Petroleum Engineers.

Liao, Y., and D. Lucas. 2009. A literature review of theoretical models for drop and bubble breakup in turbulent dispersions. *Chemical Engineering Science* 64 (15): 3389–406.

Liao, Y., and D. Lucas. 2010. A literature review on mechanisms and models for the coalescence process of fluid particles. *Chemical Engineering Science* 65 (10): 2851–64.

Lim, S. J., B. Gim, K. Fezzaa, and B. M. Weon. 2016. Short time dynamics of water coalescence on a flat water pool. *Current Applied Physics* 16 (12): 1554–59.

Lim, S. J., M. C. Choi, B. M. Weon, and B. Gim. 2017. Lattice Boltzmann simulations for water coalescence. *Applied Physics Letters* 111 (10): 101602.

Liu, L., O. K. Matar, C. J. Lawrence, and G. F. Hewitt. 2006. Laser-induced fluorescence (LIF) studies of liquid–liquid flows. Part I: flow structures and phase inversion. *Chemical Engineering Science* 61 (12): 4007–21.

Loisel, V., M. Abbas, O. Masbernat, and E. Climent. 2013. The effect of neutrally buoyant finite-size particles on channel flows in the laminar-turbulent transition regime. *Physics of Fluids* 25 (12): 123304.

Lovick, J., and P. Angeli. 2004a. Droplet size and velocity profiles in liquid–liquid horizontal flows. *Chemical Engineering Science* 59 (15): 3105–15.

Lovick, J., and P. Angeli. 2004b. Experimental studies on the dual continuous flow pattern in oil–water flows. *International Journal of Multiphase Flow* 30 (2): 139–57.

Lu, J., S. Fang, and C. M. Corvalan. 2016. Coalescence dynamics of viscous conical drops. *Physical Review E* 93 (2): 023111.

Maaß, S., S Wollny, A Voigt, and M Kraume. 2011. Experimental comparison of measurement techniques for drop size distributions in liquid/liquid dispersions. *Experiments in Fluids* 50 (2): 259–69.

Manninen, M., V. Taivassalo, S. Kallio, et al. 1996. *On the mixture model for multiphase flow.*

Marmet, P., A. Scacchi, and J. M. Brader. 2017. Shear-induced migration in colloidal suspensions. *Molecular Physics:* 1–9.

Martin, D. W., and F. Blanchette. 2015. Simulations of surfactant effects on the dynamics of coalescing drops and bubbles. *Physics of Fluids* 27 (1): 012103.

Matas, J.-P., J. F. Morris, and É. Guazzelli. 2003. Transition to turbulence in particulate pipe flow. *Physical Review Letters* 90 (1): 014501.

Matas, J.-P., J. F. Morris, and É. Guazzelli. 2004. Inertial migration of rigid spherical particles in Poiseuille flow. *Journal of Fluid Mechanics* 515:171–95.

Matas, J.-P., J. F. Morris, and É. Guazzelli. 2009. Lateral force on a rigid sphere in large-inertia laminar pipe flow. *Journal of Fluid Mechanics* 621:59–67.

Maxey, M. R. 2017. Droplets in turbulence: A new perspective. *Journal of Fluid Mechanics* 816:1–4.

Maxwell, J. C. 1881. *A treatise on electricity and magnetism.* Vol. 1. Clarendon press.

Menchaca-Rocha, A., A. N.R. S. Martinez-Davalos, R. Nunez, S. Popinet, and S. Zaleski. 2001. Coalescence of liquid drops by surface tension. *Physical Review E* 63 (4): 046309.

Mendez-Diaz, S., J. C. Serrano-García, R. Zenit, and J. A. Hernández-Cordero. 2013. Power spectral distributions of pseudo-turbulent bubbly flows. *Physics of Fluids* 25 (4): 043303.

Mercado, J. M., D. C. Gomez, D. Van Gils, C. Sun, and D. Lohse. 2010. On bubble clustering and energy spectra in pseudo-turbulence. *Journal of Fluid Mechanics* 650:287–306.

Middleman, S. 1974. Drop size distributions produced by turbulent pipe flow of immiscible fluids through a static mixer. *Industrial & Engineering Chemistry Process Design and Development* 13 (1): 78–83.

Mitra, S., and S. K. Mitra. 2015. Symmetric drop coalescence on an under-liquid substrate. *Physical Review E* 92 (3): 033013.

Mohamed-Kassim, Z., and E. K. Longmire. 2004. Drop coalescence through a liquid/liquid interface. *Physics of Fluids* 16 (7): 2170–81.

Morgan, R. G., C. N. Markides, C. P. Hale, and G. F. Hewitt. 2012. Horizontal liquid–liquid flow characteristics at low superficial velocities using laser-induced fluorescence. *International Journal of Multiphase Flow* 43:101–17.

Morgan, R. G., C. N. Markides, I. Zadrazil, and G. F. Hewitt. 2013. Characteristics of horizontal liquid–liquid flows in a circular pipe using simultaneous high-speed laser-induced fluorescence and particle velocimetry. *International Journal of Multiphase Flow* 49:99–118.

Morgan, R. G., R. Ibarra, I. Zadrazil, O. K. Matar, G. F. Hewitt, and C. N. Markides. 2017. On the role of buoyancy-driven instabilities in horizontal liquid–liquid flow. *International Journal of Multiphase Flow* 89:123–35.

Morris, J. F., and J. F. Brady. 1998. Pressure-driven flow of a suspension: Buoyancy effects. *International Journal of Multiphase Flow* 24 (1): 105–30.

Mukhaimer, A., A. Al-Sarkhi, M. El Nakla, W. H. Ahmed, and L. Al-Hadhrami. 2015. Pressure drop and flow pattern of oil–water flow for low viscosity oils: role of mixture viscosity. *International Journal of Multiphase Flow* 73:90–96.

Munro, J. P., C. R. Anthony, O. A. Basaran, and J. R. Lister. 2015. Thin-sheet flow between coalescing bubbles. *Journal of Fluid Mechanics* 773.

Nädler, M., and D. Mewes. 1997. Flow induced emulsification in the flow of two immiscible liquids in horizontal pipes. *International Journal of Multiphase Flow* 23 (1): 55–68.

Ng, T. S., C. J. Lawrence, and G. F. Hewitt. 2002. Laminar stratified pipe flow. *International Journal of Multiphase Flow* 28 (6): 963–96.

Ngan, K. H. 2011. Phase inversion in dispersed liquid-liquid pipe flow. PhD diss., University College London.

Ngan, K. H., K. Ioannou, L. D. Rhyne, W. Wang, and P. Angeli. 2009. A methodology for predicting phase inversion during liquid–liquid dispersed pipeline flow. *Chemical Engineering Research and Design* 87 (3): 318–24.

Ngan, K. H., K. Ioannou, L. D. Rhyne, and P. Angeli. 2011. Effect of glycerol addition on phase inversion in horizontal dispersed oil–water pipe flows. *Experimental Thermal and Fluid Science* 35 (4): 628–35.

Nigmatulin, T. R., F. J. Bonetto, A. E. Larreteguy, R. T. Lahey Jr, and J. B. McQuillen. 2000. An experimental study of dispersed liquid/liquid two-phase upflow in a pipe. *Chemical Engineering Communications* 182 (1): 121–62.

Nobach, H., and M. Honkanen. 2005. Two-dimensional Gaussian regression for subpixel displacement estimation in particle image velocimetry or particle position estimation in particle tracking velocimetry. *Experiments in Fluids* 38 (4): 511–15.

Norman, J. T., H. V. Nayak, and R. T. Bonnecaze. 2005. Migration of buoyant particles in low-Reynolds-number pressure-driven flows. *Journal of Fluid Mechanics* 523:1–35.

Nott, P. R., and J. F. Brady. 1994. Pressure-driven flow of suspensions: Simulation and theory. *Journal of Fluid Mechanics* 275:157–99.

Nowak, E., N. M. Kovalchuk, Z. Che, and M. J. H. Simmons. 2016. Effect of surfactant concentration and viscosity of outer phase during the coalescence of a surfactant-laden drop with a surfactant-free drop. *Colloids and Surfaces A: Physicochemical and Engineering Aspects* 505:124–31.

Nowak, E., Z. Xie, N. M. Kovalchuk, O. K. Matar, and M. J. Simmons. 2017. Bulk advection and interfacial flows in the binary coalescence of surfactant-laden and surfactant-free drops. *Soft Matter* 13:4616–28.

Oddie, G., and J. A. Pearson. 2004. Flow-rate measurement in two-phase flow. *Annual Reviews of Fluid Mechanics* 36:149–72.

Oliemans, R. V. A. 1986. The lubricating-film model for core-annular flow. PhD diss., Delft University of Technology.

Ooms, G., and P. Poesio. 2003. Stationary core-annular flow through a horizontal pipe. *Physical Review E* 68 (6): 066301.

Ortiz-Dueñas, C., J. Kim, and E. K. Longmire. 2010. Investigation of liquid–liquid drop coalescence using tomographic PIV. *Experiments in Fluids* 49 (1): 111–29.

Pal, R. 2001. Evaluation of theoretical viscosity models for concentrated emulsions at low capillary numbers. *Chemical Engineering Journal* 81 (1): 15–21.

Park, K. H., M. Chinaud, and P. Angeli. 2016. Transition from stratified to non-stratified oil–water flows using a bluff body. *Experimental Thermal and Fluid Science* 76:175–84.

Paul, H. I., and C. A. Sleicher. 1965. The maximum stable drop size in turbulent flow: Effect of pipe diameter. *Chemical Engineering Science* 20 (1): 57–59.

Paulsen, J. D. 2013. Approach and coalescence of liquid drops in air. *Physical Review E* 88 (6): 063010.

Paulsen, J. D., J. C. Burton, and S. R. Nagel. 2011. Viscous to inertial crossover in liquid drop coalescence. *Physical Review Letters* 106 (11): 114501.

Paulsen, J. D., J. C. Burton, S. R. Nagel, S. Appathurai, M. T. Harris, and O. A. Basaran. 2012. The inexorable resistance of inertia determines the initial regime of drop coalescence. *Proceedings of the National Academy of Sciences* 109 (18): 6857–61.

Paulsen, J. D., R. Carmigniani, A. Kannan, J. C. Burton, and S. R. Nagel. 2014. Coalescence of bubbles and drops in an outer fluid. *Nature Communications* 5:3182.

Percy, J. S., and C. A. Sleicher. 1983. Drop breakup in the flow of immiscible liquids through an orifice in a pipe. *AIChE Journal* 29 (1): 161–64.

Pereyra, E., R. S. Mohan, and O. Shoham. 2013. A simplified mechanistic model for an oil/water horizontal pipe separator. *Oil and Gas Facilities* 2 (03): 40–46.

Pérez, C. A. 2005. Horizontal pipe separator (HPS©) experiments and modeling. PhD diss., University of Tulsa.

Perry, R. H., D. W. Green, and J. O. Maloney. 1997. Perry's handbook of chemical engineering. *Perry's Handbook of Chemical Engineering.*

Phan-Thien, N., and D. C. Pham. 1997. Differential multiphase models for polydispersed suspensions and particulate solids. *Journal of Non-Newtonian Fluid Mechanics* 72 (2): 305–18.

Phillips, R. J., R. C. Armstrong, R. A. Brown, A. L. Graham, and J. R. Abbott. 1992. A constitutive equation for concentrated suspensions that accounts for shear-induced particle migration. *Physics of Fluids A: Fluid Dynamics* 4 (1): 30–40.

Pilehvari, A, B. Saadevandi, M. Halvaci, and P. E. Clark. 1988. Oil/water emulsions for pipeline transport of viscous crude oils. In *Spe annual technical conference and exhibition.* Society of Petroleum Engineers.

Pilhofer, T., and D. Mewes. 1979. *Siebboden-Extraktionskolonnen: Vorausberechnung unpulsierter Kolonnen.* Verlag Chemie.

Pope, S. B. 2001. *Turbulent flows.* IOP Publishing.

Pouplin, A., O. Masbernat, S. Décarre, and A. Liné. 2011. Wall friction and effective viscosity of a homogeneous dispersed liquid–liquid flow in a horizontal pipe. *AIChE Journal* 57 (5): 1119–31.

Pouraria, H., J. K. Seo, and J. K. Paik. 2016. Numerical modelling of two-phase oil–water flow patterns in a subsea pipeline. *Ocean Engineering* 115:135–48.

Prakash, V. N., J. M. Mercado, L. van Wijngaarden, E. Mancilla, Y. Tagawa, D. Lohse, and C. Sun. 2016. Energy spectra in turbulent bubbly flows. *Journal of Fluid Mechanics* 791:174–90.

Prasser, H.-M., M. Misawa, and I. Tiseanu. 2005. Comparison between wire-mesh sensor and ultra-fast x-ray tomograph for an air–water flow in a vertical pipe. *Flow Measurement and Instrumentation* 16 (2): 73–83.

Ramachandran, A., and L. G. Leal. 2016. Effect of interfacial slip on the thin film drainage time for two equal-sized, surfactant-free drops undergoing a head-on collision: a scaling analysis. *Physical Review Fluids* 1 (6): 064204.

Rao, R., L. Mondy, A. Sun, and S. Altobelli. 2002. A numerical and experimental study of batch sedimentation and viscous resuspension. *International Journal for Numerical Methods in Fluids* 39 (6): 465–83.

Reynolds, O. 1875. On the action of rain to calm the sea. *Nature* 11:279–80.

Reynolds, O. 1881. On the floating of drops on the surface of water depending only on the purity of the surface. *Proc. Manchester Lit. Phil. Soc* 21 (1).

Reynolds, O. 1883. An experimental investigation of the circumstances which determine whether the motion of water shall be direct or sinuous, and of the law of resistance in parallel channels. *Proceedings of the royal society of London* 35 (224-226): 84–99.

Riboux, G., D. Legendre, and F. Risso. 2013. A model of bubble-induced turbulence based on large-scale wake interactions. *Journal of Fluid Mechanics* 719:362–87.

Ristenpart, W. D., J. C. Bird, A. Belmonte, F. Dollar, and H. A. Stone. 2009. Non-coalescence of oppositely charged drops.

Rodriguez, O. M. H., and R. V. A. Oliemans. 2006. Experimental study on oil–water flow in horizontal and slightly inclined pipes. *International Journal of Multiphase Flow* 32 (3): 323–43.

Rosin, P., and E. Rammler. 1933. The laws governing the fineness of powdered coal. *Journal of the Institute Fuel* 7:29–36.

Sadhal, S., P. S. Ayyaswamy, and J. N. Chung. 2012. *Transport phenomena with drops and bubbles.* Springer Science & Business Media.

Saffman, P. G., and G. Taylor. 1958. The penetration of a fluid into a porous medium or Hele-Shaw cell containing a more viscous liquid. In *Proceedings of the royal society of london a: mathematical, physical and engineering sciences*, 245:312–29. 1242. The Royal Society.

Schaflinger, U., A. Acrivos, and K. Zhang. 1990. Viscous resuspension of a sediment within a laminar and stratified flow. *International Journal of Multiphase Flow* 16 (4): 567–78.

Schonberg, J. A., and E. J. Hinch. 1989. Inertial migration of a sphere in Poiseuille flow. *Journal of Fluid Mechanics* 203:517–24.

Schümann, H., M. Khatibi, M. Tutkun, B. H. Pettersen, Z. Yang, and O. J. Nydal. 2015. Droplet size measurements in oil–water dispersions: A comparison study using fbrm and pvm. *Journal of Dispersion Science and Technology* 36 (10): 1432–43.

Schümann, H., M. Tutkun, Z. Yang, and O. J. Nydal. 2016a. Experimental study of dispersed oil-water flow in a horizontal pipe with enhanced inlet mixing, Part 1: Flow patterns, phase distributions and pressure gradients. *Journal of Petroleum Science and Engineering* 145:742–52.

Schümann, H., M. Tutkun, and O. J. Nydal. 2016b. Experimental study of dispersed oil-water flow in a horizontal pipe with enhanced inlet mixing, Part 2: In-situ droplet measurements. *Journal of Petroleum Science and Engineering* 145:753–62.

Scott, D. W. 2009. Sturges' rule. *Wiley Interdisciplinary Reviews: Computational Statistics* 1 (3): 303–6.

Scott, L. S., W. B. Hayes, and C. D. Holland. 1958. The formation of interfacial area in immiscible liquids by orifice mixers. *AIChE Journal* 4 (3): 346–50.

Semwogerere, D., J. F. Morris, and E. R. Weeks. 2007. Development of particle migration in pressure-driven flow of a brownian suspension. *Journal of Fluid Mechanics* 581:437–51.

Shah, R. K., and M. S. Bhatti. 1987. Laminar convective heat transfer in ducts. In *Handbook of single-phase convective heat transfer.* Wiley, New York.

Shi, J., and H. Yeung. 2017. Characterization of liquid-liquid flows in horizontal pipes. *AIChE Journal* 63 (3): 1132–43.

Simmons, M. J. H., and B. J. Azzopardi. 2001. Drop size distributions in dispersed liquid–liquid pipe flow. *International Journal of Multiphase Flow* 27 (5): 843–59.

Simmons, M. J. H., S. H. Zaidi, and B. J. Azzopardi. 2000. Comparison of laser-based drop-size measurement techniques and their application to dispersed liquid-liquid pipe flow. *Optical Engineering* 39 (2): 505–9.

Sleicher, C. A. 1962. Maximum stable drop size in turbulent flow. *AIChE Journal* 8 (4): 471–77.

Soleimani, A., C. J. Lawrence, and G. F. Hewitt. 2000. Spatial distribution of oil and water in horizontal pipe flow. *SPE Journal* 5 (04): 394–401.

Solsvik, J., and H. A. Jakobsen. 2015. The foundation of the population balance equation: a review. *Journal of Dispersion Science and Technology* 36 (4): 510–20.

Sprittles, J. E., and Y. D. Shikhmurzaev. 2012. Coalescence of liquid drops: Different models versus experiment. *Physics of Fluids* 24 (12): 122105.

Stone, H. A. 1994. Dynamics of drop deformation and breakup in viscous fluids. *Annual Review of Fluid Mechanics* 26 (1): 65–102.

Subia, S. R., M. S. Ingber, L. A. Mondy, S. A. Altobelli, and A. L. Graham. 1998. Modelling of concentrated suspensions using a continuum constitutive equation. *Journal of Fluid Mechanics* 373:193–219.

Sun, K., T. Wang, P. Zhang, and C. K. Law. 2015. Non-newtonian flow effects on the coalescence and mixing of initially stationary droplets of shear-thinning fluids. *Physical Review E* 91 (2): 023009.

Takehara, K., and T. Etoh. 1998. A study on particle identification in PTV particle mask correlation method. *Journal of Visualization* 1 (3): 313–23.

Tam, K. C., and C. Tiu. 1989. Steady and dynamic shear properties of aqueous polymer solutions. *Journal of Rheology* 33 (2): 257–80.

Taylor, G. I. 1932. The viscosity of a fluid containing small drops of another fluid. *Proceedings of the Royal Society of London. Series A, Containing Papers of a Mathematical and Physical Character* 138 (834): 41–48.

Theron, F., and N. Le Sauze. 2011. Comparison between three static mixers for emulsification in turbulent flow. *International Journal of Multiphase Flow* 37 (5): 488–500.

Thielicke, W., and E. Stamhuis. 2014. PIVlab–towards user-friendly, affordable and accurate digital particle image velocimetry in MATLAB. *Journal of Open Research Software* 2 (1).

Thompson, A. B., and J. Billingham. 2012. Inviscid coalescence in the presence of a surrounding fluid. *The IMA Journal of Applied Mathematics* 77 (5): 678–96.

Thoroddsen, S. T., K. Takehara, and T. G. Etoh. 2005. The coalescence speed of a pendent and a sessile drop. *Journal of Fluid Mechanics* 527:85–114.

Thoroddsen, S. T., B. Qian, T. G. Etoh, and K. Takehara. 2007. The initial coalescence of miscible drops. *Physics of Fluids* 19 (7): 072110.

Thurston, G. B., and G. A. Pope. 1981. Shear rate dependence of the viscoelasticity of polymer solutions: II. Xanthan gum. *Journal of Non-Newtonian Fluid Mechanics* 9 (1-2): 69–78.

Thurston, G. B. 1981. Shear rate dependence of the viscoelasticity of polymer solutions.: I. Theoretical model. *Journal of non-Newtonian Fluid Mechanics* 9 (1-2): 57–68.

Tidhar, M., J. C. Merchuk, A. N. Sembira, and D. Wolf. 1986. Characteristics of a motionless mixer for dispersion of immiscible fluids—II. Phase inversion of liquid-liquid systems. *Chemical Engineering Science* 41 (3): 457–62.

Tiwari, P., S. P. Antal, and M. Z. Podowski. 2009. Modeling shear-induced diffusion force in particulate flows. *Computers & Fluids* 38 (4): 727–37.

Trallero, J. L., C. Sarica, and J. P. Brill. 1997. A study of oil-water flow patterns in horizontal pipes. *SPE Production & Facilities* 12 (03): 165–72.

Trier, O. D., and T. Taxt. 1995. Evaluation of binarization methods for document images. *IEEE Transactions on Pattern Analysis and Machine Intelligence* 17 (3): 312–15.

Tropea, C., and A. L. Yarin. 2007. *Springer handbook of experimental fluid mechanics.* Vol. 1. Springer Science & Business Media.

Vasseur, P., and R. G. Cox. 1976. The lateral migration of a spherical particle in two-dimensional shear flows. *Journal of Fluid Mechanics* 78 (2): 385–413.

Verdier, C., and M. Brizard. 2002. Understanding droplet coalescence and its use to estimate interfacial tension. *Rheologica acta* 41 (6): 514–23.

Voulgaropoulos, V., and P. Angeli. 2017. Optical measurements in evolving dispersed pipe flows. *Experiments in Fluids* 58 (12): 170.

Voulgaropoulos, V., L.-S. Zhai, K. Ioannou, and P. Angeli. 2016. Evolution of unstable liquid-liquid dispersions in horizontal pipes. In *10th north american conference on multiphase technology*. BHR Group.

Wallis, G. B. 1969. One-dimensional two-phase flow.

Wang, L., G. Zhang, H. Wu, J. Yang, and Y. Zhu. 2016. Note: a top-view optical approach for observing the coalescence of liquid drops. *Review of Scientific Instruments* 87 (2): 026103.

Wang, W., J. Gong, K. H. Ngan, and P. Angeli. 2009. Effect of glycerol on the binary coalescence of water drops in stagnant oil phase. *Chemical Engineering Research and Design* 87 (12): 1640–48.

Ward, J. P., and J. G. Knudsen. 1967. Turbulent flow of unstable liquid-liquid dispersions: Drop sizes and velocity distributions. *AIChE Journal* 13 (2): 356–65.

Wegmann, A., and P. R. von Rohr. 2006. Two phase liquid–liquid flows in pipes of small diameters. *International Journal of Multiphase Flow* 32 (8): 1017–28.

Weheliye, W. H., T. Dong, and P. Angeli. 2017. On the effect of surfactants on drop coalescence at liquid/liquid interfaces. *Chemical Engineering Science* 161:215–27.

Welle, R. Van der. 1985. Void fraction, bubble velocity and bubble size in two-phase flow. *International Journal of Multiphase Flow* 11 (3): 317–45.

Westerweel, J. 1997. Fundamentals of digital particle image velocimetry. *Measurement Science and Technology* 8 (12): 1379.

Westerweel, J. 2008. On velocity gradients in PIV interrogation. *Experiments in Fluids* 44 (5): 831–42.

Westerweel, J., and F. Scarano. 2005. Universal outlier detection for PIV data. *Experiments in Fluids* 39 (6): 1096–100.

Westerweel, J., D. Dabiri, and M. Gharib. 1997. The effect of a discrete window offset on the accuracy of cross-correlation analysis of digital PIV recordings. *Experiments in Fluids* 23 (1): 20–28.

Westerweel, J., G. E. Elsinga, and R. J. Adrian. 2013. Particle image velocimetry for complex and turbulent flows. *Annual Review of Fluid Mechanics* 45:409–36.

Whittaker, E. T., and G. N. Watson. 1996. *A course of modern analysis*. Cambridge university press.

Wright, S. F., I. Zadrazil, and C. N. Markides. 2017. A review of solid–fluid selection options for optical-based measurements in single-phase liquid, two-phase liquid–liquid and multiphase solid–liquid flows. *Experiments in Fluids* 58 (9): 108.

Wu, M., T. Cubaud, and C.-M. Ho. 2004. Scaling law in liquid drop coalescence driven by surface tension. *Physics of Fluids* 16 (7): L51–L54.

Wu, X., F. Babatola, L. Jiang, B. T. Tolbert, and J. Liu. 2016. Applying subsea fluid-processing technologies for deepwater operations. *Oil and Gas Facilities* 5 (04).

Xie, F., X. Zheng, M. S. Triantafyllou, Y. Constantinides, Y. Zheng, and G. E. Karniadakis. 2017. Direct numerical simulations of two-phase flow in an inclined pipe. *Journal of Fluid Mechanics* 825:189–207.

Xu, J. H., G. S. Luo, G. G. Chen, and J. D. Wang. 2005. Experimental and theoretical approaches on droplet formation from a micrometer screen hole. *Journal of Membrane Science* 266 (1): 121–31.

Yamamoto, T., H. Kawasaki, and H. Kumazawa. 2007. Relationship between the dispersed droplet diameter and the mean power input for emulsification in three different types of motionless mixers. *Journal of Chemical Engineering of Japan* 40 (8): 673–78.

Yan, Y., and J. Koplik. 2009. Transport and sedimentation of suspended particles in inertial pressure-driven flow. *Physics of Fluids* 21 (1): 013301.

Yang, Z. 2014. A study of viscous oil and water pipe flow. In *9th north american conference on multiphase technology*. BHR Group.

Yanowitz, S. D., and A. M. Bruckstein. 1988. A new method for image segmentation. In *Pattern recognition, 1988., 9th international conference on*, 270–75. IEEE.

Yao, W., H. J. Maris, P. Pennington, and G. M. Seidel. 2005. Coalescence of viscous liquid drops. *Physical Review E* 71 (1): 016309.

Yaron, I., and B. Gal-Or. 1972. On viscous flow and effective viscosity of concentrated suspensions and emulsions. *Rheologica Acta* 11 (3): 241–52.

Yeo, K., and M. R. Maxey. 2011. Numerical simulations of concentrated suspensions of monodisperse particles in a Poiseuille flow. *Journal of Fluid Mechanics* 682:491–518.

Yeo, L. Y., O. K. Matar, E. S. P. de Ortiz, and G. F. Hewitt. 2003. Film drainage between two surfactant-coated drops colliding at constant approach velocity. *Journal of Colloid and Interface Science* 257 (1): 93–107.

Yiantsios, S. G., and B. G. Higgins. 1988. Linear stability of plane Poiseuille flow of two superposed fluids. *The Physics of Fluids* 31 (11): 3225–38.

Yilmazer, U., and D. M. Kalyon. 1989. Slip effects in capillary and parallel disk torsional flows of highly filled suspensions. *Journal of Rheology* 33 (8): 1197–212.

Yin, X., and D. L. Koch. 2007. Hindered settling velocity and microstructure in suspensions of solid spheres with moderate Reynolds numbers. *Physics of Fluids* 19 (9): 093302.

Yokota, M., and K. Okumura. 2011. Dimensional crossover in the coalescence dynamics of viscous drops confined in between two plates. *Proceedings of the National Academy of Sciences* 108 (16): 6395–98.

Yu, Z., T. Wu, X. Shao, and J. Lin. 2013. Numerical studies of the effects of large neutrally buoyant particles on the flow instability and transition to turbulence in pipe flow. *Physics Of Fluids* 25 (4): 043305.

Yue, P., C. Zhou, and J. J. Feng. 2006. A computational study of the coalescence between a drop and an interface in newtonian and viscoelastic fluids. *Physics of Fluids* 18 (10): 102102.

Yusoff, N. H. 2012. Stratifying of liquid-liquid two phase flows through sudden expansion. PhD diss., University of Nottingham.

Zarraga, I. E., D. A. Hill, and D. T. Leighton Jr. 2000. The characterization of the total stress of concentrated suspensions of noncolloidal spheres in newtonian fluids. *Journal of Rheology* 44 (2): 185–220.

Zhai, L.-S., N. Jin, Y. Zong, Z. Wang, and M. Gu. 2012. The development of a conductance method for measuring liquid holdup in horizontal oil–water two-phase flows. *Measurement Science and Technology* 23 (2): 025304.

Zhai, L.-S., P. Bian, Z.-K. Gao, and N.-D. Jin. 2016. The measurement of local flow parameters for gas–liquid two-phase bubbly flows using a dual-sensor probe array. *Chemical Engineering Science* 144:346–63.

Zhai, L.-S., X.-Y. Li, P. Bian, and N.-D. Jin. 2017. Measurement of droplet sizes in bubbly oil-in-water flows using a fluid-sampling device. *Measurement* 102:296–308.

Zhang, F. H., M.-J. Thoraval, S. T. Thoroddsen, and P. Taborek. 2015. Partial coalescence from bubbles to drops. *Journal of Fluid Mechanics* 782:209–39.

Zhang, K., and A. Acrivos. 1994. Viscous resuspension in fully developed laminar pipe flows. *International Journal of Multiphase Flow* 20 (3): 579–91.

Zhou, G., and S. M. Kresta. 1998. Evolution of drop size distribution in liquid–liquid dispersions for various impellers. *Chemical Engineering Science* 53 (11): 2099–113.

Zhu, T., S. J. Du, and X. X. He. 2015. Enrichment and separation of coal mine ventilation methane and engineering education. *Advanced Materials Research* 1073:2078–81.

Zuiderveld, K. 1994. Contrast limited adaptive histogram equalization. In *Graphics gems IV*, 474–85. Academic Press Professional, Inc.